universiteit hasselt
KNOWLEDGE IN ACTION

2014 | Faculty of Sciences

DOCTORAL DISSERTATION

Solution processing of n-type doped ZnO

Doctoral dissertation submitted to obtain the degree of
Doctor of Science: Chemistry, to be defended by

Hanne Damm

Promoter: Prof. Dr Marlies K Van Bael | UHasselt
Co-promoter: Prof. Dr An Hardy | UHasselt

D/2014/2451/63

universiteit hasselt | imec
IMO - IMOMEC
INSTITUUT VOOR MATERIAALONDERZOEK

Members of the Jury

Chairman

Prof. Dr. Karin CONINX
Dean Faculty of Sciences, UHasselt

Promoter

Prof. Dr. Marlies K. Van Bael, UHasselt

Co-promoter

Prof. Dr. An Hardy, UHasselt

Members of the Jury

Prof. Dr. Jean MANCA, UHasselt
Prof. Dr. Christophe Detavernier, UGhent
Prof. Dr. Jan D'Haen, UHasselt
Prof. Dr. Peter Adriaensens, UHasselt
Prof. Dr. Bart Partoens, University of Antwerp
Prof. Dr. Mariadriana Creatore, TUe
Dr. Andrea Illiberi, TNO

Acknowledgement

Laten we beginnen met iets luchtig: een dankwoord. Want na deze pagina's zullen sommige van jullie waarschijnlijk al afhaken. Hopelijk niet allemaal, want het schrijven van wat ik nu de afgelopen vier jaar heb gedaan ging echt niet zonder slag of stoot. Gedurende de afgelopen vier jaar heb ik jullie proberen uit te leggen wat ik precies heb gedaan. Bij de ene is dat al wat beter doorgedrongen dan bij de andere, maar geloof me iedereen in dit deel heeft hier op één of andere manier aan bijgedragen! DANK JE WEL!

Soms schieten woorden tekort, soms is nu...

In eerste instantie wil ik mijn Promotor, Prof. dr. Marlies K. Van Bael, en Co-promotor, Prof. dr. An Hardy, bedanken voor de opportuniteit om een doctoraatsstudie te voltooien over transparante geleidende oxides. Ik weet nog heel goed dat jullie tegen me zeiden dat er een project was dat perfect bij mij paste. Niet minder dan 9 jaar geleden had ik immers op de universiteit een projectje gemaakt over duurzame energie en dit doctoraat sloot daar helemaal bij aan. Iedereen die mij kent weet immers dat duurzaamheid en het milieu heel belangrijke aspecten in mijn leven zijn en ik was dan ook enorm blij om op één of andere manier een steentje bij te dragen. Ik denk dat ik dat ook heb gedaan! Gedurende de afgelopen vier jaar heb ik niet alleen veel kennis opgedaan, maar heb ik ook andere kwaliteiten van mezelf (her)ondekt: doorzettingsvermogen, netwerken, managen van deadlines, begeleiden van studenten, ... Hartelijk bedankt voor alle fijne en ook moeilijke momenten, want zelfs voor die laatste ben ik dankbaar. Er is geen doctoraat zonder veel watertjes te doorzwemmen.

Ik had het genoegen om mijn doctoraat uit te voeren binnen een groot consortium nl. SIM. Dit zorgde ervoor dat vele experten mij met raad en daad hebben bijgestaan doorheen de jaren. Daarom zou ik nu graag deze mensen van de UA, UGent, KULeuven, Umicore, Agfa, AGC, het IWT ... willen bedanken. Ik had het genoegen om samen te werken met enkele zeer sterke microscopisten nl. Prof. dr. Joke Hadermann, dr. Maria Batuk, Anne Bertha en hun collega's. Bedankt om jullie expertise te willen loslaten op mijn stalen. Dit heeft zeker een extra dimensie gegeven aan mijn doctoraat.
De mensen van de CoCooN groep: Boris Capon en Prof. dr. Christophe

Detavernier. Jullie hebben een fantastisch labo dat state-of-the-art metingen kan uitvoeren. Bedankt voor de vele anneals en additionele karakterisatie.
De NMR mensen van Gent: Freya en Prof. dr. José Martins. Bedankt voor de vele zeer specifieke karakterisatie die enorm veel heeft bijgedragen in mijn allereerste publicatie. Freya, ook bedankt voor de fijne tijd in Amerika!

Doorheen de jaren zijn er al enkele collega's de revue gepasseerd, hoewel de meeste bleven plakken aan de universiteit.
Linny, Bertie en Daan, ondertussen al eventjes weg op de unief, maar uit het oog is zeker niet uit het hart. Bedankt voor jullie vriendschap en de fijne tijd aan de unief.
Ken, één van onze anciens met tonnen ZnO ervaring. Bedankt voor je begeleiding, steun, kalmte en collegialiteit. Je hebt je handen vol gehad om het ZnO team in goede banen te leiden waarvan ook Anke en Kevin deel van uitmaakten. Jullie bijdrage aan mijn doctoraat is niet te overzien.
Alexander, onze clown, historisch! Als jij de deur achter je dicht slaat van deze universiteit zal de pretbeleving serieus dalen. Het waren zalige kaartmomenten (al dan niet met snot) en historische filmpjes voor verschillende doctoraten. Zalig!
Nick, onze newby post-doc. . . ! Ik zal onze (koffie)breaks en de leuke babbels missen. Olmen tuttert, Krakau/Warschau en The Chambers Trophy zijn enkele van die fijne dingen die we hebben meegemaakt. Buiten het plezier, kon ik bij jou ook terecht voor een wetenschappelijke discussie tijdens een wandeling of mocht ik achter je (duracell konijn) aan lopen tijdens de middag. Thanks!
Nikolina, thanks for the great time in Leuven during the physical characterization course and your friendship over the past years.
Sven, 9 jaar volgden we al een beetje hetzelfde traject, maar nu scheiden onze wegen. Ik wens je super veel succes bij het afronden van je doctoraat en laat eens iets horen hoe je het stelt.
Giedrius, always a bit from the sideline . . . I can't blaim you with such a big diversity of personalities. You must have gone crazy while we were all stacked together in the landscape office. Good luck with your PhD!
Dan de jongere generatie, Maarten en Thomas: allebei speciaal, heel vriendelijk en behulpzaam. Ik vind het leuk dat ik jullie nog bij Jong-KVCV zal tegenkomen. Samen gaan we nog leuke dingen doen! Bedankt voor BÃ¨r en pizzahut avonden. Dat zijn de dingen die je overeind houden tijdens een doctoraat.
Ellen, vergeet niet in jezelf te geloven en af en toe een beetje stoom van de ketel af te laten. Je bent een geweldige meid. Merlijn mag zich gelukkig prijzen met zo'n wife-to-be.
Giulia, you have a wonderful personality and I wish I could have spent more time with you. Thanks for EMRS and the pants, I still love them! We will keep in touch!

Jonathan, Boaz, Gilles, en Wouter ik ken jullie niet zo goed, maar ik wil jullie vooral veel succes wensen met alles wat jullie doen, zowel professioneel en privé. Boaz, niet teveel worstenbroodjes eten...
The new guys: Dries, Fulya, Alexander,... and all those who might every join the IPC group and read this thesis: good luck and be persistent!

Dan zijn er nog een hele hoop andere collega's op de UHasselt, die mijn doctoraat iets makkelijker maakten.
De collega's van TOES/TANC: Elsy, Ivo, Martine, Guy, Prof. dr. Robert Carleer, Jens, Inge, Kenny ... bedankt voor jullie expertise te delen en mij altijd op weg te helpen met jullie toestellen. Elsy, merci voor de leuke babbels en de vriendschap. Ik hoop dat we elkaar nog geregeld zien. Prof. dr. Peter Adriaensens en Gunter voor de vele NMR metingen en besprekingen van resultaten. Zonder jullie ondersteuning zou ik 50 pagina's moeten schrappen van deze thesis!
De collega's van organische: Rafael, Jurgen, Inge, Hanne, Pieter, ... Merci voor de hulp en de leuke sfeer in de gangen. Jurgen, the states waren awesome!
De collega's van didactiek: Hilde, Eugene, Rita, ... zonder jullie steun waren de labo's een regelrechte ramp geworden! Dank je wel.
De collega's van de fysica: Jeroen, Matthias, Andreas, Koen, Bert, Bart, Christel en Hilde. Bedankt voor alle metingen, hulp en technische ondersteuning! Jullie zijn een super team. Prof. dr. Jan D'Haen, bedankt voor al de maandagvoormiddag momenten. De wetenschappelijke discussies waren een grote toegevoegde waarde aan mijn doctoraat. Bedankt voor je kritische kijk en eerlijkheid! Prof. dr. Jean Manca, bedankt voor alle ondersteuning van jou en jouw team.

Ook mijn thesisstudenten zou ik uitdrukkelijk willen bedanken voor hun harde werk! Caroline, Tine en Evelyn: jullie hebben allemaal super hard gewerkt voor mij en mijn thesis en ik hoop dat jullie jullie bijdrage hier dan ook vlot in kunnen terugvinden. Veel succes in jullie verdere studies en werk! Ik ben nu al een beetje fier!

Voorts wil ik ook mijn nieuwe collega's en bazen bedanken, want na een doctoraat is het altijd een beetje zoeken naar waar je naartoe gaat en wat je rol verder in de maatschappij zal zijn. Als chemist en materiaalwetenschapper zijn je opties niet beperkt. Zoals je ziet kan je zelfs overstappen naar de voedselindustrie, meer bepaald zelfs de drankensector, waar Konings NV meer is dan een alledaags bedrijf.
Graag zou ik dan ook dr. ir. Sonja Vanhamel en CEO Dirk Maris bedanken voor de uitdagende job als R&D ingenieur bij de verwerking van hard fruit: appels en peren, tot sappen, ciders en concentraten. Ik hoop dat de talenten die ik tijdens mijn doctoraatsstudie heb ontplooid tot zijn recht komen bij jullie. Ook Jos Rutten, Jef Moors en Luc Nulens bedankt voor deze kans!

Sabrina, Hilde en Caroline bedankt om mij met open armen te ontvangen binnen jullie team. Ik ben zo fier om van jullie groep deel uit te mogen maken. De smaakvolle dranken die jullie ontwikkelen bezorgen heel veel mensen over heel de wereld genot. Vooral Sabrina bedankt om mij thuis te laten voelen op K2.
Het lijstje van mensen op Konings begint al serieus aan te dikken en spijtig genoeg ken ik nog niet altijd iedereen met naam . . . , maar ik ga toch een poging doen. Pascal, onze top-atleet zowel binnen als buiten het labo, bedankt voor de helpende hand. Gilles en Yannick, bedankt voor de technische ondersteuning. Wouter en Wim bedankt om jullie kennis met mij te delen en mij op gang te helpen binnen de verwerking van appelen en peren. Ik wil ook nog de operatoren op K2 specifiek bedanken voor alle hulp op de werkvloer: Tom, Ronny, Luc, Dominique, Jurgen en alle andere! Merci mannen! Ook onze dames (en heren) van beneden wil ik niet vergeten. Bedankt voor de leuke sfeer, warmte, gezelligheid en de steun de afgelopen maanden: Martine, Nele, Kandy, Natalie, Stefanie, Anita, Thomas, Carlo en Jeroen. Ook de andere mensen op K1 helpen me altijd: Natalie, Wouter, Isabelle, Frank, Niek, Kris, Ellen, Pascal, Erwin, Sylvie, Heidi, Kim, Koen en zijn team, Marleen, Stefano, Evi, Kristien, ... Om niet te vergeten, al de mensen die het fabriek laten draaien op K1, K2 en K3 waarvan ik jammer genoeg de namen niet allemaal weet: bedankt voor de collegialiteit!

De KVCVers! Als ik ergens veel heb bijgeleerd dan was het wel bij jullie. Ik vind het een eer om mee te mogen werken aan popularisatie van (bio)chemie in de maatschappij. We hebben zo'n sterk en goed team! Bedankt Christophe, Christopher, Ken, Yannick, Karel, Frederique, Tim, Kersten, Jens, Wouter, Ellen, Sven, Thomas, Liene, Jens, Daniel, Geert-Jan, Frank, Bart en al de nieuwkomers. Jens, Frank en Geert-Jan succes de komende jaren, maar natuurlijk kunnen jullie op me blijven rekenen!

Christopher en Lize, zoals jullie hebben gemerkt ben ik jullie niet vergeten maar heb ik jullie niet meer tussen de collega's gezet, want de dingen die we delen gaan verder dan collegialiteit. Buiten de wetenschappelijke ondersteuning heb ik van jullie zowel als van jullie partners, Katrien en Tom, veel vriendschap gehad en hebben we samen super toffe momenten beleefd.
My girls: Anke, Ine en Michelle! Samen zijn we 9 jaar geleden gestart aan de UHasselt en vandaag de dag ondersteunen we elkaar nog. Jullie zijn super meiden. Ik ben blij om jullie in mijn leven te hebben. Veel succes met alles wat jullie nog doen, want wat dat ook mag zijn, van één ding ben ik zeker: jullie gaan daarin uitblinken. Bovendien sta ik altijd paraat voor een helpende hand toe te steken. Geloof in jezelf en geniet van iedere dag! Zie jullie graag!
Dieter en Inge, jullie zijn zo'n lieve mensen en ik ben (wij zijn) echt vereerd om deel te mogen uitmaken van jullie vriendengroep. Bedankt voor je begrip, vertrouwen, luisterend oor en warmte en vriendschap.

Kurt, bedankt voor je steun en motivatie! Het leven is niet altijd gemakkelijk, maar we moeten genieten van iedere dag en dat doen we met onze etentjes en leuke momenten!
Leen (en Benjamin), jammer genoeg zie ik je iets te weinig, maar wat begon met een kotgenootje groeide uit tot een zalige vriendschap. Ik hou van je down-to-earth ingesteldheid en je warme persoonlijkheid. Jouw gezinnetje is een pareltje. Koester jouw schatjes!
Kim, onze Spaanse passie bracht ons samen. Ik hoop dat we in de toekomst nog meer leuke dingen samen kunnen doen! Veel succes met het huisje!
Evi (en Geert), Pilar (en Niels) en Petra: bedankt voor jullie vriendschap en steun en de super leuke zumba momenten! Jullie zijn super madammen.
Ook mijn oude vertrouwde fitness buddies wil niet vergeten: Petra, Liesbeth, Kelly, Maritha, Rosita, Debbie, Miche, ... Jullie zorgden ervoor dat ik de stress kon weg shaken.

Dan kom ik bij mijn familie, dewelke het ook zwaar heeft moeten ontgelden de afgelopen maanden. Tante Sophie, Nonke Nick, Tante Christel, Yolanda, Stefan, Sabien en Wim, jullie zijn de beste familie iemand zich wensen. Hartelijk dank voor al de fijne gesprekken doorheen de jaren. Ook de leuke nichtjes en neven niet te vergeten: Sarah, Lore, Elke, Inge, Yzelle, Ben, Britt, Lars, Lotte, ... we zien elkaar misschien niet zo veel maar ik vind het fijn dat we toch een beetje op de hoogte blijven van elkaars leven en af en toe een babbeltje slaan.
Mijn zussen, ondertussen heb ik er 2 bijgekregen! Ze steunen me door alle moeilijke momenten. Ine en Kelly, bedankt voor de extra huiselijke warmte en liefde! En dan mijn kleine, grote zus! Lieve zus, bedankt om mij van kleinsbeen af te leren schrijven en tellen. Zelfs toen hadden we het moeten weten dat je leerkracht zou worden. Het grote leeftijdsverschil is niet altijd 'leuk' geweest, maar toch ben ik dankbaar voor een zus zoals jij! Ik hoop dat ik je een beetje fier maak, want dit is ook deels jouw verdienste! Pascal, Kevin en Edwin ook jullie zorgen voor een luchtige babbel. Merci voor alle gezelligheid.
Matisse, Birger en Veva! Mijn schatjes en oogappeltjes. Jullie betekenen zoveel voor mij en ik ben zo fier op jullie. Alles wat jullie ondernemen doen jullie zo goed. Ik ben een fiere tante!
Mama en papa, goh ... Hier schiet ik echt woorden tekort! Ik weet niet goed waar te beginnen. Bedankt om mij te vormen tot wie ik ben. Bedankt voor alle kansen die ik heb gekregen, ook al was het niet altijd makkelijk voor jullie. Bedankt voor de opofferingen die jullie voor mij hebben gedaan. Bedankt voor de sponsoring, de steun, de warmte, de liefde, ... Bedankt om er altijd voor mij te zijn, no matter what! Ik zie jullie graag en koester onze familie!

Randy, al iets meer dan 6 jaar ben je mijn steun en toeverlaat en ik ben dan ook heel blij met jou als beste vriend en partner. Samen hebben we al veel mooie momenten beleefd, maar de laatste maanden waren voor jou ook een enorm zware beproeving. Je bent niet iemand van veel woorden en je bent

zo romantisch als een pannenkoek. Desalniettemin heeft romantiek voor mij een totaal andere definitie als voor de meeste vrouwen. De manier waarop je de afgelopen vier jaar en vooral de afgelopen maanden voor mij hebt gezorgd waren super. Love ya!

Contents

Outline

Transparent Conductive Oxides (TCOs) play an important role in our every day life, acting as electrode in photovoltaic modules, displays, electrochromic windows,... In commercial applications and to obtain state-of-the-art characteristics, the TCOs are mostly deposited through vacuum deposition methods. Nevertheless, solution processing is often put forward as an interesting alternative from which the theory and drawbacks are not completely understood.

Chapter 1 gives a general introduction to the characteristics of TCOs. The concepts transparency and conductivity are explained in relation to different materials and applications. Further on, solution processing is addressed with all different types, making a distinction between direct deposition methods such as chemical bath and electro-deposition, nanoparticulate routes and molecular precursors. Although combustion precursors are considered to be a subdivision of molecular precursors, they are more elaborately explained as an interesting low temperature alternative for the synthesis of TCOs. In the quest of the ideal TCO material, due to the excellent transparency and state-of-the-art conducitivity, indium tin oxide (ITO) is still up to today the most commercialized TCO. Nevertheless, by the increased demand of different applications, indium is becoming more expensive and alternatives are considered. Multiple alternatives like organic substitutes as graphene, carbon nanotubes, polymers, and even inorganic metallic nanowires and (doped) oxides have been developed. From an inorganic point of view doped ZnO is considered to be a low cost, abundantly available, non-toxic and easy to fabricate TCO. Especially Al-doped ZnO (AZO or ZnO:Al) is put forward as ideal candidate. All this makes n-type doped ZnO an interesting material to investigate for solution processing. Here, the focus will be on the development and understanding of suspensions of Al-doped ZnO nanoparticles as well as molecular precursors to obtain n-type ZnO.

After a general introduction, the used materials for synthesis are given in Chapter 2. During this whole process from precursor development to deposition of doped ZnO films, multiple analytical characterization methods are applied. The working principle and the experimental details behind every procedure are briefly explained.

Within Part I the exploration of the nanoparticulate route of Al-doped ZnO is studied.

Chapter 3 deals with the co-precipitation synthesis of AZO nanoparticles (NPs). As this method is highly applicable on an industrial scale, the intrinsic parameters of these NPs are elaborated and highlighted.

Within Chapter 4 and 5 the thermal decomposition synthesis of AZO NPs is studied in different solvents. Chapter 4 reports on an in-situ stabilization during synthesis of AZO NPs in dibenzyl ether, leading to profound insights in the synthesis mechanism as well as generating conductive AZO films. The obtained knowledge on the thermal decompostion synthesis is transferred from dibenzyl ether to benzyl amine in Chapter 5. A high-yield synthesis of AZO nanorods (NRs) in benzyl amine is achieved here. In addition to the considered beneficial morphology of the building blocks, in-depth characterization showed an extremely high substitutional tehrahedral incorporation of Al inside the ZnO lattice, which is considered to significantly improve the electrical characteristics of these building blocks.

Part II elaborates on the synthesis and deposition of molecular precursors.

Organic solvents are probably most commonly used for the development of molecular precursors. Especially 2-methoxyethanol with its high dielectric constant is interesting to dissolve chemicals. Besides 2-methoxyethanol a less teratogenic 2-butoxyethanol is made for the deposition of thick films Al-doped ZnO. Here the surface effects on the bulk resistivity of the obtained films are investigated. In addition, the 2-methoxyethanol precursor is tuned to a combustion precursor, from which deposition of crystalline doped ZnO was possible at temperatures of 200 °C. This all emphasizes in Chapter 6 the importance of organic precursors in the TCO field.

From an environmental point of view, aqueous precursors are more appealing as explained in Chapter 7 and 8. A more general understanding of a citrato-Zn precursor is obtained and Al, Ga and In-doped ZnO films are obtained in Chapter 7. To our knowledge Cl-doping is up to today only achieved through electro-deposition of Cl-doped ZnO, although often metal chlorides are used during synthesis of n-type doped ZnO. This encourages the investigation of Cl-doping (by substitution of O) for solution processing of molecular precursors. Al-doped ZnO results often in the most efficient, with highest transparency and lowest resistivity, and cheap TCO. Therefore the mechanism behind this conductivity is elaborated in Chapter 8. In addition the development of low temperature (T) aqueous (combustion) processing will be explored.

By addressing almost the complete window of solution processing, not only new precursors and synthesis methods are developed, also a lot of general insights

are obtained. Although different initiatives already lead to deposition of doped ZnO at low temperatures, the real key to low temperature solution processed conductive TCOs needs to be unraveled. This could trigger a complete shift from industrial vacuum deposition to solution processing.

1 Introduction

Figure 1.1: Solar panels, displays and electrochromic windows as applications for transparent conductive oxides.

Within this chapter, a general introduction of solution processing of TCO materials will be elaborated. TCOs find a lot of applications in nowadays industry ranging from solar panels, electrochromic windows and displays. First, the physical characteristics as transparency and conductivity are discussed. Further on, the theoretical background from precursor or suspension formulation to deposition and thermal processing will be given. All this background is given in function of obtaining low cost, abundantly available, and non-toxic based TCO materials. The material of choice is n-type doped ZnO with a preference for Al-doped ZnO as both Al and Zn are abundantly available.

1.1 Motivation and Objectives

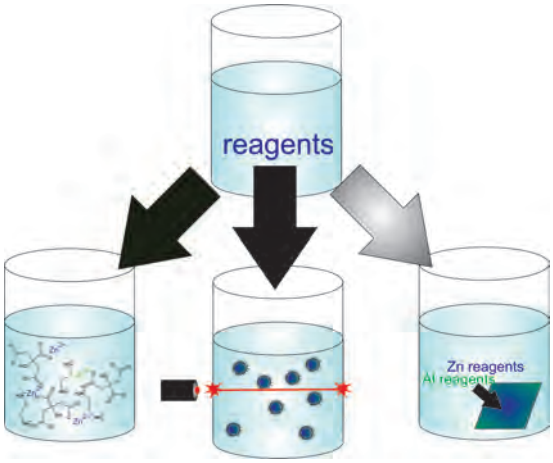

Figure 1.2: Overview of solution processing for e.g. Al-doped ZnO. Left: Nanoparticle synthesis with or without stabilization can be done through different reactions in various solvents. They have the characteristic of inducing a Tyndall effect. Middle: Direct deposition such as e.g. chemical bath deposition and electro-deposition were reagents are dissolved and precipitate on a seeded substrate through addition of bases and increased temperature. Right: Molecular precursors are obtained by dissolution of reagents in different solvents.

Transparent Conductive Oxides (TCOs) are currently applied in many everyday devices and have their roots in 1907 by the discovery of *Badeker*. Back then a solution processed conductive cadmium oxide film became transparent after being exposed to air. [18] This discovery triggered the research of many alternative transparent and conductive materials. Although *Badeker* deposited the film through evaporation, the research in TCOs boomed with the development of vacuum deposition techniques like sputtering and chemical vapor deposition. Up to the beginning of this century, the most investigated materials have been indium tin oxide (ITO), tin oxide, indium oxide, and zinc oxide.[209] N-type doped zinc oxide is one of the most promising transparent conducting oxides to replace ITO that, due to predicted future shortages of indium, is becoming more and more expensive. Although the optoelectronic properties of ITO are superior to Al-doped ZnO, Zn and Al are abundantly available and inexpensive. Also amorphous oxides like indium zinc oxide and indium gallium zinc oxide have been explored. The advantages of these materials are diverse. They have a smooth surface, no grain boundary scattering and are less brittle. All this makes the amorphous materials more easy to be used in combination with flexible substrates. [172] The use of amorphous TCOs triggered the shift from

physical vapor deposition back to atmospheric solution processing. This reorientation was encouraged by the ease of fabrication, the potential scalability and the maybe lower manufacturing costs.[241] It is indisputable that the cost of the equipment for solution processing are far lower than those associated with vacuum methods. Nevertheless *Pasquarelli et al.* indicated that the applied solution processed chemical precursors can elevate the price significantly. [209] Therefore, study of inexpensive chemical precursors is necessary, and more profound insight in the mechanisms which dictate how a precursor affects the properties of the final oxides needs to be obtained. In addition, it has been obvious that the chracteristics, obtained by vacuum processing, are not easily achieved with solution processing. In general, solution processing limps one order of resistivity behind with values of 10^{-3} Ohm cm in contrast to results in the 10^{-4} Ohm cm of vacuum processing. Although occasionally solution processing transcends itself and peers with vacuum processing as indicated by *Alam et al.*, although the reason how is possible not understood. [11]

Solution processing can be divided into three generally accepted approaches: a route based on the use of nanoparticles, direct deposition, and a route based on molecular/ sol(ution)-gel precursors. All syntheses methods have been applied and studied to obtain n-type doped ZnO. Nevertheless profound knowledge, environmental friendly methods and even low temperature processes are lacking. Amorphous oxides have been addressed as a low temperature alternative since the beginning of this century, but with an end application often limited to displays. This requires high mobilities and not necessarily high carrier concentrations, which are both influencing the conductivity (1.2.1). For other applications the amount of charge carriers is also of importance. Only recently there has been a publication from *Hagendorfer et al.* implementing low temperature processed crystalline Al-doped ZnO in a solar panel.[111] They were able to produce functional low temperature synthesized Al-doped ZnO by chemical bath deposition. Nevertheless this method is quite cumbersome from an industrial and economical point of view as big batches or 'baths' are needed, which cannot be recycled and generate a large amount of waste.[96] Also *Rousset et al.* were able to obtain a low temperature deposition Cl-doped ZnO for a solar panel.[226] Then again, none of these direct methods can be applied in an easy process, like printing or roll-to-roll processing, which limits the applicability.

Many synthesis methods for n-type doped ZnO have been reported, as will be indicated further on, and are even commercialized. In contrast, low temperature methods are rarely reported and in case they are published, nobody really understands the theory of low temperature solution processing and the transfer to conductive materials. In view of low temperature synthesis, alternative efforts like combustion processing have been researched to produce crystalline doped ZnO. In addition, alternative high temperature (T$>$ 450 °C) routes have been explored and in-depth investigated to grasp the chemistry behind solution

processing of n-type, but especially, Al-doped ZnO.

Within this framework of this PhD thin ZnO based films have been synthesized with a thickness between 30-1000 nm by simple and inexpensive methods like molecular and nanoparticulate routes, with non-toxic, abundantly available and cheap materials. Here, it is of importance that the obtained characteristics of the TCO match those obtained by vacuum deposition (sputtering) to be able to compete with them. This induces that the transparency has to be equal or exceed 85 % in the optically active wavelength range (200-1200 nm in case of CIGS), the conductivity has to be equal or exceed 10^3 S/cm with a carrier concentration of the order of 10^{20} cm^{-3} and the band gap energy of the used materials (metal oxides) has to be larger than 3 eV.

1.2 Transparent Conductive Oxides

Transparent conductive oxides are a very important component of e.g. PV devices, where they act as electrode elements, structural templates, and diffusion barriers, and their work function [1] controls the open-circuit device voltage, V_{oc} [2] . For TCOs the desirable characteristics include high optical transmission across a wide spectrum and low resistivity. If this is compared to bulk metals, which are highly conductive, they will not transmit visible light. Untill recently, if conductive materials are minimized to a nm thick layer, they become transparent. [114] On the contrary, highly transparent media like oxides behave as insulators. Important for the conductivity and transparency is that a compromise has to be reached during film deposition, since a high concentration of charge carriers will increase the conductivity, but will decrease the transparency (carrier concentration needs to be in the order of 10^{20} cm^{-3}). Materials that combine optical transparency over much of the solar spectrum with reasonable electrical conductivity generally fall into three classes: very thin pure metals, highly doped conjugated organic polymers, and degenerately doped wide-band gap oxide or nitride semiconductors. [89]

When synthesizing TCO materials, the transparency and the conductivity are the key factors in obtaining state-of-the-art layers. In the sections below, the fundamentals behind these chracteristics are explained.

[1] The work function is the minimum energy (eV) needed to remove an electron from a solid to a point immediately outside the solid surface (or energy needed to move an electron from the Fermi level into vacuum).

[2] The open-circuit voltage is the maximum voltage available from a solar cell, and this occurs at zero current.

1.2.1 Conductivity

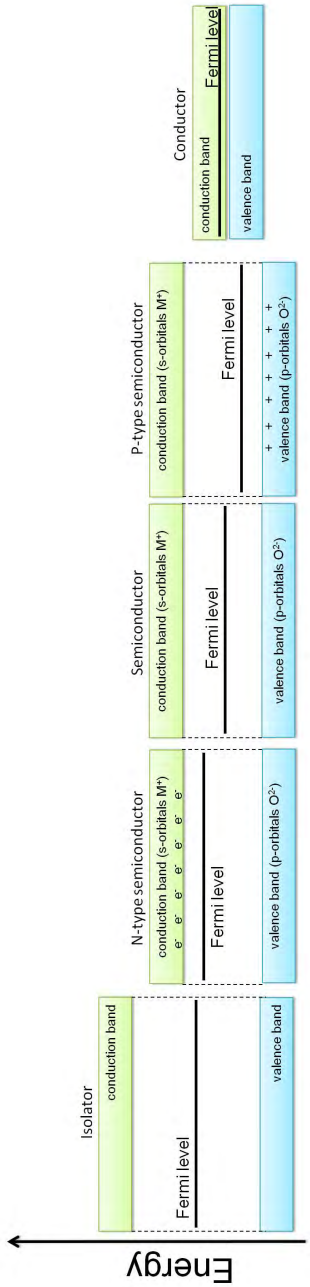

Figure 1.3: Energy difference and positioning of the Fermi level of different materials.

Depending on their ability to conduct electrons, solid-state materials can be categorized into either conductors, semiconductors, or isolators (Figure 1.3). For TCOs semi-conducting oxides are of specific interest. For these metal oxides the conduction band (CB) is built out of the unfilled ns orbitals of the metal with n the principal quantum number, while the valence band (VB) covers the filled oxygen anion energy levels (built out of the 2p orbitals). Electrical conductivity σ of electrons in the CB, (expressed in S cm^{-1}) is inversely related to resistivity ρ (Ohm cm) and is built on several characteristics. The conductivity is the product of the carrier concentration N (amount cm^{-3}), the charge carrier e (C) and the mobility μ (cm^2 V^{-1} s^{-1}) (Equation 1.1). For electron conductivity the charge is 1.602 10^{19} C.

$$\sigma = Ne\mu \tag{1.1}$$

The conductivity is influenced by the mobility, which is defined in Equation 1.2. The 'flow-ability' of charges through these oxides experiences different influences. τ is the average scattering time and m* is the effective mass.

$$\mu = \frac{e\tau}{m*} \tag{1.2}$$

The effective mass is dependent on the used material, while the scattering time depends on the film quality. The average scattering time is built out of several contributions. Matthiesen's rule declares that the resistivity (inversely related to the conductivity) arises from independent and additive scattering processes like impurity, defect, grain boundary, ... scattering. Ionized impurity scattering is very important for the conductivity in semiconductors, although according to *Minami* it only becomes dominating if at least 10^{21} charge carriers per cm^3 are present. Further on, grain boundary scattering is only important if the grains are smaller than the mean free path of the electrons. [60] To obtain as large grains as possible, higher temperatures might accelerate grain growth. In addition, it is possible that the grain growth is disturbed by the introduction of dopants inside a lattice, which will result in smaller grains. [117] [130] This reduced grain size will decrease the conductivity. [82] Also phase separation and porosity will result in further scattering. [67] For solution processing, porosity is one of the most important issues as the used precursors contain complexants, additives, and other organics which need to be removed to obtain the functional oxide film. With the removal of these organics, pores and cracks can be induced which will reduce the conductivity.

Semi-conducting oxides have a fundamental band gap of 3 eV or more and are insulators at room temperature (Figure 1.3). Improved conductivity at room temperature can be achieved by intrinsic or extrinsic doping, introducing charge carriers.[80] This type of doping can either be n-type, electron conductivity or p-type, hole conductivity. (Figure 1.3) Intrinsic doping is caused by the creation

of lattice defects, like oxygen vacancies or metal atoms on interstitial sites. This can be done during sputtering deposition by adjusting the oxygen partial pressure and deposition rate during the deposition of TCO materials. [87] Also a reduction process of the oxide after deposition, like annealing in vacuum or in a hydrogen containing atmosphere, belongs to one of the possibilities. [301] [44]

On the other hand extrinsic doping is realized by introducing elements with more or less electrons than the original metals in the metal oxide lattice. In fact there is a combination of both intrinsic and extrinsic doping during deposition of TCO materials. When the oxide is n-type doped, the free carrier density is increased, whereby the Fermi level is moved into the CB (Figure 1.3). This doping requires a source of electron donors with an ionization energy close to the CB, which also limits the choice of TCO materials. In oxides, with d^{10} cations like indium oxide, zinc oxide, tin oxide and cadmium oxide, native stoichiometric point defects like oxygen vacancies are readily ionized and thereby donating electrons to the CB. Nevertheless, oxygen vacancies are believe to be deep levels, which excludes their intrinsic doping capability. [126] Extrinsic dopants like Al in ZnO have to find substitutional sites in the lattice [136], while they decrease the carrier mobility and represent a trade-off when optimizing the resistivity of the material. Doping results in more plausible scattering. These slightly reduced metal oxide systems can show n-type electrical conductivity provided that charge-compensating electrons can be promoted to the CB of the metal oxide from defect energy levels lying close in energy to the CB minimum.

P-type conductivity has been documented in certain metal oxide systems where defect energy levels lie proximate to the valence band (VB) of the metal oxide. In such materials, electron promotion to these defect levels creates holes in the VB thereby promoting conductivity. [101] The preparation of TCO thin films consisting of p-type metal oxide semiconductors was reported in 1993. [238] The conductivity but certainly also the transparency of p-type materials is lower than for n-type materials.

1.2.2 Transparency

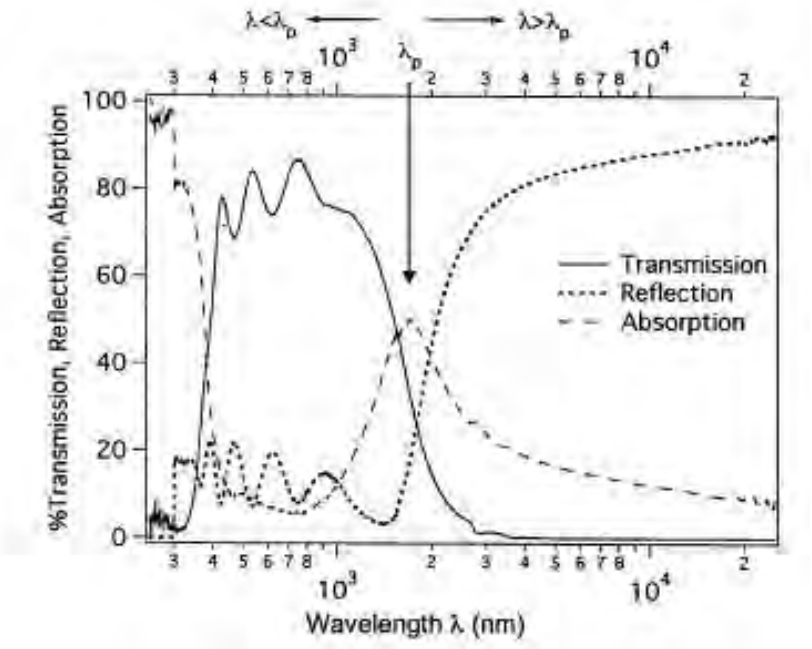

Figure 1.4: Optical reflection (R), transmission (T) and absorption (A) spectra of a typical TCO on glass.[209]

The second important characteristic of TCO is that it must transmit freely across the visible spectrum.[101][209] The short-wavelength (UV) cutoff corresponds to the fundamental band-gap of the material, whereas the long-wavelength (IR) edge corresponds to the free carrier plasma resonance frequency (Figure 1.4). These critical optical properties are influenced by the carrier density and mobility.[108] For a material to be transparent across the visible spectrum, its band-gap needs to be greater than 3 eV to enable transmission up to near UV (0.4 μm) wavelength, and its free carrier plasma resonance absorption (plasma wavelength λ_p) must lie in the near-infrared (1.5 μm) or longer wavelengths. At plasma wavelength, the frequency of incoming light is the same as the frequency of the collective oscillation of electrons in the material (Figure 1.4). The electrons oscillating in phase with the electric field component of the light will generate absorption. For $\lambda < \lambda_p$, the material is transparent. The radiation propagates through an oscillating wavefunction. For a decaying wavefunction ($\lambda > \lambda_p$), only reflection is possible.[209] Increasing the carrier density decreases the resistivity but also has the drawback of shifting the IR absorption edge toward the visible, thus narrowing the transmission window. [149] This shift at the IR end of the spectrum is determined

by the plasma oscillation of the free carriers that screen the incident electromagnetic wave via intraband transitions within the CB. The position of the UV edge is dependent, in part, on the free carrier density in the material. Analysis of the density of states in the CB reveals that the UV edge will shift to shorter wavelengths with increasing carrier density (n) because the change in optical band gap ($\triangle$E) increases with carrier density as $\triangle E \sim n^{3/2}$. [152] [62]

1.3 Applications

The applications of TCO materials are quite widespread. The most common application might be the use of TCOs in photovoltaics (PV). Besides PV, TCOs are applicable in displays and even architectural glass. Depending on the application, the specifications of the TCOs will vary. Although no end device will be presented in this thesis, the focus of synthesis will be on crystalline n-type doped ZnO, which has as end application built-in in photovoltaic modules. The theory of the applications below indicate that although the TCO as such might be promising, the integration in a device is complex. When building a device various requirements have to be taken into account and the TCO material of choice depends on the application.

1.3.1 Photovoltaics

Recently, there has been a focus of research and development on the reduction of costs to produce electricity out of solar energy conversion to achieve grid parity and beyond. One tries to increase the efficiency at the cell, module, and system level so that the thickness of the semiconductor material can be decreased. Further, there is the need to reduce the costs associated with the active materials and with the production processes. Hereby the active Si material is to be reduced and less expensive semiconductor materials are of interest. Also it is of interest to create high-throughput processes to replace vacuum-based production technologies. Solution-based deposition of cell materials that enable faster and larger volume production will be developed for transparent conductive oxides (TCOs). These TCOs have their goal as front electrodes on PV cell architectures.

Although the focus won't be on the actual solar panel, the main objective is to understand and tune these TCOs towards active electrodes, which can be used in modules that have been investigated due to their breakthrough potential. PV with high efficiencies at reasonable costs (copper indium galium (di)selenide (CIGS)) or on reasonable efficiencies at very low cost (organic photovoltaics (OPV)) are chosen as active layer.[105][98] The next paragraphs illustrate the basics and the working principle of the electrode as well as the solar panel itself. In addition perovskites have emerged quickly over the past years [106],

and although they won't be discussed, it might be of interest to consider them in future PVs as active layer.

Copper Indium Gallium Selenide Photovoltaics

CIGS solar cells have demonstrated efficiencies near 20 % in the lab [220] and are being commercialized. [221] [105] The defect chemistry of CIGS is complex, and the active layers in these cells are highly temperature sensitive and susceptible to defect and impurity diffusion. [89] The complex CIGS substrate PV cells is displayed in Figure 1.5. The CdS layer is a stabilizing thin layer to maintain stoichiometry at the surface and to prevent point defect creation caused by selective evaporative loss at the surface. Further is CdS applied to form the initial contact junction with the TCO layer deposited above it. The intrinsic ZnO is placed in between to prevent leakage currents. The stack ends with an anti-reflective coating and often metal grids are deposited on top of the TCO layer to enhance its conductivity. All the layers on top of the CIGS layer need to be deposited at lower temperatures to prevent leakage currents.[89] The superstrate CIGS PV cell is given in Figure 1.5 and the TCO layer is first deposited on the glass substrate. Due to this structure the restrictions for the processing, such as the maximum temperature etc. are not extremely fixed. CdS is left out since otherwise intermixing with CIGS would occur. Although the superstrate configuration enable lower costs, easier encapsulation, and the possible integration as the top cell in future tandem cells, the conversion efficiencies are several percentages lower than those of the substrate cells. For the substrate CIGS solar cells the temperature is of utmost importance. Intensive research is required to achieve compatible preparation conditions with the underlying layers, while maintaining high general performance.

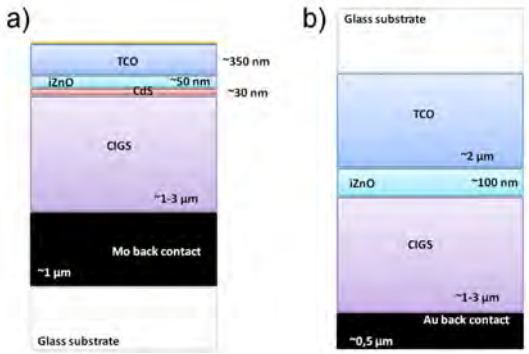

Figure 1.5: a) CIGS substrate PV cells whereby the TCO is deposited on top of the active stack. (left) b) CIGS superstrate PV cells whereby the TCO is deposited first on the glass substrate. (right)

For the development of TCOs for CIGS cells the challenges are the interfacial

stability with CdS, the resistance to diffusion and short circuiting, as well as establishment/ improvement of the junction and low temperature deposition.

Organic Photovoltaics

On the contrary to CIGS solar cell, the efficiencies for OPV solar cells are far below 20%.[105] Here is still a lot of room for improvement (as well as for the TCO materials used for OPV).[33] For OPV solar cells it is of utmost importance that the interfaces of the TCOs with the organic materials are stable. [108] The chemical stability against hydrolysis leading to formation of a surface hydroxide in TCOs is strongly dependent on the type of oxide. The non uniform chemical reactivity and doping, lead to heterogeneous electrical properties on sub-μm length scales in the TCO layer. Control of this requires the application of specific surface pretreatments, such as oxygen RF plasma or brief exposure to etchants such as HI or $HCl/FeCl_3$. In order to maximize OPV power conversion efficiencies, the energetic and kinetic barriers to charge injection/collection must be minimized. Chemical modification of the oxide surface to lower their surface free energy, to stabilize against hydrolysis and attack by acidic over-layers, to tune the effective work function, to planarize the oxide film, increase contact compatibility with non-polar organic layers and to enhance the electron transfer across the interfaces have been considered using small molecules such as silanes, carboxylic acids, ultrathin conducting polymer films ... [15] [73]

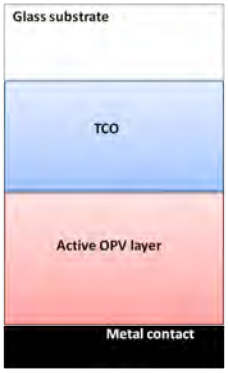

Figure 1.6: OPV architecture, where the TCO is deposited onto the glass support.

Especially for TCO materials in OPV devices one has to take into account a lot of various factors. First of all the work function matching is required to optimize open-circuit voltage and facilitate charge injection.[25] Also there is a need for flexible solar cells, so that the TCOs have to stable on deformable surfaces.[108] Further suitable surface chemistry for optimal wetting by the organic absorber layer is also asked, as well as low resistivity (sheet resistance

below 10 Ohm/ □), high mobility and not too high carrier density, since this can limit the transparency.[108] The temperature limitation is determined here by the choice of substrate, since the active OPV layer is deposited on top of the TCO. In case of flexible substrates, there is a need to choose for less brittle and low temperature deposition.

1.3.2 Electrochromic windows

These TCOs can also be incorporated in electrochromic or 'smart' windows, which are known for their energy saving in building technologies. An ion conductor or electrolyte is sandwiched between twe TCO layers, an active and counter electrode. By applying small voltages, the windows can be darkened or lightened and thereby control the amount of transmitted light and the generated heat by solar radiation. In addition they can also be used to contain the heat as a low-emissivity window. This is made possible by the incorporation of charge carriers inside the TCO, which according to surface plasmon interaction reflect in the infrared region. In addition commonly applied TCO materials absorb within the UV region of the solar spectrum and create a cut-off for harmful radiation. [100, 160]

The requirements here are again an as high as possible transmittance, to enable the maximum capacity of the ion conductor. In addition, a good electronic conductivity is required, to provide a low voltage drop along the conductor surface. The exact value of sheet resistance is not given, but from the paper of *Baetens et al.* a value below 200 Ohm/ □ is preferred. [19] Nevertheless, here the conductivity is sacrified for the IR reflectivity and the transmittance. [160]

1.3.3 Displays

The variety of displays goes from smart phones to televisions and beyond and although the display requirements depend strongly on the applications, the TCO has in every display the same functionality. TCOs pass the electrical signal and enable the pixel to be switched on/off and simultaneously allow light to be transmitted out. [160]

For touch screens the resistance is used to map the x-y coordinates. If the resistance changes the contact position will shift. By this effect not the sheet resistance value is that much of importance, but rather the long-term stability. [160]

For thin film transistors, the mobility is very important to ensure high current. This improves the screen quality. [132]

1.4 Solution processing

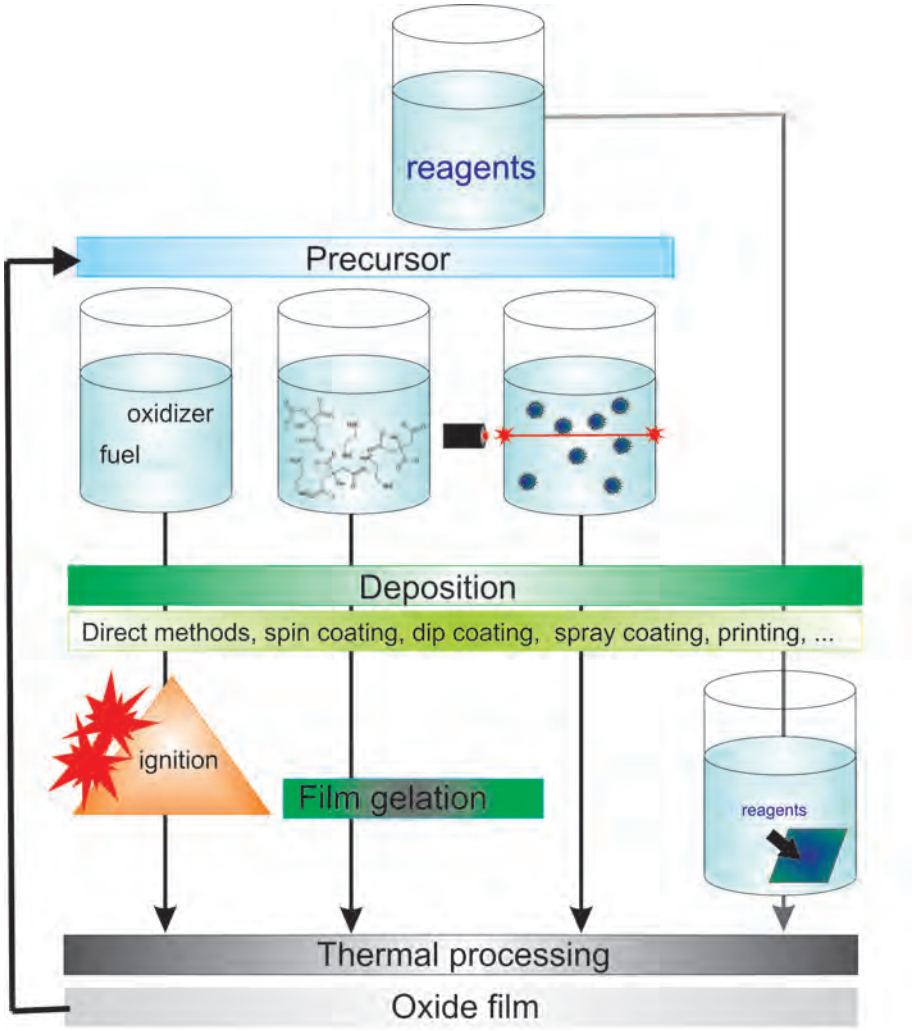

Figure 1.7: General overview of (left) combustion processing as a division of (middle left) the molecular precursors, (middle right) the nanoparticulate routes and (right) the direct deposition methods. A solution of metal ions, additives, ... is prepared. The synthesized precursor can be deposited or the solution as such can be used. Further on, thermal processing is applied to obtain a metal oxide film. It is possible to apply the precursor deposition in a multi-step manner.

Solution processing of TCOs goes back to 1907 with the discovery of conductive cadmium oxide by *Badeker*. This solution processed film becomes transparent after being exposed to air. [18] This discovery triggered the research of many alternative transparent and conductive materials. Although *Badeker* deposited the film through solution processing, the TCO research boomed with the development of vacuum deposition techniques.[86] Nowadays most commonly applied techniques to synthesize TCOs are: sputtering [93], pulsed laser deposition [139], chemical vapor deposition (CVD) [285], chemical bath deposition [111], electro-deposition [227], spray pyrolysis [28] and sol-gel techniques [158].[86] Magnetron sputtering is a form of physical vapor deposition (PVD) and includes dc sputtering, rf sputtering and reactive sputtering.[86] Although high-purity films can be obtained through the least expensive method of PVD processes, the method is also quite cumbersome.[3] Low sputtering rates, non-uniform films, expensive sputter targets, and the necessity to control the gas composition are some important parameters when choosing for sputtering of films. [3] Furthermore, pulsed laser deposition (PLD) is a very effective deposition strategy which needs moderate up to ultrahigh vacuum. It is versatile and amenable to coupling with UV irradiation [61], oxygen radical assisted deposition [174], or magnetic field promoted deposition [7]. Like sputtering, a target is used to transfer a stoichiometric ratio to a substrate. Nevertheless, some disadvantages are present. The generated plasma plume is highly forward directed, which leads to a non-uniform deposition and macroscopic globules might be formed. [2] Also, chemical vapor deposition is applied, where volatile species interact with a hot surface. The precursors dissociate by high temperature, light or by means of a plasma. [53] Within CVD there can also be a subdivision, based on metal-organic precursors, known as metal-organic chemical vapor deposition (MOCVD). MOCVD does not necessarily need high vacuum and delivers high quality chemically and structurally of deposited layers. A huge downside is the required purity and the preparation costs of metal-organic precursors.[86] All of the physical vapor techniques discussed above have some advantages and disadvantages. Probably, the most significant disadvantages for are the costs (associated with equipment and reagents) as well as the unapplicability in a roll-to-roll of printing process. Promising results regarding conductivity, transparency and processability are delivered by wet processing of TCO materials, even though relatively high temperatures above 500 °C are often required.[158] [52]

Solution processing contains three pathways: nanoparticle route, molecular or sol(ution)-gel route and a direct deposition method (Figure 1.7). Direct deposition method such as chemical bath deposition and electro-deposition will not be investigated experimentally (righter process in grey in Figure 1.7). Our main focus is the synthesis of a precursor which can be applied in either deposition technique. Of course some minor modifications (regarding viscosity,

density, ...) might be necessary according to the deposition method. The deposition techniques are quite diverse and will be briefly discussed further on in section 1.6. On lab-scale, spin coating is commonly applied due to low cost, simplicity and high reproducibility. Therefore, precursors will be developed in view of this deposition technique.

1.5 Precursor development

The division of solution processing is given in Figure 1.7. Here, the focus is placed on the molecular precursors and nanoparticulate dispersion routes. Within the molecular precursors a recent publication of *Hardy and Van Bael* has drawn attention to combustion processing. [113] Due to very different and specific characteristics a separation between regular molecular precursors and combustion processing is made. The details of the precursor development and synthesis of oxide will be discussed further on.

1.5.1 Nanoparticulate dispersions

Nanoparticles (NPs) have been synthesized a lot as building blocks for TCO films. Two general approaches are available for the synthesis of NPs, i.e., the bottom-up and the top-down approach. The bottom-up chemical synthesis and self-assembly approaches offer much more flexibility for creating very small nanostructures with a high yield and control of the size, the shape, the composition and the physical properties in comparison with the top-down techniques. The top-down approach is capable of synthesizing very monodisperse NPs, but with a low yield and with dimensions not small enough in size. Using various bottom-up methods like co-precipitation, micro-emulsion or solvo/hydrothermal synthesis, NPs of different size, shapes and atomic composition have been synthesized. The most interesting advantage of this chemical processing way is the separation of the heat treatment that is required for the crystallization of the material (and the formation of charge carriers) from the process of film formation. Downside of this method is the carrier scattering at the grain boundaries, which makes it hard to obtain high conductance or even any conductance. This was confirmed by *Gross et al.*, who found poor electrical properties between the particle aggregates and high inter-grain porosity.[107] Improvements of the electrical properties can be obtained through sintering of the NPs (as explained further on in section 1.7.3) or by curing of the NPs (interconnecting the NPs). [218] [217]

Co-precipitation synthesis

Co-precipitation is an easy, water-based, low-temperature method to synthesize high-yields of oxides. Precipitation in a solution can be triggered through pH

adaptation, which influences the solubility of metal ions.[156] [151] (Hydr)oxides will be formed, which might require an additional calcination to be turned to oxides. [279] In the beginning of the precipitation a lot of small crystallites form (i.e., the nucleation stage), but they tend to aggregate quickly together to form larger, more thermodynamically stable particles (growth). The nucleation and growth of NPs will be further explained in the LaMer model (Figure 1.8). Coarsening or Ostwald ripening [3] can only be stopped or controlled by stabilizers, making it difficult in standard coprecipitation to control the size and shape of the particles. This size, shape and the composition of the NPs are determined by the reagents, the temperature, the pH and the ionic strength of the media applied. [156][64]

Micro-emulsion synthesis

Micro-emulsion resembles co-precipitation but has a better control over the NP size due to the use of nanoreactors or micelles. Micelles can be used as nanoreactors through the use of two unmixable liquids. [279] The reagents are dissolved in nanoreactors, which limit the precipitation reaction to their dimensions.[206] [76] Although the size and shape control during micro-emulsion is better than co-precipitation, the yield is very low.

Solvo/Hydrothermal and Thermal Decomposition synthesis

Micro-emulsion already allows a good control of the size and shape of the NPs, but with a rather low yield. Co-precipitation has a high yield, but almost no standard control over the size and shape. The nucleation and growth of the NPs is of importance to control. This is possible using the LaMer model. Figure 1.8 illustrates the nucleation and growth of nanoparticles in solvo/hydrothermal and thermal decomposition synthesis, which is used to obtain uniform nanoparticles. While solvo/hydrothermal processes take place under pressure in organic solvent or aqueous environment, thermal decomposition is known to occur at standard atmospheric pressure.[134] The LaMer model separates the nucleation from the growth, since in a first step the nuclei are generated by the release of monomers, which are considered to be derivatives of the reagents. At the moment that the monomer concentration reaches a supersaturated level, a burst nucleation takes place. Once the nuclei are formed, the size and the shape of the nanoparticles can be tuned during the growth.

[3] Coarsening or Ostwald ripening is the phenomenon by which smaller particles are consumed by larger particles during the growth process.

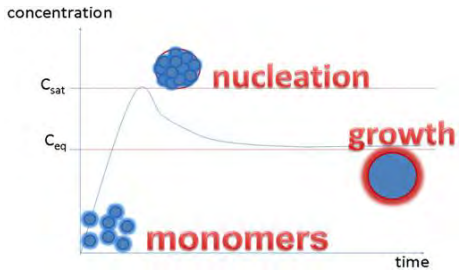

Figure 1.8: LaMer model of nucleation and growth. In a first step the monomers are released to form nuclei. When the concentration of nuclei reaches a saturated level, burst nucleation occurs. After nucleation, they can grow further.

Synthesis of capped nanoparticles The preference of this solvo/hydrothermal or thermal decomposition is often based on the presence of capping agents, which coat and stabilize the NPs. In addition they enable size-selective crystallization, dispersibility in water, control over surface functionality and assembly into a range of morphologies. [203]

Due to the high Brownian mobility of the NPs, they will constantly collide in a solution and tend to aggregate. Nanoparticle interactions originate mainly due to four different phenomena: van der Waals forces (attractive), electrostatic forces (attractive or repulsive), steric hindrance (repulsive) and the hydrophobic effect. In order to obtain uniform size and shape of nanoparticles, the stabilizing repulsive interactions at the nanoparticle's surface need to dominate. The capping agents applied in synthesis can be further modified by a ligand addition, an extra ligand comes around the already capped NPs, or a ligand exchange, where the original capping agents are replaced by others. This might be necessary to increase the stability or to alter the polarity of the dispersibility. [270]

1.5.2 Dispersions

After the synthesis of NPs the formulation of dispersions is necessary for further deposition of uniform layers. The suspension can either be directly synthesized through the use of surfactants during the reaction as explained above. In a next step, the ligands can be altered or modified by ligand exchange or ligand addition processes in function of the aimed solvent and/or application. Also 'naked' NPs are produced through several methods, which will readily agglomerate. After synthesis, to obtain a stable suspension, dis-agglomeration is needed. This can either be achieved by bead milling the dispersions or through the use of ultra-sonication.[201] [171] During (or after) this deagglomeration a solvent and often surfactants are added to obtain a stable suspension.

1.5.3 Molecular Precursors

The goal of the synthesis of molecular precursors is to obtain a precursor solution of the desired cations, which can later be deposited and transformed into a TCO. During the preparation of the solution, reagents (containing the wanted cations) and the solvent are selected. Possible reagents and solvents are discussed below. This solvent defines to a large extent the solubility of reagents. To obtain complete dissolution of the reagents, chemical modifiers might be needed. On the other hand, these chemical modifiers could also restrict chemical reactions. In the end, depending on general synthetic pathway a categorization of routes has been made: Pechini, nitrate, metallo-organic decomposition, chelate or sol-gel. References for these routes and explanations can be found here.[129][183][241][279]

Reagents Three classes of metal organic or metallo-organic compounds are most commonly used: metal alkoxides ($M(OR)_x$), metal carboxylates ($M(OOCR)_x$), and metal beta-diketonates ($M(OC(CH_3)CHCH_3)CO)_x$) with M representing the metal ion. These species differ in their solubility and reactivity, as well as tendency to react with on and another. Alkoxides are most reactive with alcohols, water or other starting reagents added to the solution. The reactivity of the metal ion can be controlled by shielding through the use of longer alkyl chains, which induce steric hindrance. The number of bonds between metal center and the ligand might also be controlled to influence the reactivity. The solubility of metal carboxylates can be modified by tailoring the chain length. The longer the chain, the more apolar the character. The metal beta-diketonates are the least reactive, although they are highly soluble. In addition also nitrates, citrates, oxo-alkoxides, and mixed ligand reagents (alkoxy-carboxylates and alkoxy-β-diketonates are used reagents.

Solvents Solvents are not solely the medium for dissolution, since they can influence the reaction rate and pathway. Solvents can be characterized according to polarity and proticity. While protic solvents are in the ability to form hydrogen bonds, by the presenece of N-H and/or O-H, aprotic solvents don't. Most commonly used solvents are alcohols, which are not only able to dissolve reagents, but also induce alcohol exchange reactions. Of course other solvents such as xylene, toluene, water, ... are also used. 2-methoxyethanol is probably one of the most common used solvents.[209] Due to its dielectric constant (ε_r=16.93)[59] and the dissolving characteristics it is a very commonly used solvent. Nevertheless, it is highly teratogenic, which disfavors its use. [224] 2-butoxyethanol is a less harmful alternative. [239] In addition to polarity and proticity, the molecular weight, boiling point, density, viscosity and dipole character all have an influence in the film deposition and drying behavior.

Metal-organic decomposition processes

Metal-organic decomposition or MOD covers the dissolution of individual metal reagents in a non-interacting apolar solvent, which are consequently mixed. Mostly the reagents are metal carboxylates which contain long aliphatic R groups, excluding hydrolysis and condensation reactions. In contrast to many other methods, this is purely dissolving of reagents, without the formation of gel upon drying. As no oligomerization occurs, a lot of mass fraction is thermally decomposed. This results in cracks and pores, which significantly reduce the quality and the required characteristics of the obtained film. [279] [165]

Polymer complex controlled processes

This route is based on cations in an organic polymer network. This interaction can be generated either in-situ (during polymerization) or directly (interaction of metal cations and polymer). While monomers are being cross-linked, a gel with coordinated metal ions is constructed in the in-situ method. This process is also known as the Pechini route, where carboxylic acids and carboxylato-metal complexes dissolved in ethylene glycol react to form ester bonds upon heating.[204] [279]

Viscosity controlled processes

The viscosity controlled route makes use of polymers, who do not complexate with metal ions. Their role is not limited to the homogeneous distribution of metal ions, they also increase the viscosity upon solvent evaporation and spatially fixate the metals. [279]

Colloidal sol-gel processes

This route deals with colloidal solutions of particles, with an average diameter between 1-100 nm. After removal of the solvent, a gel will be formed in which the particle interaction is controlled by electrostatic and/or steric interactions. Brownian motion, electrostatic forces and van der Waals forces define these interactions. Chemical interactions are limited to H-bridging. [279]

Alkoxide sol-gel processes

In addition to the colloidal sol-gel processes, molecular sol-gel processes occur with a distinction between the processes in alcohol solvents with alkoxide reagents and in aqueous medium. For those in alcohol, the choice of solvent and reagents is critical in function of the control over hydrolysis (Eq. 1.3) and condensation (water elimination Eq. 1.4) and alcohol elimination (Eq. 1.5) that lead to oligomerization[4].[241]

[4]Oligomerization is the formation of short polymeric species.

$$M(OR)_x + H_2O \longrightarrow M(OR)_{x-1}(OH) + ROH \tag{1.3}$$

$$2M(OR)_{x-1}(OH) \longrightarrow M_2O(OR)_{2x-2} + H_2O \tag{1.4}$$

$$2M(OR)_{x-1}(OH) \longrightarrow M_2O(OR)_{2x-3}(OH) + ROH \tag{1.5}$$

Compared with other solution-based processes, as discussed above, sol-gel offers control of the precursor with respect to molecular shape, extent of oligomerization, composition, and organic fraction. These properties are controlled by the various conditions like the solvent, the used alkoxide reagent(s) and their concentration, water concentration and the method of water addition, catalyst, and solution conditions. Nevertheless, the often limited commercial availability of these metal-alkoxides makes them rather expensive. Also their sensitivity to moisture and high reactivity, due to the high inductive effect of the alkoxide-groups, complicates their use. [279] Nevertheless, metal alkoxides posses several advantages such as purity and purification possibilities, solubility in organic solvents, chemical reactivity and options for chemical modifications. [241]

Chelating processes The high reactivity of metal alkoxides can be suppressed by the addition carboxylates or stabilizing compounds. Here occurs then a chelating effect, also known as a hybrid process. The main advantage of chelating is that it combines the reactivity of alkoxide sol-gel route with the stabilization of the metal-organic decomposition processes (see part 1.5.3). [241]

Aqueous sol-gel processes

From an environmental and economical point of view the alkoxide sol-gel route is not very attractive. Besides this route an aqueous sol-gel route has been developed. [241] Water has a high polarity (μ = 1.84 debye) and dielectric constant (ϵ_r = 78.5), making it a good medium for the dissolution of ionic compounds. Due to solvatation, the electrostatic forces between the metal ions decrease and an aqua complex is formed (Eq. 1.6). The number of water molecules for a metal ion is linearly dependent on its polarizing strength[5]. Only this first shell is involved with the hydrolysis and condensation reactions.

$$M^{z+} + nH_2O \longrightarrow [M(OH_2)_n]^{z+} \tag{1.6}$$

[5]Small cations or those with a large charge have a larger polarizing strength (z/r^2) with z the charge and r the radius of the metal ion.

Hydrolysis The acidity of the medium as well as the valency of the cation determines the degree of hydrolysis; the release of a proton from a solvating water molecule. Through this process, aqua (H_2O), hydroxo (HO^-), and oxo (O^{2-}) ligands can exist in the coordination.

$$[\mathrm{M(OH_2)_n}]^{\mathrm{z+}} + \mathrm{wH_2O} \rightleftharpoons [\mathrm{M(OH)_w(OH_2]_{n-w}}]^{\mathrm{(z-w)+}} + \mathrm{wH_3O^+} \tag{1.7}$$

Whereby w ($0 < w < 2$) the hydrolysis ratio is, which can be calculated according to equation:

$$w = \left(\frac{1}{1 + 0.0138pH}\right)\left[(1.36z) + N(0.038pH - 0.25) - \frac{2.62 - 0.02pH - \chi_M^*}{\sqrt{\chi}_M^*}\right] \tag{1.8}$$

In this equation is N the coordination number, z the valency of the cation and χ_M^* the Allred-Rochow electronegativity value of the corresponding metal ion. Hereby the assumption has been made that proton exchange takes place until the average electronegativity of the formed hydrolyzed metal ion equals that of the solvent ($\chi_{[\mathrm{M(OH)_w(OH_2)_{n-w}}]^{\mathrm{z-w}}} = \chi_s$). The relation of the average electronegativity for the metal ion and the pH-dependence of the electronegativity of solvent is given in the equations below with χ_i the electronegativity of each involved atom. More elaborate explanations can be found in textbooks of *Jolivet et al.* and *Schneller et al.*.[129][241]

$$\chi_{[\mathrm{M(OH)_w(OH_2)_{n-w}}]^{\mathrm{z-w}}} = \frac{\sum_i \sqrt{\chi_i} + 1.36z}{\sum_i \frac{1}{\sqrt{\chi_i}}} \tag{1.9}$$

$$\chi_s = 2.621 - 0.02pH \tag{1.10}$$

Condensation After hydrolysis, condensation reactions lead to the precipitation of hydroxides or oxides through inorganic polymerization reactions, which have an initiation, propagation, and termination. The initiation depends on the presence of nucleophilic hydroxo ligands and the electrophilic force of the cation, which empirically translate in δ (OH)< O and δ (M)> 0.3. The propagation is either based on an olation and/or an oxolation by linking the metal ions by an hydroxo- or oxo bridge through a dissociative nucleophilic substitution (S_N^1) (equation 1.11) or associative nucleophilic substitution (S_N^2) (equation 1.12). The termination of these polymerization reactions is induced by the formation of precipitation.

$$\mathrm{M{-}OH + M{-}OH_2 \rightarrow M{-}OH\cdots M + H_2O \rightarrow M{-}OH{-}M + H_2O} \tag{1.11}$$

$$\mathrm{M{-}OH + M{-}OH \rightarrow M{-}OH{-}M{-}OH \rightarrow M{-}O{-}M{-}OH_2 \rightarrow M{-}O{-}M + H_2O} \tag{1.12}$$

Chelating processes Although the reactivity is significantly less than for alkoxide sol-gel processes, again chelating ligands are needed to avoid precipitation. Once metal complexes are formed, undesired hydrolysis is prevented and a cross-linked three-dimensional network is formed. In that manner, no precipitation will occur upon solvent evaporation. [243]

1.5.4 Combustion controlled processes

Conventional precursors, based on sol-gel methods, use metal hydroxides and/or alkoxide conversion by an endothermic process. This requires sufficient external energy input for oxidizing organic impurities, to achieve phase-pure products. More recently, solution combustion synthesis (SCS) has been explored by *Kim et al.* as an attractive route in solution processing of amorphous oxide materials.[142] Indium, zinc, and tin oxide films with processing temperature of only 200 ℃ were implemented in thin-film transistors. This synthesis route generates high local temperatures converting precursors into the corresponding oxides and enabling low-cost large-scale bulk syntheses. This has already a long history from powder synthesis, but only during the last decade, the tendency of directly applying combustion processing for (thin) film fabrication has been further studied. [85] In the past, the focus was mainly put on obtaining ultra-fine particles with high porosity. These combustion reactions with balanced redox chemistry, and through the use of local oxidizer supply can efficiently remove organic impurities without coke formation. The followed strategy follows the combustion triangle.[113] This means that all necessary ingredients like oxidizer and fuel to start a fire need to be in the precursor. An ignition can be ex-situ generated. SCS transforms the thermal decomposition process into a one-step intense exothermic signal, which is sufficient to drive the reaction rapidly to completion. Generally, combustion processing has been applied for amorphous metal oxide systems, since for crystallization generally very high energy needs to be added to system. Therefore it would be of interest to evaluate SCS for the generation of crystalline oxides.

Characteristics

Combustion processing dates back to the prehistoric times when carbon black was produced to paint the caves. Also the Chinese produced carbon black in this manner. By the end of the 19^{th} century termite[6] was made. Further on, the Pechini process is also an implementation of combustion processing.[153] Depending on the characteristics of the reagents and the exothermicity (adiabatic temperature T_{ad}) combustion synthesis has been described as self-propagating high temperature synthesis (SHS), low temperature combustion synthesis (LCS), solution combustion synthesis (SCS), gel-combustion[222], sol-gel combustion,

[6] Termite is a pyrotechnic composition of metal powder fuel and metal oxide.

... [211] Various of these methods can be subdivided under the regular precursors from solution processing.

Combustion processes use a combustion reaction to produce inorganic solid materials in a redox reaction. This reaction is characterized by high activation energies, an exothermic peak, a reaction temperature between 500 and 4000 K, and a heat production in the order of 10^{12}-10^{14} W/ m^3.[192] In addition to μm sized powders and coarsed powders of oxides, metallics, borides, nitrides, solid solutions, and others, also nanoparticles of these materials are made by combustion processing. [211] More detailed information about the synthesis of nanocrystalline oxides can be found in the book of *Patil et al.* on the chemistry of nanocrystalline oxide materials: combustion synthesis, properties and applications. [210] Also *Lackner et al.* summarized a lot of combustion characteristics. [153]

Solution combustion synthesis

SCS of oxide materials was unexpectedly discovered during the reaction between aluminum nitrate and urea. When rapidly heating (around 500 °C in a muffle furnace) a mixture of $Al(NO_3)_3 \cdot 9\,H_2O$ and urea solution, the reaction foamed and ignited to burn with an incandescent flame yielding a voluminous white product, which was identified as α-Al_2O_3. [143]

Solution combustion synthesis has proven to be a suitable method for the synthesis of metal oxides. Metals salts like nitrates and carboxylates are dissolved together with organic fuels in aqueous solutions. The nitrates are the oxidizers, while the organic fuels supply heat and can even complexate the metal ions. In that manner the metal ions are homogeneously distributed. This method has been applied to synthesize (doped) oxide powders.[210] Only more recently publications on direct film deposition from combustion precursors have been successfully explored. [85, 142]

Oxidizer-to-Fuel ratio Concepts of propellant chemistry are applied to understand the highly exothermic nature of the combustion reaction. The specific impulse I_{sp} of a propellant is a measure of the energy released during combustion and is proportional to the highest produced heat (T_c temperature of chamber) and the molecular weight of the gaseous (Equation 1.13), when the equivalence ratio (ϕ_e) is 1.

$$I_{sp} \propto \sqrt{\frac{T_c}{\text{molecular weight of gaseous products}}} \tag{1.13}$$

Jain et al. developed a method in 1981 for the calculation of this equivalence ratio or elemental stoichiometric coefficient ϕ_e which could easily be applied

to multicomponent fuel-oxidizer systems. [125] This coefficient is defined by total amount of oxidizing components divided by the total of fuel components (Equation 1.14). For solution combustion processing oxygen is the only oxidizing element and has negative valencies, while carbon, hydrogen, and metal cations are reducing elements and have positive valencies, and nitrogen is neutral. Carbon is +4, hydrogen +1, metal ion (with z+ as charge) is z+, oxygen is -2, and nitrogen is 0.

$$\phi_e = \frac{\sum(\text{Coefficient of oxidizing elements in specific formula})(\text{Valency})}{(-1)\sum(\text{Coefficient of reducing elements in specific formula})(\text{Valency})} \tag{1.14}$$

For example a reaction with zinc nitrate $Zn(NO_3)_2 \cdot 6\,H_2O$ and glycine $C_2H_5NO_2$ in solution gives the following sums (Equation 1.15 (H_2O can be neglected) and Equation 1.16). The oxidizer-to-fuel ration is $\frac{10}{9}$ and ensures a balanced chemistry in Equation 1.17.

$$Zn(NO_3)_2 \cdot 6\,H_2O = -10 \qquad [Zn = +2, N = 0, (6)O = (6)(-2)] \tag{1.15}$$

$$C_2H_5NO_2 = 9 \qquad [(2)C = (2)4, (5)H = (5)1, N = 0, (2)O = (2)(-2)] \tag{1.16}$$

$$9Zn(NO_3)_2 \cdot 6\,H_2O_{(aq)} + 10C_2H_5NO_{2(aq)} \longrightarrow 9ZnO_{(s)} + 20CO_{2(g)} + 5N_{2(g)} + 61H_2O_{(g)} \tag{1.17}$$

This type of stoichiometric balance of a redox mixture for a combustion reaction is fundamental to the synthesis of an oxide material by the solution combustion method.

Fuels Fuels are a source of carbon and hydrogen, which form carbon dioxide and water during combustion processing. The route of decomposition is often followed through components from which they are formed, which in their turn decompose to HNCO and NH_3 which ignite with NO_x. In addition, fuels are able to form complexes with the metal ions, inducing homogeneous mixing of cations. [210] Compounds containing N-N bounds in their moieties are particularly found to assist the combustion better. [210] Simple compounds like glycine and urea are also considered to be fuels. [222] Some fuels are considered to be linked to a certain metal ion to improve complexation. [210]. Urea is for example ideal for the combustion synthesis of high temperature aluminum

oxide. Other fuels are hydrazine based fuels like carbohydrazide, oxalyl dihydrazide, and malonic dihydrazide, with their low ignition temperature and presence of N-N bounds that exothermically decompose in N_2.

Up to now, the fuels needed to be water soluble, have a low ignition temperature ($< 500\,℃$), be compatible with metal nitrates and induce a smooth controlled combustion reaction without explosion, synthesize the oxide without residual mass, be commercially available or easy to prepare.

Although the method of *Jain et al.*, to determine the elemental stoichiometric coefficient, is very well accepted in literature with 617 citations up to this moment, it currently only applies for aqueous solution combustion powder synthesis. [125] Most SCS is done in aqueous suspension. What if a precursor is made by the dissolution of oxidizers and fuels in other solvents than water? Up to the point of combustion the solvent will be vaporized. Nevertheless residual solvent fractions might influence this ratio determination. Especially solvents like 2-methoxyethanol are considered to be a fuel. The amount of residual solvent is difficult to establish. Also for small amount of doping it fractional ratio's need to be taken in account when calculating the oxidizer-to-fuel ratio.

Thermodynamics According to the textbook of *Ring et al.* one can assume that for solution combustion processing a thermally isolated system exists. [210] In a very short period of time extremely high temperature of more than 1000 ℃ can be achieved which cannot be dispersed to the surroundings in that time window. The maximum temperature to which the product is exposed is assumed to be the adiabatic temperature T_{ad}. The liberated heat during this reaction is the enthalpy of the system as indicated in Equation 1.18 and is the difference between the enthalpy of the products and the reagents at standard temperature and pressure (STP) (Equation 1.19). If $\Delta H_f < 0$, the reaction is endothermic, while for $\Delta H_f > 0$ the reaction is exothermic. With the reaction enthalpy the adiabatic temperature or flame temperature can be determined (Equation 1.18).

$$\Delta H_f^0 = \int_{298}^{T_{ad}} \Delta C_p(product)dT \tag{1.18}$$

$$\Delta H^0\text{reaction} = \Delta H_f^0(\text{products}) - \Delta H_f^0(\text{reagents}) \tag{1.19}$$

To be able to achieve crystalline films with combustion processing, not only an exothermic process is necessary, but the heat liberated during this reaction needs to be sufficiently high to generate sufficient energy.

1.6 Deposition

Table 1.1: Overview of the advantages and disadvantages of each deposition technique

Deposition technique	Advantages	Disadvantages
Direct coating	Low T	High amount of waste
Dip coating	Deposition on complex size and shape	Thickness variations, Two-side coverage of substrate
Spray coating	Fast, complex size and shape coverage	Homogeneity of the film
Doctor blade	Large area, no waste and good uniformity	Micrometric precision of blade regulation
Printing	Reduced waste & cost friendly	More difficult adaptation of precursor
Drop casting	Simple & No waste	Poor uniformity, thickness control
Spin coating	Good uniformity & reproducibility	Waste of materials, limited area

The formulation of the precursor will influence the film formation and requires the appropriate deposition technique. Different deposition techniques will be elaborated as indicated in Figure 1.9 from which their advantages and disadvantages are summed up in Table 1.1.[209] A more elaborate explanation about all of these tehcniques can be found in various textbooks. [243] [183] [241]

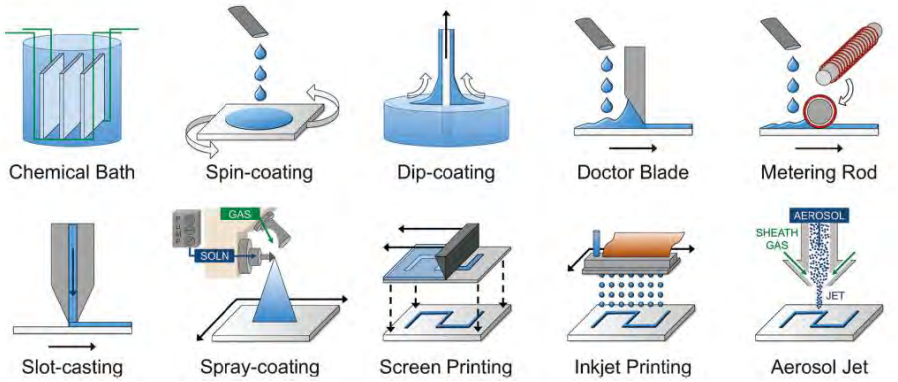

Figure 1.9: Overview of the different deposition techniques according to *Pasquarelli et al.* [209].

1.6.1 Direct coating

Under direct coating are chemical bath deposition and electro-deposition categorized. Substrates are submerged in a bath or vessel, containing a solution of ions and additives. By raising the temperature or influencing the voltage on the substrates a precipitation occurs. [111] [227] The chemistry behind this is based on nucleation and growth as described above and synthesizes layers up to several μm. The largest disadvantage might be the generation of high amounts of waste.

1.6.2 Dip coating

Dip coating enables the easy deposition on top of complex and irregular shapes. Although this technique might be limited by thickness variations, voids and pinholes and a two-side coverage. During dip coating, a substrate is immersed in a precursor solution and removed at a constant rate. Afterwards the solvent needs to evaporate. This process is defined by the viscous drag, gravitational forces, and surface tension in the concavely shaped meniscus. [241]

1.6.3 Doctor blade coating

In contrast to dip coating, doctor blade coating only covers one side of the substrate. A precursor, preferably with high viscosity, is dropped on the sub-

strate and divided by a moving blade on top of the substrate. Slit, slot and die casting are analog techniques. [30]

1.6.4 Spray coating

Also spray coating is fast, adaptable to complex size and shapes, has a high conformal step coverage and high efficiency. Even multiple-layer deposition on non-planar surfaces can be done. Largest disadvantage might be the homogeneity of the deposited film. The precursor is transformed by an atomizer or nebulizer into a fog (fine droplets and carrier gas), which is deposited by gravitational or electrostatic forces. [241]

1.6.5 Printing

Screen, ink-jet and aerosol printing are also commonly applied. Screen printing needs a mask and ink jet and aerosol printing are considered to be direct write methods. These methods have several advantages going from maximum material utilization (screen) to no waste environmental and cost friendly approach of the direct methods.[30]

1.6.6 Drop casting

Drop casting will be used in this thesis as a very fast method on lab-scale to evaluate precursors. This process is, as the name says, based on dropping of the precusor and the evaporation of the solvent. This makes it a very easy method with no waste generation. Nevertheless, the method has a lot of flaws: limitations in large area coverage, hard to control the thickness, and poor uniformity.

1.6.7 Spin coating

The other main method of choice here will be spin coating. This is motivated by the low cost, excellent thickness control, which allows deposition of layers from a couple of nm up to several μm with high reproducibility and uniformity. Nevertheless, a lot of precursor material is lost during this application and there is the requirement of flat surfaces, which need to be pretreated to ensure wettability. Also multiple layer deposition might be challenging depending on the precursor. Further on, continuous processes are not possible, making it a lab-scale technique. The substrate, on which the precursor is dropped, is placed on a vacuum chuck and accelerated to high angular velocities ($\sim$ 300 to 10,000 rpm). After the excess of liquid is spun off, a coated substrate stays behind. This process is based on the equilibrium between the centrifugal forces, created by rapid spinning and the viscous forces, determined by the viscosity of the precursor. [241]

1.7 Thermal processing

1.7.1 Molecular precursors

After the deposition of the precursor through either method, thermal processing is needed to decompose the precursors with the removal of organics, to induce crystallization or phase transformations (if desired), and to control electronic carrier concentration.[209] Some deposition techniques as spray pyrolysis, chemical bath deposition and electro-deposition might need no further thermal treatment. This thermal processing is labeled depending on the conditions: thermolysis, in case of conduction in an oxygen containing atmosphere and pyrolysis, if the reaction occurs in absence of oxygen.[209] Hot plates, tube furnaces or rapid thermal processing (RTP) are generally applied for thermal processing. A process in a tube furnaces, with resistive heating as well as RTP, with high intensity lamps, can be conducted under a controlled atmosphere. Although RTP delays the decomposition to higher temperatures, this can be an advantage as the kinetics are faster. Crystallization and decomposition can simultaneously be induced.

This thermal processing has a large impact on the generation of charge carriers. For the deposition of functional TCOs various atmospheres are applied in order to render conductive layers. Atmospheric processing is generally insufficient for solution processed films. Reductive hydrogen containing anneals, vacuum, UV or even plasma processing is often needed. [111] [301] [44]

1.7.2 Nanoparticle suspensions

In contrast to molecular precursors, the deposition of suspensions with nanoparticles might be expected to require a less intensive thermal treatment, since the crystalline NPs are formed beforehand. The suspensions contain, in addition to the solvent, often stabilizers, with either electro-statically or which induce steric hindrance to avoid agglomeration. For the thermal processing of suspensions, a difference is made between curing and sintering. [209] Curing is the process where the suspension medium and the residual organics are removed, and 'naked' NPs can be found on top of the substrate. These NPs have a lot of grain boundaries which significantly reduce the conductivity. To obtain films with a minimal of grain boundaries, sintering is needed. [212] The sintering of materials is explained further on and often requires even higher temperatures as for molecular precursors. [209]

1.7.3 Sintering

The textbook of *Ring* about the fundamentals of ceramic processing and synthesis gives an overview from the synthesis of ceramic powders up to sintering

of these materials. [223] The driving force for sintering is the reduction of the total free energy of the system. During sintering very high temperatures are applied, approaching the melting point of the ceramic. This induces changes in grain size and shape as well as changes in pore size and shape. This process can be subdivided into three substages with an initial, intermediate and final stage of sintering (Figure 1.10). During the initial stage neck formation of particles occurs. In the next stage, pore shape approximates a continuous cylindrical channel coincident with three grain edges throughout the matrix. Cylindrical pores shrink and break up into a string of spherical pores. In the end, closed pores are removed, and densification takes place.

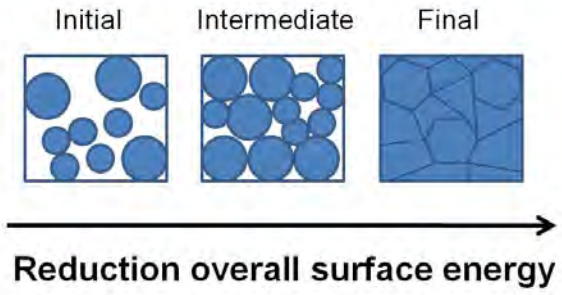

Figure 1.10: The initial, intermediate and final stage of sintering are displayed. In the initial stage, neck growth will occur with a loss of up to 50 % surface area. Almost no coarsening and insignificant amount of densification occurs. The intermediate stage is known for pore rounding and elongation with almost complete loss of open porosity. Coarsening leads to increase in grain size and pore size together with significant densification. For the final stage, pore closure, extended grain and pore growth, and final slow and minimal densification occurs. The additional loss of surface area is negligible.

Initial sintering stage After removal of the solvent and additives, a so-called green body, consisting of ceramic particles, is left. During the temperature increase, to induce sintering, materials flow from different sources of the green body to the neck at the intersection between particles as displayed in Figure 1.11. The neck has an energetically more favorable location due to its negative curvature in comparison to the positive curvature of the spherical ceramic particle. The pathways, surface, lattice, and grain boundary diffusion as well as vapor phase diffusion, are drawn in Figure 1.11. More detailed information on the kinetics of this transport mechanism can be found in the textbook of *Ring*. [223]

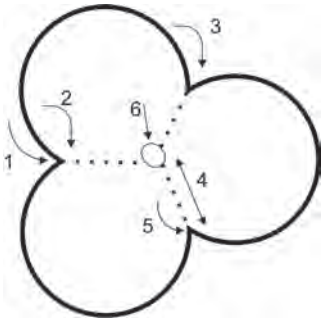

Figure 1.11: Pathways for the transport of material during the initial stage of sintering. 1) surface diffusion for coarsening, 2) lattice diffusion for coarsening, 3) vapor transport for coarsening, 4) boundary diffusion for sintering, 5) lattice diffusion from grain boundary for sintering, and 6) lattice diffusion from dislocations for sintering.

Intermediate sintering stage During the initial stage a pore and grain-boundary matrix is obtained which is built out of equilibrium dihedral angles formed on the solid-vapor (pore) surface at the intersections with the solid-solid (grain boundary interfaces). After grain and pore shape changes, the intermediate stage of sintering starts. The pore shape will now approximate a continuous cylindrical channel coincident with three grain edges throughout the matrix. This cylindric pore will shrink with the formation of spherical pores in correlation to the Rayleigh instability (Figure 1.12). When the length of the cylinder is much longer than the diameter, Rayleigh instability occurs. [223] The spherical pores are located at the grain boundaries within the green body. Here, a first densification occurs.

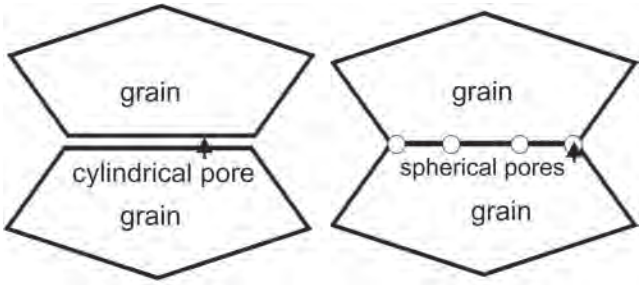

Figure 1.12: Breakup of a cylindrical pore into a string of spherical pores triggered by Rayleigh instability.

Final sintering stage The formed closed pores during the intermediate stage are removed in the final stage. Densification is the important process here. This is dependent on the association of pores with grain boundaries and

the rate of grain growth. The string of pores at the grain boundaries will migrate to the lowest energy point, either the intersection of three grains in 2D or four grains in 3D. [223]

Grain growth is considered to be a part of the final stage. There are two types of grain growth: 1) normal and discontinuous and 2) abnormal or secondary recrystallization or cannibalistic grain growth. During cannibalistic grain growth, a few large grains develop and eventually consume all smaller grains. For normal grain growth, the grain size distribution is relatively narrow and has a fixed distribution shape throughout growth. Many characteristics such as magnetic and electronic properties of the material are affected by grain size. [14] As the properties of the grain boundaries differs from the bulk of the material, grain size and grain boundaries are expected to have a significant influence on the properties of the oxides. [150] The degree of disorder, lattice defects and oxygen vacancies at the grain boundary can cause them to act as relatively conducting regions for anions as well as oxygen. These grain boundaries can adjust more quickly to changes in either atmosphere and temperature than the interior of the grains and thus alter their electrical conductivity more quickly. [223] In case of additives or a second solid phase is associated with grain boundaries, grains will become more isolated and prevent passage of charge carriers from one grain to another. [223] *Atkinson* and *Cahn* elaborated more in detail on the theoretical background of the grain growth process. [16, 40]

1.7.4 Reduced temperature sintering

Since sintering occurs at temperatures close to the melting point of the ceramic, which is rather high, the reduction of the sintering temperature is often needed. The use of nanoparticles could effectively lead to higher densification rates. The smaller the particles, the higher the specific surface area and the less the diffusion distances. The relation to improve the densification is expressed by the Herring scaling law (Eq. 1.20). t_i and r_i are the sintering time and grain size and n is a constant depending upon the sintering mechanism.

$$t_2 = (\frac{r_2}{r_1})^n t_1 \tag{1.20}$$

The use of very small nanoparticles is necessary since otherwise it is very difficult to effectively use the nanoparticles for the construction of a TCO film. Laser sintering [26], micro-wave sintering [212], pressure sintering [223] and electrical sintering [12] are used to reduce the effective processing temperature. These options might simplify the use of particles as building blocks for TCOs.

1.8 Which TCOs?

The first published report on conducting transparent oxides was about CdO.[18] Since then several articles have been published on undoped tin oxide, either doped with antimony, fluorine, or with phosphor, arsenic, indium, thallium, tellurium, tungsten, chlorine bromine and iodine.[52] But also (un)doped indium oxide gained interest as well as (un)doped zinc oxide (Al and In). More recently *Pasquarelli et al.* and *Löbmann* gave a detailed overview of the recent status of solution processed TCOs. [209] [241] From all oxides, the choice is limited by cations with d-shells completely occupied, because otherwise d-d transitions would cause absorption of electromagnetic radiation and cause coloration.

1.8.1 Tin-doped Indium Oxide

For all the synthesized and deposited TCOs, indium tin oxide (ITO; 90% In_2O_3 and 10% SnO_2) is probably the most commercialized one as its electric properties are superior to others. ITO was already developed in 1978 by *Tsunashima et al.* and is currently well implemented. [274] ITO is used either crystalline or amorphous with good electrical conductivity and optical transparency.

Some ITO films prepared from sol-gel processing are competitive with physical vacuum-based technologies as resistivities in the 10^{-4} Ohm cm region are obtained. [164] [11] [10] Although this result is very good, *Löbmann* does not consider the preparation methods to be representative for current state-of-the art techniques. [241] Future developments and precursors should adress stability and cost-efficient processing of materials.

On the contrary to molecular precursors ITO nanoparticles are used in dispersions with solvents and dispersants. The crystalline NPs are either commercially available particles [50] or can be synthesized [102]. The obtained sheet resistance is only low enough for some applications in case of sufficiently thick ITO films. The crystalline particles have low sintering activity and even high temperature treatment does not reduce the porosity nor improve the conductivity. [241] Although, locally it could be shown that the resistivity is as low as 7 10^{-4} Ohm cm, this does not account for the overall electronic performance.[79]

Although TCO based on ITO are generally good performing, alternatives are searched. Indium is a high cost element, from which the supply is limited since it ranks 61^{st} in abundance in the Earth's crust at approximately 0.25 ppm. [78] As a rare element, In occurs predominantly in Zn ores, mostly in the mineral sphalerite (Zn,Fe)S. This together with the high amount of applications with TCOs explains the high price of In.

Table 1.2: Criteria for choosing transparent conductor material [209] [111] [227]

Property application	Materials
Highest Transparency	ZnO:F, Cd_2SnO_4, Zn_2SnO_4
Highest Conductivity	In_2O_3:Sn
Highest mobility	CdO, In_2O_3:Ti, In_2O_3:Mo
Lowest plasma frequency	SnO_2:F, ZnO:F
Highest plasma frequency	Ag, TiN, In_2O_3:Sn
Lowest work function	ZnO:F
Highest work function	SnO_2:F, $ZnSnO_3$, ZnInSnO
Best thermal stability	SnO_2:F, TiN, Cd_2SnO_4
Best mechanical durability	TiN, SnO_2:F
Best chemical durability	SnO_2:F
Easiest to etch	ZnO:F, TiN
Lowest deposition temperature	In_2O_3:Sn, ZnO:B, ZnO:Al, ZnO:Cl a-InZnO
Least toxic	ZnO:F, SnO_2:F
Lowest cost	SnO_2:F
TTFT channel	ZnO, a-InZnO, a-ZnSnO, a-InGaZnO

1.8.2 Alternatives

Already in 1983 *Chopra et al.* gave an interesting review on the 'current' status of TCOs.[52] Since then a lot of additional alternatives have been developed as more recently described by *Hecht et al.* and *Pasquarelli et al.*.[114, 209] The search for alternatives is encouraged by the expanding need for transparent electrodes for optoelectronic device applications. Generally, it isn't the case that one TCO suits all applications as stated in Table 1.2. Each TCO has specific superior characteristics.
In search of TCOs as electrode, literature reported alternatives like graphene, [287] carbon nanotubes (CNTs), [271] metallic nanowire networks, [70] polymers, [283] and other oxides[209] as described in Table 1.2.

Graphene, a monolayer of carbon atoms sp^2-bonded in a 2D honeycomb lattice, is a building block for other carbon allotropes: graphite, nanotubes, and fullerenes. In addition to being the strongest measured material, as well as the ballistic thermal conductance [7], graphene has a ballistic electronic transport [8] with remarkably high mobilities.[232] *Pang et al.* have recently reviewed graphene as a transparent electrode material for organic electronics. [207]

CNTs consist of one or more (single or multiwalled) graphite sheets with a

[7] Ballistic thermal conductance is a phenomenon with negligible thermal conductivity.
[8] Ballistic conduction is a phenomenon with negligible electrical resistivity caused by scattering.

hexagonal lattice wrapped up into a cylinder. CNTs have a high aspect ratio of 1,000 or greater with a diameter of a few nanometers and a high elastic modulus of 1-2 TPa and a high electrical conductivity 1,000 times greater than a Cu-wire. *Wu et al.* found that CNTs have the capability of forming a natural robust random network in the film and provide low sheet resistance and high transmittance with a minimal amount of CNTs. These structural and physical properties of CNTs are superb features for flexible PV cells with high transparency and conductivity. [292]

Conductive polymers on the other hand are also being developed as electrode. These have a lower conductivity than inorganic materials, but are more flexible, inexpensive and environmentally friendly in processing and manufacture.

In order to be able to deposit on flexible substrates, low temperature alternatives have been developed based on metallic nanowires (NWs). Silver is the most conductive material (6.3 10^5 S cm^{-1}) and can only be for 80% transparent in case the film is thinner than 3 nm. A film of nanowires combines the conductivity of a metal with an open structure that transmits light. *De et al.* demonstrated a nm-thick films Ag NWs with electrical and optical properties comparable to ITO. [70] After flexing the films (even more than 1000 times) the physical properties remained unchanged.

Within this thesis the focus will be more on oxides, mainly n-type TCO materials. The most widely studied oxides are impurity doped oxides of Sn, Cd, In, Zn, and Ga, as well as their compounds and alloy mixtures. [179]

1.8.3 n-type doped ZnO

Although multiple alternatives have been put forward, the preference goes out to a low cost and environmentally friendly material: ZnO. Although the resistivity of doped ZnO is generally higher than for ITO, TCO materials based on ZnO are beneficial from the cost perspective and are characterized by high thermal stability. Moreover, amphoteric ZnO can be chemically etched easily, which increases its roughness and thus light scattering, ensuring an improved performance for thin-film silicon solar cells. [32] Nevertheless, this poor corrosion stability and the persistent photo-conductivity [9] of ZnO based materials are considered to be drawbacks and need to be taken into consideration when choosing for (doped) ZnO materials.

Up to today, to my knowledge, nobody was able to achieve p-type doping of ZnO. N-type doping of ZnO is on the other hand very easy due to the intrinsic nature of ZnO. Lattice defects such as oxygen vacancies and zinc interstitials,

[9] Photo-conductivity is an optical and electrical phenomenon in which a material becomes more electrically conductive due to the absorption of electromagnetic radiation.

introduced during synthesis or annealing make ZnO and intrinsic n-type doped semiconductor. [81] ZnO can be further extrinsically n-type doped with H, Li, B, Al, Ga, In, ... [177] Group III together with group IV dopants are expected to substitute Zn.[56, 88, 135, 168] Alternatively can oxygen be replaced by group VII elements.[48, 65, 227, 264]

Crystal structure

The ZnO lattice has the wurtzite structure, consisting of a hexagonal closed packing of oxygen ions, with Zn ions placed in half of the tetrahedral holes. The other half of the tetrahedral holes and all of the octahedral holes are empty. Ideally, a three-valent (or four-valent) cation must substitute for Zn at a tetrahedral position (substitutional tetrahedral coordination), but both types of empty holes can also accommodate dopants, forming interstitial tetrahedral or interstitial octahedral coordination. Group VII doping needs to be allocated at the oxygen position. [264]

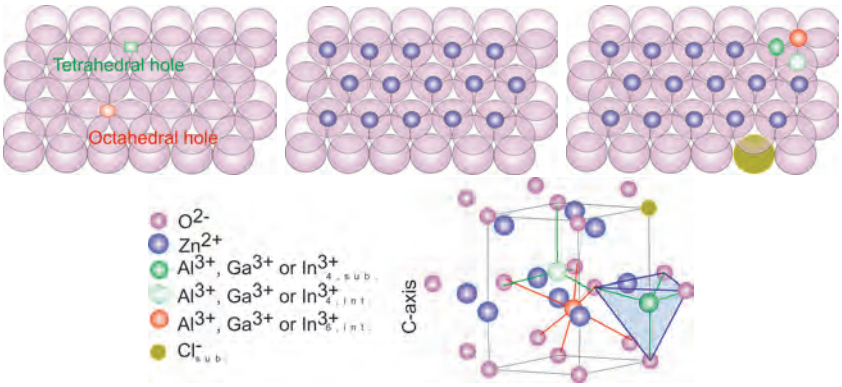

Figure 1.13: Hexagonal closed packing of oxygen atoms in wurtzite crystal lattice with tetrahedral and octahedral holes (left on top). Wurtzite crystal lattice of ZnO in top-view (middle on top). Trivalent doping of ZnO in top-view (right on top). Doping of ZnO with trivalent cations substituting Zn or Cl-doping as substitute for O (below).

Electrical properties

Pure ZnO has an intrinsic n-type conductivity behavior which is often ascribed to Zn interstitials, O vacancies and H-doping.[81] While H is acknowledged as a shallow donor in ZnO, Zn interstitials and O vacancies are still under debate. [126] Different opinions are presented regarding the oxygen vacancies. Some believe that it attributes to the improved conductivity[198][111][159][11], while *Ágoston et al.* indicate the deep level of these oxygen vacancies[5]. The existence, or in this case the absence, is very difficult to prove. Nevertheless, *Lany*

and Zunger published a theory emphasizing the paradoxal coexistence or contribution of a metastable oxygen vacancy defect, induced by photo-excitation, to the conductivity.[155] This is supported by the UV behavior of ZnO and AZO. [173][111] Furthermore, grain boundary adsorption of oxygen is reported to increase the resistivity by the introduction of possible trap states for electrons inside the film.[284] This all makes the role of oxygen in the conductivity mechanism not very straightforward.

The crystalline grains have an influence on the electrical properties through scattering at the grain boundaries. Although, when doping is applied these ionized impurities reduce the grain boundary potential and create a high electron mobility due to a denser and less porous morphology. Also an increase in the transparency in the UV region and in the conductivity is observed due to doping according to *Copuroglu et al.*.[58] Depending on the synthesis, the optimal dopant concentration varies for each dopant. This is possible due to the fact that dopant will be placed interstitial instead of substitutional in the ZnO lattice when doping exceeds a certain %. This will lead to accepting behavior of dopants and reduction of the conductivity. Furthermore, there will be a decrease in crystallite size and increase in grain boundaries and scattering centers. Also a possible segregation of different phases will reduce the quality of the film. For Al-doping, alumina or gahnite will be formed at the grain boundaries due to solubility limit of aluminum oxide in zinc oxide.[20]

For doped ZnO films with a carrier concentration of the order of 10^{20}-10^{21} cm^{-3} , the Hall mobility is dependent on the carrier concentration. *Minami et al.* stated that if the carrier concentration exceeds 10^{21} cm^{-3} ionized impurity scattering becomes the important scattering mechanism in decreasing the mobility and also thus the conductivity.[179] The Hall mobility increases with increasing thickness of the TCO film, while the carrier concentration is independent of the thickness. This scattering is characterized by an decrease in Hall mobility caused by an increase in carrier concentration up to approximately 10^{21} cm^{-3}. More carriers creates a higher potential barrier as well as the trapping of free electrons due to oxygen adsorbed on grain boundaries and the film surface. In contrast, grain boundary scattering may be unimportant for AZO films with a carrier concentration of the order 10^{21} cm^{-3} because of the lowering of potential barrier height resulting from the carrier screening effect. The narrow width of the barriers between the grains can be tunneled by electrons. Nevertheless, the increase of mean free path which leads to increase of mobility in doped ZnO films with a carrier concentration of 10^{21} cm^{-3}, may be assigned to the improvement of crystallinity, which is related to carrier scattering mechanisms such as grain boundary scattering and dislocation scattering.[180]

The higher the crystal orientation (002), the lower the resistivity due to shorter carrier path length in a c-plane and due to the reduction in the scattering of

the carriers at the grain boundaries and crystal defects, which increased the apparent mobility. The main difference between impurity-doped ZnO and ITO is that the decrease of carrier mobility occurred at much lower concentrations for ITO than for zinc oxides. *Ellmer et al.* explained this due to the different grain barrier trap densities N_t for zinc oxides and ITO. Doped zinc oxide exhibits N_t values between 5 10^{12} and 3 10^{13} cm^{-2}, while ITO has a lower grain boundary trap density of 1.5 10^{12} cm^{-2}. [82]

It is very hard to prepare impurity-doped ZnO thin films with a carrier concentration of 10^{21} cm^{-3}. Oxygen adsorption on the surface and grain boundaries of the films is affected by the oxidizing atmosphere during deposition. Controlling the oxidizing atmosphere during deposition is of great importance for the preparation of highly transparent and conducting doped ZnO thin films with a carrier concentration of 10^{21} cm^{-3}. A weaker oxidizing atmosphere is required than with the deposition of other TCO materials such as ITO. Thus for the deposition of doped ZnO with a low resistivity it is important to control the oxidizing atmosphere during the deposition. Optical and electrical properties of doped ZnO thin films could be obviously improved by optimized deposition conditions and doping [268, 269], since the properties of doped ZnO films are strongly dependent on the fabrication method, co-doping species and the conditions of the post-growth treatment.[247]

Not all dopants in higher concentrations need a crystalline network. For indium zinc oxide (IZO) for example there is an amorphous or crystalline structure. (The amorphous form requires that the materials also must be a TCO in the crystalline form.) Due to the existence of a disorder network, the amorphous form is better suited to accommodate strain, which makes it applicable for flexible electronic applications and has a high conductivity. The conductivity is determined by the overlap of the s-orbitals which are invariant for disorder, on the contrary to traditional amorphous semiconductors.[116]

1.8.4 Al-doped ZnO

Al-doped ZnO is often preferred, as both Al and Zn are abundantly available non-toxic and cheap. Al-doped ZnO (AZO or ZnO:Al) is due limited orbital size only possible to obtain conductive layers in crystalline form.[116] The allocation of Al inside the ZnO lattice can be studied with solid-state ^{27}Al magic-angle-spinning (MAS) nuclear magnetic resonance (NMR) spectrometry. Figure 1.14 gives an overview of the Al location for the conductivity. Traditionally only tetrahedral and octahedral incorporation are expected, from which only substitutional tetrahedral occupation is believed to lead to improved conductivity. Interstitial tetrahedral Al is thought to be an acceptor [109], although *Zhan et al.* believe it is a thermally unstable shallow donor. [297] Also the octahedral coordination is not expected to improve the conductivity or can even

indicate the segregation of different crystal phases. [17] With recent studies in addition to the expected tetrahedral and octahedral position often an penta-coordination is found. *Miao et al.* studied the Al incorporation with solid-state ^{27}Al MAS NMR inside NPs, synthesized through co-precipitation.[178] In addition to the tetrahedral and octahedral coordination of Al, they observed this 5-fold coordination, but did not explain the origin. Furthermore, *Avadhut et al.* reported the possible formation of a 5-fold or penta-coordination, linking this Al incorporation with the performance of a spin coated layer build out of NPs. They ascribed the 5-fold to an interaction of Al and H, which originated from the reagents. [17] Also *Kemmitt et al.* studied the Al incorporation of powders from sol-gel processed precursors and purely found the regular 4-fold and 6-fold coordination for Al^{3+}. [136]

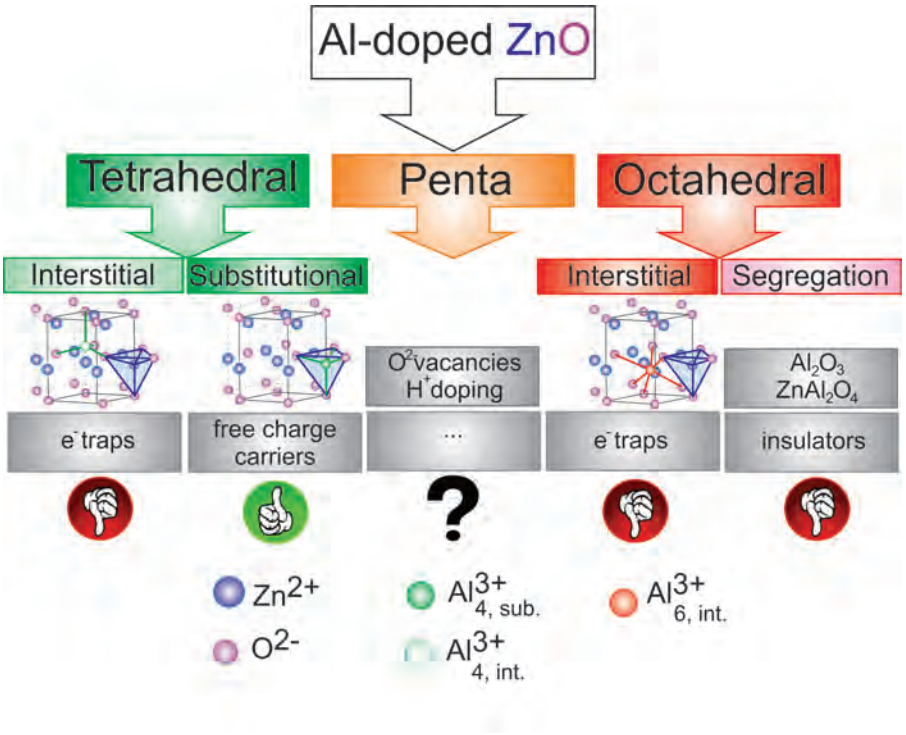

Figure 1.14: Representation of the wurtzite crystal lattice with a hcp of oxygen atoms, an occupation of half of the tetrahedral holes by zinc and substitutional or interstitial incorporation of Al as dopant. Their consequences for the conductivity are also included.

Solution processing of Al-doped ZnO

AZO has been deposited using various techniques such as DC and RF magnetron sputtering[140], electron beam evaporation [230], pulsed laser depo-

sition [259], chemical vapor deposition[182] and (aqueous) chemical solution deposition [186] [209]. During the decades most synthesis of AZO had been performed through vacuum deposition. As this method needs expensive equipment, cheaper alternatives have been found through solution processing with spray pyrolysis [9], sol-gel processing[262], or through the use of NPs[112].

Since the beginning of the 21^{th} century several promising synthesis methods for AZO nanocrystals have been presented, although often still high temperature anneals are needed to obtain conductive films or sometimes even no functional film is presented. [37, 263, 267]

Commonly applied sol-gel routes use organic solvents such as methanol[262], ethanol[262], isopropanol[242], methoxyethanol[158], butoxyethanol[239], ethylene glycol and glycerol[273], in which Zn and Al reagents are dissolved in combination with a stabilizer such as monoethanolamine, diethanolamine or tetramethyl ammonium hydroxide[200, 273]. Often, the use of water-based methods is preferred, as these are environmentally friendly and can be handled with ease, certainly in comparison with some organic solvents such as 2-methoxyethanol, which is known to be hazardous.[67]

1.9 Summary

Various methods have been discussed within solution processing of n-type doped ZnO. For this thesis the focus will be on the development of new molecular precursors and nanoparticle building blocks which can serve as a TCO in solar panels. As *Pasquarelli et al.* emphasized, there is need of inexpensive solution processed layers.[209] Preferably, low temperature precursors or suspensions are synthesized, which are competitive with vacuum processing.

N-type doped ZnO materials are studied and synthesized to be able to obtain a transparency of at least 85 % in the optically active wavelength range and the conductivity has to be equal or exceed 10^3 S/cm with a carrier concentration of the order of 10^{20} cm^{-3}.

First of all AZO NPs are synthesized with a good understanding of the intrinsic parameters, such as the presence of charge carriers and the occupation of substitutional tetrahedral placing by Al.

In a second part, molecular precursors are investigated which are approaching the generally produced resistivity of 10^{-4} Ohm cm by vacuum processing. Further on, combustion processing is adressed to be able to obtain low temperature deposited crystalline n-type doped ZnO films, either through the use of organic solvents or with environmental friendly aqueous solutions.

2 Materials and Methods

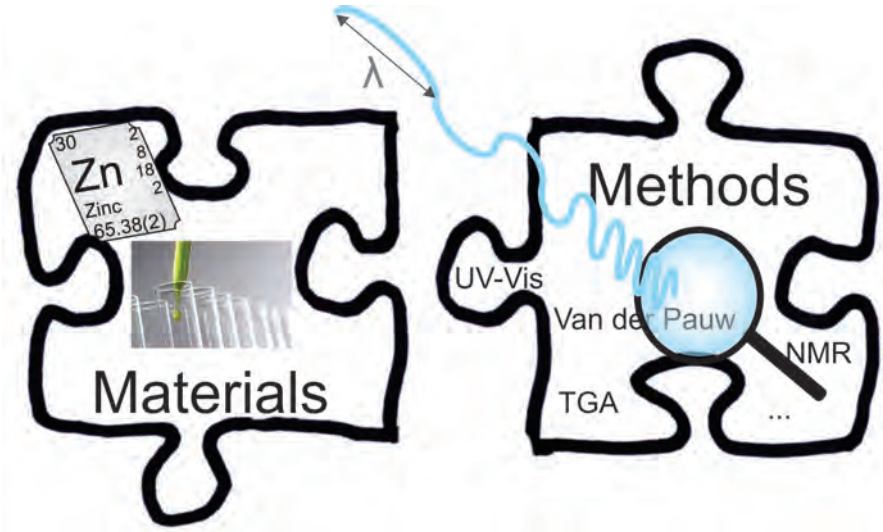

In this chapter, an introduction and summary of different characterization techniques will be given. All these analytical methods can either be used to analyze powders (containing nanoparticles) or are applied to have an indication of the characteristics of the obtained film. The major parts are summarized using different books and articles. [31, 54, 66, 75, 94, 252] Although sometimes only basic concepts are summarized, more elaborate explanations are written for more specific techniques. The first section gives insights about the specifications of the used materials for nanoparticles and molecular precursor synthesis. Afterwards the use of electromagnetic radiation is introduced to identify and characterize compounds.

2.1 Materials

In this section, the materials for the synthesis recipes in each chapter are given.

2.1.1 Aqueous Co-precipitation Synthesis

For the co-precipitation synthesis of Al-doped ZnO NPs the reagents were used as received: Zinc nitrate hexahydrate ($Zn(NO_3)_2 \cdot 6\,H_2O$, 98 %, Sigma Aldrich), Aluminum nitrate nonahydrate ($Al(NO_3)_3 \cdot 9\,H_2O$, $\geq$ 98 %, Sigma Aldrich), and ammonia (NH_3, 32 %, Merck).

2.1.2 Thermal Decomposition Synthesis in Dibenzyl Ether

All the reagents were used as received for the synthesis of nanoparticles in dibenzyl ether. Zinc acetylacetonate hydrate ($Zn(acac)_2 \cdot xH_2O$) (23.6 % Zn determined with EDTA), aluminum acetylacetonate ($Al(acac)_3$) (99 %), 1,2-hexadecanediol (90 %), 1,2-tetradecanediol (90 %), oleic acid (90 %), oleyl amine (70 %), dibenzyl ether (BE, 98 %), benzyl amine (99 %) and stearic acid (95 %) were obtained from Aldrich Chemical Co. Hexane ($\geq$ 95 %) absolute ethanol ($\geq$ 99.5 %) and 1,2-propanediol (99 %) were purchased from VWR.

2.1.3 Thermal Decomposition Synthesis in Benzyl Amine

For the NPs synthesized in benzyl amine following reagents were used:
$Zn(acac)_2 \cdot xH_2O$ (23.6 % Zn determined with EDTA, Sigma Aldrich), $Al(acac)_3$ (99 %, Sigma Aldrich), benzyl amine (BA, $C_6H_5CH_2NH_2$, 99 %, Sigma Aldrich), ethylene glycol (EG, 99.8 %, Sigma Aldrich) and methanol (CH_3OH, 99.9 %, VWR Prolabo).

2.1.4 Organic Molecular Precursors

For the synthesis of the organic precursors, all reagents were used as received. 2-butoxyethanol (2-BOE, $C_6H_{12}O_2$, 99 % extra pure, Acros), zinc acetate dihydrate ($Zn(CH_3COO)_2 \cdot 2\,H_2O$, $\geq$ 98 %, Sigma Aldrich), Aluminum nitrate nonahydrate ($Al(NO_3)_3 \cdot 9\,H_2O$, $\geq$ 98 %, Sigma Aldrich), Aluminum Chloride ($AlCl_3 \cdot 6\,H_2O$, 99 %, Sigma Aldrich). For the low temperature decomposing precursor in 2-methoxyethanol following reagents were used as received: $Zn(acac)_2$ .xH_2O (23.6 % Zn determined with EDTA), $Al(acac)_3$ (99 %), Indium acetylacetonate ($In(acac)_3$, $\geq$ 99.99 %), Gallium acetylacetonate ($Ga(acac)_3$, $\geq$ 99.99 %) and 2-methoxyethanol (2-MOE, $C_3H_8O_2$, $\geq$ 99.3 %) were obtained from Aldrich Chemical Co. Ammonium nitrate (NH_4NO_3, analytical reagent) was purchased from VWR.

2.1.5 Aqueous Molecular Precursors

For the aqueous precursor synthesis all chemical reagents were used without further purification:
ZnO (puriss., 99 %, Sigma Aldrich), $Al(OH)_3$ (reagent grade, Sigma Aldrich), $In(OH_3)$ (99.99% trace metals basis, Sigma Aldrich), $Ga(NO_3)_3 \cdot xH_2O$ (Gallium(III)nitrate hydrate, 99.9% trace metals basis, Sigma Aldrich), NH_4Cl (99.99% trace metals basis, Sigma Aldrich), citric acid monohydrate (CA, $C_6H_8O_7 \cdot H_2O$, 99%, Sigma Aldrich), glycine (Gly, NH_2CH_2COOH, $\geq$ 99 %, Merck), ammonium nitrate (NH_4NO_3, analytical reagent, VWR) and ethylenediamine (en,$C_2H_4(NH_2)_2$ 99%, Alfa Aesar). Milli-Q water with a resistivity of 18 MOhm was used as solvent. All filtrations were carried out at room temperature using Pall Life Sciences Supor®100 filters with 0.1 μm pore sizes.

For more general analysis the chemicals listed below have been used. Potassium bromide (KBr , Merck (MDA)) is always used for the sample preparation for Fourier Transform Infrared Spectroscopy. HNO_3 (J.T. Baker, 69-70%, Baker Instra-analyzed Reagent) was used for sample preparation for Inductively Coupled Plasma-Atomic Emission Spectroscopy (ICP-AES) analysis. If water is used, it is deionized water (milli-Q, resistivity 18.0 MOhm cm).

2.2 Electromagnetic radiation

Spectroscopy covers the interaction of radiation with matter and can be used in analytical characterization. It mainly relies on electromagnetic radiation as displayed in Table 2.1 with a dual wave-particle character. [252]

Table 2.1: Overview of the electromagnetic radiation in spectroscopy with λ, the wavelength, absorption (abs.), emission (em.), fluorescence (fl.), diffraction (diffr.), scattering (sc.), and * stands for in an applied magnetic field.

Spectroscopy	λ-range	Quantum transition
γ-ray em.	0.005-1.4 Å	Nuclear
X-ray abs., em., fl., & diffr.	0.1-100 Å	Inner e^-
Vacuum UV abs.	10-180 nm	Bonding e^-
UV-Vis abs., em. & fl.	180-780 nm	Bonding e^-
IR abs. & Raman sc.	0.78-300 μm	Rotation/vibration molecules
Microwave abs.	0.75-375 mm	Rotation molecules
Electron spin resonance	3 cm	Spin of e^- *
Nuclear magnetic resonance	0.6-10 m	Spin of nuclei *

[252]

Diffraction is a process in which a parallel beam of radiation is bent by encoun-

tering a slit or obstacle. To effectively produce a diffraction pattern, the phase differences remain constant in function of time, producing coherent radiation.

Transmission is associated with the permeability of a medium for electromagnetic radiation. Compared to vacuum a medium contains atoms, ions or molecules which will interact and can scatter the applied radiation. If the dimensions of the molecules / aggregates are smaller than the applied wavelength, it is called Rayleigh scattering. In case of large particles, the Mie scattering can be different in various directions and can be applied to determine the size and shape of large molecules and colloidal particles. Raman scattering differs through quantized frequency changes. The polarization process induces vibrational energy level transitions in molecules. If multiple media are used, the direction of the wavefront alters and returns (partially) into the medium from which it originates. This phenomenon is known as reflection.

Absorption is a phenomenon where energy from the electromagnetic radiation is transferred to atoms, ions, or molecules. This enables an unique fingerprint identification of each species. Atoms, ions, and molecules are characterized by definite amounts of energy divided over discrete states. Either absorption or emission of energy correspondingly to energy difference between different states can occur. This energy is quantized according to Equation 2.1 with E_1 a higher state (or excited state) and E_0 a lower state (or excited or ground state), h as Planck constant (6.62606957(29) 10^{-34} J s), c the speed of light (299792458 m s^{-1}) and λ the wavelength and ν the frequency. The ground state or lowest energy state is mostly preferred by chemical species at room temperature. Further on the excited states can addressed. Here, a difference can be made between electronic states, quantized vibrational and rotational states. An example of absorption (dotted black lines) and emission (full grey lines) is given in Figure 2.1.

$$E_1 - E_0 = h\nu = \frac{hc}{\lambda} \tag{2.1}$$

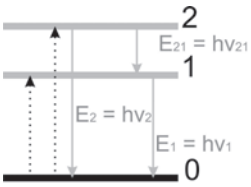

Figure 2.1: Absorption and emission process. The sample is excited from the ground state (0) through thermal, electrical, or chemical energy (black dotted arrows). This species can relaxate to the ground state by the emission of photons (grey full arrows). This coincides with the emission of a photon(s), with corresponding wavenumber (λ_{21}, λ_1, and λ_2) of the frequencies (ν_{21},ν_1, and ν_2).

Photoluminescence spectroscopy, fluorescence and phosphorescence result from absorption of EM radiation, followed by dissipation of energy through photon emission. Fluorescence is a prompt phenomenon while phosphorescence is being delayed.

2.2.1 FTIR

This part of Fourier Transform Infrared Spectroscopy (FTIR) is based on the principles from the textbook of *Skoog et al.*. [252]

Infrared (IR) spectrometry can be divided into three areas: near ($\tilde{\nu}$ 12800-4000 cm^{-1}), middle ($\tilde{\nu}$ 4000-200 cm^{-1}) and far ($\tilde{\nu}$ 200-10 cm^{-1})infrared. Various energy changes are due to transitions between vibrational or rotational energy states. This results in infrared absorption, emission and reflection spectra. Absorption of IR covers molecular species with small energy differences between these vibrational and rotational energy states. To absorb IR radiation, the dipole moment of a molecule must change when it vibrates or rotates. An electric field of the radiation can induce a change in amplitude. This stresses the necessity of heteronuclear species. Homonuclear species like oxygen (O_2) or nitrogen (N_2) cannot absorb IR, since they do not display any net change in dipole moment.

Rotational transitions require only small amounts of energy and are situated in the far-IR. As the rotational levels are quantized, well-defined lines are expected. This is the case for gases, but in liquids and solids, intra-molecular collisions and interactions cause broadening of lines into a continuum.
The energy differences between vibrational energy levels, again quantized, can be found in the mid-IR. For gases the spectra consists of a series of closely spaced lines. This is due to the presence of several rotational energy levels for each vibrational level. As rotation is restricted in liquids and solids, no vibrational-rotational lines and only broadened vibrational bands are present.

Vibrations can be divided into stretching and bending. The first covers a continuous change in inter-atomic distance along the bond axis between two atoms either symmetric or asymmetric, while the latter deals with bond angle changes through scissoring, rocking, wagging and twisting. The amount of vibrations for a linear molecule is given by 3N-5, while non-linear molecules have 3N-6 vibrations, with N the amount of atoms. This amount is set by the need for 3 coordinates for each atom, resulting in 3N degrees of freedom. Three degrees are needed to describe the rotation of a molecule as a whole. Plus, the motion of the entire molecule through space, the rotational motion of the entire molecule around its gravity center, and the motion of each atom is relative to the other atoms, further reduces the vibrational degrees of freedom with three. This amount can be even further reduced through different reasons. First, the symmetry of the molecule is as such that no change in dipole moment occurs through a particular vibration. Further, can (near) identical vibrational transitions occur. The absorption intensity is too low or the detection limits of the equipment confine the spectra. On the other hand, it is possible to find more absorption bands than expected, also known as overtones. These can be found at 2 or 3 times the original frequency.

Fourier transform instruments have several advantages like high resolving power and wavelength reproducibility as well as higher throughput. The latter is possible through the minimal incorporation of optical elements and the absence of attenuated slits. This all ensures a higher signal-to-noise ratio. In addition the elements of the source all reach the detector simultaneously and generate spectra in one second or even less. In contrast to conventional spectroscopy or frequency-domain spectroscopy, time-domain spectroscopy can be achieved by Fourier transform. The interconversion of time- and frequency is complex and can only practically be obtained through algorithms with computers. As high-frequency signals need to be converted to measurable frequencies without distorting the time relationship, through interferometers. Often a Michelson interferometer is used.

Experimental This technique is commonly applied in this thesis, not only to distinguish the presence of different organics, the formation of Zn-O (absorption band below 600 cm^{-1} [134]) but also to verify the presence of charge carriers.[37] The latter absorption is identified by a broad absorption band between 1000 and 3000 cm^{-1} which indicates free electrons in the conduction band.[37, 245] This effect in the infrared region emphasizes the n-type substitutional tetrahedral doping of Al.[134, 245] These charge carriers caused by good intrinsic properties are expected to increase the conductivity of the material.

The transmittance of several KBr pellets, containing 0.5 wt% of (Al-doped) ZnO powders, was measured on a Vertex 70 FTIR spectrometer from Bruker

Optics. The studied area was set between 4000 and 400 cm^{-1} with a resolution of 4cm^{-1}.

(G)ATR-FTIR

Internal-reflection spectroscopy allows to obtain IR spectra of samples that are difficult to deal with, like solids of limited solubility, films, and others. Reflection occurs when a radiation beam passes from a more dense to a less dense medium. During the reflection the beam or evanescent wave penetrates over a small distance into the less dense medium. Attenuation of the beam occurs at wavelengths where the less dense medium absorbs the evanescent radiation. This allows attenuated total reflectance (ATR) FTIR spectroscopy. The spectra obtained with ATR can differ from IR absorption in intensity as well as in signals. Distortions can occur near strong absorption bands where the sample refractive index may change rapidly. Also the orientation of the sample on the ATR crystal can influence the band shape and the relative intensities.

The GATR™grazing angle ATR accessory even allows analysis and characterization of monolayers on semiconductor and metallic substrates. By pressuring the sample with a distinct force intimate contact is assured between the film and crystal. This increases the sensitivity at least one order of magnitude relative to grazing angle methods.

Experimental FTIR analysis was carried out on AZO NPs synthesized in dibenzyl ether at room temperature on a Bruker Vertex 70 spectrometer equipped with a PIKE Attenuated Total Reflection (ATR) accessory from Spectra Tech (4000-600 cm^{-1}, 128 scans, 4 cm^{-1}). To this end, ZnO:Al NPs in suspension were deposited onto an ATR crystal (diamond/ZnSe composite) and then dried to remove the hexane.

Not only powders are analyzed, the strength of GATR-FTIR is the ability to characterize films. The films obtained from aqueous n-type doped Zn precursors were characterized through GATR-FTIR at room temperature. This was done using a 65° single reflection Ge-ATR (Harrick) unit, placed inside the sample compartment of a FTIR spectrometer (Bruker Vertex 70, 32 scans, 4000-600 cm^{-1}). To ensure intimate contact between the sample and the Ge-crystal, 0.4 Nm of torque is applied.

2.2.2 DLS

Dynamic light scattering (DLS) or photon correlation spectroscopy is a technique to determine the hydrodynamic size as well as the zeta potential of small spherical particles in suspension. A monochromatic light source, a laser is used

on the particles in suspension. Once the light hits the particles, the light scatters in all directions due to Rayleigh scattering. In correlation of time the scattered radiation is modified due to the Brownian movement of the particles. The scattered light undergoes a constructive or destructive interference caused by the surrounding particles. The speed of the moving particles is determined by the diffusion coefficient, which can be used to correlate the size of the particles using the Stokes-Einstein Equation 2.2. D is the translational diffusion coefficient, R the hydrodynamic diameter, η the viscosity, k_B Boltzmann constant, and T the temperature.

$$D = \frac{k_b T}{6\pi\eta R} \tag{2.2}$$

The zeta potential is an electrokinetic potential in a colloidal suspension. The potential varies around a particle in function of the distance (from the particle), the charge and the permittivity to the cross-section of the double layer. From liquid dynamics it is understood that the liquid layer close to the surface of a particle moves with the same velocity as the particle's surface. Near the surface, the relative velocity is zero. Further away from the surface the immobilized liquid layer will transfer into a mobile liquid. This border is called the shear plane or slipping plane. The potential at this slipping plane is the zeta potential ζ and is more or less equal to the Stern potential ψ_s and is smaller than the surface potential ψ_0. The zeta potential is determined by applying a voltage to the suspension. This will induce an attraction of charged NPs to the oppositely charged pole. The speed of the movement is measured with Laser Doppler Velocimetry and converted to an electrophoretic mobility through Equation 2.3. U_E is the electrophoretic mobility, v the velocity of the moving NPs and E the electric field. This electrophoretic mobility is given by the Henry equation 2.4 which is related to the zeta potential ε is the dielectric constant, f(ka) is the Henry's function and is in aqueous suspensions approximated 1.5 (Smoluchowski).

$$U_E = \frac{v}{E} \tag{2.3}$$

$$U_E = \frac{2\varepsilon\zeta f(ka)}{3\eta} \tag{2.4}$$

Experimental Log-normal number distributions of Dynamic Light Scattering measurements on ZnO and ZnO:Al suspensions (ZnO-ST, 2Al-ST, 3Al-ST, 5Al-ST, 8Al-ST and 10Al-ST see section 4.2.1) were taken on a ZetaPALS equipped with an optional particle sizer from Brookhaven Instruments Corporation. The examined suspensions were diluted (1:20) in hexane. The obtained hydrodynamic diameter was compared with the dry diameter observed from TEM images (ZnO-ST, 2Al-ST, 3Al-ST, 5Al-ST, 8Al-ST and 10Al-ST).

The zeta potential of the suspension of AZO NRs, synthesized in benzyl amine was recorder for 1:10 diluted suspension in ethanol (EtOH) and ethylene glycol (EG) on a ZetaPALS equipped with an optional particle sizer from Brookhaven Instruments Corporation.

2.2.3 headspace GC-MS

Headspace gas chromatography mass spectrometry or headspace GC-MS is the analysis of the gas in the chromatography vial and is commonly applied in the characterization of volatile or semi-volatile organics in solids, liquids and gases. The gas in the vials is injected in a chromatography column and transported through an inert gaseous mobile phase. The analytes interact with the stationary phase of the column and will have hereby different retention times. The detection can be done through various methods from flame ionization, thermal conductivity, photo-ionization, ..., up to mass spectrometry. Mass spectrometry is also briefly described in Section2.6

Headspace GC-MS was done to analyze the evolved gases during thermal decomposition synthesis of AZO NPs in dibenzyl ether. The headspace Gas Chromatography Mass Spectrometry (GC-MS) analyses were carried out on a HS-40 from Perkin Elmer, with a He carrier flow, combined with a Trace GC Ultra and a Trace DSQ from Thermoquest. After dissolution of 2 mmol $Zn(acac)_2 \cdot xH_2O$, 5 mol % $Al(acac)_3$, 10 mmol 1,2-hexadecanediol, 6 mmol oleic acid and 6 mmol oleyl amine in 25 mL dibenzyl ether at 60 ℃ under N_2 atmosphere, 100 µL of this 'start' solution was put in a vial for analysis. The reaction conditions inside the vial were mimicked by raising the temperature up to 200 ℃, isothermally holding for 2 h. Afterwards the temperature was raised up to 300 ℃ and kept for another hour. After obtaining 200 ℃ for 2 h the headspace vial was punctured. This process was repeated after the second temperature step at 300 ℃ for 1 h. The released gases during the step at 200 ℃ and 300 ℃ were sequentially separated and identified by MS using electron impact as the ionization mode. A 30 m DB-WAX capillary column (0.25 mm x 0.25 µm) was heated from 30 ℃ up to 200 ℃ (12 ℃/min).

2.2.4 ICP-AES

Inductively coupled plasma atomic emission spectroscopy (ICP-AES) was applied to determine the ion concentration or ratio of synthesized nanoparticles and precursors. The liquid sample is vaporized by a nebulizer into an Argon plasma generated by a torch. Thereby Zn^{2+}, Al^{3+}, Ga^{3+} and In^{3+} ions will collide with charged ions and electrons from the plasma. After absorption of EM radiation, they will radiate wavelengths characteristic for the involved elements. For our analysis only Al, Ga, In and Zn have been analyzed. Their characteristic emission lines are 369.149, 308.211, 394.401, and 237.308 nm for

Al; 417.196, 294.356, and 209.134 nm for Ga; 230.603, 325.609, 303.936, and 451.131 nm for In; 206.194, 213.854, 202.544, and 451.131 nm for Zn.

The Al-to-Zn ratio of nanoparticles synthesized by co-precipitation and thermal decomposition (in benzyl amine) were analyzed with ICP-AES. 30 mg (or 60 mg) of the NPs (NRs) was dissolved in 50 mL (or 100 mL) of a 5% HNO_3 solution and sonicated for the higher Al content. These solutions were directly analyzed to determine the Al content using a 1-10 ppm Al calibration curve. After additional dilution (100 times in HNO_3) the Zn concentration was determined. Also here a 1-10 ppm Zn calibration curve was made. In that manner the appropriate Al-to-Zn ratio is established.
The aqueous Zn^{2+}, Al^{3+}, Ga^{3+} and In^{3+} precursors were diluted with HNO_3 (J.T. Baker, 69-70%, Baker Instra-analyzed Reagent) to a concentration approximately in the middle of the 1-10 ppm calibration curve of the corresponding element.

2.2.5 XPS

X-ray photo-electron spectroscopy (XPS) gives an insight in the atomic composition and their oxidation state. One of the photons of a monochromatic X-ray beam with known energy ($h\nu$) displaces an electron from a e.g. K shell an generates an excited ion with a positive charge one greater than that of the original atom. The kinetic energy (E_k) of the emitted electron will be measured in an electron spectrometer. The binding energy (E_b) of that electron can be determined through Equation 2.5 with wf the work function of the spectrometer. This factor assures a correction for the electrostatic environment in which the electron is formed and measured. This binding energy is characteristic for an atom and orbital from which the electron is emitted.

$$E_b = h\nu - E_k - wf \tag{2.5}$$

XPS is applied in a qualitative and quantitative manner for the elemental composition of matter, often at the surface. All elements with exception of hydrogen and helium emit core electrons with characteristic binding energies. Mostly, the peaks in XPS spectra are well resolved. From time to time, peak overlaps are encountered or Auger electrons [1] are emitted. To differentiate Auger electrons from photoelectrons, the X-ray source can be altered. The signals coming from the Auger effect remain at the same spectral position, while the photoelectrons peaks are displaced. The peaks of the XPS spectra are to a small degree dependent on the chemical environment of the characterized atom.

[1] Auger electron is an emitted electron from a higher shell in order to refill the electron deficiency in a lower shell.

This covers variations of the amount of valence electrons or oxidation state, the type of bonds, and influence of the binding energies of the core electrons.

For the quantitative analysis of homogeneous samples, the amount of photo-electrons per second, I can be expressed according to Equation 2.6 with n the number density of atoms (atoms cm^{-3}), ϕ flux of the incident X-ray (photons cm^{-2} s^{-1}), σ the photo-electron cross section for the transition (cm^2/ atom), ε the angular efficiency factor for the instrument, η the efficiency of photo-electron production (photoelectrons/ photon), A the area from which the photo-electrons are detected (cm^2), T the efficiency of photo-electron detection, and l the mean free path of the photoelectrons (cm). For a given transition the last six terms are constant and can be summarized as atomic sensitivity factor S according to Equation 2.7. The quantity I is usually taken as peak area or sometimes peak heights are used. Often an additional internal standard is introduced, to assure the accuracy. Differences between bulk and surface composition can lead to errors in the measurement and can be overcome by depth profiles. In the end a quantitative analysis makes sense at at least 5 % of the atom.

$$I = n\phi\sigma\varepsilon\eta ATl \tag{2.6}$$

$$I = n\phi S \tag{2.7}$$

Depth profiles allow the determination of elemental composition through etching/ sputtering of the surface (and latter bulk matter) with Argon ions. As the etching rate is in correlation to time, a depth profile can be obtained.

Experimental XPS experiments were performed on the Al-doped ZnO layers synthesized and deposited through aqueous processing. 10 layers of drop casted 2.5 % Al-doped ZnO powder dispersed in ethylene glycol and dried on a hot plate in static air at 200 °C for 5 min (each layer) were analyzed using a Physical Electronics (PHI) 5600LS electron spectrometer equipped with a small-spot X-ray source providing monochromatized Al-K_α photons (1486.6 eV). This was compared to single crystal ZnO from MTI Corporation. In addition also the 2 % Al-doped ZnO film was submitted to XPS analysis analog to the powder characterization.

2.2.6 XRD

The electric vector of X-radiation will interact through scattering with electrons in the atoms. Constructive and destructive interference occurs when X-rays are scattered by the ordered environment in a crystal. The distance between

scattering centers are of the same magnitude order as the wavelength of the radiation and will result in X-ray diffraction.

If a narrow beam of radiation penetrates a crystal surface at an angle θ, scattering will occur as a result of interaction of the incoming radiation with atoms according to Bragg's law (Equation 2.8). Here, n is an integer and d represents the interplanar distance of the crystal. This restricts the constructive diffraction. At all other angles, only destructive interference will occur.

$$n\lambda = 2d\sin\theta \tag{2.8}$$

Experimental During the reductive annealing process of the films, the sheet resistance (two-point contact measurement, Keithley 2000 multimeter) and the crystallinity (XRD, Bruker D8 Discover in θ-2θ mode with a parallel bundle geometry using a Göbel mirror with a Vantec Linear Detector) were simultaneously monitored in-situ. The crystallinity of the films/powders was also studied ex-situ. This was done either using a Bruker D8 diffractometer with Cu $K_{\alpha 1+2}$ radiation operating in θ-2θ mode with a 1D lynxeye detector or using a Siemens D5000 working in Bragg-Brentano geometry, is equipped with a Ge (111) monochromator that transmits Cu $K_{\alpha 1}$= 1.54056 Å radiation and detection through a scintillation detector. For the UV treated film obtained from an aqueous citrato precursor the detection was done by means of XRD (PANalytical X'pert Pro, Cu K_α) in a Bragg-Brentano configuration (coupled - 2 scan) with a PIXcel detector in scanning mode (step size 0.0098°). Mostly the scanning was done between 10° and 60° 2θ, although sometimes the scanning range was limited between 30° and 40° 2θ.

2.2.7 UV-Vis

Molecular absorption spectroscopy is based on the measurement of transmittance (trans.) or absorbance (abs.) of mostly solutions, but is in TCOs applied to verify the transmittance. For solutions the concentration of an absorbing analyte in solution is linearly related to the absorbance according to Lambert-Beer's law (Equation 2.9). P_0 is the incident radiant power, P the transmitted radiant power, b the path length of the sample, c' the concentration of the absorber and ε the molar absorptivity.

$$abs. = -\log trans. = \log\frac{P_0}{P} = \varepsilon bc' \tag{2.9}$$

In this work the focus will be put on the interaction of UV-Vis radiation with films. A number of things happen when a beam comes into contact with a solid. Depending on the incident beam's angle in relation to the solid, the incoming radiation may be reflected, transmitted, diffused, absorbed, refracted or polarized. This will give rise to deviating measurements as the transmitted

beam will not fully be picked up by the detectors. The transmitted beam differs strongly to the incident beam through possible refraction, uneven surface of the sample, convex/concave surfaces. In addition the beam can also be diffused in all directions generating a difference between overall transmittance and diffuse transmittance. Both forms can only be recorded using an integrating sphere. [205] This integrating sphere also has it advantages towards reflectance (R), since there is a division between specular and diffuse reflectance. The first is produced if part of the incoming beam is reflected at the same angle of incident beam (like mirrors). The latter covers part of the beam reflected in all directions. The integrating sphere can be applied to record diffuse reflectance. For specular reflectance a different set-up is required. In addition, some absorbance might take place, diminishing the incoming radiation even further and reducing the transmittance. In that manner the incoming beam is built out of reflectance (refl.), absorbance and transmittance as given in Equation 2.10

$$100\% = abs.\% + refl.\% + trans.\% \tag{2.10}$$

Experimental UV-Vis spectroscopy of n-type doped films deposited on borosilicate glass was carried out on a UV-Vis-NIR Varian Cary 500 spectrophotometer (600 nm/min) with a data-interval of 1 nm. A blank borosilicate glass was taken as reference/blanc.

2.3 NMR

Nuclear magnetic resonance (NMR) spectroscopy is based on the absorption of EM radiation by nuclei. These nuclei are placed in a magnetic field to develop energy states for this absorption.

This NMR section is a subdivision of the electromagnetic radiation section and is based on several textbooks and articles. [252] [77] [8]

2.3.1 Nuclear spin

One needs to assume that nuclei rotate about an axis and have a spin. This spin induces an angular momentum p with a quantized maximum observable component. The value must be an integral or a half-integral multiple of $\frac{h}{2\pi}$ (h Planck constant). Nuclei with an odd mass number will have a half-integer spin, those with an even mass number will have an integer spin, and nuclei with even number of protons and neutrons have zero nuclear spin. The spin quantum number, I, determines the maximum number of spin values, with $2I + 1$ discrete states, which have the same energy in absence of an external field. ^{1}H and ^{27}Al nuclei, which have been used throughout this research, have $I = \frac{1}{2}$ and $I = \frac{5}{2}$. The electrical charge for $I = \frac{1}{2}$ is homogeneously, spherically

distributed. For a ^{27}Al nucleus, generally nuclei with $I > \frac{1}{2}$, the charge is distributed in an ellipsoid generating an electrical quadrupole moment. While nuclei with $I = \frac{1}{2}$ have NMR spectra with sharp lines, the latter nuclei ($I > \frac{1}{2}$) will induce broad lines in the NMR spectra

Analog to a magnetic field produced when electricity flows throughout a coil or wire, the charged spinning nucleus create a field with a magnetic moment μ (along the axis of the spin) proportional to the angular momentum p (Equation 2.11). The proportional constant γ also known as the magnetogyric, or gyromagnetic ratio varies for each nucleus.

$$\mu = \gamma p \tag{2.11}$$

The relationship in Equation 2.11 generates observable quantum states m with $m = I, I-1, I-2, \ldots, -I$. The ^{1}H nucleus has two magnetic quantum numbers, $m_I = +\frac{1}{2}$ and $m_I = -\frac{1}{2}$, while for ^{27}Al the splitting in energy levels is more complex. The magnetic quantum numbers are: $m_I = +\frac{1}{2}$ and $m_I = -\frac{1}{2}$, $m_I = +\frac{3}{2}$ and $m_I = -\frac{3}{2}$, and $m_I = +\frac{5}{2}$ and $m_I = -\frac{5}{2}$ (Figure 2.2).

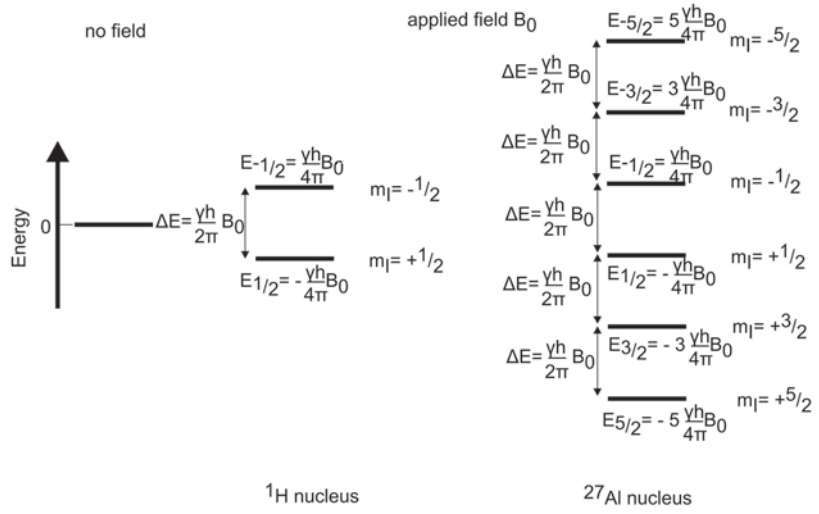

Figure 2.2: Magnetic moments and energy levels for a ^{1}H and ^{27}Al nucleus with spin quantum number $I = \frac{1}{2}$ and $I = \frac{5}{2}$.

2.3.2 Energy levels in an external magnetic field

According to the classical description, if an external magnetic field is applied along the z-axis causes a circular motion of the nucleus in a perpendicular plane around the orientation axis of the external magnetic field. This circular motion, also known as precession, has an angular velocity and is characterized

by the angle of the precession cone θ (Figure 2.3). Quantum mechanics limits the variation of angular velocity to discrete values as is elucidated below.

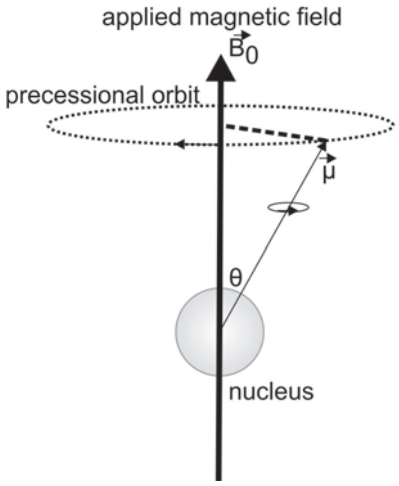

Figure 2.3: Precession of a rotation nucleus in a magnetic field.

Without a magnetic field the spin states are degenerated. When placed in a magnetic field B_0, the degeneracy is lifted according to the Zeeman effect (Figure 2.2). The energy is then expressed as the scalar product of the magnetic moment and the external field. As the magnetic field is applied in the z-axis, the z-component equals the magnitude and no vectors are necessary. (Equation 2.12). This results in the general Equation 2.13 with the energy difference between adjacent levels calculated by Equation 2.14. For a nucleus with a spin quantum number of $I = \frac{1}{2}$ under the influence of a magnetic field, its magnetic moment becomes oriented in one of two directions with respect to the field, depending on its magnetic quantum state (Figure2.2). The initial energy E of a nucleus in the orientations is given by Equation 2.13 with the energy difference (ΔE) between two states according to Equation 2.14. For nuclei with $I \geq \frac{1}{2}$ quantum mechanics states that the only transitions that are allowed are those with a change in the magnetic quantum number equal to 1 ($\Delta m = \pm 1$) according to Equation 2.13. This energy difference corresponds to the Planck relationship $\Delta E = h\nu_0$ and establishes a correlation between the frequency and the applied magnetic field (Equation 2.15). The precession frequency as described by classical theory is equal to the resonance or Larmor frequency ($\nu_0 = \nu_L$) (Equation 2.15).

$$E = -\overrightarrow{\mu}\overrightarrow{B_0} = \mu_z B_0 \tag{2.12}$$

$$E = -\frac{\gamma m_I h}{2\pi} B_O \tag{2.13}$$

$$\Delta E = \frac{\gamma h}{2\pi} B_O \tag{2.14}$$

$$\nu_0 = \frac{\gamma B_O}{2\pi} \tag{2.15}$$

2.3.3 Occupation of energy levels

Transitions between two energy levels are due to irradiation of the system with EM radiation. Transitions can either be triggered by the absorption of energy (lower to higher energy states) or can lead to the emission of energy (higher to lower energy states). Through these transitions, spins will change in orientation. The Boltzmann equilibrium indicates a higher occupation of the lower energy level and makes energy absorption the dominating transition. The intensity of the signal is proportional to the population difference, the total number of spins in the system, and the concentration of magnetic resonance active species. In case of saturation, both energy levels are equally occupied and absorption and emission cancel each other out.
This transition is only possible if the EM radiation matches the energy difference between both energy states. The frequency of this EM radiation is called the resonance frequency or Larmor frequency ν_L (Equation 2.15).

As stated before in the absence of a magnetic field, the magnetic quantum states of a nucleus are identical. When placed in a magnetic field, the nuclei ($I = \frac{1}{2}$) tend to orient themselves with a predominance for the lower energy state ($m_I = +\frac{1}{2}$). This predominance is also known as the Boltzmann equilibrium (Equation 2.16) with N_j the number of protons in the higher energy state ($m_I = -\frac{1}{2}$), and N_0 the number of protons in the lower energy state ($m_I = +\frac{1}{2}$), k Boltzmann's constant (1.38 10^{-23} J/ K), and T the absolute temperature.

$$\frac{N_j}{N_0} = \exp(-\frac{\Delta E}{kT}) = \exp(-\frac{\gamma h B_0}{2\pi kT}) \tag{2.16}$$

2.3.4 Modification of the magnetization

Pulses

Transitions form lower to higher energy until both spin states are equally occupied modulate the magnetization. This can be done through the excitation with a radio frequent pulse, with the appropriate frequency and a pulse time τ_p (μs). This pulse originates from an additional, oscillating magnetic field $\overrightarrow{B_1}$ along the x-axis. 90° and 180° pulses are commonly applied. With a 90° pulse, the magnetization $\overrightarrow{M_0}$ is brought in to the xy-plane along the y-axis. The latter 180° pulse inverts the magnetization along the z-axis and by this also the population of spin states.

Relaxation

Every applied pulse disturbs the thermal or Boltzmann equilibrium. After application of either a 90° or 180° pulse the equilibrium will be reinstated through spin-lattice (longitudinal or T_1) as displayed in Figure 2.4 (Equation 2.17).

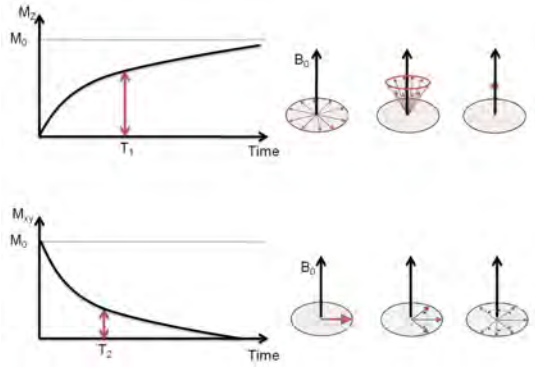

Figure 2.4: T_1 (above) and T_2 (below) relaxation after a 90° pulse.

The longitudinal relaxation enables energy transfer from the excited spins to their surrounding molecular framework according to Equation 2.17 with time t, and T_1 the spin-lattice relaxation time in the order of s. 99 % of the longitudinal relaxation is recovered after a period 5 times T_1. This relaxation is strongly influenced by temperature solution viscosity, structure and molecular size. Alternatively energy is transferred to neighboring nuclei via transverse or T_2 relaxation. This will induce a fan-out and eventual loss of the net magnetization in the transverse plane giving by Equation 2.18 as displayed in Figure 2.4. T_2 is the spin-spin relaxation time in the μs - s region and is smaller or equal to T_1. This T_2 time can be determined using a spin-echo pulse sequence which consists of a $90°_x$ pulse followed by a waiting period τ, a $180°_y$ pulse, again the same waiting period τ. The size of the echo is recorded for different spacing of the two applied pulses and reveals the coherence, which is not refocused by the latter pulse.

$$M_z = M_0(1 - e^{-t/T_1}) \tag{2.17}$$

$$M_{xy} = M_0 e^{-t/T_2} \tag{2.18}$$

The T_1 can easily be determined following the recovery of the thermal equilibrium after a perturbation. Inversion recovery is a two-pulse sequence of a 180° and a 90°. The magnetization vector is aligned with the -z-axis and will gradually shrink to the xy-plane and will completely be recovered at the +z-axis. Since the vector cannot be observed on the z-axis, it is placed in the xy-plane through a 90° pulse after a certain period t. For $t = 0$, the magnetization will

have a full intensity along the -y-axis. This gives an inverted spectrum. If the experiment is repeated with increasing t, the relaxation of the spins can be monitored. In the end when t is sufficiently long ($t > 5T_1$) complete relaxation will occur between two pulses and the maximum positive signal is recorded. The intensity of the detected magnetization, I_t follows Equation 2.19.

$$I_t = I_0(1 - 2e^{-t/T_1}) \tag{2.19}$$

NMR spectrum

In comparison to continuous wave (CW) NMR spectroscopy, nowadays FT NMR is applied. CW with a fixed magnetic field, probes the NMR response at individual frequencies in succession with a poor signal-to-noise ratio. This can be mitigated by averaging through addition of spectra from repeated measurements, but is still not very efficient in comparison to FT NMR. Now, short pulses (μs) of radio-frequency (10^2 to 10^3 MHz) radiation, with the interval T (s) between the pulses are applied. During T, a time-domain RF signal, called the free-induction decay (FID), is emitted perpendicular to the static magnetic field by the excited nuclei as they relax. If a sample contains various nuclei in a specific chemical environment, the different transverse magnetization components are superimposed and give rise to a complex FID. The direct interpretation of FID is very difficult. Therefore, Fourier Transformations are done to convert the time domain to the frequency domain.

There are different types of NMR spectra depending on the application. Wide-line spectra are most commonly obtained at relatively low magnetic field strength. Here a bandwidth of the source of the lines is used to obscure fine structure coming from the chemical environment. Wide-line spectra are useful for the quantitative determination of isotopes and are also used to interpret the physical environment of the absorbed species. In contrast, most NMR spectra are high-resolution spectra and can differentiate small ppm differences. Each isotope has several resonances in the NMR spectrum coming from differences in the chemical environment.

There are different interactions which give rise to a NMR spectrum. Zeeman splitting lies on the basis of NMR and has been discussed above. Further on, there are shifts that change the NMR frequency from which the chemical shift is discussed below. Other shifts are the Knight shift and a paramagnetic shift. Additionally there are couplings, like a J-coupling, a dipolar coupling, and a quadrupolar coupling that split the NMR signal.

Chemical shift The resonances of nuclei are strongly influenced by the chemical environment which shield the nucleus from the external magnetic field, $\overrightarrow{B}_0$.

The nucleus will experience the effective magnetic field $\overrightarrow{B}_{effective,i}$ which is related to the external magnetic field according to Equation 2.20.

$$B_{effective,i} = B_0 - \sigma_i B_0 \tag{2.20}$$

σ_i is a dimensionless shielding constant dependent on the electron density around the nucleus. This means it varies for other nuclei in respect to the chemical environment. This results in different resonance signals according to Equation 2.21.

$$\nu_{L,i} = \frac{\gamma}{2\pi}(1 - \sigma_i)B_O \tag{2.21}$$

Through the correlation of the resonance frequencies and the magnitude of the external magnetic field a relative scale known as the chemical shift (δ_i) is employed. Frequencies differences are given in respect to the resonance frequency of an arbitrary compound. For ^{1}H NMR this is tetramethylsilane, while for ^{27}Al NMR here $AlCl_3 \cdot 6\,H_2O$ is used. This eliminates the correlation to the external magnetic field strength and establishes a relation of the chemical shift in function of the chemical environment of the observed nucleus (Equation 2.22).

$$\delta_i = \frac{\nu_i - \nu_{reference}}{\nu_{reference}} 10^6 = \frac{\sigma_{reference} - \sigma_i}{\sigma_{reference}} 10^6 (ppm) \tag{2.22}$$

This contribution can be divided in an isotropic and an anisotropic component. Under influence of a magnetic field, electrons precess around the nucleus in a plane perpendicular to the applied magnetic field (Figure 2.3). This induces a secondary field, opposing the primary field. This generates a shielding of the nucleus through the influence of a smaller magnetic field as originally. This effect is also named as diamagnetic isotropy. In contrast anisotropic electron motions additionally influence the spectra. The effective magnetic field and the resonance frequency of a spin is correlated $(3\cos^2\theta - 1)$ to the spatial orientation of the surrounding groups. This chemical shift anisotropy (CSA) is averaged out in liquids by the rapid motion of molecules in solutions. For solids this is a cause of major line broadening.

Quadrupolar coupling Dipole interaction between spins is the most important mechanism for relaxation as $I = \frac{1}{2}$. Dipoles that approach each other will have interacting magnetic fields. Fluctuations here will induce relaxation. Different is it for nuclei where $I > \frac{1}{2}$, where quadrupole relaxation is the dominating mechanism. An electrical quadrupole can be visualized as two back-to-back electrical dipoles induced by the ellipsoidal charge distribution of the nucleus. Tumbling of the molecule at an appropriate frequency alters the local electrical field and influences the quadrupole moment through spin relaxation. The magnitude of the quadrupole itself has a large influence on this quadrupole

relaxation. Large values result in more efficient spin relaxation and induces broader line widths in the NMR spectra. For ^{27}Al the quadrupole moment is 15 10^{-30} m^2.

In addition to the Zeeman effect, this quadrupolar coupling causes a large energy level shift. This effect cannot be treated solely as a first order interaction but covers a first and second order interaction. The first interplay has an angular dependency with respect to the magnetic field ($P_2(cos\theta) = \frac{1}{2}(3cos^2\theta - 1)$ also known as the P2 Legendre polynomial)(see 2.3.5). The second order interaction has a dependence on the P4 Legendre polynomial ($P_4(cos\theta) = \frac{1}{8}(35cos^4\theta - 30cos^2\theta + 3)$).

Dipolar coupling In addition to the applied magnetic field a nucleus will experience local fields that are induced by neighboring nuclei. The magnitude of these local fields depends on the distance and angle between the nucleus and the dipolar coupled spin S. The spin experiences an effective (different) magnetic field $B_{effective}$ which is spatially resolved according to Equation 2.23 with γ the gyromagnetic ratios of the spins, r the internuclear distance and θ is the angle between the vector joining the spins with respect to the applied magnetic field. By modification of the experienced magnetic field, the resonance frequency will be altered.

$$B_{effective} \propto \pm \frac{\gamma_{nucleus}\gamma_{coupledspin}(3\cos^2\theta - 1)}{r^3} \tag{2.23}$$

This dipole-dipole interaction or dipolar coupling is averaged out for small molecules in solution through fast Brownian motion. The time scale is much shorter for Brownian motion than the time required for the development of dipolar coupling. In solid-state NMR, this coupling will give rise to strong line broadening.

Scalar coupling Neighboring nuclei will also interact through the bonds and will also change the effective magnetic field, $B_{effective}$ and the resonance frequency. Spinning nuclei create a magnetic field and influence the distribution of electrons in the bonds between that nucleus and others. This is known as spin-spin scalar coupling or J-coupling. In solution the direct dipole-dipole coupling is canceled and only indirect spin-spin coupling remains. The result in the NMR spectrum is the splitting over a distance (Hz) equal to the coupling constant J of the NMR signal in multiple signals.
Double resonance experiments covers a group of techniques in which a sample is simultaneously irradiated with two or more signals of different radio frequencies. Techniques like spin decoupling nuclear overhauser effect, spin tickling and internuclear double resonance simplify the interpretation of complex NMR spectra.

Qualitative to quantitative NMR Quantitative information can also be obtained by integrating the peak area of signal in the NMR spectrum. The peak area is proportional to the amount of chemically equivalent nuclei in the sample and to the concentration.

2.3.5 Solid-state NMR

MAS

As molecules are less mobile in solids nuclear spin interactions such as chemical shift anisotropy, dipolar and quadrupolar interactions induce excessive line broadening and lose the fine structure. Magic Angle Spinning (MAS) is a technique to average out these time-dependent spin interactions. By spinning the sample at magic angle ($\theta = 54.75°$ where $cos^2\theta = \frac{1}{3}$)in respect to the applied magnetic field, the normally broad line becomes narrower. Through MAS the dipolar interaction averages to zero while the CSA averages to a non-zero value. On the other hand the quadrupolar interaction cannot be completely averaged since it is unable to remove the second-order quadrupolar interaction. This second order interaction has a dependence on the P4 Legendre polynomial ($P_4(cos\theta) = \frac{1}{8}(35cos^4\theta - 30cos^2\theta + 3)$) with zero values at 30.6° and 70.1°. Techniques like double rotation (DOR)[235] where you spin at two angles at the same time or dynamic angle spinning (DAS) [49, 281] where you switch very fast between two angles can average out the second order interaction. [255]

2.3.6 Two-dimensional NMR

Two-dimensional NMR or 2D NMR makes it possible to unravel complex spectra through identification of resonances connected through bond coupling, space interactions or by chemical exchange. Data are acquired as a function of time t_2 analog to ordinary FT-NMR. Prior to obtaining the FID signal, the system is perturbed by a pulse for a period t_1. Fourier transformation of the FID as a function of t_2 for a fixed t_1 yields a spectrum similar to that obtained in an ordinary pulse experiment. This process is then repeated for various t_1 values. This leads to a 2D spectrum in terms of two frequency variables ν_1 and ν_2 or chemical shift parameters δ_1 and δ_2.

Within the explanation presented here, different liquid techniques like diffusion ordered and nuclear overhauser effect spectroscopy as well as a solid-state multiple-quantum magic-angle spinning technique for 2D spectra are addressed. Correlation spectroscopy (COSY), J-spectroscopy and exchange spectroscopy (EXSY) are all 2D techniques which enable the gathering and simplification of NMR information. Nevertheless as none of these were used during the analysis of experiments, we refer to more common textbooks for their applications and theory. [55, 63, 250]

DOSY

Although diffusion ordered spectroscopy or DOSY is considered to be a 'pseudo'-2D technique, the essential theory behind it is briefly explained in this paragraph. More detailed information can be found in Chapter 9 of High-resolution NMR techniques in organic chemistry by Claridge. [54] Diffusion NMR spectroscopy gives insights on the molecular level to their physical properties. Through this analysis information about the size, shape, aggregation, encapsulation, complexation and hydrogen bonding can be obtained. The distance that a molecule travels in one direction, z_{RMS} can be given by Equation 2.24 with D (m^2/ s), the self-diffusion coefficient and t (s), the time.

$$z_{RMS} = \sqrt{2Dt} \tag{2.24}$$

With DOSY, spectra of mixtures are separated based on their different mobility rates in 'pseudo'-2D spectra. One axis represents the chemical shifts and the second diffusion coefficients.

NOESY

Cross relaxations between nuclear spins are used to establish correlations in NOESY or Nuclear Overhauser Effect spectroscopy. A 2D spectrum is generated with diagonal and cross peaks. The latter correlate nuclei that are in each others proximity, not bonded to each other. In addition the spectra also contain extra axial peaks. These peaks do not give additional information and can be eliminated through inversing the first pulse.

Two nuclei that are in each others neighborhood are given a 90° pulse. These vectors will now undergo a precession in the xy-plane, with each there own frequency. After an evolution time the angle between the two vectors will be 180° and is their maximal dipolar interaction. A second 90° pulse transfers the projections from the y-axis to z-axis, resulting in a homonuclear dipolar longitudinal T_1 cross-relaxation. This dipolar cross-relaxation is relatively slow and continues during the mixing time. This induces a further adaptation of the length of the vectors. A third 90° pulse enables detection with signals that vary in intensity. A larger and positive signal is expected for the fastest relaxing nuclei while a negative and smaller signal is observed for slower nuclei. The degree of magnetization transfer depends thus on the mixing time and the distance of the interacting atoms.

MQMAS

For solid-state NMR, 2D techniques can resolve the spectra and can facilitate the interpretation. MAS can remove the first-order interaction for quadrupolar nuclei, but more dedicated techniques like DAS and DOR are necessary to remove the second-order interaction. As DAS and DOR require dedicated NMR

probes, their implementation is not straightforward. In addition, through the angle switching in DAS, some signal may be lost in case of fast longitudinal relaxation (< 150 ms). Further on, for strong dipolar coupled systems this system has additional shortcomings: spin-exchange has to be sufficiently small as this cannot be eliminated during the relatively long flipping time of the rotor axis. Therefore nowadays multiple-quantum magic angle spinning (MQMAS) a 2D NMR technique is an interesting alternative.[92] It only requires a regular MAS probe, making the practical applicability more easy. MQMAS is an analysis where the narrowing of the central transition is achieved by correlation of the phase evolutions of the symmetric multiple-quantum (MQ) and single-quantum (1Q) under MAS. For more elaborate information textbooks like New techniques in solid-state NMR by Klinowski can be consulted. [146]

2.3.7 Experimental

Liquid NMR NMR experiments on the AZO NPs synthesized in dibenzyl ether were performed on a Bruker AVANCE III 500 spectrometer, operating at a ^{1}H frequency of 500.13 MHz and equipped with a 5 mm ^{1}H, BBBBI-Z probe. The suspensions (2Al-ST, 2Al-BAm and 2Al-SAc) were first completely dried, using a rotary evaporator and subsequently an oil pump. Afterwards, the samples were redissolved in deuterated toluene (99.94 at% D, purchased from Eurisotop). The temperature was set to 298.15 K. 2D Nuclear Overhauser Effect Spectroscopy (NOESY) spectra are recorded using a ^{1}H spectral width of 11.52 ppm. 512 t_1 increments, consisting of 8 scans of 2048 sampled data points each, were recorded with a 1.5 s relaxation delay. Mixing time was set to 300 ms.

All NMR spectra on the unsaturated, saturated aqueous Zn precursor and reference sample (en + CA) were measured on a Bruker Avance III Spectrometer operating at a ^{1}H frequency of 500.13 MHz, equipped with a 5 mm BBI-Z probe, temperature was set to 298.15 K. One dimensional (1D) ^{1}H and 2D NOESY (Nuclear Overhauser Effect Spectroscopy) spectra were acquired using standard pulse sequences from the Bruker library. NOESY was recorded with excitation sculpting as water suppression and mixing time was set to 300 ms. Diffusion measurements (2D DOSY) were performed using a double stimulated echo sequence for convection compensation and with monopolar gradient pulses.[57] Smoothed rectangle gradient pulse shapes were used throughout. The gradient strength was varied linearly from 2-95 % of the probe's maximum value (calibrated at 50.2 G/ cm) in 32 steps, with the gradient pulse duration and diffusion delay optimized to ensure a final attenuation of the signal in the final increment of less than 10 % relative to the first increment. The diffusion coefficients were obtained by fitting the appropriate Stejskal-Tanner equation to the signal intensity decay.[251] 1,4-dioxane was added as an internal reference for calibrating the 1D ^{1}H spectra and normalizing the diffusion data.

Solid-state NMR The position of Al in the wurtzite structure in function of the different dopant concentrations of the co-precipitation NPs is derived by ^{27}Al MAS NMR. The ^{27}Al solid-state magic angle spinning nuclear magnetic resonance measurements are performed at room temperature on an Agilent VNMRS 400 MHz spectrometer (9.4 T wide bore magnet) equipped with a Varian-Chemagnetics T3HX 3.2 mm probe. The resonance frequency of the aluminum nuclei is 104.22 MHz. The samples are packed into a 3.2 mm zirconia rotor and sealed with tight fitting Torlon caps. The spectra are obtained at a rotor spinning rate of 18 kHz by using a single pulse experiment with a $\pi/2$ pulse of 4.0 μs, an acquisition time of 10 ms, a preparation delay of 20 s and a spectral width of 420 kHz. Depending on the Al content, the number of accumulations is varied between 1000 and 3000. The chemical shift scale, in parts per million (ppm), is externally referenced to $AlCl_3 \cdot 6\,H_2O$ at 0 ppm.

Gels and powders of the aqueous citrato precursors were analyzed before and after reductive anneal with solid-state ^{27}Al magic-angle-spinning (MAS) nuclear magnetic resonance (NMR) spectrometry at room temperature on an Agilent VNMRS 400 MHz spectrometer (9.4 T wide bore magnet) equipped with a Varian-Chemagnetics T3HX 3.2 mm probe. The reductively treated 2% Al-doped ZnO was monitored in time. The resonance frequency of the aluminum nuclei is 104.22 MHz. The samples were packed into a 3.2 mm zirconia rotor and sealed with tight fitting Torlon caps. For comparison with the recent work of *Avadhut et al.*, the spectra were obtained under similar excitation conditions, i.e. using a $\pi/2$ pulse of 3 μs. The sample-rotation rate was 18 kHz, the signal-acquisition time 10 ms, the preparation delay 12 s and the spectral width 416 kHz. The spectra were obtained at a rotor spin rate of 18 kHz by using a single pulse experiment with a $\pi/2$ pulse of 3 µs, an acquisition time of 10 ms, a preparation delay of 12 s and a spectral width of 416 kHz. Depending on the Al content, the number of accumulations was varied between 2500 and 30000. The chemical shift scale, in parts per million (ppm), has been referenced externally to $AlCl_3 \cdot 6\,H_2O$ at 0 ppm. The ^{27}Al T_1 relaxation times were measured on the same spectrometer via the inversion recovery method in which the evolution time t (19 values) was varied between 0.5 ms and 30 s. The repetition delay was set to 20 s and about 900 scans were accumulated. The T_1 relaxation data were analyzed by a non-linear least-squares fit (Levenberg-Marquardt algorithm) using the KaleidaGraph 4.03 software (Synergy Software).The integrated signal intensity I(t) of the tetrahedral resonance was analyzed bi-exponentially as a function of the variable recovery time t according to:

$$I(t) = I_o^S.(1 - 2exp(t/T_{1H}^S)) + I_o^L.(1 - 2exp(t/T_{1H}^L)) + cst \qquad (2.25)$$

The superscripts S and L refer to the fractions with short or long decay time, respectively. The MQMAS ^{27}Al NMR spectrum of sample ZnO:Al 2% in 6 was recorded on a Bruker DSX400 spectrometer equipped with a 2.5-mm MAS

probehead. The three-pulse sequence p_1-t_1-p_2-τ-p_3-t_2 for triple-quantum generation/reconversion and z-filtering was used with strong pulses p_1 = 0.9 µs and p_2 = 0.3 μs at a nutation frequency ν_1 = 350 kHz (as measured on a saturated $Al(NO_3)_3$ solution), soft pulse p_3 = 20 μs at ν_1 = 1 kHz, z-filter time τ=20 μ s and interscan delay 0.1 s. The sample-rotation rate was 20 kHz. For this 2D spectrum 80 traces were recorded with 3600 scans per trace and with increasing evolution time at multiples of the sample rotation time 25 µs. Using the same strong pulse power, the 1D ^{27}Al NMR spectrum with a single 25 °excitation pulse of 0.2 μs and an interscan delay of 6 s was obtained. The 1D and 2D NMR spectra were analyzed using the program DMFit.24 The ^{1}H-MAS spectra (400 MHz) of ZnO and ZnO:Al 2% before and after reductive anneal were measured on the same spectrometer at a rotor spin rate of 18 kHz and by using a single pulse experiment with a spectral width of 50 kHz, an acquisition time of 10 ms, a $\pi/2$ pulse of 2.45 μs, a preparation delay of 8 s and 20 accumulations.

2.4 Microscopy

2.4.1 AFM

Scanning probe microscopes (SPMs) are able to resolve details onto the atomic level in three dimensions. These SPMs cover different kind microscopic techniques like scanning tunneling microscopy (STM), scanning electrochemical microscopy, and atomic force microscopy (AFM). AFM achieves atomic resolution on conducting and insulating surfaces. A flexible force-sensing cantilever with a tip is scanned in a raster pattern over the surface of the sample. Deflections of the cantilever are optically detected and are caused by the force between cantilever and sample. The movement of the tip is achieved with a piezoelectric tube. During a scan, the force on the tip is held constant while the tip moves up and down. Often a laser beam is reflected off a spot on the cantilever to a segmented photo-diode. Here, topographical information is given.

There are three commonly applied methods in AFM: contact, non-contact and tapping mode. In contrast to contact, tapping mode can make surface damage disappear. Only brief contact through an oscillating cantilever. This oscillation with a frequency of a few hundred kilohertz is driven by a constant driving force and the amplitude is monitored continuously.

Experimental Atomic force microscopy (AFM) images were obtained with a Bruker Multimode 8 AFM connected to a computer via a V series controller employing PeakForce Tapping^{TM} and ScanAsyst®. The probe used during this measurement had a spring constant of 0.4 N/m. Each sample was measured at

2 different locations and at 2 different scan sizes to confirm whether or not the resulting images represent the true morphology. The roughness was calculated from 2x2 µm^2 images, Rq represents the root mean square deviation while Ra represents the average deviation from a center plane.

2.4.2 SEM

During the past decades the necessity of resolving the smallest dimensions, pointed out the limitations of optical microscopy. Their has been a need for techniques such as scanning electron microscopy (SEM) and transmission electron microscopy (TEM). For SEM imaging, a focused electron beam impinges on the surface of a sample. The surface is scanned and the received signal is collected (above the surface) and used to form an image. These signals have various origins. Backscattered, secondary and Auger electrons as well as X-ray fluorescence photons and other photons with different energies can be found. For SEM the backscattered and secondary electrons are detected and used for surface imaging. While backscattered electrons are due to elastic interactions between the incident beam and the specimen (E > 50 eV), secondary electrons are caused by inelastic interactions (E < 50 eV). SEM provides topographic information about a variety of solid surfaces.

Experimental To investigate the surface morphology, scanning electron micrographs of the deposited layers were obtained with a FEI Quanta 200FEG SEM equipped with an EDX system from Bruker or with a Philips XL30 FEG-SEM equipped with an EDX system EDAX.

2.4.3 TEM

Like with SEM, with TEM the electrons are generated from thermionic emission from a filament, but here the beam of electrons is transmitted through the specimen. The generated electrons are accelerated through a potential and focused with electrostatic and electromagnetic lenses on the sample. After interaction, an image is formed by magnification and focusing onto an imaging device such as a fluorescent screen on a layer of photographic film or could be detected through a sensor such as a charge-coupled device (CCD) [2] camera. Contrast visible in TEM images at smaller magnifications is due to absorption of electrons also known as inelastic scattering in the material. When applying higher magnifications, imaging becomes more complex trough complex wave interactions modulate the intensity of the image.

There are different operation modes, depending on the required analysis. Most commonly applied is bright field (BF) imaging where an aperture is placed in

[2]CCD converts EM radiation into electric charges

the back focal plane of the objective lens, allowing the direct beam to pass. The formed image is based on mass-thickness and diffraction contrast meaning that dark contrast is formed for heavy atoms and crystalline areas. In contrast to bright field , also dark-field (DF) images are used. Here, the direct beam is blocked to pass the objective aperture. One or more diffracted beams, which have strongly interacted with the specimen are used instead. DF images contain information about planar defects, stacking faults or particle size.

Selected area electron diffraction (SAED) is a technique to reduce the area and the intensity of the beam which are contributing to a diffraction pattern through the insertion of an aperture into the image plane of the objective lens. For thin crystalline samples of a single crystal, an diffraction pattern is formed existing out of dots. Most samples are polycrystalline or amorphous and then a series of rings is formed.

Precessing electron diffraction (PED) is very similar to conventional SAED, although PED has the advantage of removing strong dynamical effects from the pattern. The diffraction pattern moves following the movement of the incident electron beam along the circumference of a circle with the diameter depending on the precession angle. Both primary and diffracted electron beams are descanned, analog to stationary diffraction patterns. In order to produce a stationary spot pattern, the movement of the diffraction pattern is stopped by performing simultaneously a scan and descan.[184]

Scanning transmission electron microscopy (STEM) can be distinguished from TEM since it focus the electron beam into a narrow spot which is scanned in a raster over the sample. Often this is used together with high-angle annular dark-field imaging (HAADF) where the annular dark field image is formed by very high angle incoherently scattered electrons. These electrons are the opposite from Bragg scattered electrons and are highly sensitive to variations in the atomic number of the atoms (Z-contrast imaging).

Experimental Dry diameter was measured from TEM images (ZnO-ST, 2Al-ST, 3Al-ST, 5Al-ST, 8Al-ST and 10Al-ST). For a statistical overview of the NPs dry diameter size, ≈500 NPs of different batches were manually measured and counted (Maximum Feret diameter).

Medium magnification bright field images were taken with a FEI Tecnai Spirit Transmission electron microscope operated at 120 kV. Energy Dispersive X-ray (EDX) spectra and maps, High Resolution Transmission Electron Microscopy (HRTEM) images and HAADF-STEM images were recorded using a FEI Tecnai G2 electron microscope operated at 200 kV, equipped with an EDAX system or using a FEI Titan (300 kV). Calculated HRTEM images were made using JEMS commercial software. Precession Electron Diffraction (PED) ring pat-

terns were taken on a Philips CM20 TEM (200 kV) equipped with a Spinning Star precession instrument. From the PED patterns of the pure ZnO and doped ZnO:Al NPs (ZnO-ST, 2Al-ST, 3Al-ST, 5Al-ST, 8Al-ST and 10Al-ST), the cell parameters of the different samples were obtained by extracting the peak profiles using the ELD software and refining the cell parameters to these profiles using Jana2006 (Crystallographic Computing System for Standard and Modulated Structures). For each sample, two types of ring patterns were recorded: with gold NPs as an internal standard and without. The latter were needed as all wurtzite peaks with l≠0 are hidden by an overlap with peaks from the gold NPs. For each sample several ring patterns of each type were used and a weighted average was made using the standard deviations obtained in the refinement. Initially, the a-parameters were obtained from the ring patterns of the samples with gold NPs. Afterwards the c-parameters were obtained from the ring patterns of the samples without gold NPs, using the already determined a-parameter to calibrate the patterns and for determining the zero-shift. TEM samples were prepared directly from the obtained suspension (after centrifugation and purification) by dropping a few drops of the suspension on a holey carbon grid and drying in ambient conditions under an IR lamp.

Cross sections of the films for transmission electron microscopy (TEM) studies were prepared using focused ion beam milling with a Helios NanoLab 650 after the deposition of a protective layer of platinum nanoparticles. Of these cross sections, low magnification and HRTEM images were taken using a Tecnai FEI G2 operating at 200 kV.

2.5 Conductivity

The main characteristics for TCOs are the transparency and the conductivity of the films. Although infrared analysis might proof the presence of free charge carriers, additional techniques like Van der Pauw and Hall bar measurements give a more complete overview of the conductivity.

Conductivity (σ, S/ cm) is inversely related to the specific resistance (ρ, Ohm cm). The conductivity can be calculated from basic semiconductor properties in case of dominating electron conduction according to Equation 2.26 with the elementary charge q(1.602 10^{-19} Coulomb), the carrier mobility μ (cm^2/ V s), and the carrier density n (cm^{-3}). This specific resistance is also related to sheet resistance (R_S Ohm/□ or Ohm/ Square) according to Equation 2.27 with d the thickness of the film.

$$\sigma = q\mu n \tag{2.26}$$

$$\rho = R_S d \tag{2.27}$$

2.5.1 Van der Pauw

It is the sheet resistance which is standard measured with a four-point probe of spring-loaded needles on a equal distance s. The needles need to ensure good near-ohmic contacts without damaging the sample. The current I is applied to two needles and through the other needles the voltage V is measured. Using Ohm's law the sheet resistance can be calculated (Equation 2.28). Important points of attention during measurement in addition to the nearly ohmic contacts: negligible heating of sample (I mA range), no excess injection of carriers (excess conduction), and no extreme surface potential induced surface band bendings (difference bulk and surface). The difference between a four-point measurement and the characterization through a regular multimeter is the absence of resistivity for the contact points. This results in more accurate measurements.

$$R_S = \frac{V}{I} \tag{2.28}$$

Experimental The actual resistivity of the films is calculated using the thickness, as determined by cross-sectional SEM combined with ex-situ sheet resistance measurement (four-point contact measurement, Keithley 2000 multimeter).

2.5.2 Hall bar

The mobility of the majority charge carriers is calculated with Equation 2.26 by measurement of the specific resistance and determination of the charge carriers. The term $|\frac{1}{qn}|$ is the Hall constant (R_H), indicative of the carrier concentration n, and contains information about the polarity of the charges. The Hall effect is due to current in a conductor. It is based on the onset of voltage (V_H) at a long thin sample with length a where the current flows through, and a magnetic field (B) perpendicular to the sample. The charges will experience a force, known as Lorentz force (F) (Equation 2.29 as a consequence from this magnetic field. v is the velocity of the charges and E is the electric field force (E_H) of the Hall voltage.

$$F = q(E_H + vB) \tag{2.29}$$

For a n-type sample Equation 2.30 can be used. For a p-type the sign will be positive.

$$V_H = -\frac{1}{qn}\frac{1}{d}IB \tag{2.30}$$

Through the acquisition of Hall's constant, the carrier concentration can be deduced. In the end the mobility can be determined through the application of Equation 2.26.

Experimental In order to perform electrical characterizations, a Hall-bar pattern was etched using a MJB3 Karl Suss Mask Aligner (MA55) and microposit S1818 positive photoresist (Shipley). Electrical contact was made with a wirebonded aluminum wire. For temperature control, the samples were put into an Oxford instruments Microstat He Cryostat with a range of 4.2 to 400K. The Hall effect was measured by placing the sample between a tapered pole electromagnet Bruker B-E 15 v with magnetic field strengths of up to 2.07 T. A constant current of 100 µA was applied with a Keithley 2400 in the 4-sense setting.

2.6 Thermogravimetric analysis

Thermogravimetric analysis or thermal gravimetric analysis (TGA) is an analytical method to study the decomposition of materials through chemical and physical processes with increasing temperatures. It is applied to distinguish oxidative from non-oxidative processes, as well as absorption, adsorption and desorption of gases, together with vaporization, ...

Solid (or liquid) samples are placed in an inert crucible, Platina pan or sometimes a glass pan and are heated up to a certain temperature. The atmosphere during the TGA can be chosen to discriminate oxidative processes from others. The balance chamber, where the sample is placed, can be horizontally or vertically designed. Depending on the required analysis an upper limit of temperature is set. This can be done with applying a distinct heating rate. Various heating rates will influence the thermal degradation graph. This graph gives an overview of the weight loss (% or mg) in function of temperature, T (°C) or time, t (s or min). Often the first derivative of the mass (i.f.o. T or t)is given complementary or additionally.

Simultaneous, it is often possible to monitor differential thermal analysis (TGA-DTA), also known as differential scanning calorimetry (TGA-DSC). Thermal effects that are not accompanied by a change in mass, e.g. melting, crystallization, or glass-transitions can be distinguished by exothermic or endothermic signals. Also self-igniting/ combustion reactions can be assigned by a greater than net enthalpy effect. This is a reaction according to the fire triangle: combustible gases at a sufficiently high temperature, with an ignition source (oxygen). In the end also quantitative enthalpy differences can be determined.

Evolved gas analysis (EGA) is an additional tool to qualify the emitted volatiles. [94, 191] Therefore the TGA can be coupled to an mass spectrometer (TG-MS), an infrared spectrometer (TG-(FT)IR) or others. The expelled gases from the TG are guided through an inert ceramic (heated) capillary into the MS. In the ionization chamber a bombardment with electrons forms the gases into

positive ions. These ions can be separated through a quadrupole according to mass/charge (m/z) ratio and their ion current can be measured.

Experimental 2 at% Al-doped ZnO nanoparticles, synthesized through co-precipitation, were analyzed before and after calcination on a TA instrument SDT Q600 for simultaneous TGA-DSC analysis. Approximately ∼8 mg was heated from room temperature up to 800 °C with a heating rate of 10 °C/ min in DA and N_2 (100 mL/min).

The AZO NPs in hexane, synthesized through thermal decomposition in dibenzyl ether, were analyzed on the TA instrument SDT Q600. 20, 50 or 100 μL of the suspension was pipetted into an alumina pan and heated at 10 °C/ min to 100 °C (100 mL/ min DA) and 20 °C/ min to 800 °C (100 mL/ min N_2).

Amorphous powders (or sometimes even gels) of all the precursors were obtained by drying a few drops of the solutions on a petri dish at 60 °C overnight in an oven. This was further crushed and analyzed on a TA instrument SDT Q600 for simultaneous TGA-DSC (differential scanning calorimetry) analysis. All precursor gels (∼8 mg) were heated from room temperature up to 800 °C with a heating rate of 10 °C/ min in DA (100 mL/min). Combustion precursors were only heated up to 500 °C (heating rate of 10 °C/ min in DA (100 mL/min)).

Additional in-depth TG-MS analysis was performed on 2-MOE combustion (oxidizer:fuel 4:1) precursors. 20 μL of the samples was characterized using a TGA Q5000 coupled with a Pfeiffer Vacuum Thermostar^{TM} MS. First a ramping at 10 °C/ min was applied up to 100 °C, which was kept isothermally for one hour. This was done to remove the solvent (2-MOE). After cooling to room temperature the sample was heated to 500 °C again at 10 °C/ min. Both analysis were performed either under a flow of air of Helium (50 mL/ min) while the balance chamber was flushed with N_2 or Helium (25 mL/ min). Fragments, formed during the ionization of the evolved gases, were recorded in the m/z region 5-70. The capillary between the TGA and MS was heated up to 250 °C to exclude condensation of gases.

Part I

Elaborate study of Al-doped ZnO nanoparticles

3 Aqueous Co-precipitation Synthesis

Figure 3.1: The co-precipitation set-up.

In this chapter an aqueous co-precipitation is elaborated as a simple method to synthesize Al-doped ZnO nanoparticles in large quantities. These AZO NPs are in-depth characterized and the Al is located by solid-state ^{27}Al MAS NMR. Within these results a solubility limit for the substitutional tetrahedral Al incorporation is found.

3.1 Introduction

Co-precipitation is a very easy applicable method to synthesize oxides. Even Al-doped ZnO NPs have been synthesized through precipitation reactions.[162] [296] [219] [99] The obtained nanoparticles are most often analyzed through XRD, FTIR, UV-Vis and TEM, giving a good overview on the crystallinity, transparency and the morphology. In case of analyzing the conductivity properties, pellets are often made of the nanoparticles.[296] Nevertheless as the NPs are to be used as building blocks for TCO films, the transfer from pellet to film is not that straightforward. First of all, it would be of interest to fully characterize the nanoparticles, through the determination of the amount of charge carriers and Al allocation. Within this chapter, an evaluation of the co-precipitation method for Al-doped ZnO NPs is made in function of charge carriers, linked to the Al incorporation. This is discussed in-depth to evaluate possible TCO applications.

3.2 Synthesis

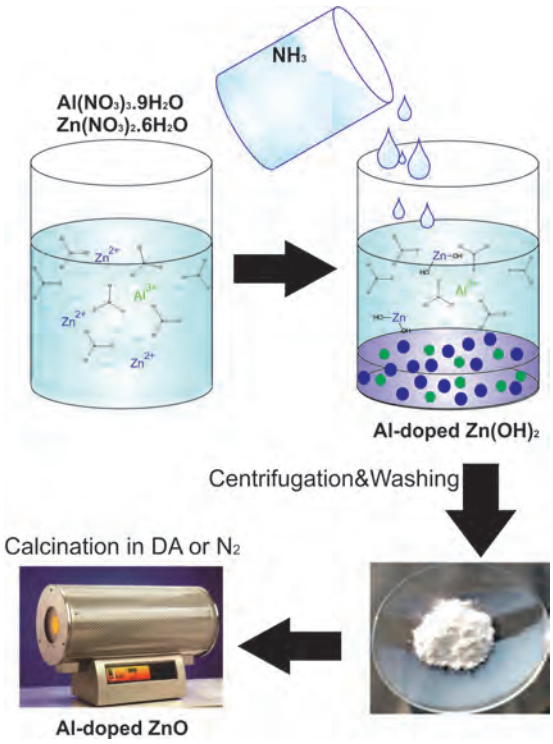

Figure 3.2: Overview of the aqueous co-precipitation synthesis

For the synthesis (Figure 3.2) of 2 at% Al-doped ZnO NPs through co-precipitation 98 mmol $Zn(NO_3)_2 \cdot 6\,H_2O$ and 2 mmol $Al(NO_3)_3 \cdot 9\,H_2O$ was dissolved in 100 mL of water. The precipitation of doped zinc hydroxides was triggered by increasing the pH slowly from 3 up to 8 with NH_3 (Schott Geräte pH-Electrode BlueLine Type 18 pH electrode). The resulting product was centrifuged at 4000 rpc for 5 minutes. The pellet was redispersed in water using a vortex and sonication. The previous two steps were repeated three times. Then the NPs were dried in an oven at 60 °C. Finally the powder was annealed in a carbolite furnace for one hour at 400 °C with dry air (DA) or annealed in nitrogen (N_2) (500 mL/min). Additional doping percentages: 1, 3, 4, 5 and 10 at% Al were synthesized through this method.

3.3 Nanoparticles in function of the at% of Al-doping

As the precipitation behavior of each metal ion is different, an important parameter to check if it is possible to synthesize Al-doped ZnO NPs and if the ratio of Al:Zn is maintained after calcination. ICP-AES was performed to establish the proper Al-to-Zn content (Table 3.1). For ICP-AES sample preparation, ± 30 mg of the NPs was dissolved in 50 mL of a 5% HNO_3 solution. For the 5 and 10 % of Al-doping sonication was applied to ensure the dissolution of the powder. As indicated in Table 3.1 the obtained Al % are even higher than the aimed values. This might be caused by a difference in precipitation behavior of Al and Zn and/or Al contamination might be coming from the use of alumina boats to calcinate the powders. For calcination in nitrogen, the amount of Al is the highest. This can only be caused through the calcination in N_2, since the steps up to the calcination are the same.

Table 3.1: The effective Al incorporation from ICP-AES

At% Al / Atmosphere	1	2	3	4	5	10
DA	1.08	2.06	3.07	4.23	5.12	8.53
N_2	1.11	2.05	3.37	4.28	5.87	10.71

3.4 Influence of the calcination atmosphere on the crystallinity and the morphology of AZO NPs

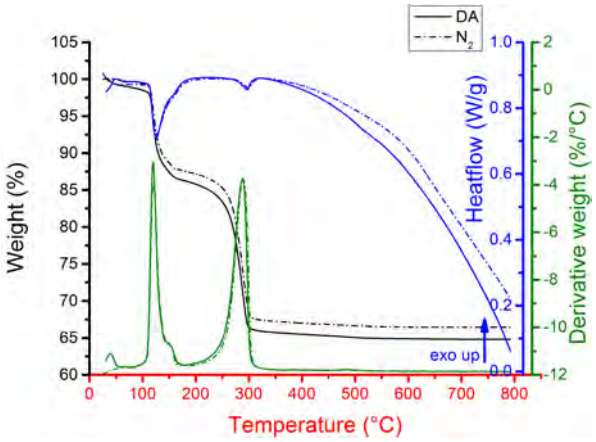

Figure 3.3: TGA analysis of the 2 at% ZnO:Al NPs at 10 °C/min in DA and N_2 atmosphere.

The different atmospheres, DA and N_2 during calcination, were evaluated to establish any difference in Al incorporation. As already indicated by ICP-AES, the obtained % of Al are higher for nitrogen and generally higher than expected (based on the input), except for 10 at% Al calcined in DA where the content is lower. In addition to determination of the compositional ratio, the precipitated products were analyzed by TGA (before calcination) and by FTIR as displayed in Figure 3.3 (after calcination) and Figure 3.4. During thermal decomposition no real differences are established purely by varying the atmosphere, since the removal of nitrates and ammonia is purely non-oxidative. The total weight loss of the powders calcinated in DA is approximately 1.5% higher than those in N_2, although this variation could be caused by the error on the measurement itself. At 100 °C the removal of water and ammonia is probably induced, while at 300 °C the remaining nitrates are decomposed.

FTIR confirms the formation of ZnO by the presence of vibration peaks between 800-500 cm^{-1}. However, additional to the adsorption of hydroxyl groups (bending: 1500-1300 cm^{-1} and stretching: 3500-3200 cm^{-1}) a more intense asymmetric stretch vibration of nitrates is observed (1379 cm^{-1}), indicating some remaining fraction of nitrates.[68, 134, 300] Although this signal is clearly present by infrared analysis, additional TGA measurement up to 800 °C on the calcinated (in DA) 2% ZnO:Al powder only shows a 0.04 weigth % loss, which

should be negligible. FTIR is commonly applied to analyze the presence of free charge carriers. [37] [134] Here, no surface plasmon absorption is observed in the 4000-1500 cm^{-1} range of the FTIR analysis, questioning the functionality of these building blocks in a TCO film.

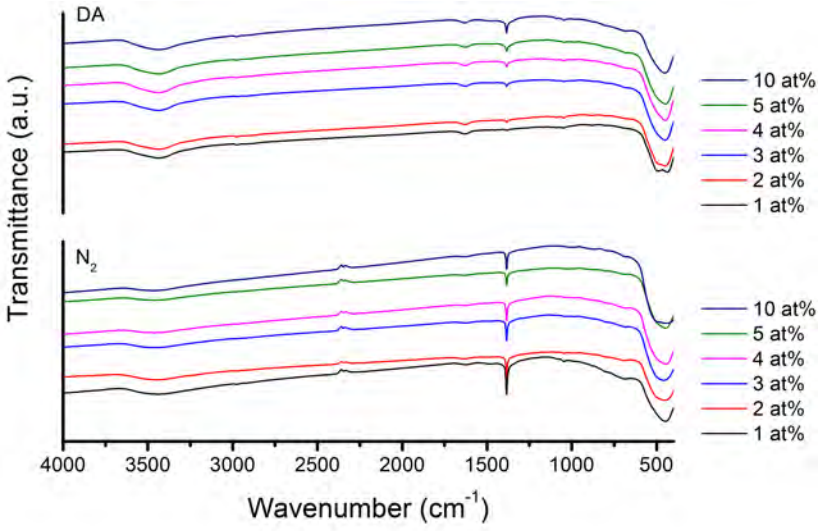

asa

Figure 3.4: FTIR analysis of the 1, 2, 3, 4, 5, 8 and 10 at% ZnO:Al NPs after calcination.

The formation of ZnO was further investigated by XRD analysis in Figure 3.5. The powder samples were homogeneously mixed with LaB_6 in a 1:1 ratio to doped ZnO powders. This experiment is done to verify if more Al doping generates a shift in diffraction peak, indicating a difference in Al incorporation either substitutional or interstitial.[134] The addition of an external standard or use of spiking method is necessary to exclude calibration errors of the diffractometer or other flaws. All these powers were placed on a Si substrate as support during XRD measurements. For all Al-doped ZnO samples the wurtzite crystal lattice is found (JCPDS 75-0576). No secondary Al containing phases, like gahnite ($ZnAl_2O_4$) or alumina (Al_2O_3) are found within the detection limits of the apparatus. This does not mean that no secondary phases are present. In-depth TEM analysis might show some crystals with a phase different from wurtzite.[68] For the 2% ZnO:Al powders annealed in DA, an additional peak of the Si substrate (JCPDS 72-1426) is visible. Depending on the coverage of the substrate this diffraction peak might be present or absent. The introducing Al as dopants inside ZnO, the wurtzite crystal lattice will endure stress. This might have an influence on the lattice parameters through shrinkage or expansion. Bragg's law and the understanding of the Miller indices state that

a lattice expansion results in a shift to lower 2θ and a shrinkage induces a shift to higher 2θ:

$$\frac{1}{d^2} = \frac{4}{3}\left(\frac{h^2 + hk + k^2}{a^2}\right) + \frac{l^2}{c^2} \tag{3.1}$$

$$n\lambda = 2d\sin\theta \tag{3.2}$$

If Equation 3.2 is inserted in equation 3.1, a direct relationship between θ and the lattice parameters a and c is visible:

$$\frac{4\sin^2\theta}{n^2\lambda^2} = \frac{4}{3}\left(\frac{h^2 + hk + k^2}{a^2}\right) + \frac{l^2}{c^2} \tag{3.3}$$

However, no such peak shifts are clearly observed in Figure 3.5, indicating no lattice expansion nor shrinkage. With this information it is not possible to verify if increasing the amount of Al leads to more substitutional or interstitial Al placing. Substitutional Al would result in a shrinkage of the ZnO lattice, while interstitial Al is expected to lead to lattice expansion.[144]

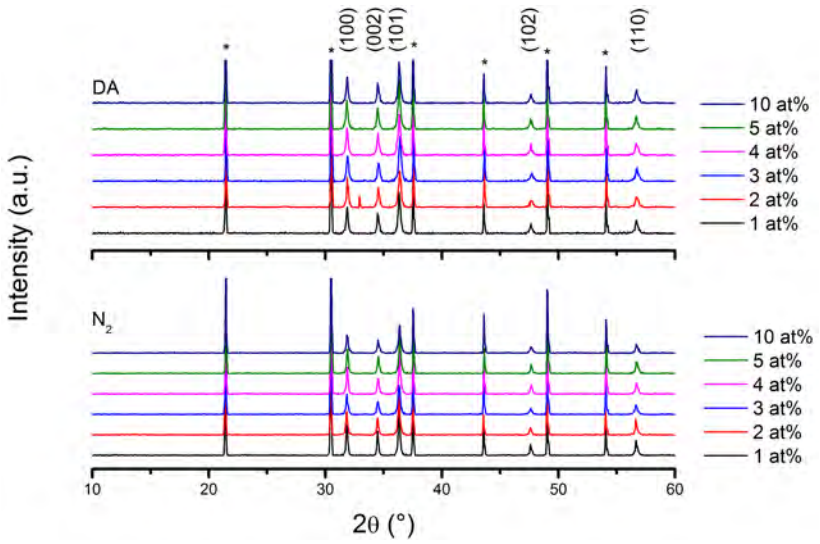

Figure 3.5: XRD analysis of the 1, 2, 3, 4, 5, 8 and 10 at% ZnO:Al NPs after calcination. Al-doped ZnO powders are placed on top of a Si substrate during XRD analysis. For all Al-doped ZnO samples the wurtzite crystal lattice is found (JCPDS 75-0576), while the stars (*) assign the diffraction peak of LaB_6. The 2% ZnO:Al powders annealed in DA have an additional peak of the Si substrate (JCPDS 72-1426) in their diffraction peaks.

In addition, the diffraction peaks are used to determine the crystallite size of the NPs based on the diffraction peaks: (100), (002), and (101) with the

Table 3.2: Determination of the crystallite size (D in nm) of AZO NPs calcinated in DA with FPM in function of different diffraction peaks ((100), (002), and (101)). The R/RO ratio gives an indication of the quality of the fit.

D for	(100)	R/RO	(002)	R/RO	(101)	R/RO	$\bar{x}$	σ
1 at% Al	65	0.99	79	1.18	66	1.31	70	8
2 at% Al	78	1.35	59	1.00	34	1.20	57	22
3 at% Al	43	1.07	46	0.88	33	1.28	41	7
4 at% Al	62	0.87	40	1.06	29	1.39	44	17
5 at% Al	34	1.41	47	1.04	40	1.30	40	7
10 at% Al	58	0.89	48	1.14	40	1.04	49	9

Table 3.3: Determination of the crystallite size (D in nm) of AZO NPs calcinated in N_2 with FPM in function of different diffraction peaks ((100), (002), and (101)). The R/RO ratio gives an indication of the quality of the fit.

D for	(100)	R/RO	(002)	R/RO	(101)	R/RO	$\bar{x}$	σ
1 at% Al	54	1.21	69	0.81	56	1.21	60	8
2 at% Al	65	0.93	55	1.03	51	1.38	57	7
3 at% Al	43	1.18	66	1.33	64	1.07	58	13
4 at% Al	63	1.14	46	0.85	62	1.23	57	10
5 at% Al	61	0.73	52	0.90	54	0.98	56	5
10 at% Al	73	0.88	62	0.93	46	1.05	60	14

Debye-Scherrer formula [136]:

$$D = \frac{k\lambda}{B\cos\theta} \tag{3.4}$$

with D the crystallite size, k the shape factor, λ the wavelength of the applied X-ray, θ the Bragg angle of diffraction line and B the line broadening at half the maximum intensity (FWHM). The software EVA has the possibility to apply a full peak model (FPM) to extrapolate the crystallite size.[1] With the application of this model a R/RO factor is given, indicating the quality of the fit. In case of approximating perfection R/RO is equal to 1. This FPM was applied for the wurtzite crystal lattice (JCPDS 75-0576) and the (100), (002), and (101) diffraction peaks were separately fitted. The boundaries are fixed for the calculation: 31.24-32.32° 2θ for (100), 34.03-35.06° 2θ for (002) and 35.82-36.96° 2θ for (101) reflections. The crystallite size (D in nm) is given per diffraction peak (DP) ((100), (002), and (101)) in Table 3.2 and Table 3.3, plus the average size ($\bar{x}$) and the standard deviation (σ) per at% Al are displayed. Table 3.2 nor Table 3.3 displays any trend within the standard deviations, indicating that all NPs, independently of doping %, are $\sim$ 50 nm for those thermally treated in DA and $\sim$ 60 nm for those in N_2. On the other hand, the calcination atmosphere has an influence on the crystallite size. The NPs formed

in N_2 are larger than those in DA. The reason for this is not understood.

XRD analysis enables the determination of the crystallite size, while TEM analysis allows differentiation of the NPs. No clear morphology of nanoparticles is distinguisable by TEM analysis as seen in Figure 3.6. Mostly aggregated and clustered NPs are found. Based on these images it is very difficult to compare grain sizes from TEM images with crystallite sizes from X-ray diffractograms. No statement can be made whether these crystals are mono- or polycrystalline. Certain is that it is very difficult to deagglomerate the NPs formed by co-precipitation, since for TEM sample preparation sonication was applied. Perhaps ball-milling might assist to deagglomerate.

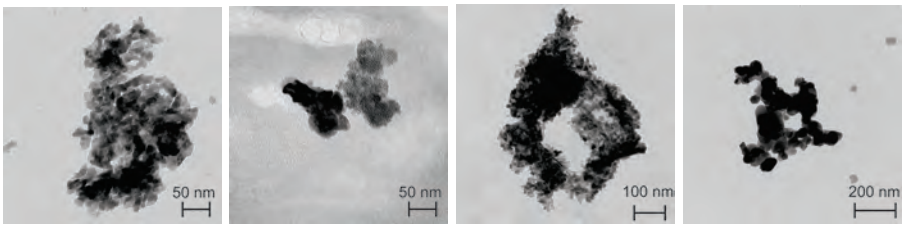

Figure 3.6: TEM images of 2% ZnO:Al NPs calcinated in N_2, 2% ZnO:Al NPs, 4% ZnO:Al NPs, and 5% ZnO:Al NPs calcinated in DA. (left to right)

3.5 Al allocation

According to *Kemmitt et al.* Al should be substitutional tetrahedrally coordinated inside the ZnO lattice in order to improve the conductivity.[136] Interstitial tetrahedral and octahedral incorporation is believed to create electron traps or could even indicate the formation of segregated phases like gahnite and alumina, which are known to be isolators.[109] XRD results indicate no formation of gahnite or alumina within the experimental detection limits. Based on ICP-AES results, the Al is believed to be taken up into the crystal lattice, although Additional experiments for the Al incorporation were done with ^{27}Al MAS NMR. The ratio Al:Zn obtained by ICP-AES (vide supra) is used as the at% of Al. From these values and in combination with NMR a difference between tetrahedral (around 85 ppm) and octahedral (around 10 ppm) incorporation is observed in Figure 3.8 and displayed in Figure 3.7. From the results in Figure 3.8 it can be seen that with increasing doping concentration, the peak area for octahedral coordination is larger than that of the tetrahedral position. According to *Saniz et al.* the substitutional doping inside ZnO leads to the lowest formation energy, which implies that Al would preferably be allocated tetrahedral and substitutional.[237] This might indicate that, although the tetrahedral substitutional position might be preferred, there is a solubility limit for this position.[245]

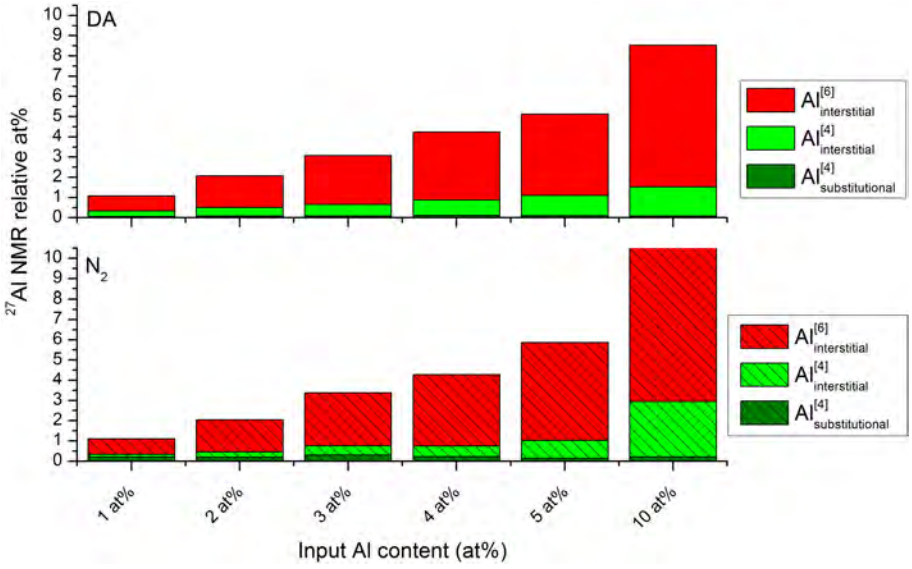

Figure 3.7: Al incorporation inside ZnO based on ^{27}Al MAS NMR fitted spectra. The substitutional tetrahedral amount of Al is barely visible, since it is only 0.1 at% for DA anneal and maximum 0.3 at% for the N_2 anneal.

As stated before, the lineshape of an Al resonance signal can be broadened by distributions of environments in disordered, amorphous phases and/or by the quadrupolar interaction. In Figure 3.8 it can be seen that the higher doping % display tetrahedral peak broadening or could contain multiple signals, which indicate a difference in coordination. For samples treated in DA, this tetrahedral shift is broad or constructed out of more than one signal for all percentages. The line broadening due to the quadrupolar interaction however vanishes when the Al nucleus is in a highly symmetrical environment.[178] This strongly indicates that the sharp signal around 85 ppm in the Al NMR spectra originates from Al accommodated in substitutional sites of crystalline ZnO.[178] By fitting the experimental results in Figure 3.8, the substitutional tetrahedral coordination can clearly be fitted and these results are summarized in Figure 3.7.

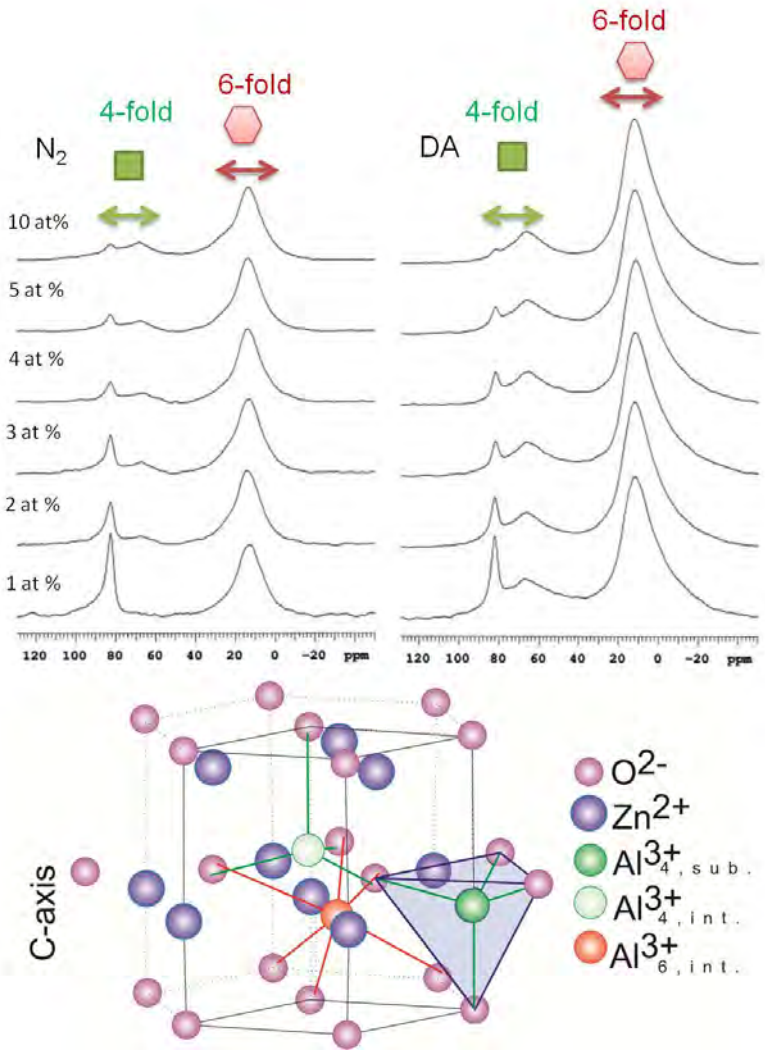

Figure 3.8: ^{27}Al MAS NMR spectra of the Al-doped ZnO NPs calcinated either in N_2 (left) or in DA (right).

From Figure 3.7 can be seen that the substitutional tetrahedral Al content stays relatively low and constant with increasing doping %. Also *Kelchtermans et al.* and *Serier et al.* found a solubility limit for Al inside ZnO, which is directly visible here for the substitutional tetrahedral with a limit of maximum 0.30 at% for all doping %. [134] [245] If a comparison is made between the different calcination atmospheres, it seems that this solubility limit is a bit higher for those thermally treated in N_2. The NPs calcinated in DA only contained maximum 0.10 at% of subtitutional tetrahedral Al.

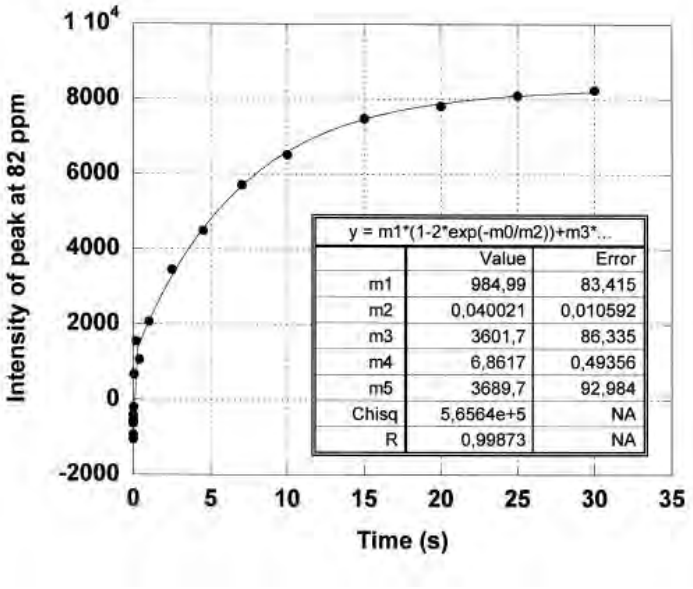

Figure 3.9: T_1 relaxation study of the 4% ZnO:Al powder calcinated in DA bi-exponentially fitted.

T_1 spin-lattice relaxation decay time behavior evaluation can give some semi-quantitative information about the substitutional Al placing in, for example, the 4% ZnO:Al powder calcinated in DA. This sample was chosen to avoid long recording time. The higher the amount of Al, the faster results are generated. The signal around 85 ppm is bi-exponentially fitted with a clear difference between relaxation behavior of interstitial, in the order of ms, and substitutional, in the order of s, tetrahedral coordination (Figure 3.9). This confirms the applied fit of the sharp tetrahedral signal to substitutional Al incorporation together with the fit of the broad signal to interstitial tetrahedral occupation as interpreted for Figure 3.7.

3.6 Conclusion

Al-doped ZnO nanoparticles have been synthesized through an aqueous co-precipitation method with calcination in DA or N_2. After thermal treatment, the X-ray diffractograms confirm a wurtzite crystal lattice with a crystallite size of ∼50-60 nm, although some residual nitrates are found by FTIR analysis. No secondary phases are found within the detection limits of the XRD apparatus. Nevertheless, this does not exclude the existence of secondary phases completely. ICP-AES confirms a transfer from the input ratio Al:Zn to the AZO NPs, although a higher content of Al is established. This higher content of Al

can be explained by a difference in precipitation behavior of Al and Zn and/or by a possible Al contamination from the used alumina boats. Assuming that only wurtzite is present in combination with ICP-AES analysis, a first indication is given that Al is incorporated inside the ZnO lattice. ^{27}Al MAS NMR allows to make a placing distinction of octahedral and tetrahedral Al incorporation. By fitting these spectra and making a comparison with T_1 relaxation measurements, a rather low solubility limit for the tetrahedral substitutional Al is established. This low content and the absence of surface plasmon absorption in the infrared analysis indicate the low potential of these AZO NPs as building blocks for TCO films.

4 Thermal Decomposition Synthesis in Dibenzyl Ether

Al-doped ZnO nanoparticles are synthesized by means of a solution based heating up thermal decomposition method. The synthesis involves a reaction of zinc acetylacetonate hydrate, aluminum acetylacetonate and 1,2-hexadecanediol in the presence of oleic acid and oleyl amine. A proposed reaction mechanism from reagents to monomers is corroborated by analysis of the evolving gases using headspace GC-MS analysis. The Al-doped ZnO nanoparticles synthesized are dynamically stabilized by adsorbed oleate ions, after deprotonation of oleic acid by oleyl amine, as was found by NOESY proton NMR and complementary FTIR spectroscopy. Precession electron diffraction shows a simultaneous increase in lattice parameters with Al concentration. This, together with HAADF-STEM and EDX maps, indicates the incorporation of Al into the ZnO nanoparticles. By the combination of complementary characterization methods during all the stages of the synthesis, it is concluded that Al is incorporated into the ZnO wurtzite lattice as a dopant.

Table 4.1: Overview of the different applied parameters for ZnO:Al nanoparticles syntheses obtained by heating-up thermal decomposition.

Reagens	ZnO-ST	2Al-ST	3Al-ST	5Al-ST	8Al-ST	10Al-ST	2Al-no	2Al-PD	2Al-TD	2Al-BAm	2Al-SAc	2Al-12OAc	2Al-OAm
Dibenzyl ether	X	X	X	X	X	X	X	X	X	X	X	X	X
$Zn(acac)_2 \cdot xH_2O$	X	X	X	X	X	X	X	X	X	X	X	X	X
2% $Al(acac)_3$	-	X	-	-	-	-	X	X	X	X	X	X	X
3% $Al(acac)_3$	-	-	X	-	-	-	-	-	-	-	-	-	-
5% $Al(acac)_3$	-	-	-	X	-	-	-	-	-	-	-	-	-
8% $Al(acac)_3$	-	-	-	-	X	-	-	-	-	-	-	-	-
10% $Al(acac)_3$	-	-	-	-	-	X	-	-	-	-	-	-	-
10 mmol 1,2-hexadecanediol	X	X	X	X	X	X	-	-	-	X	X	X	X
10 mmol 1,2-propanediol	-	-	-	-	-	-	-	X	-	-	-	-	-
10 mmol 1,2-tetradecanediol	-	-	-	-	-	-	-	-	X	-	-	-	-
6 mmol oleic acid	X	X	X	X	X	X	X	X	X	X	-	-	-
6 mmol oleyl amine	X	X	X	X	X	X	X	X	X	-	X	-	-
6 mmol benzyl amine	-	-	-	-	-	-	-	-	-	X	-	-	-
6 mmol stearic acid	-	-	-	-	-	-	-	-	-	-	X	-	-
12 mmol oleic acid	-	-	-	-	-	-	-	-	-	-	-	X	-
12 mmol oleyl amine	-	-	-	-	-	-	-	-	-	-	-	-	X

4.1 Introduction

The previous chapter (Chapter 3) elaborated on a very easy and versatile synthesis method: the co-precipitation. An investigation of the Al allocation inside ZnO with ^{27}Al MAS NMR indicates that this co-precipitation cannot simply substitutional dope Al in high amounts. Even further, aggregation is very common and the resuspension of nanoparticles has to occur through ball-milling and/or sonication. In this chapter, the focus is put on the in-situ stabilization of nanoparticles during synthesis. The improved substitutional Al allocation is studied in the next chapter (Chapter 5).

More recently, in addition to the co-precipitation method, the thermal decomposition has been used for the synthesis of Al-doped ZnO NPs.[267] The biggest asset of this thermal decomposition route is that it results in highly monodisperse NPs with a high colloidal stability, made possible by the separation of nucleation and growth in function of temperature and the use of surfactants. There are two approaches for conducting thermal decomposition synthesis: the hot-injection method and the heating-up method.[196] Hot-injection induces a nucleation burst through the fast injection of the reagents into a hot precursor solution, whereas the starting solution of the heating-up route is prepared at room temperature and is gradually heated. During this heating-up stage the reagents are progressively decomposed which induces a more gradual nucleation of NPs. However, there is still debate about the mechanism of nanoparticle formation in the heating up method. Also, it is believed that no work has been reported revealing insights into the formation of doped metal oxides by means of the heating up method, focusing on aspects such as the reaction mechanism, stabilization of the particles and incorporation of the dopant atoms/ions. In this chapter, these aspects are explored of the heating-up thermal decomposition method for the synthesis of monodisperse wurtzite type ZnO and Al-doped ZnO nanoparticles.

ZnO:Al NPs are synthesized by thermal decomposition of Zn and Al acetylacetonates, as adapted from a original thermal decomposition synthesis route for ferrites.[257] A pathway of this decomposition synthesis was studied by *Pinna et al.* and *Ambrozic et al.* for monometal oxides including iron oxide and zinc oxide.[215][13] The complexity of this thermal decomposition is probably by doping monometal oxides. Other monomers will be generated and influence the formation of doped nanoparticles. Therefore the thermal decomposition pathway for doped ZnO:Al nanoparticles will be studied by identifying the decomposition products that evolve during the synthesis process. Additionally, the incorporation of the dopant into the ZnO lattice is studied by means of complementary electron microscopy techniques in order to effectively obtain doped nanoparticles. Furthermore, the stabilization of the

ZnO:Al nanoparticles in suspension is studied. Among various surfactant systems reported up till now, the combination of oleic acid and oleyl amine is commonly used in thermal decomposition synthesis to obtain a high colloidal stability.[257][36][4][299][249][293] Some suggest the formation of a acid-base complex between oleic acid and oleyl amine to control size and shape of the particles.[147] Recently, it was reported that the oleic acid and oleyl amine react to form dioleamide which was found to influence the formation of nuclei during the thermal decomposition of the reagents.[42][290] As no reports are dedicated so far to the mechanism of stabilization of ZnO:Al NPs in thermal decomposition synthesis, we apply Fourier Transform Infrared Spectroscopy (FTIR) to verify the presence of the surfactants, while their effective interaction with the NPs is further elucidated by means of Nuclear Magnetic Resonance (NMR) studies.

Al-doped ZnO nanoparticles are synthesized through the use of zinc acetylacetonate in combination with aluminum acetylacetonates using a heating-up thermal decomposition synthesis. The obtained nanocrystals are in-situ stabilized through surfactants like oleic acid and oleyl amine, which are commonly used to generate stable suspension in apolar media. By an in-depth study of the synthesis process (Figure 4.1) and the product, a contribution is made to the field of the solution based synthesis of ZnO:Al nanoparticles. The reaction mechanism of Al-doped ZnO nanoparticles is unraveled using a stepwise approach, with a fundamental study of nanoparticle stabilization and even in-depth nanoparticle characterization. Understanding the process is of utmost importance in order to realize improved solution deposition of TCO layers from ZnO:Al nanoparticle building blocks.

4.2 Synthesis

4.2.1 Synthesis of Al-doped ZnO NPs in dibenzyl ether

The synthesis route applied was based on a recipe of *Sun et al.* .[257] Synthesis was carried out with 2 mmol of $Zn(acac)_2 \cdot xH_2O$ (ZnO-ST; ST= standard synthesis) for pure ZnO, and in combination with $Al(acac)_3$ at 2 (2AL-ST), 3 (3AL-ST), 5 (5AL-ST), 8 (8AL-ST) or 10 mol % (10AL-ST) for the doped ZnO:Al NPs.

The reagents were mixed with 10 mmol 1,2-hexadecanediol and dissolved in a mixture of 6 mmol oleic acid, 6 mmol oleyl amine and 25 mL dibenzyl ether in a three-necked round bottomed flask. This is further on named as standard synthesis or ST. The solution was magnetically stirred and flushed with nitrogen while heating to 60 °C in a heating mantle coupled to a JKEM scientific 310 controller. After obtaining a clear solution at 60 °C, the flask was closed

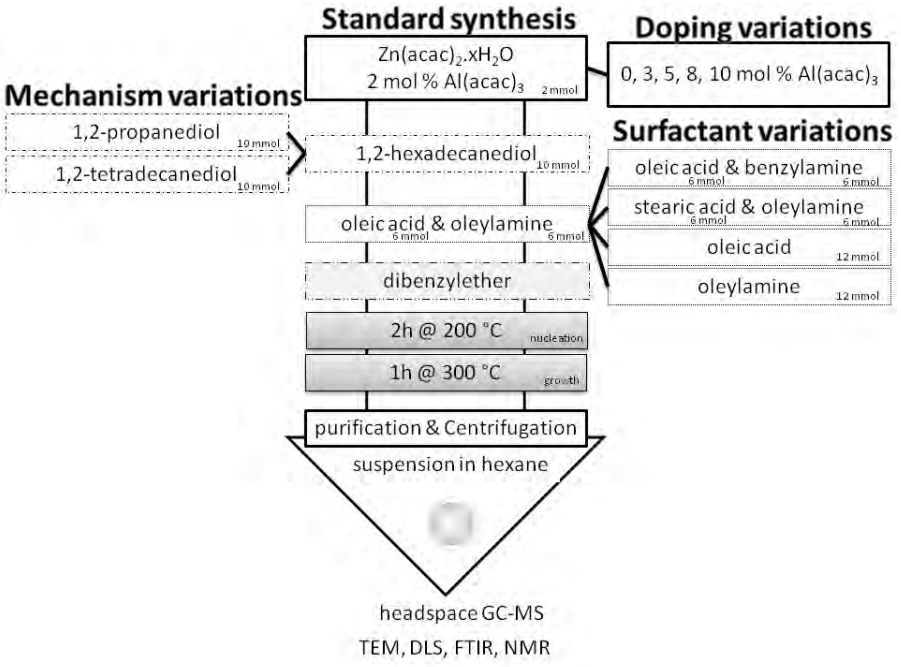

Figure 4.1: Flowchart of the thermal decomposition synthesis route for ZnO:Al NPs.

under nitrogen and the temperature was increased to 200 °C. The solution was refluxed at 200 °C for 2 h and 1 h at 300 °C. After reflux, the obtained sol was cooled down to room temperature in the closed N_2 setup. Absolute ethanol (180 mL) was added (in atmospheric conditions) to destabilize the sol and to induce precipitation of the NPs. The precipitated particles were purified by means of centrifugation in an Eppendorf microcentrifuge (30 minutes at 4000 rpc). The supernatant was discarded and the white powder with NPs was re-suspended in 8 mL of hexane. The precipitation and centrifugation steps were repeated once. The resulting purified NPs were finally suspended in hexane (16 mL) and again centrifugated for 30 minutes at 4000 rpc to remove larger NPs. In this final step, the precipitated pellet with the excessive population was discarded and the supernatant, containing the desired NPs, was transferred into a container to be stored for further use.

To evaluate and understand the reaction mechanism, the influence of different synthesis parameters on the ZnO:Al nanoparticles formed, was evaluated. The importance of 1,2-hexadecanediol was shown by comparison of the synthesized standard batch with (2AL-ST) and without diol (2AL-no; no= without diol), either with a different synthesis using another commercially available diol: 1,2-propanediol (2AL-PD; PD= propanediol) or 1,2-tetradecanediol (2AL-TD; TD=tetradecanediol). The effect of the surfactants was studied by compar-

ing the standard reaction mixtures containing 6 mmol oleic acid and 6 mmol oleyl amine (2AL-ST) with reactions using 6 mmol oleic acid and 6 mmol benzyl amine (2AL-BAm; BAm= benzyl amine), or 6 mmol stearic acid and 6 mmol oleyl amine (2Al-SAc; Sac= stearic acid) or only either 12 mmol oleic acid (2Al-12OAc; 12OAc= 12 mmol oleic acid) or 12 mmol oleyl amine (2Al-12OAm; 12OAm; 12 mmol oleyl amine).

All synthesis parameters of the samples are summarized in Table 4.1 and a schematic synthesis overview is given in Figure 4.1.

4.2.2 Deposition of a apolar suspension of Al-doped ZnO NPs

A thick window glass substrate was used to the deposit a hexane and toluene 5Al-ST suspension of Al-doped ZnO nanoparticles. Both completely covered substrates were placed under a beaker to assure slow drying after drop-casting of the suspensions. The AZO suspension of hexane was drop-casted on top of a toluene layer, which already covered the substrate. The 5Al-ST suspension was drop-casted on a thick window glass substrate covered with toluene. After two hours of drying the substrates were gradually heated (to reduce the chance of thermal shock) for removal of oleic acid on the NPs surface. This was done using hotplates in static air at 100 °C for one minute, 300 °C for one minute, and at 500 °C for 5 minutes. In the end, additional heating up to 350 °C for 0.5 hour in a 5% H_2 containing atmosphere was done.

4.3 Reaction Mechanism

The reason for choosing similar bidentate acetylacetonate complexes for both Al and Zn was motivated by the aim to obtain homogeneous doping of Al into the ZnO wurtzite crystal lattice. An improved monodispersity of nanoparticles obtained from bidentate acetylacetonate precursors in comparison to NPs synthesized from monodentate ligands supports this approach.[13, 231] However, as the thermal decomposition of $Zn(acac)_2$ and $Al(acac)_3$ differs,[45] it is important to characterize and verify the formation of monomers, the stabilization mechanism of the ZnO:Al nanoparticles, and the doping of ZnO with Al. *Pinna et al.* proposed a reaction mechanism for the formation of monometal oxide nanoparticles under solvothermal conditions, involving the C-C cleavage of the corresponding acetylacetonate by a solvolysis reaction with benzyl amine.[215] Later, *Ambrozic et al.* experimentally confirmed a similar mechanism for undoped ZnO NPs, this time under reflux conditions with an alcohol as the reactive solvent. Here dibenzyl ether and 1,2-hexadecanediol has been kept for synthesis, like the recipe of *Sun et al.*.[257] To determine the mechanism of ZnO:Al NPs formation in the presence of a diol dissolved in dibenzyl ether, a

systematic set of experiments were performed whereby the nucleophile and the surfactants are varied with respect to the standard synthesis of ZnO using hexadecanediol, oleic acid and oleyl amine.Evolved gases formed during syntheses are analyzed by means of headspace GC-MS. As shown in Figure 4.2, acetone, acetic acid, a mixture of alkanes and alkenes, carbon dioxide and water are released during the thermal decomposition in the reaction mixture (Figure 4.3). A number of benzyl derivatives were also detected (benzyl acetate, benzyl alcohol, toluene, benzene and benzaldehyde). These benzyl derivatives can be attributed to impurities in the dibenzyl ether as they were observed upon analysis of the pure solvent with headspace GC-MS as well.

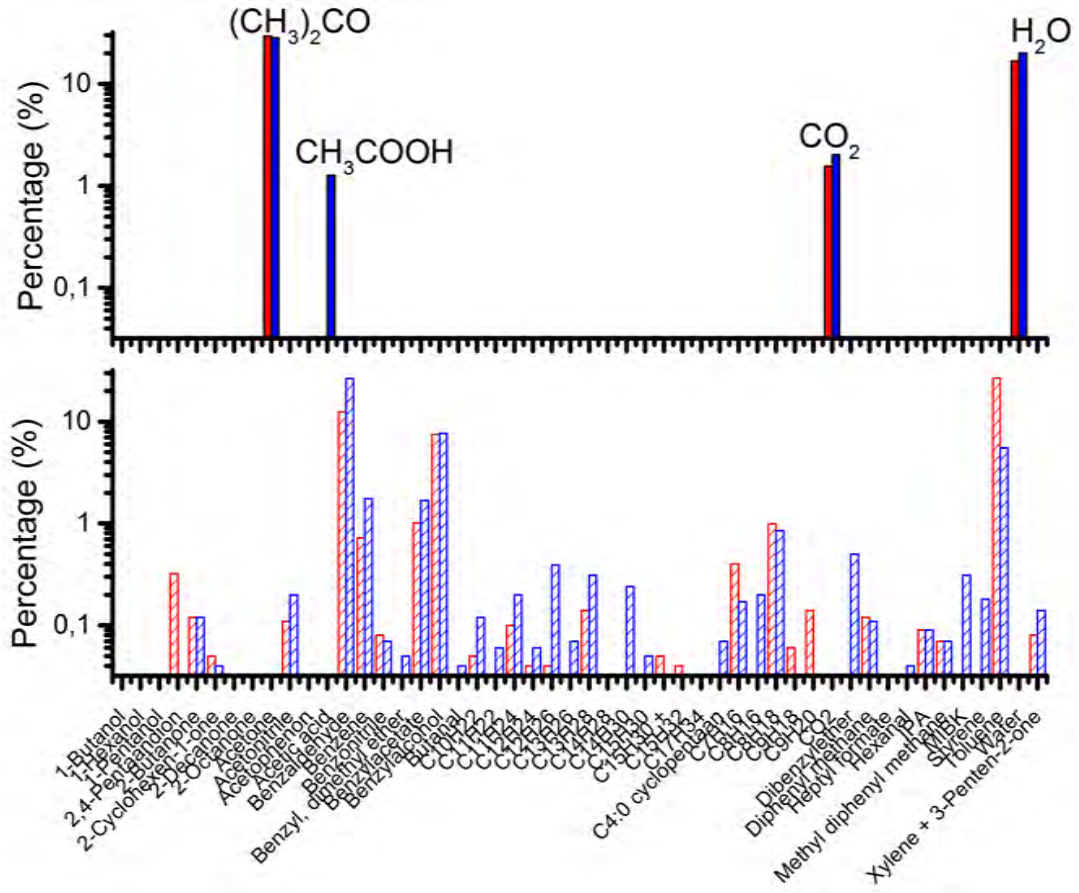

Figure 4.2: Released gases during the synthesis of ZnO:Al nanoparticles analysed with headspace GC-MS. The red bars represents the released gases during the nucleation step at 200 °C, while the blue bars represents gases evolved during the growth step at 300 °C. The released products confirm the mechanism. The striped pattern (bottom image) displays the released alkanes/alkenes and the contaminants of the solvent.

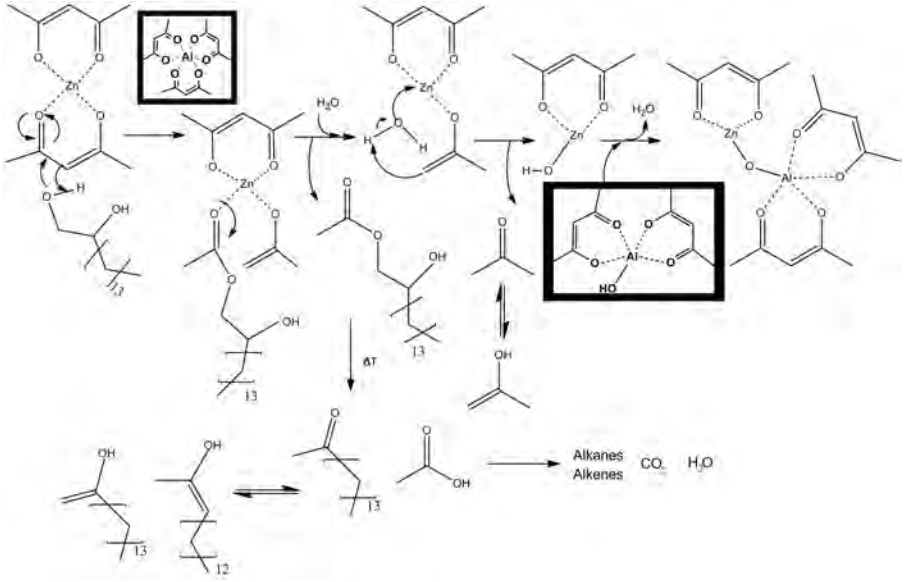

Figure 4.3: Synthesis mechanism of the heating-up thermal decomposition mechanism of ZnO:Al nanoparticles.

The Headspace GC-MS analysis is consistent with the C-C cleavage reaction proposed by Pinna and Ambrozic [215][13], which allows us to propose a similar reaction scheme for the formation of Al-doped ZnO nanoparticles by the reaction of the acetylacetonate metal complexes with 1,2-hexadecanediol. This vicinal diol is a weak nucleophile which performs a nucleophilic attack on the electron deficient C-atom of the acetyl acetonate's carbonyl group. This induces a cleavage of the C-C bond of the acetylacetonate ligand.[13, 215] Together with the cleavage of this bond, a proton is transferred from the diol to the enolate to release the formed ester. Upon heating, this ester will further decompose into acetic acid, a mixture of alkenes and partially into alkanes, carbon dioxide and water. The release of acetic acid (Figure 4.2) has already been reported before [121, 215]. After releasing the ester, the hydrate water of the acetylacetonate complex is able to perform a nucleophilic substitution with the release of acetone. This gives rise to the formation of R $\cdots$ Zn-OH monomers followed by nucleation of ZnO nanocrystals by condensation.

For the Al-acetylacetonate start product, the same decomposition pathway is hypothesized, leading to the formation of (R$\cdots$)Al-OH monomers. Although R$\cdots$Zn-OH and (R$\cdots$)Al-OH monomers may not be formed simultaneously during decomposition [45], it is believed that both monomers are released before supersaturation is accomplished. This enables the formation of nuclei by a condensation reaction involving both monomers. This is a crucial prerequisite to allow a homogeneous Al incorporation into the ZnO crystals and was

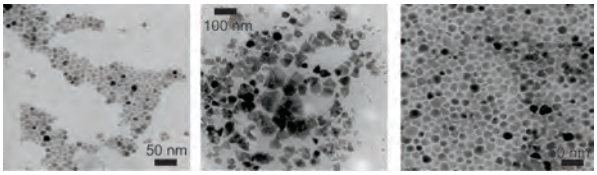

Figure 4.4: 2% Al-doped ZnO NPs synthesized with 1,2-hexadecanediol (left) (2AL-ST), 2% Al-doped ZnO NPs synthesized with 1,2-propanediol (center) (2AL-PD), and 2% Al-doped ZnO NPs synthesized with 1,2-tetradecanediol (right) (2AL-TD).

further investigated by an in depth TEM study of the resulting nanocrystals (Section 4.5).

In order to further understand and determine the synthesis process, especially the specific role of the reactants, an experimental matrix was set up whereby reagents were varied in a systematic manner (Table 4.1). In the thermal decomposition of iron oxide nanoparticles, 1,2-hexadecanediol was reported to act as a reducing agent, control the particle growth, and prevent particle aggregation.[257] Literature reports that replacement of 1,2-hexadecanediol by 1,2-dodecanediol results in a similar outcome for iron oxide NPs however the mechanism for the latter is not known.[41, 257] Also it appears that a vicinal diol with a similar chain length (1,2-tetradecanediol) results in particles that resemble those of the original hexadecanediol in terms of shape and monodispersity. Independently, a synthesis was carried out using a diol with a much shorter alkyl chain, 1,2-propanediol (2Al-PD) which resulted in particles with irregular shape (Figure 4.4). These experiments show that the length of the alkyl chain of the diol has an important influence on the formation of the NPs. Potentially the length of the alkyl chain influences the release of monomers and hence the nucleation and growth kinetics. Figure 4.4 shows the inverse relationship between the diols and the size of the NPs: the shorter the diol, the larger the NPs. More growth is stimulated using 1,2-propanediol. When the synthesis was carried out without any vicinal diol (2Al-no), no particles are observed in TEM after the standard purification procedure. This suggests that an alternative mechanism of direct nucleophilic attack by water on the acetylacetonate has led to particles (or aggregates) with diameters sufficiently large to be collected in the precipitated pellet during the final centrifugation step (Figure 4.1) and no small particles remain in the supernatant.

4.4 Nanoparticle Stabilization

Oleyl amine and oleic acid are commonly used as surfactants in many synthesis reactions. [138, 147, 257, 267] They are added during thermal decomposi-

tion synthesis to control the size and shape and to stabilize in-situ the formed NPs.[257] They consist of a coordinating head group (respectively a carboxylic acid and an amine), a long alkyl chain and are believed to adsorb reversibly on the surface and provide steric hindrance which mediates the growth of NPs, in addition to providing stabilization.

In our study, an equimolar combination of both, oleic acid and oleyl amine, results in an efficient stabilization of the NPs. Exclusive use of oleic acid (2Al-12OAc) leads to a precipitate which is not dispersible in hexane. On the other hand, the use of oleyl amine (2Al-12OAm) alone leads to a lower yield of ZnO:Al nanoparticles with irregular shape. Although different reports [29, 257] mention the use of an alkyl amine to stabilize oxide nanoparticles by means of chemisorption of the NH_2-group, the lower yield of the reaction compared to the synthesis using both oleic acid and oleylamine is acknowledged. [257] Additionally the exclusive use of oleyl amine has been found to affect the morphology of various nanoparticles like FePt, FeMo and magnetite. [147, 148, 256, 257] The equimolar combination of oleic acid and oleyl amine has a preference in other studies as well, although the reason is not understood.[257] *Klokkenburg et al.* observe a possible acid-base reaction with the exchange of a proton between oleic acid and oleylamine.[147] The resulting carboxylate group of oleic acid would then chemisorb on the particle surface. Recently, *Calatayud et al.* report the use of both surfactants for the synthesis of TiO_2 nanoparticles, whereby the formation of an amide (dioleamide) is observed.[42]

In order to understand both findings and to transfer the knowledge to our system, infrared analysis (Figure 4.5 is performed on the ZnO:Al suspension (2Al-ST) in hexane. Here, two carboxylate stretch vibrations are detected around 1500-1400 cm^{-1} (ν_a COO^-, ν_s COO^-), indicating the presence of carboxylates coming from oleic acid. Also CH_2 stretching vibrations as well as CH_3 stretching vibrations can be observed between 3000 cm^{-1} and 2850 cm^{-1} (ν_a CH_2, ν_s CH_2 and ν_a $CH_2{-}COO^-$, ν_a CH_3, ν_s CH_3), which can be indicative of both oleic acid and oleyl amine. These vibrations can be indicative for hexane as well. The absorption between 800 and 500 cm^{-1} is due to ZnO lattice vibrations. Purely by infrared data for 2Al-ST, the presence of the carboxylate group of oleate (deprotonated oleic acid) is confirmed and no indication for the dioleamide is found, for which vibrations would have been expected at 1645 cm^{-1} for C=O stretching and 1552 cm^{-1} for N-H bending.[290] However, (protonated) oleyl amine cannot be clearly distinguished since all its infrared bands (symmetric: 1650-1550 cm^{-1} and asymmetric: 1370-1000 cm^{-1} bending and rocking:950-590 cm^{-1} vibrations of NH_3^+ as well as not clearly visible N-H stretch vibration: 3100-2700 cm^{-1}) overlap with oleic acid bands (resp. O-H stretch, symmetric and asymmetric carboxylate vibrations and the CH_2 rocking vibration). Therefore, a comparison is made with a synthesis wherein oleic acid and benzyl amine (2Al-BAm) are used.

Table 4.2: Band assignment for the FTIR spectra of ZnO:Al suspensions (2Al-ST, 2Al-BAm, and 2Al-SAc).

Wavenumber (cm^{-1})	Assignment
3100-3020	ν HC=
3000-2850	ν_a CH_2, ν_s CH_2, ν_a CH_2−COO^-, ν_a CH_3, ν_s CH_3
1680-1620	ν C=C
1500-1400	ν_a COO^-, ν_s COO^-
800-500	ν_a Zn-O

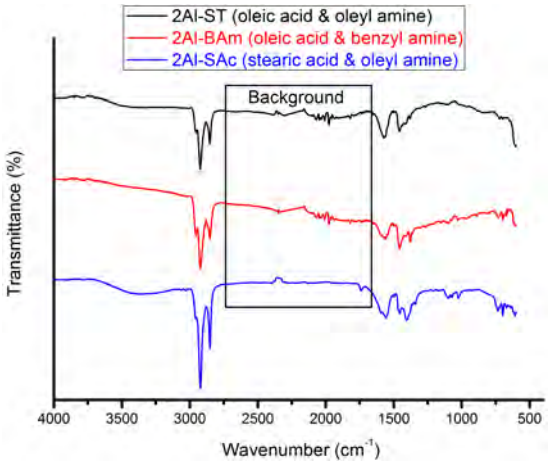

Figure 4.5: Infrared transmission spectra (FTIR) of ZnO:Al nanoparticles with different surfactants. The black spectrum represents the standard synthesis with oleic acid and oleyl amine (2Al-ST) (top), the red spectrum displays the use of benzyl amine and oleic acid (2Al-BAm) (middle) and the blue spectrum refers to stearic acid and oleyl amine (2Al-SAc) (bottom).

When oleyl amine is substituted by benzyl amine, the functional amine group remains present but the long alkyl chain is replaced by an aromatic group. Hence, the observation of alkyl vibrations (Figure 4.5 red dotted line) will provide unambiguous proof for the presence of the oleic acid, while aromatic benzyl vibrations would account for the presence of the amine. Ideally this interchange should not affect the decomposition reaction, nucleation and growth, nor the stabilization of the NPs, but since benzyl amine can also act as a nucleophile we cannot be entirely certain of this.[215] The infrared spectrum (Figure 4.5) of the combination of oleic acid and benzyl amine (2Al-BAm) is similar to that of the standard synthesis (2Al-ST). The absence of vibrations related to an aromatic group indicates that the amine might be washed away after acceptance of a proton. Nevertheless as indicated a counter ion should be present to

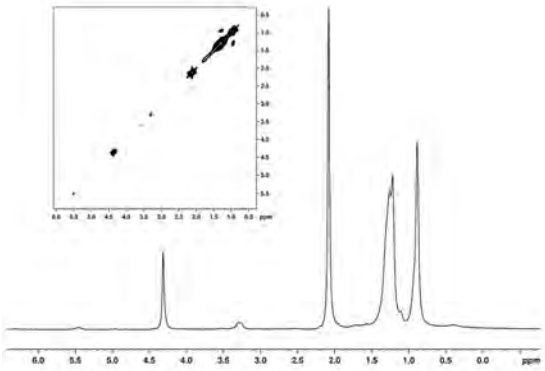

Figure 4.6: 1D ^{1}H NMR spectrum of ZnO:Al NP synthesized using both oleyl amine and stearic acid (2AL-SAc). The insert shows a 300 ms 2D NOESY spectrum, devoid of nOe cross peaks between the alkene resonance at 5.48 ppm and the methyl resonances of oleyl amine, thus proving that oleyl amine is not bound to the NP surface.

be able to remove the protonated amine during washing with ethanol.[72] This counter-ion is hypothesized to be a hydroxyl group derived from the mechanism. This enables the assignment of the observed alkyl vibrations to the oleate group.

In summary, the FTIR results indicate the presence of residual oleic acid in the NP samples, however they do not distinguish between surfactant molecules adsorbed to the NP surface or free in the solvent of the dispersion.

To this end 2D NOESY ^{1}H NMR spectroscopy is applied.[91, 188, 189] However, also here, the high similarity in the spectral fingerprint of oleyl amine and oleic acid, both being unsaturated, prevents their unambiguous discrimination (2Al-ST). Therefore, a synthesis is carried out with stearic acid instead of oleic acid, resp. saturated and unsaturated with 1 alkene bond (2Al-SAc). Although stearic acid lacks the unsaturated bond, unpublished results indicated the mimicking behavior of stearic acid for oleic acid. The similarity of both acids' chemical structures leads us to believe that the change to stearic acid does not affect the particle's formation and growth mechanism. The particles synthesized with stearic acid and oleyl amine are characterized by ^{1}H NMR (Figure 4.6). The weak/small signal at 5.48 ppm in (Figure 4.6) can be assigned to the alkene protons of oleyl amine. In 2D NOESY spectra the different rotational mobility of the involved molecule yields strong and negative NOE peaks in the case of interaction, and very weak positive or absent NOE peaks when there is no interaction between the surfactant, oleyl amine and the particle. Since no NOE cross-peaks are apparent from the oleyl amine

alkene resonance at 5.48 ppm in the 300 ms NOESY spectrum, it can be concluded that oleyl amine remains in solution without acting as a surfactant to the formed particles, which is in agreement with the FTIR data. Looking at 2Al-ST and 2Al-BAm (Figure 4.6), only negative NOE cross-peaks from the alkene resonance at 5.48 ppm and the alkyl region are visible. Combining the

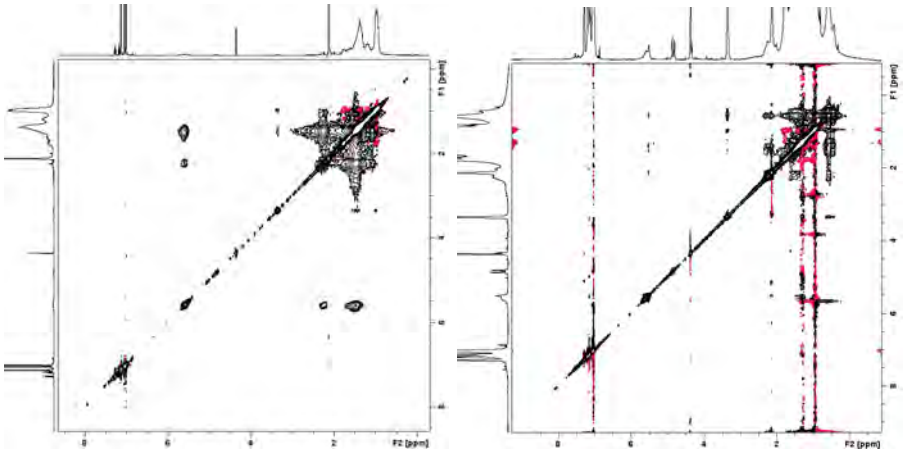

Figure 4.7: Negative NOE cross-peaks at the alkene resonance of 5.48 ppm indicate the interaction of a) oleic acid or oleylamine with the nanoparticle surface in 2Al-ST (left) and b) of oleic acid with the nanoparticle surface in 2Al-BAm (right).

NMR with the FTIR results, we demonstrate that only the oleate ions remain bound to the ZnO:Al NP. We conclude from the combined FTIR and NMR results, that oleyl amine or benzyl amine act merely as proton acceptors for the protons of oleic acid, which forms a carboxylate that remains bound to the surface of the NPs. So, both surfactants are necessary for efficient dynamic stabilization of the NPs, but play a different role. *Calatayud et al.* show the formation of the dioleamide during synthesis, which we consider to have a role during the release of monomers, which cannot be confirmed due to the presence of the solvent dibenzyl ether. This solvent needs to be removed for NMR and/or FTIR analysis and seems unpractical without heating and manipulating the sample. This dioleamide presence after synthesis is refuted based on our NMR (Figure 4.7a) and FTIR (Figure 4.5) data. Nevertheless, dioleamide probably has an influence but is decomposed by increasing the temperature and eventually only oleic acid remains to stabilize the NPs.[42] The efficient interaction during decomposition of reagents and the in-situ stabilization of NPs in suspension is probably the reason why the equimolar combination is commonly used. In addition, *De Roo et al.* supported the interaction of the nanoparticles with only oleic acid and did not found any proof of oleyl amine being bound to the surface of the nanoparticles. [72]

4.5 Nanoparticle Characterization

For the 0-10 at% Al-doped NPs, more DLS and TEM analyses are performed to correlate particle size to the doping percentages. Figure 4.8a displays the log-normal number distribution of the hydrodynamic diameter measured by DLS. Figure 4.8b shows the measured dry diameter obtained from TEM imaging. For all doping percentages, spherical and triangular shaped NPs are observed by TEM. The same trend regarding particle size is observed: $5 < 3 < 2 < 0$ at% Al doping.

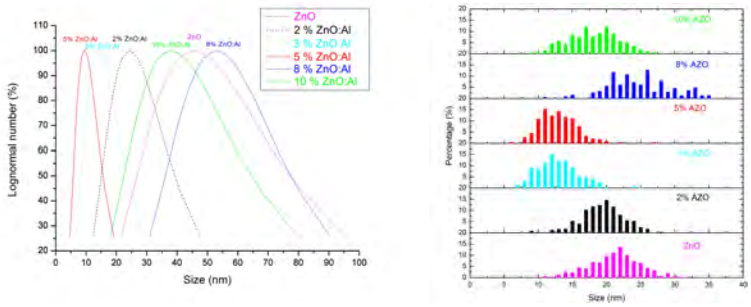

Figure 4.8: Left: DLS results of the hydrodynamic diameter of the 0, 2, 3, 5, 8 and 10 at% Al-doped ZnO. The size of the hydrodynamic diameter of the 5 < 3 < 2 < 0 at% Al doping.
Right: Analysis of the particles' size from the TEM images of the 0, 2, 3, 5, 8 and 10 at% ZnO:Al NPs. The average dry diameter of the 5 < 3 < 2 < 0 at% Al doping

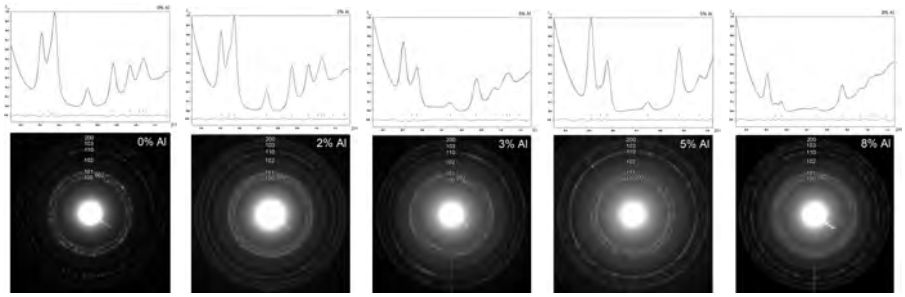

Figure 4.9: (Profile of the precession electron diffraction ring pattern of 0, 2, 3, 5 and 8 at% ZnO:Al (ZnO-ST, 2AL-ST, 3Al-ST, 5Al-ST and 8Al-ST) (shown at the bottom), fitted (Le Bail fit) to the ZnO wurtzite crystal structure.

The confirmation of phase purity in ZnO:Al by X-ray diffraction is not straightforward due to the low doping percentages and inadequate detection limit.

HAADF images showing single crystalline NPs, together with overall EDX spectroscopy for Al detection have been reported by *Thu et al.*, allowing no local composition analysis. [267] Recently, *Gardner et al.* demonstrated the effectiveness of precession electron diffraction (PED) by detecting impurity phases present among NPs with a sensitivity surpassing that of X-ray diffraction.[97] Here, EDX maps are combined with HAADF-STEM and HRTEM images and PED to study the incorporation of Al into the ZnO host. PED patterns are recorded for the different Al% doping samples (ZnO-ST, 2Al-ST, 3Al-ST, 5Al-ST, 8Al-ST and 10Al-ST). In Figure 4.9 a representative ring pattern of the pure ZnO up to 8 at% Al powders can be indexed with the wurtzite crystal structure. The top image in Figure 4.9 displays the integrated intensity over each ring as function of the 2θ values. No impurity peaks are observed. In contrast, for the 10 at% Al (10Al-ST) NPs, not only the wurtzite phase is found but also gahnite (as an impurity) is found (Figure 4.10).

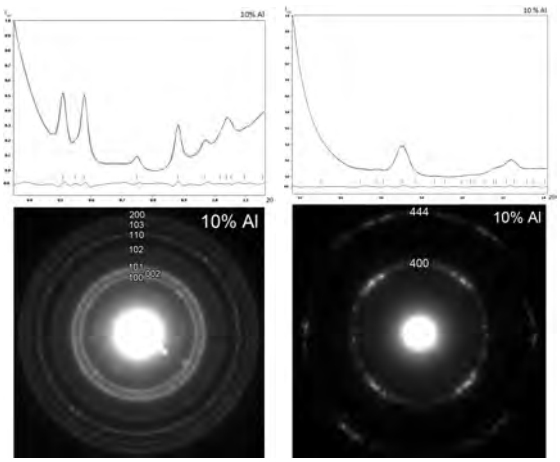

Figure 4.10: (Profile of the precession ring diffraction pattern of 10 at% ZnO:Al, fitted with the wurtzite (left) and gahnite (right) crystal structure. Precession ring diffraction pattern of these nanoparticles are displayed below and state that all the rings can be indexed with the wurtzite (left) and gahnite (right) structure parameters.

Table 4.3: Cell parameters for ZnO:Al NPs with different percentages of aluminum doping (at%) obtained from recorded PED ring patterns.

Cell parameters	ZnO-ST	2Al-ST	3Al-ST	5Al-ST	8AL-ST
a	3.2374	3.2409	3.2489	3.2485	3.2487
	± 0.008	±0.009	± 0.0014	± 0.0005	± 0.0006
c	5.1969	5.1961	5.2161	5.2208	5.2119
	± 0.0018	±0.0013	± 0.0020	± 0.0032	± 0.0021

Unit cell parameters are determined from the PED ring patterns. The cell dimensions of 0 and 2% are similar, followed by an increase in the cell dimensions upon reaching 3 at% Al, after which further addition of Al no longer leads to a change in cell parameters (within experimental error). The observed cell parameter variation is in accordance with the hypothesis that the initial 2% Al might be incorporated into substitutional positions in the ZnO lattice, although a slight decrease was expected. Next, the increase from 2 to 3% leads to interstitial positions of the Al within the wurtzite structure.[69, 248] Finally the absence of a continuous increase in cell parameters for higher percentages of aluminum indicates that aluminum is no longer incorporated, but possibly forms a segregated phase, as indicated by the presence of the gahnite phase which is observed for the 10 mol% Al excess (10Al-ST). Interesting to note is that an increase in Al doping leads to a decrease in NP size (ZnO-ST; 8Al-ST), while simultaneously the lattice parameters increase (Table 4.3). For 8 and 10 at% Al doping, the NPs are larger than the 5 at% particles and do not follow the same trend as the lower doped particles. This might be caused by the limited uptake of Al or the formation of gahnite.[275] Here it seems to be the case that the uptake of Al in the ZnO lattice is limited below 5 at%.

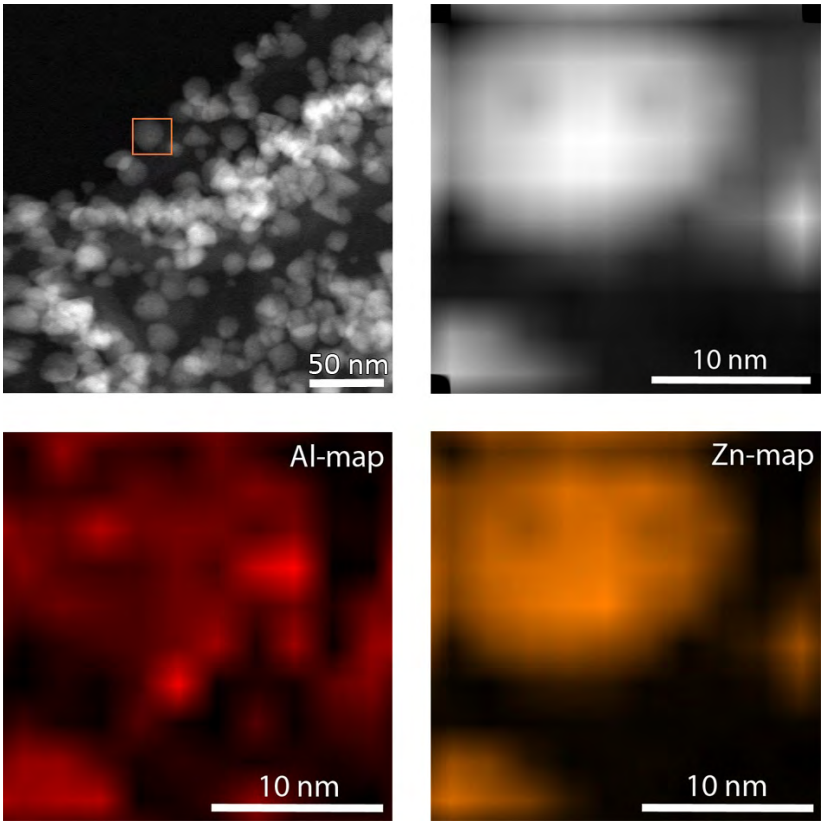

Figure 4.11: (top left) Overview TEM image. The particle selected for the EDX map is indicated with a red rectangle; (top right) HAADF-STEM image of the selected particle; (bottom left) aluminum map, and (bottom right) zinc map of the selected particle.

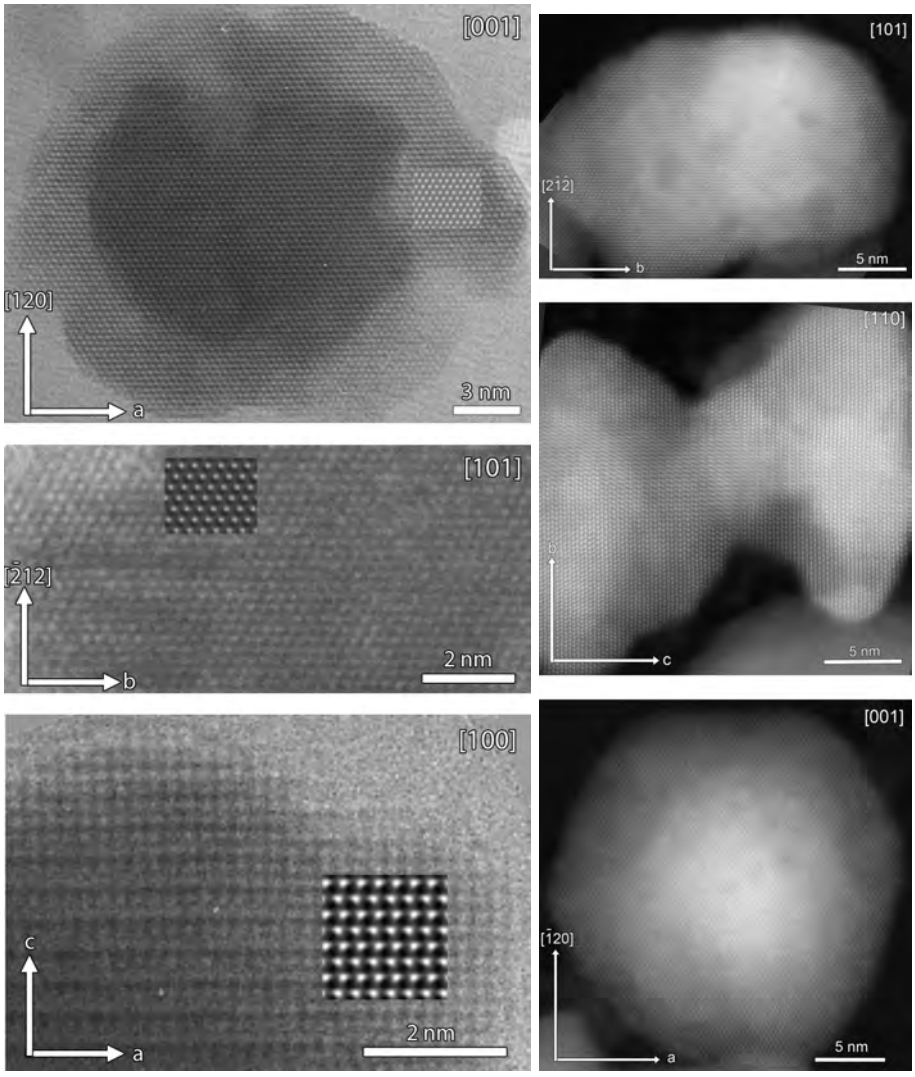

Figure 4.12: a) HRTEM images of the main zones of 2 at% ZnO:Al (2AL-ST) compared with inserted calculated images of the wurtzite structure.(left) b)HRSTEM images of the main zones of 5 at% ZnO:Al (5AL-ST).(right)

The distribution of Al throughout the ZnO:Al NPs is analyzed in detail through HAADF-STEM in combination with EDX mapping. For all ZnO:Al samples, EDX spectra show the presence of Al. A representative EDX map of a particle from the 2 at% ZnO:Al (2Al-ST) synthesis is shown in Figure 4.11. It can be seen that the Al does not coincide uniformly with the Zn, it shows a good correlation in general with the ZnO nanoparticle although the doping results

in inhomogeneous Al concentrations, without leading to the formation of a secondary phase. HRTEM (Figure 4.12) shows no features that indicate secondary phases. The observed phase agrees well with the wurtzite structure, as shown by comparison of the calculated images of the wurtzite structure (insert Figure 4.12) viewed along its main zones. It may be inferred that aluminum is incorporated in the ZnO lattice, without showing deviations of the wurtzite structure. HAADF-STEM images taken for the highly doped sample (5 at% ZnO:Al NPs (5Al-ST) Figure 4.12) also show no deviations from the wurtzite structure, which agrees with the PED ring patterns (Figure 4.9).

4.6 Film Deposition

4.6.1 Apolar suspension

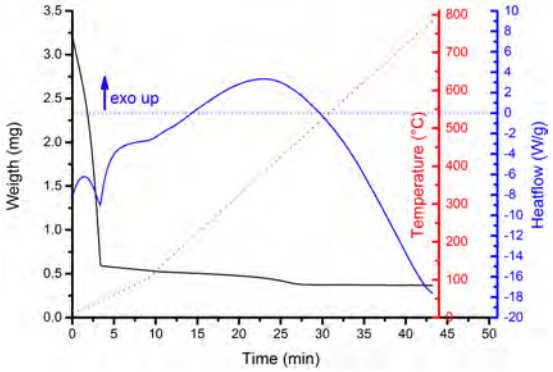

Figure 4.13: TGA of 100 µL 5Al-ST suspension in hexane heated at 10 °C/ min to 100 °C (100 mL/ min DA) and 20 °C/ min to 800 °C (100 mL/ min N_2).

After obtaining more information about the Al incorporation and the in-situ stabilization, the thermal decomposition of the hexane suspension needs to be elucidated to obtain functional TCO layers (Figure 4.13). Before 100 °C the solvent, hexane is completely vaporized in an endothermic process, while at 400 °C the surfactant, oleic acid is completely burned. The obtained suspension has a solid load of 3.7 mg/ mL AZO nanocrystals.

In addition to the synthesis and characterization of the AZO nanocrystals, the 5Al-ST suspension was drop-casted on a thick window glass substrate covered with toluene. By placing the substrate under a glass cover/beaker together with the additional toluene use, one expects to minimize the crack formation during drying of the hexane AZO suspension.[6] If the NPs are directly redispersed in toluene instead of hexane after purification and dried under a glass cover, more cracks will be visible in the film morphology at the end of

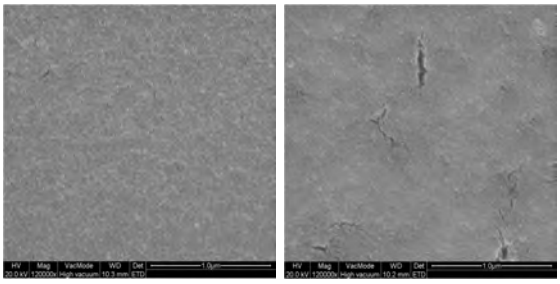

Figure 4.14: a) 5Al-ST suspension in hexane drop casted on top of toluene on a window glass substrate after drying and thermal treatment.(left) b) 5Al-ST NPs resuspended in toluene and drop casted on a window glass substrate after drying and thermal treatment.(right)

the thermal process (Figure 4.14). After two hours of drying the substrates are gradually heated (to reduce the chance of thermal shock) for removal of oleic acid on the NPs surface. After additional heating up to 350 ℃ for 0.5 hour in a 5% H_2 containing atmosphere a sheet resistance around dozens of kΩ/ □ is achieved. Assuming the drop-casted layers are in the μm range, the resistivity is up to 1000 times larger as the aimed 10^{-3}. Even further, shows the sheet resistance rapid increase after exposure to air. This questions the applicability and the need for further investigation of AZO nanocrystals towards functional applications.

4.6.2 Polar suspension

Nevertheless, the biggest asset of using NPs is to be able to separate the crystallization from the deposition temperature, which is not really a bonus if still temperatures of 400 ℃ or more are needed to remove surfactants. Oleic acid stabilized suspensions require these high thermal treatments (Figure 4.13) to remove the organic fraction between the nanoparticles, through which (almost) no deposition on flexible substrates will be possible. Additionally it might be of interest to functionalize the NPs in polar media e.g. water. Therefore the removal/substitution or coverage of oleic acid is essential. Also the conduction pathway might be hindered by inclusion of isolators, resulting in a poor performance of the TCO film. Alternatives for stabilization is the use of electrostatic stabilization instead of chemisorbed surfactants. Tetramethylammonium hydroixde (TMA(OH)) was used to perform a ligand exchange. This electrostatic stabilization can be even removed at lower temperature for film deposition. So far no conductive layers with good morphology have been obtained, although the versatility of these building blocks for divers solvents is demonstrated.

4.7 Conclusion

A first in-depth view for the synthesis of doped oxides such as Al-doped ZnO is given for the thermal decomposition route. A mechanism for the formation of ZnO :Al NPs is proposed starting from the reagents and the reaction pathway is corroborated using headspace GC-MS. During synthesis in-situ steric stabilization takes places where in the suspension carboxylate groups of oleic acid chemisorb on the surface of the NPs. Oleyl amine, on the other hand, is clearly not bound to NP surface, but shows an interaction with oleic acid after accepting a proton from oleic acid, resulting in a more efficient stabilization of the NPs. The effective incorporation of Al inside the ZnO lattice is demonstrated with mappings of HAADF-STEM images in combination with PED. This technique indicates that the lattice parameters increase with Al content, suggesting interstitial Al substitution, while diameters of the synthesized NPs diminish with increasing lattice parameters.

These results provide a better understanding of the thermal decomposition route for the synthesis of Al-doped ZnO nanoparticles and have to potential to be used as building blocks in functional TCO layers. A first attempt towards deposition of the building blocks was done and evaluated and showed that obtaining state-of-the-art conductivity with nanoparticles is not straightforward. Additionally the chemisorbed oleic acid can be altered by tetramethyl ammonium hydroxide and might be fine-tuned to obtain low temperature deposited AZO, although conformation by additional research still needs to confirm this.

5 Thermal Decomposition Synthesis in Benzyl Amine

Figure 5.1: Thermal decomposition setup

In this chapter a stable suspension of AZO nanoparticles is developed without any additives, still ensuring a long term stability. These building blocks contain charge carriers, indicated with FTIR. This can probably be linked to the ^{27}Al MAS NMR study of Al incorporation inside ZnO. In addition to finding a high amount of substitutional tetrahedral Al incorporation, a favorable rod morphology of the nanocrystals is seen with TEM. This morphology is probably the key to the high stability of the suspension. All of these characteristics are beneficial for the use of these nanoparticles as building blocks for TCO films.

5.1 Introduction

An in-situ stabilization method for an AZO ink through thermal decomposition has been established, but here, like in many methods, the yield is rather low.[68] This is a large pitfall for industrial processes to overcome in the case that synthesis methods will be commercialized. Therefore, an attempt of upscaling an other existing method from *Kelchtermans et al.* is tried here.[134] These building blocks have been intensively investigated and show to be promising to function in a TCO film. Further on a stable suspension of AZO nanoparticles is developed without any additives, since this might reduce the deposition temperature.

5.2 Synthesis

The synthesis of AZO nanoparticles is an up-scaled method based on earlier published work.[134] Here, the standard synthesis for 0.5 at% of Al-doping at atmospheric and reflux conditions in benzyl amine is repeated and compared to an upscaled method (batch synthesis). A mixture of 3.79 mmol $Zn(acac)_2 \cdot xH_2O$ and 0.018 mmol $Al(acac)_3$ in 40 mL benzyl amine was poured in a three-neck flask (250 mL) and heated to 200 ℃ using a heating mantle coupled to a JKEM scientific 310 controller. (200 ℃ was never reached as the mixture boils at lower temperature.) The mixture was refluxed for one hour while stirring. Afterwards the obtained sol was cooled down to room temperature and centrifuged in an Eppendorf microcentrifuge (4000 rpc for 1 hour). The mixture was washed two times with milli-Q and two times with methanol. Between each washing step, the NPs were redispersed using a vortex and a sonicator bath. Depending on the goal the particles can be dried at 60 ℃ or redispersed in another medium for instance EG. For FTIR, ^{27}Al MAS NMR, and XRD analysis a dried powder is needed, while for TEM the powder is redispersed in methanol. In case of deposition the NPs are suspended in EG. The redispersion in EG was done by replacing the last washing step of the NPs in methanol by suspending these NPs in EG. The batch synthesis was carried out in a 1 L three-neck round bottom flask with 15 g of $Zn(acac)_2 \cdot xH_2O$, 0.08625g $Al(acac)_3$, and a total volume of 600 mL benzyl amine. The synthesis and washing procedure is the same as described above, but a probe sonicator was used in between washing steps to resuspend the pellet after decantation of the supernatant. If the last washing step is replaced by EG, the NPs cannot be collect in the pellet through centrifugation. Already here, there is an indication that the obtained suspension is very stable and needs further in-depth characterization.

Table 5.1: Comparison between the experimental parameters of the standard and batch synthesis

Reagens	Standard Synthesis	Batch Synthesis
$Zn(acac)_2 \cdot xH_2O$	1 g	15 g
0.5 at% $Al(acac)_3$	0.00575 g	0.08625 g
Benzyl amine	40 mL	600 mL
Three Neck Round Bottom Flask	250 mL	1 L

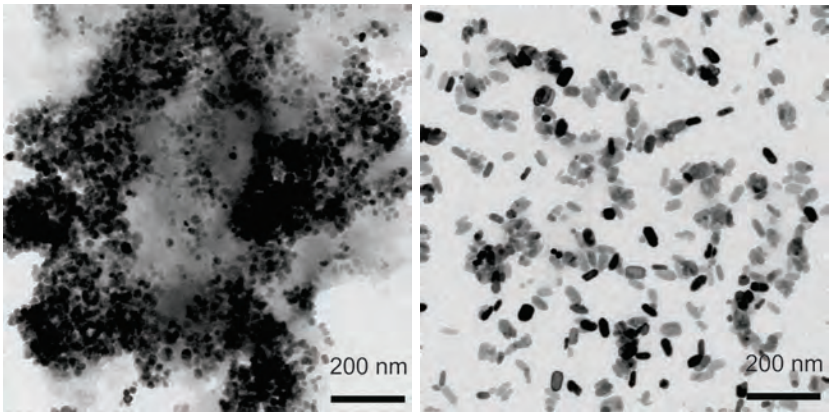

Figure 5.2: TEM images of the synthesis of the regular synthesis (left) and upscaled batch (right) resulting in either NPs or NRs.

5.3 Characteristics

The strength of a thermal decomposition synthesis lies in the uniform size and shape of the obtained crystalline nanoparticles, with relatively decent yield. For the small batch this results in NPs with a Feret diameter (Φ_{dry}) of 17 nm as can be seen from TEM images (Figure 5.2). This is quite similar to the mean crystallite size ($\Phi_{crystal}$) of approximately 16 nm, estimated by the Debye-Sherrer equation using the XRD results (Figure 5.3). The crystallite sizes of the NPs are in the same range as the grain sizes implying that the NPs are monocrystalline. When the mixture is upscaled with a factor 15 for the amount of reagents and 4 for the volume, a remarkable change in the morphology of these NPs can be verified. The more dense packing of the material leads to more rod-like NPs (NRs). These NRs result in a very stable EG suspension. The average longest length of these NRs is 50 nm according to the TEM images. Calculation of the Debye-Sherrer to determine the crystallite size of the NRs only clarifies the larger rod size, but underestimates the influence of the rod in two dimensions. Nevertheless for both NPs and NRs, XRD results indicate the ZnO hexagonal wurtzite crystal phase (JCPDS library file 75-0576) with

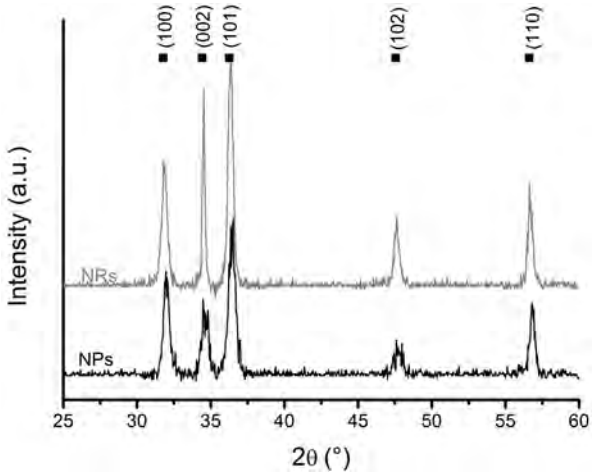

Figure 5.3: X-ray diffractogram of the NPs and NRs after synthesis, purification and drying.

a slightly preferential (101) orientation. For the NRs the (002) orientation is relatively (to (101) orientation) increased.

The batch NRs display an anisotropic shape, indicating that the growth rate along the (0001) is stimulated and suggesting an other growth mechanism than for the standard synthesis. The ratio of reagens in correlation to solvent inside the bottom flask is changed, having the reagents more closely packed in the batch than for the standard synthesis. This is known to influence the morphology.[185] This might be due to the influence of the supersaturation of monomers and indirectly also the nucleation. External conditions like chemical or thermodynamic factors influence the crystal growth. While the first covers the use of precursors and solvents, the latter stresses temperature and pressure differences. In addition, also kinetic factors are assumed to influence this morphology. One can make the hypothesis that close packing of the reagents and the possible difference in supersaturation of monomers stimulates the natural growth rate (0001 for ZnO) along different crystal directions. Benzyl amine can act as a surfactant, which could slow down the difference between growth rate of different sides of the crystal and the disappearance of faster growing faces generating uniformly shaped round nanocrystals. This would be the case for the standard synthesis, while in comparsion less benzyl amine is present for the batch synthesis. Within literature it has been seen that different and varying amounts of solvents influence the morphology. [233] Although for a clear view on what really is happening a more detailed study of every step of the proces is needed. For now the difference in morphology can purely be based on hypothesis.

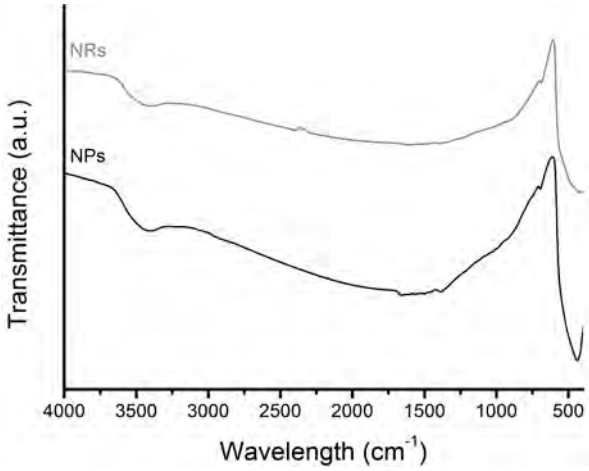

Figure 5.4: FTIR analysis of the NPs and NRs powder after synthesis, purification, and drying.

These AZO NRs result in a (stable) suspension in EG and EtOH, which is measured by the zeta potential (ζ). The zeta potential in EG is 41.7 $\pm$ 5 mV indicating moderate to good stability of the suspension. As observed before, the adsorbed EG molecules modify the Hamaker constant of the particles, making sure that the difference between this Hamaker constant and that of the medium is reduced.[303] As the difference between Hamaker constants diminishes, so does the van der Waals attraction between the AZO NRs. [300] The suspension in ethanol is only moderately stable, connected to a zeta potential of 29.8 $\pm$ 1 mV.

In addition to the morphology and stable suspension, infrared analysis has been performed to verify the presence of organics and to check the intrinsic properties of the NPs and NRs. The formation of Zn-O is confirmed by infrared analysis through the absorption band below 600 cm^{-1}, caused by Zn-O lattice vibrations. The broad absorption band at 3430 cm^{-1} is assigned to the O-H stretching vibration of adsorbed water on the NP surface. Additionally, a broad absorption band between 1000 and 3000 cm^{-1} is caused by surface plasmon absorption indicating the presence of free charge carriers, free electrons in the conduction band.[37, 245] This effect in the infrared region emphasizes the n-type substitutional tetrahedral doping of Al.[134, 245] Figure 5.4 shows a gradual blue shift for the NRs in correlation to the NPs. This indicates a higher density of free charge carriers inside the NRs.[133] These charge carriers caused by good intrinsic properties are expected to increase the conductivity of the material.

5.4 Al incorporation

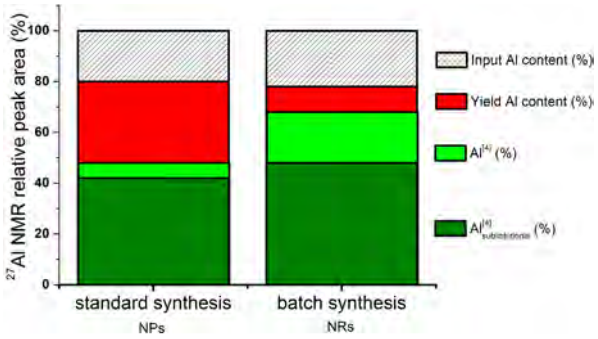

Figure 5.5: Effective Al incorporation in the nanocrystals according to ^{27}Al MAS NMR results

Infrared analysis hypothizes the higher content of free charge carriers inside the NRs and to investigate how the Al is incorporated inside the ZnO lattice ^{27}Al MAS NMR was performed. First, ICP-AES analysis was done to measure the global ratio of Al-to-Zn. These results indicate an effective incorporation of 0.40 at% Al in the NPs and 0.39 at% Al in the NRs. By means of NMR analysis, the difference in coordination of Al can be seen. Interesting to observe is the relatively high tetrahedral incorporation of Al inside the NRs, while the NPs from the standard synthesis accumulate far more octahedral Al. T_1 relaxation measurements are required to differentiate between substitutional and interstitial tetrahedral Al incorporation.[67] The largest fraction of Al is substitutional observed, as already suggested by the infrared results in Figure 5.4. To our knowledge, there haven't been reports of that high relative fraction of substitutional incorporation, rendering these NRs as the most ideal building blocks for TCO layers. This hypothesis can be further supported by the research of *Yunker et al.*, who demonstrated the beneficial characteristics of anisotropic nanoparticles towards the elimination of the coffee-ring effect during drying of suspensions.[295] Anisotropic nanoparticles, like our nanorods, posess long-ranged inter-particle attractions and thereby ensure uniform deposition.[90, 166, 167, 169]

5.5 From building blocks towards functional TCO layers

As the AZO NRs have the most promising morphology to assure uniform deposition of films on chemically cleaned SiO_2 (200 nm)/Si substrates [277], a 1 wt.% EG suspension was spin coated (3000 rpm, 30 s, 1000 rpm/s) and

over-coated with 5 layers of a 0.5 M 1 % Al-doped Zn butoxyethanol precursor (from the recipe of *Schellens et al.*).[239] Previous work has showed the necessity of a glue to interconnect nanoparticles and explain the choice of a molecular precursor.[144] The deposited layer was sequentially treated on a hot plate at 300 ℃ for 2 min and at 400 ℃ again for 2 min prior to an annealing step at 550 ℃ for 60 min (10 ℃/ min, 500 mL/min, N_2) in a carbolite tube furnace. The films were additionally subjected to a final reductive anneal with a heating rate of 10 ℃/ s up 450 ℃, 10 min isotherm in a 5% H_2/95% Ar atmosphere (ramping and cooling in N_2) in a rapid thermal processing setup. In the end a sheet resistance of 1.433 kOhm/ □, similar to that reported by *Schellens et al.* without the AZO NRs.[239] The morphology is shown in Figure 5.6 and displays big chunks of probably ZnO(:Al) which are interconnected. Although a completely covered substrate is obtained, no improvement in conductivity to pure molecular precursors is obtained. This all questions the use of NPs for the deposition TCO films. To verify these conclusions the suspensions might be deposited in a different manner, such as drop-casting, or the suspension might be needed to be adapted according to applied deposition technique, but that will require a long-time effort.

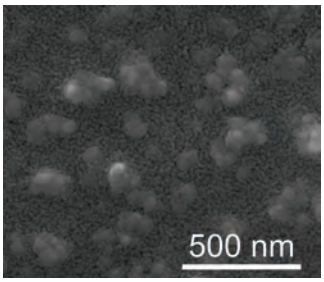

Figure 5.6: SEM image of the 1 wt.% AZO NRs EG suspension over-coated with 1 % Al-doped Zn BOE precursor.

5.6 Conclusion

A batch synthesis has been developed for crystalline AZO NRs, dispersed in EG. The resulted rods have a lot of potential as building blocks for TCO films due to good intrinsic properties. Not only are they free from organics, they display a surface plasmon absorption. In comparison to the standard synthesis, this FTIR spectra display a blue-shift, indicating the presence of more free charge carriers in comparison to the standard synthesis. By in-depth ^{27}Al MAS NMR and T_1 measurements, this has been confirmed. Almost half of the used ratio of Al in synthesis is substitutional tetrahedral incorporated. As a TCO layer was deposited using these NRs, no improvement in comparison to using pure molecular precursors could be obtained. This questions the use of NPs in

general for the creation of TCO films, although significant improvements of the suspension and deposition methods could lead to different outcome.

Part II

The potential of molecular precursors

6 Organic Molecular Precursors

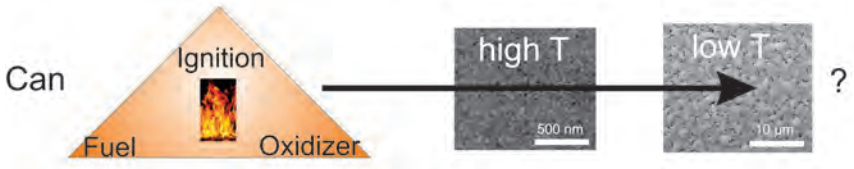

Figure 6.1: Are organic molecular precursors processable at low temperature through combustion synthesis?

Within this chapter an Al-doped Zn butoxyethanol precursor is developed. The resistivity of the obtained AZO films is evaluated in function of the thickness of the layers. In addition the optimal Al content is determined for the optimized thickness. In contrast to this method, which is capable of generating transparent conductive Al-doped ZnO layers at elevated temperatures, new precursors using combustion chemistry are synthesized to obtain functional n-type doped ZnO films at lower temperatures. In addition to Al-doping, small fractions of In and Ga are used for doping. As this is not very straightforward an in-depth investigation in the chemistry and the optimization of the morphology are performed. This all generates new knowledge and insights in the conductivity and transparency of doped ZnO films. In the end, an attempt towards low temperature combustion processed films is elucidated.

6.1 Introduction

Since it is not very easy to convert nanoparticles as building blocks into functional transparent conductive oxides, molecular precursors have been explored as an alternative route.[241] Also here a distinction can be made between organic and aqueous molecular precursors. Although aqueous precursors are very appealing from an environmental point of view, often organic precursors are preferred. As the heat capacity of water is very high, drying processes and other necessary thermal decomposition of the water based precursors require a high energy input to obtain the functional Al-doped ZnO films. Within literature, a lot of reports are made on 2-methoxyethanol (MOE) based precursors [209], although the teratogenic characteristic of this solvent needs to be taken into consideration.[224] In this chapter an alternative 2-butoxyethanol (BOE) precursor will be discussed. [239]

The ZnO films are commonly amorphous up to 400 °C, nevertheless for n-type doped ZnO, with only low amounts of doping, the film needs to be crystalline. The isotropic s orbitals of Zn are too small to overlap in an ionic semiconductor and to ensure conductivity.[116] By extrinsic doping with small percentages of Al, Ga or In a donor level is created below the conduction band. Higher doping of Ga and In generates amorphous ionic semi-conducting materials with high mobilities. For TCO applications the charge carriers and the mobility are required to be as high as possible, in contradiction to thin-film transistors where only the mobility is of importance. [172]

The synthesis of crystalline ZnO commonly requires a lot of energy input. Except for chemical bath deposition [111], not many methods are available to deposit crystalline doped ZnO. Since the beginning of this decade, there has been the motivation of turning combustion processing from powder synthesis to deposition of precursor directly as films. [142] [113] For amophous materials this route generates some promising results, but (to my knowledge) no research has been done regarding crystalline doped materials. Therefore, this route will be elucidated to synthesize n-type doped ZnO films.

6.2 Synthesis

A pure Zn as well as Al-doped Zn precursors were prepared with a total metal concentration of 0.1 and 0.5 M. The amount of dopant was determined according to this ratio [Al]/[Al]+[Zn] = 1, 2, 3, and 5 at%. Therefore, zinc acetate dihydrate, $ZnAc_2 \cdot 2\,H_2O$), and the proper amount of aluminum nitrate nonahydrate, $Al(NO_3)_3 \cdot 9\,H_2O$, were mixed in butoxyethanol. These reagents were placed inside a jar on a hot plate at 70 °C. Ethanolamine (MEA) was added drop-wise in a 1:1 ratio to Zn to the solution. This precursor was heated for

2 hours at 70 ℃, while the cap of the jar was loosely placed on top. In the end, the solution is slowly cooled to room temperature. The recipe was based on the publication of *Schellens et al.*, although recalibration of dopants was done.[239]

6.3 Film deposition

The films are deposited by spin coating (3000 rpm, 30 s, 1000 rpm/s) of the (Al-doped) Zn precursors on to chemically cleaned SiO_2 (200 nm)/Si substrates (20x20 or 25x25 mm^2).[277] The applied precursor solutions are filtered through a 0.1 μm syringe filter to remove dust. The as deposited film was treated in succession on two hot plates (at 300 ℃ and 400 ℃) in static air as follows: 2 min at 300 ℃, followed by 2 min at 400 ℃. To obtain films consisting of X layers, this entire cycle was repeated X-1 times prior to an annealing step at 550 ℃ for 60 min (10 ℃/ min, 500 mL/min, N_2) in a carbolite tube furnace. The films were additionally subjected to a final reductive anneal with a heating rate of 10 ℃/ s up 450 ℃, 15 min isotherm in a 5% H_2/95% Ar atmosphere (ramping and cooling in N_2) in a rapid thermal processing setup. From the 0.1 M and 0.5 M (1 at% Al-doped Zn precursor) 5, 10, 15, 20 and 25 consecutive layers were deposited. To study the influence of Al doping a stack of 15 layers of the 0.5 M (Al-doped) Zn precursor was evaluated. These 15 consecutive layers have also been used to study in-depth the influence of the nitrogen and reductive anneal.

6.4 Thermogravimetric Analysis

According to the thermogravimetric analysis in Figure 6.2 of the dried 0.5 M Zn and 1 at% Al-doped Zn molecular butoxyethanol precursor, weight loss appears in two major steps. The first step and major weight loss is in the temperature range below 300 ℃. This is probably due to the vaporization of BOE as solvent and the thermal decomposition of $Zn(acac)_2$, which are both endothermic processes. The second step is in the temperature region of 300 up to 400 ℃, which is probably due to the release of residual organics, coming from the reagents. Afterwards, as the decomposition is completed, an exothermic step at 400 ℃ indicates the formation of crystalline ZnO. In total a weight loss of approximately 70% takes place for both precursors. As the hot plate treatments are set to 300 ℃ and 400 ℃, not only the organics will be removed but also crystalline ZnO(:Al) will be formed. [239]

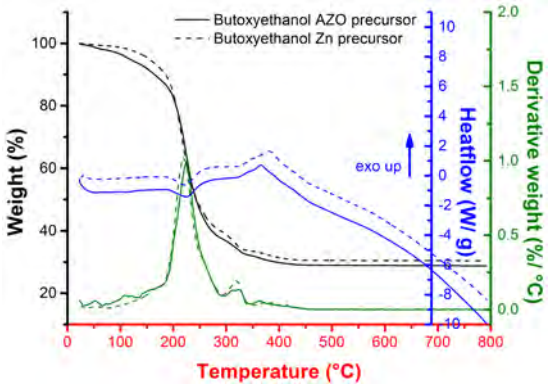

Figure 6.2: TGA (weight %), DTA (derivative weight %/ °C) and DSC (heat flow W/ g) analysis of 1 at% Al-doped Zn and pure Zn butoxyethanol precursors heated at 10 °C/ min in dry air (flow 100 ml/min).

6.5 Effect of different molar precursors and their thickness on the resisitivity

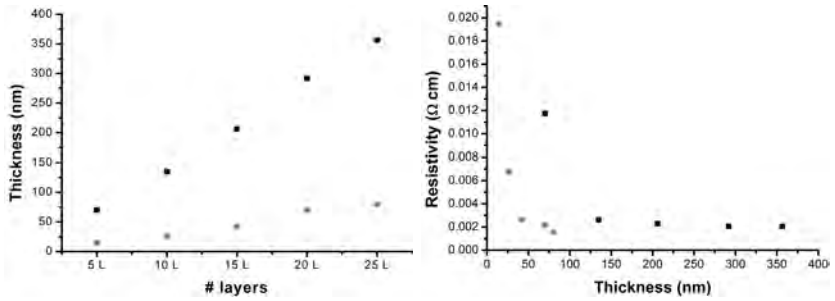

Figure 6.3: Left: Thickness (nm) of the film in function of the amount of deposited layers of the 1 at% Al-doped ZnO precursor. A comparison was made between the 0.1 M solution in grey and the 0.5 M precursor in black. Right: Resistivity (Ohm cm) of 5, 10, 15, 20, and 25 L of the 1 at% Al-doped Zn in function of the thickness (nm) of the film. A comparison was made between the 0.1 M solution in grey and the 0.5 M precursor in black.

Figure 6.3 gives an overview of the thickness (nm) and the resistivity (Ohm cm) of the 0.1 M and 0.5 M 1 at% Al-doped Zn precursor both deposited through spin coating 5, 10, 15, 20, and 25 layers after thermal treatment including reductive anneal. For both the 0.1 M and the 0.5 M the resistivity decreases with increasing thickness. For the 0.5 M precursor concentration a leveling of the resistivity is observed at higher layer thickness. The lowest measured

sheet resistance is only 57 Ohm/□ for the 25 L of the 0.5 M 1 at% Al-doped Zn butoxyethanol precursor. For the 0.1 M precursor the decrease can be seen, but no leveling is observed. Nevertheless, also for this precursor a kind of saturation is expected. This leveling of resistivity indicates two different conductivities. In addition to a bulk conductivity/resistivity, the surface of the film is expected to be influenced creating a higher surface resistivity. This effect in metal oxides has already been studied by *Graham et al.* for metallic materials. [104] *Ellmer et al.* also acknowledged the theory behind this difference.[82] The Fuchs-Sondheimer model describes the elastic scattering of electrons at the surface. In addition there has the development of a Mayadas-Shatzkes model for scattering at the grain boundaries.[82][266] As the 25 L of the 0.1 M precursor result in the lowest obtained resistivity, the minimal value of resistivity is expected around this point, although it might be even lower. To test this assumption additional layers need to be deposited. Nevertheless up to a certain point no thicker layers can be obtained by spin coating. In addition, a comparison can be made between the 25 L of the 0.1 M precursor and the 5 L of the 0.5 M precursor. Their thickness of the 25 L of the 0.1 M is almost equal to 5 L of the 0.5 M 1 at% Al-doped Zn precursor; 80 nm (25 L 0.1 M) and 70 nm (5 L 0.5 M). Nevertheless the resistivity is one order lower for the least concentrated precursor. Porosity in films of sol-gel processed precursors is expected to decrease the conductivity. [67, 200]

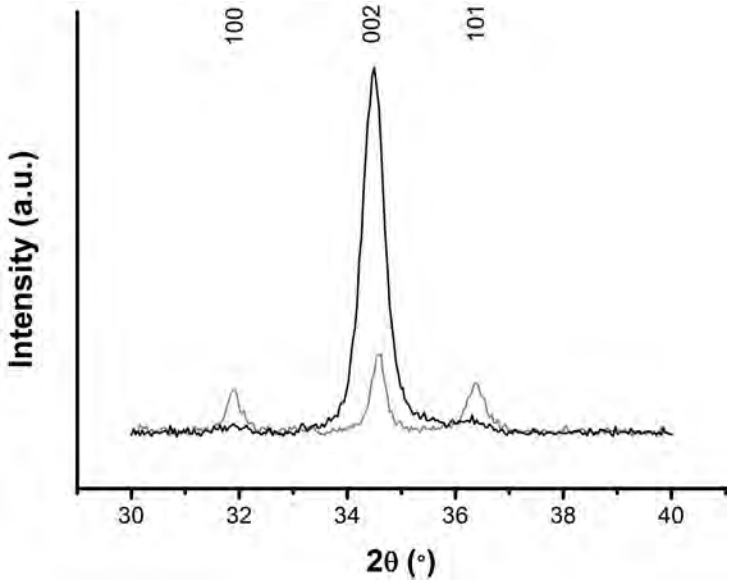

Figure 6.4: X-ray diffraction of 25 L of a 0.1 M (grey) and 5 L of a 0.5 M (black) 1 at% Al-doped Zn precursor deposited through spin coating. These diffractograms can be indexed with the wurtzite crystal lattice (JCPDS library file 79-0206).

Figure 6.4 display the crystallinity of the Al-doped ZnO films, obtained from 25 L of the 0.1 M precursor and 5 L of the 0.5 M precursor. Both films can be matched with the wurtzite crystal lattice (JCPDS library file 79-0206). The one obtained from the 0.5 M precursor displays preferential (002) orientation. From literature the hypothesis was made that a preferential c-axis orientation would result in an improved conductivity.[200, 239] Nevertheless, the film obtained from the 0.1 M precursor has only a slight preferential (002) orientation and almost equal intensities of the (100) and (101) diffraction peaks. This film (from 0.1 M precursor) still generates the lowest resistivity. This gives an indication that not only the (002) orientation is of importance but density and porosity inside Al-doped ZnO are far more important.[67] To investigate these characteristics further, BET (Brunauer-Emmett-Teller) [35] Surface Area Analysis and BJH (Barrett-Joyner-Halenda) [23] Pore Size and Volume Analysis could resolve some unanswered questions. SEM images (Figure 6.5) in top view and in cross-sectional view are unable to differentiate in that manner, but can give an indication. Further on, the SEM image for the 0.1 M precursor does not show real delineated grains. The top view image of the 0.5 M precursor gives the expected indication for porous materials and what looks like a rougher surface is visible in the cross-sectional view. Nevertheless, AFM (not analyzed) could further resolve this difference in porosity and roughness.

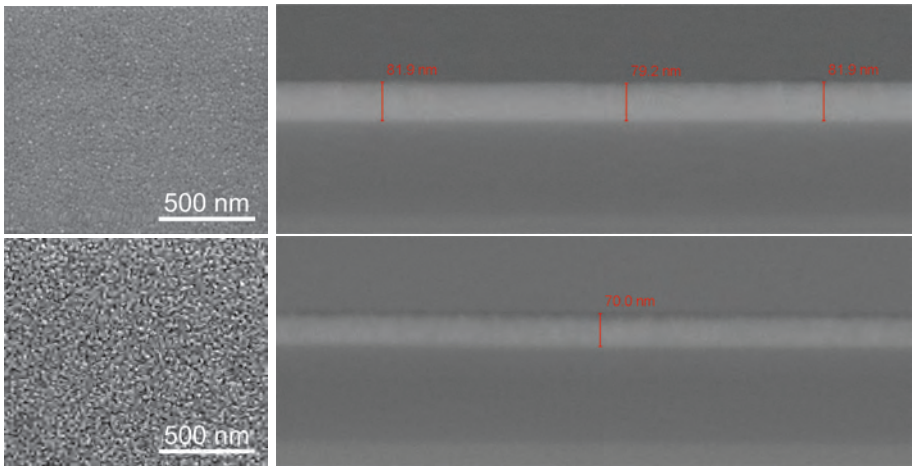

Figure 6.5: Top: SEM top view and cross-sectional image of 25 L of a 0.1 M 1 at% Al-doped Zn precursor deposited through spin coating.
Bottom: SEM top view and cross-sectional image of 5 L of a 0.5 M 1 at% Al-doped Zn precursor deposited through spin coating.

6.6 Influence of the Al doping

The optimum of Al doping is investigated for layers of approximately 200 nm, to exclude surface effects from bulk resistivity. These films can be obtained through spin coating of 15 L of a 0.5 M precursor solution with either no Al or 1, 2, 3, or 5 at% Al present. The sheet resistance of the films was measured through Van der Pauw analysis and compared to Hall bar measurements for the ZnO, 1, 2 and 3 at% ZnO:Al films (Figure 6.6).

When comparing Hall bar to Van der Pauw measurements an increase (almost always with a factor 2) in resistivity (and sheet resistance) is observed for the Hall bar measurements. The reason for this is not clear. Hall bar measurements were done after a couple of months after reductive treatment, but the samples were remeasured with VdP directly before preparing samples for Hall bar and there no (or minimal) change of sheet resistance is found. As samples undergo a thorough sample preparation with Hall bar, additional errors can be made. From the Hall bar measurements the mobility as well as the carrier concentration can be determined. The carrier concentration is the lowest for the undoped ZnO film. The mobility was expected to be the highest here, but it increases up to 2 at% and lowers again at 3 at% Al. The carrier concentration is for the measured set, the highest at 1 at% Al and decreases in function of Al doping. Through this interaction between mobility and carrier concentration to obtain a good conductivity, there is a competition between 1 and 2 at% Al. Depending on the layer quality, determining the mobility, 1 or 2 % ZnO:Al results in the best performing layer as TCO.

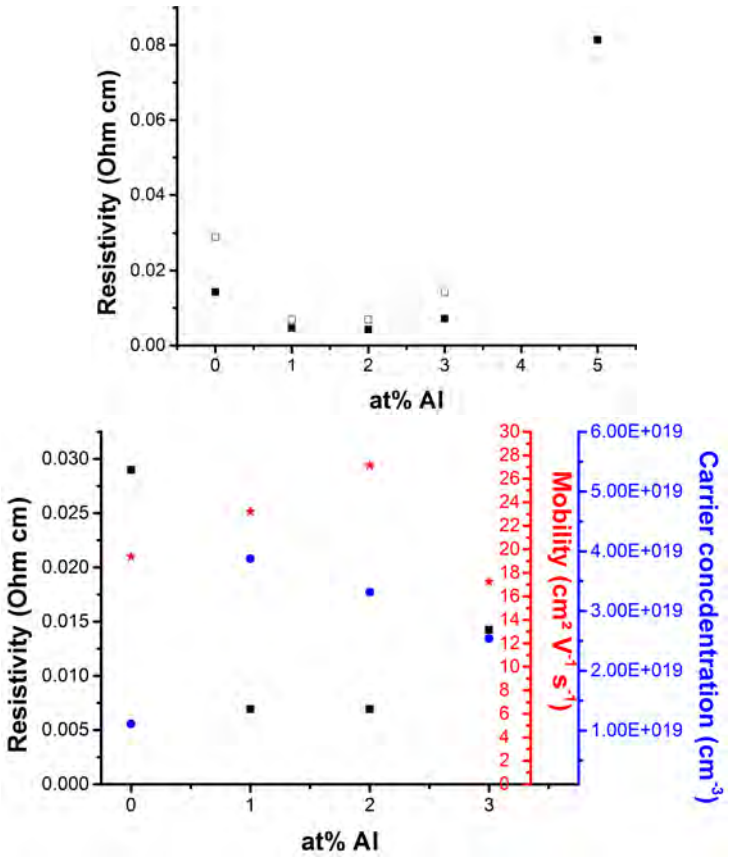

Figure 6.6: Top: Resistivity values of 15 L of 0.5 M Al-doped Zn precursor deposited through spin coating. A comparison was made with Van der Pauw (black full squares) and Hall bar (black empty squares) measurements.
Bottom: Resistivity values (black squares), mobility (red stars) and carrier concentrations (blue circles) of 15 L of 0.5 M Al-doped Zn precursor deposited through spin coating.

The crystallinity of the films in function of Al doping was monitored by X-ray diffraction in Figure 6.7. All films can be matched with the wurtzite crystal lattice with a preferential (002) orientation. The results are only displayed between 30 and 40° 2θ, since the (110) and (102) diffraction peak can barely be distinguished from the noise. Also the (100) and the (101) diffraction peak are only slightly visible. Pure ZnO has the highest preferential c-axis orientation. Incorporation of Al inside ZnO disturbs this preferential growth. The intensity of the (002) peak reduces up to 3 at% Al. For the 5 at% Al a small increase is again observed. No peak broadening or sharpening is seen in function of Al incorporation, indicating no reduction nor growth in grain size.

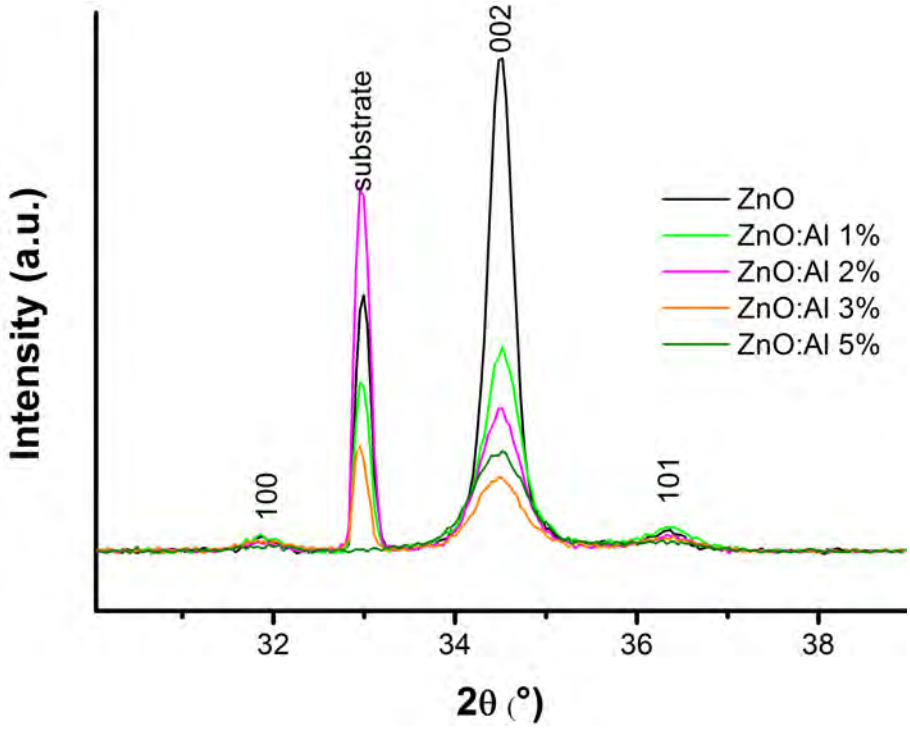

Figure 6.7: XRD diffractograms of 15 L of 0.5 M Al-doped Zn precursor deposited through spin coating. These diffractograms can be indexed with the wurtzite crystal lattice (JCPDS library file 79-0206).

The SEM images in Figure 6.8 give the top view and the cross-sectional images of the films. As mentioned before and analyzed from the molarity experiment, films of 200 nm were aimed for. Nevertheless, the films are only approximately 125 nm, with exception of 1 and 5 at% ZnO:Al, which are around 140 nm. An effective explanation cannot be found within these experiments, but there is a presumption that aging of the applied precursor might influence the deposition process. The storage temperature and humidity of the precursor might also influence the quality from the precursor. If the precursor is left standing for a period of time, eventually precipitation will occur. Although the thickness of the 125 nm films are far from the aimed 200 nm, according to Figure 6.3 the 125 nm in thickness will be sufficient in order to exclude surface effects from influencing the conductivity. In addition it is clear from the top view and cross-sectional SEM image of ZnO that this surface is a lot rougher in comparison to those doped with Al. The preferential c-axis orientation is difficult to visualize through SEM (HRTEM is needed), although indications are present. Except for the ZnO films, no real granular structure is discriminated. Doping with Al leads to smooth, dense films with excellent conductivity properties.

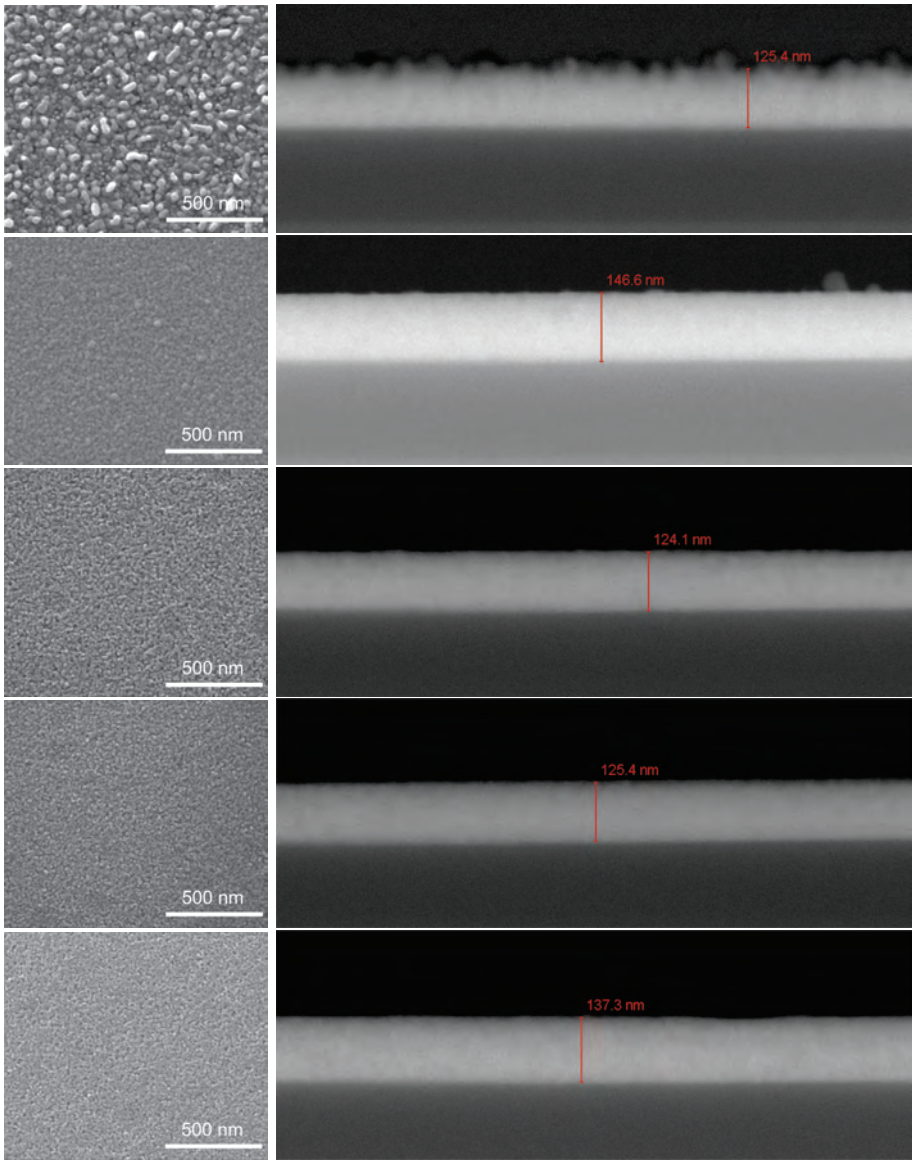

Figure 6.8: SEM top view and cross-sectional image of 15 L of a 0.1 M (Al-doped) Zn precursor deposited through spin coating. From top to bottom ZnO, 1, 2, 3, and 5 at% ZnO:Al films are displayed.

6.7 Can Cl be incorporated inside the ZnO lattice?

Electro-deposition of Cl doped ZnO can be done at room temperature and is able to improve the conductivity in comparison to undoped ZnO.[227] In addition, often the use of $AlCl_3 \cdot 6\,H_2O$ as a starting salt for Al-doped Zn precursors is reported [158, 262, 272], but rarely comments are given on the possibility that Cl can act as an additional dopant inside the ZnO lattice to substitute O. [48, 65, 227, 264] To elucidate the possibility of Cl doping through solution processing, 15 L of the 0.5 M with 1 mol% of either $Al(NO_3)_3 \cdot 9\,H_2O$ or $AlCl_3 \cdot 6\,H_2O$ was deposited through spin coating and the application of heat treatments as described in Section 6.3. The sheet resistance, thickness and corresponding resistivity are given in Table 6.1.

Table 6.1: Sheet resistance, thickness and resistivity in function of the difference in reagents.

Reagents	Sheet resistance	Thickness	Resistivity
$Al(NO_3)_3 \cdot 9\,H_2O$	320 Ohm/□	147 nm	4.70 10^{-3} Ohm cm
$AlCl_3 \cdot 6\,H_2O$	327 Ohm/□	136 nm	4.44 10^{-3} Ohm cm

Although the sheet resistance of ZnO:Al film using $AlCl_3 \cdot 6\,H_2O$ is a bit higher, the resistivity is lower. This is due by the reduced thickness of this film. Although some caution is needed since the thickness of the films is measured using cross-sectional SEM images, which do not allow a precise nm thickness determination. These differences are so minimal, that one can assume that there is no real difference. In addition the reproducibility of the incorporation of Cl has not been verified. Therefore it cannot be stated whether Cl is incorporated inside the lattice and if it is incorporated, the question remains if it has an influence. Additional EDX or XPS analysis could elucidate whether or not Cl is incorporated. As the thickness, although minimal, of the film with the Cl based precursor is thinner, an additional process should be reconsidered. During the reductive treatment, hydrogen present in the atmosphere, might form HCl with the Cl inside the layer. This acid is expected to etch ZnO and reduce the thickness and/or create pores/cracks inside the film. SEM analysis of these films is inconclusive of this hypothesis. Also here BET and BJH analysis could give some more insights, but as the sheet resistance nor resistivity is significantly better, the possibility of Cl doping is rather minimal.

Although, no real differences are seen between the use of Cl based reagents or nitrate based reagents, Cl is hypothesized not to be incorporated inside ZnO. If Cl is incorporated, it certainly has no beneficial influence on the conductivity of Al-doped ZnO films.

6.8 The anneals

Schellens et al. discussed the crystallinity and the sheet resistance in function of the applied anneals.[239] After hot plate treatment at 400 °C the deposited material is crystalline with a preferential (002) orientation. Although the inert anneal does not seem to change anything about the crystallinity the sheet resistance significantly reduces. In the end, the reductive anneal further reduces this sheet resistance but also decreases the intensity of the (002) diffraction peak.

The questions asked here are if the inert anneal is really necessary and if the temperature of reductive anneal can be reduced. If this annealing process could be reduced in temperature, it might lead to promising results for low temperature development of films. The 1 at% ZnO:Al obtained from the spin coating 15 L of this corresponding 0.5 M precursor were used. To evaluate the reductive treatment, each film had the same inert anneal (10 °C/ min up to 550 °C for 1 h and cooled down to room temperature in a nitrogen atmosphere). Afterwards a reductive treatment was applied at 10 °C/ s up to 250, 300, 350, 400, 450, or 500 °C for 15 min in a 5 % H_2/ 95 % Ar atmosphere. Independently a film without inert anneal, but with reductive anneal (at 10 °C/ s up to 450 °C for 15 min in a 5 % H_2/ 95 % Ar atmosphere) is studied. All these results are given in the Table and Figure 6.9.

From Figure 6.9 can be seen that a too low or a too high temperature during RA increases the sheet resistance significantly. At temperatures of 500 °C not only the sheet resistance increases up to 5 kOhm, but also the error of the VdP measurement is high. This is probably due to irregularities inside the morphology or the creation of holes, pores inside the layer. Additionally, a very short period of RA was evaluated. The AZO film was ramped up to 450 °C, but only for 1 s, followed by immediately cooling in a reductive atmosphere. The obtained sheet resistance is 1.4 kOhm. If no inert anneal is applied, again a high sheet resistance ($\sim$ 1 kOhm) is found. This emphasizes the necessity of an inert anneal and a reductive anneal with a reasonable temperature (450 °C in this case) for a certain period of time (15 min in this case).

The reason behind this improved conductivity with additional inert anneal and high temperature reductive treatment can be found in a whole range of factors as described for aqueous sol-gel processing.[67] First of all, the Al allocation can be further improved by a lattice reorientation; a shift from octahedral to (substitutional) tetrahedral Al. The fact that an elevated temperature is necessary for a longer period of time, might be caused by energy consumption for relocation of Al. To verify this, additional NMR analysis is done. Here, NMR was tried on a crushed wafer with 25 L of the Al-doped Zn butoxyethanol precursor after reductive anneal. Nevertheless, nothing above the noise level

is measured, indicating the necessity of either scrapping off the film or independently synthesizing the powders. The scrapping off was impossible due to excellent adhesion of the AZO film on top of the substrate. For the powder synthesis, additional analysis should be done to verify the correct transformation of conclusions from powders to film. Additionally, H can passivate defects at the grain boundaries.[74] By this the influence of grain boundary scattering will be reduced. Further on, is H as such, also a shallow donor, improving the conductivity again. [278]

Temperature (°C)	Time	Inert anneal	Sheet resistance (Ohm)	Standard deviation (Ohm)
250	15 min	X	6626	10
300	15 min	X	327	0.04
350	15 min	X	206	0.01
400	15 min	X	202	0.003
450	15 min		1185	0.79
450	1 s	X	1428	0.045
450	15 min	X	189	0.003
500	15 min	X	5433	1172

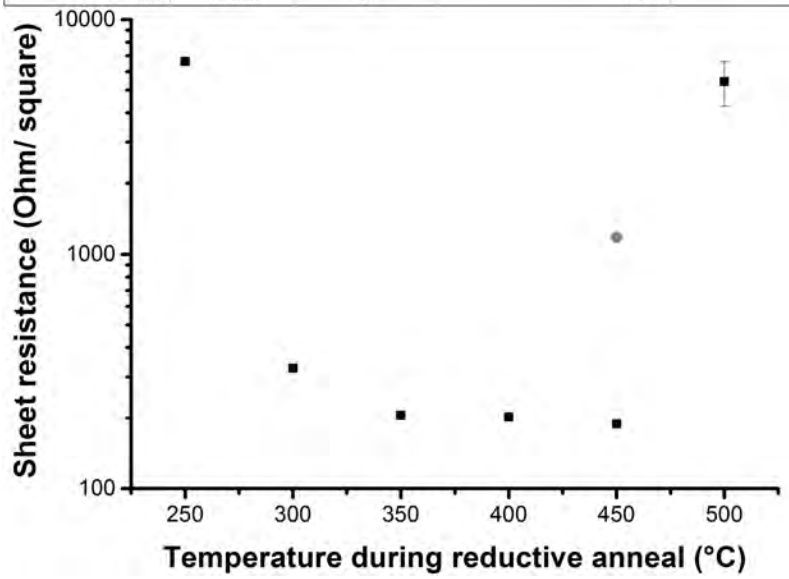

Figure 6.9: Sheet resistance of 15 L of 0.5 M Al-doped Zn precursor deposited through spin coating. The black squares come from films which had the inert anneal (10 °C/ min up to 550 °C for 1 h and cooled down to room temperature in a nitrogen atmosphere) before receiving a reductive treatment at 10 °C/ s up to 250, 300, 350, 400, 450, or 500 °C for 15 min in a 5 % H_2/ 95 % Ar atmosphere. The grey circle comes from a film without inert anneal, but had a reductive treatment at 10 °C/ s up to 450 °C for 15 min in a 5 % H_2/ 95 % Ar atmosphere.

6.9 Towards low T processing

Although very conductive AZO layers can be obtained through solution processing of BOE precursors, still high temperature treatments are necessary to obtain resistivities within the 10^{-3} Ohm cm region. Recently combustion syntheses has been explored as an attractive route in low temperature solution processing.[142] This synthesis route generates high local temperatures converting precursors into the corresponding oxides and enabling low-cost large-scale bulk syntheses. This has already a long history from powder synthesis but only recently there has been the tendency of directly applying combustion processing for mainly amorphous thin film fabrication. Conventional precursors, like sol-gel methods, are based on metal hydroxide and/or alkoxide conversion by an endothermic process. The synthesis of oxides requires sufficient external energy input for oxidizing organic impurities, to achieve phase-pure products. On the contrary, combustion reactions have a balanced redox chemistry and the local oxidizer can efficiently remove organic impurities without coke formation. This translates with exhibiting a single intense exothermic signal, which is sufficient to drive the reaction rapidly to completion. Generally this combustion processing has been applied for amorphous metal oxide systems, since for crystallization very high energy needs to be added to system. The ZnO films are commonly amorphous up to 400 °C, nevertheless for ZnO:Al the film needs to be crystalline. The orbitals of Al are too small to overlap and to ensure conductivity.[116]

In the quest of generating crystalline ZnO:Al, molecular combustion precursors were developed, which decompose at temperatures of about 200 °C. Further on, a discussion on the morphology and an investigation on the influence of dopants is conducted.

6.9.1 Synthesis

$Zn(acac)_2 \cdot xH_2O$ was dissolved with NH_4NO_3 in 10 mL 2-methoxyethanol (MOE). A total metal concentration of 0.2 M with 1 at% of Al was obtained. The oxidizer-to-fuel ratio for the 1 at% Al-doped Zn precursor was evaluated between 1:4; 1:2; 1:1.

$Zn(acac)_2 \cdot xH_2O$ and $Ga(acac)_3$ or $In(acac)_3$ were dissolved with NH_4NO_3 in 2-methoxyethanol. A total metal concentration of 1 M with 0.5 and 1 at% of Ga or In was obtained. The oxidizer-to-fuel ratio for the Ga or In-doped Zn precursor was set at 1:1.

In addition to the highly concentrated precursors a 0.1 M precursor was made for pure $Zn(acac)_2 \cdot xH_2O$ and by doping it with 0.5 at% $Al(acac)_3$ or $In(acac)_3$

and 1 at% $Al(acac)_3$ or $In(acac)_3$. The oxidizer-to-fuel ratio was set 1:1 by dissolving NH_4NO_3 in 2-methoxyethanol.

6.9.2 Film deposition

The film deposition of Zn, Al-doped Zn, Ga-doped Zn, and In-doped Zn films were prepared by spin coating the precursor solutions (0.1 μm syringe filter is used) onto chemically cleaned SiO_2 (200 nm)/Si substrates.[277] After coating (30 s, 3000 rpm, 1000 rpm/s), the as deposited wet film was treated on a hot plate (in static air). The specifics (molarity, hot plate treatment, amount of layers deposited, and additional anneal) of each experiment are given in each subsection.

6.9.3 Thermal decomposition to optimize oxidizer-to-fuel ratio

While many combustion investigations have been elucidated using metal nitrates as source of metal ions and oxidizers [142] [85] [119], the preference here goes out to metal acetylacetonates [141] [84]. The oxidizer-to-fuel ratio for the 1 at% Al-doped Zn acetylacetonates precursor with ammonium nitrate was evaluated between 1:4; 1:2; 1:1.

Extensive thermogravimetric analysis was done on 50 μL of the 1 at% Al-doped Zn precursors with different oxidizer-to-fuel ratio's. These precursors were aged for one day. The investigated ratio's were 1:4; 1:2; 1:1 for a 0.2 M metal ion solution of 10 mL. First the precursor was heated up to 100 °C at 10 °C/ min and kept isotherm for 15 minutes in a dry air atmosphere (flow 100 ml/min). This pretreatment was done to remove the access of solvent, MOE. Afterwards a second thermal decomposition profile was recorded up to 500 °C at 10 °C/ min in a dry air atmosphere (flow 100 ml/min).

Figure 6.10 shows the thermogravimetric analysis of the various ratio's of oxidizer-to-fuel. After vaporization of the solvent the thermal decomposition differs from gradual weight loss up to a thermal runaway effect. Only the dotted line (oxidizer:fuel= 1:2) of the DSC signal in Figure 6.10 shows an endothermic peak, due to probably even further volatilization of the solvent or maybe even acetylacetonates. Afterwards, this precursor and the one with less oxidizer (oxidizer:fuel= 1:4) show gradual decomposition, starting around 150 °C. This weight loss is accompanied by a small exothermic signal at 200 °C. Even at 400 °C, further exothermic weight loss is visible up to 500 °C. If more oxidizer is added (oxidizer:fuel= 1:1), a thermal runaway is visible with a strong exothermic peak at 200 °C.

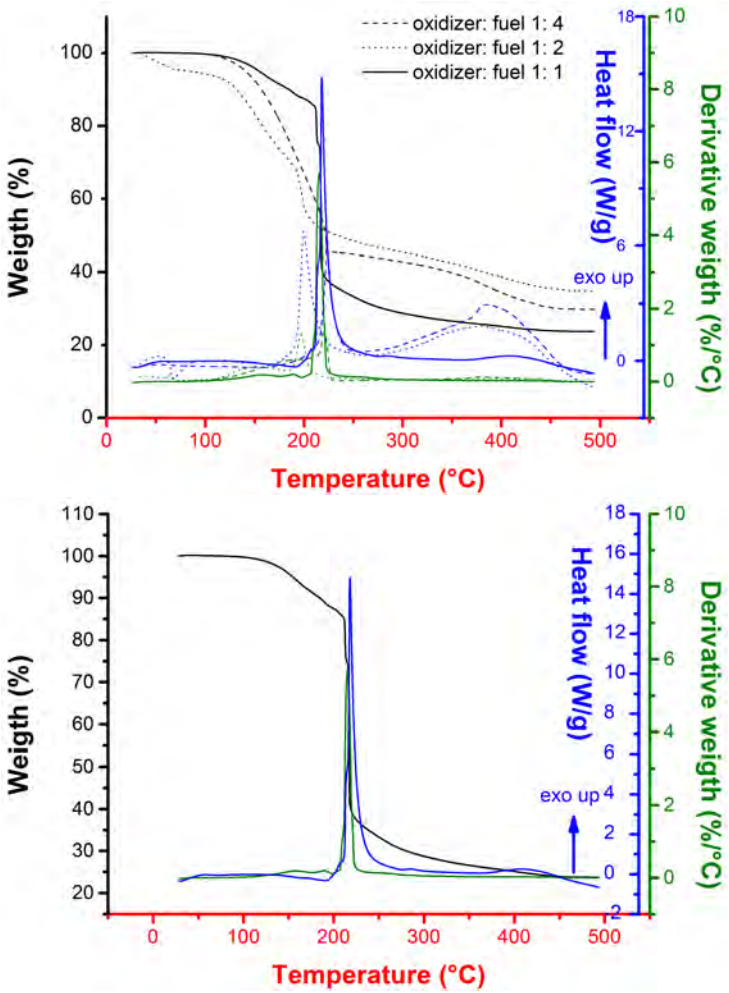

Figure 6.10: TGA (weight %), DTA (derivative weigth %/ ℃) and DSC (heat flow W/ g) analysis of 1 at% Al-doped Zn precursors with different oxidizer-to-fuel ratio's: 1:4 (dashed line); 1:2 (dotted line); 1:1 (full line) heated at 10 ℃/ min in dry air (flow 100 ml/min). In the top image the overview of all ratio's is given while in the bottom image only the 1:1 oxidizer:fuel precursor is displayed.

The residual fractions (%) and end weights (mg) of these precursors are different (Table 6.2). The end weight in % is expected to be the lowest for the 1:4 oxidizer:fuel ratio, since this precursor contains the highest amount of organics. On the contrary this residual mass fraction is expected to be the highest for the 1:1 oxidizer:fuel ratio. Nevertheless the 1:2 oxidizer:fuel ratio contains more residual weight. If this is compared to the end weights in mg only the precursor with the 1:4 oxidizer:fuel ratio satisfies the calculated theoretical value of 0.8

Table 6.2: Overview of the residual mass fractions for the different oxidizer-to-fuel ratio's.

oxidizer-to-fuel ratio	end weight (%)	end weight (mg)
1:4	30	0.8
1:2	35	1
1:1	24	0.6

mg 1 at% Al-doped ZnO. For the precursor with the 1:2 oxidizer:fuel ratio, additional weight loss is expected since the obtained yield of 1 mg is overestimated. For the precursor with the highest oxidizer ratio (1:1 oxidizer:fuel), a lower end weight 0.6 mg is obtained. This end weight should be the same, indifferent of the amount of oxidizer used. The starting weight of the 1:1 (oxidizer:fuel) precursor also should be the highest. However, this is not the case. The hypothesis can be made that acetylacetonates have been volatilized before heating up to 500 ℃ and changed the molarity of Zn (and/or Al).[282] This process could have taken place during the antecedent thermal decomposition up to 100 ℃ with an isothermal period of 15 minutes or as these precursors were made at different times, the molar mass of $Zn(acac)_2 \cdot xH_2O$ could be modified by adaptation of hydrate water.

The 1:1 (oxidizer:fuel) precursor is the only one with a single-step exothermic combustion reaction at 200 ℃. Therefore, this precursor is in-depth analyzed regarding the thermal decomposition using TGA-MS (Figure 6.11 and Figure 6.12).

Before the combustion at 200 ℃, mass fragments of the solvent are found. The presence of m/z 12, 17, 18, 27, 28, 29, 30, 31, 43, 44, 45, 46 and 58 (Table 6.3) indicate residual vaporization of MOE.

Equation 6.1 describes the reaction process during combustion. *Kim et al.* described a similar combustion reaction for In_2O_3.[141] In Equation 6.1, the 1 at% of Al doping is neglected, purely to interpret in a simplified manner the decomposed gases during combustion synthesis. Further on, is oxygen is as reagents, since the reaction takes place in a oxygen containing atmosphere. The formation of water ($H_2O^{+\bullet}$ (m/z 18) and OH^+ (m/z 17)), ammonia ($NH_3^{+\bullet}$ (m/z 17), nitric oxide (NO^+ (m/z 30)) and carbon dioxide ($CO_2^{+\bullet}$ (m/z 44)). Although Equation 6.1 indicates the formation of N_2, the ion current of corresponding mass fragments $N_2^{+\bullet}$ (m/z 28) and N^+ (m/z 14) only reduces during the combustion reaction. Also *Kim et al.* do not display m/z 28 nor 14, raising questions about what is happening to nitrogen. [141] Nevertheless, nitrogen is often said to be formed during combustion reactions. [119] [103] [141] Nitrogen can be adsorbed by porous structures [35], which are formed during combustion. Nitric oxide NO (m/z 30)(Equation 6.2) can on react with oxygen to form

NO_2 (m/z 46) according to Equation 6.2.[34]. In addition to m/z 17, 18, 30, 44 and 46 additional mass fragments are displayed in Table 6.3 and Figure 6.11, which can be assigned to MOE, residual metal acetylacetonates or ammonium nitrate or derivatives.

$$Zn(C_5H_7O_2)_2 + 2\,NH_4NO_3 + 10\,O_2 \longrightarrow ZnO + 8\,H_2O + NO + N_2 + NH_3 + 10\,CO_2 \tag{6.1}$$

$$2\,NO + O_2 \longrightarrow 2\,NO_2 \tag{6.2}$$

Directly after the combustion the ion current of almost all mass fragments experiences a steep dip, which results afterwards in a little lower value. As the combustion reaction generates a lot of local heat, the measurement probably suffers from this local 'explosion'. Also small fractions of m/z 47, 50, 51, 52, 53, and 54 are released during combustion, but cannot be directly assigned to any of the reagents. Alternative side reactions should be considered.

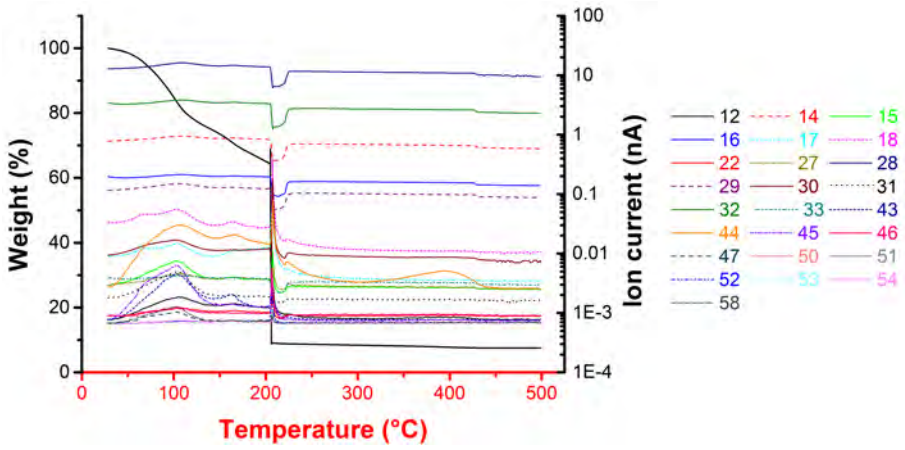

Figure 6.11: TGA (weight %) coupled with MS, ion current (nA) of 1:1 (oxidizer:fuel) 1 at% Al-doped Zn MOE precursor heated at 10 °C/ min in dry air (flow 50 ml/min).

Table 6.3: Mass fragments which exhibit significant changes in the TGA-MS analysis of the 1:1 (oxidizer:fuel) 1 at% Al-doped Zn MOE precursor analyzed in dry air.[216][253][34]

m/z	Assignment	Reagens
12 ↗	$C^{+\bullet}$	$Zn(C_5H_7O_2)_2 \cdot xH_2O$, MOE
14 ↘	N^+	dry air
15 ↘	CH_3^+	$Zn(C_5H_7O_2)_2 \cdot xH_2O$
16 ↘	O^+, O_2^{++}, NH_2^+	dry air
17 ↗	OH^+, $NH_3^{+\bullet}$	$Zn(C_5H_7O_2)_2 \cdot xH_2O$, NH_4NO_3, MOE
18 ↗	$H_2O^{+\bullet}$, NH_4^+	$Zn(C_5H_7O_2)_2 \cdot xH_2O$, NH_4NO_3, MOE
22 ↗	CO_2^{2+}	$Zn(C_5H_7O_2)_2 \cdot xH_2O$
27 ↗	$C_2H_3^+$	MOE
28 ↘	$C_2H_4^{+\bullet}$, $CO^{+\bullet}$, $N_2^{+\bullet}$	MOE, NH_4NO_3, dry air
29 ↘	$C_2H_5^+$	MOE, dry air
30 ↗	NO^+, $CH_2O^{+\bullet}$	NH_4NO_3, MOE
31 ↗	CH_2OH^+	MOE
32 ↘	$O_2^{+\bullet}$	dry air
33 ↘	$CH_3OH_2^+$	MOE
43 ↗	CH_3CO	$Zn(C_5H_7O_2)_2 \cdot xH_2O$, MOE
44 ↗	$CO_2^{+\bullet}$	$Zn(C_5H_7O_2)_2 \cdot xH_2O$, MOE
45 ↗	$^{13}CO_2^{+\bullet}$, $CH_3OCH_2^+$	$Zn(C_5H_7O_2)_2 \cdot xH_2O$, MOE
46 ↗	NO_2^+	NH_4NO_3, MOE
58 ↗	$^+CH_2CH_2OCH_2^\bullet$	MOE

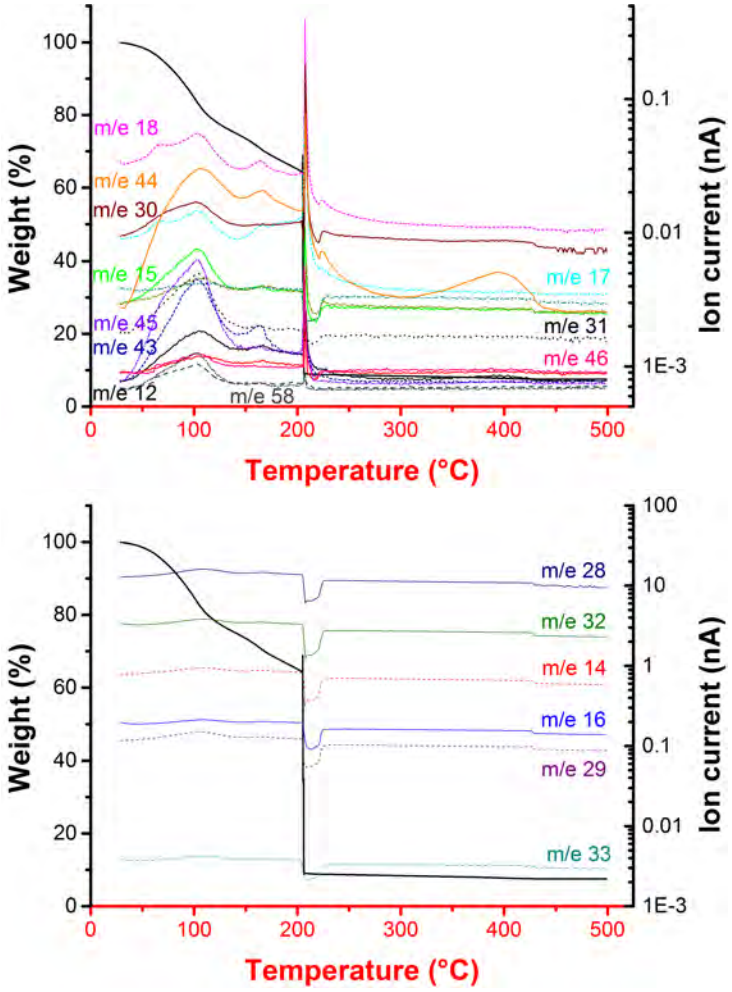

Figure 6.12: TGA (weight %) coupled with MS, ion current (nA) of 1:1 (oxidizer:fuel) 1 at% Al-doped Zn MOE precursor heated at 10 °C/ min in dry air (flow 50 ml/min). The relevant m/z of the solvent are displayed in the top image. Below the m/z are shown which undergo a reduction during the combustion reaction.

To elucidate whether the reaction is oxidative, this TGA-MS analysis is repeated in an inert atmosphere; He. This result is displayed in Figure 6.13. In an inert atmosphere a lower ion current for (almost) all m/z is generally observed. During the inert thermal decomposition MOE is still vaporized before 200 °C. During the inert combustion the same mass fragments are released as during the oxidative TGA-MS analysis, although differences are visible. During the inert analysis, only oxygen is diminished during combustion, while mass fragments 14, 16, 28, 29 and 33 are released and can be assigned according to

Table 6.3. The release of these mass fragments indicates a possible incomplete combustion and possible vaporization of some products. Mass fragment 16 can be assigned to oxygen, but as fragment 32 diminishes, this mass fragment might be assigned to NH_2^+. Mass fragment 14, 28 and 29 can be assigned to the presence of nitrogen. Nevertheless m/z 28 can also be assigned to carbon monoxide. To differentiate which molecule is involved, TGA-FTIR analysis could resolve this struggle, since carbon monoxide is and N_2 isn't infrared active. For m/z 33 no certain assignment can be made. During the oxidative process a decrease of m/z 33 was observed, while during the inert analysis a release was observed during combustion. This means that this fragment is expected to have a connection with the oxygen molecule (dry air TGA-MS), or is related to other species (helium TGA-MS).

After combustion, the ion current of almost all mass fragments experiences again a steep dip, analog to the oxidative TGA-MS analysis in Figure 6.11. This local 'explosion' might indicate a blockage of the capillary between the TGA and the MS.

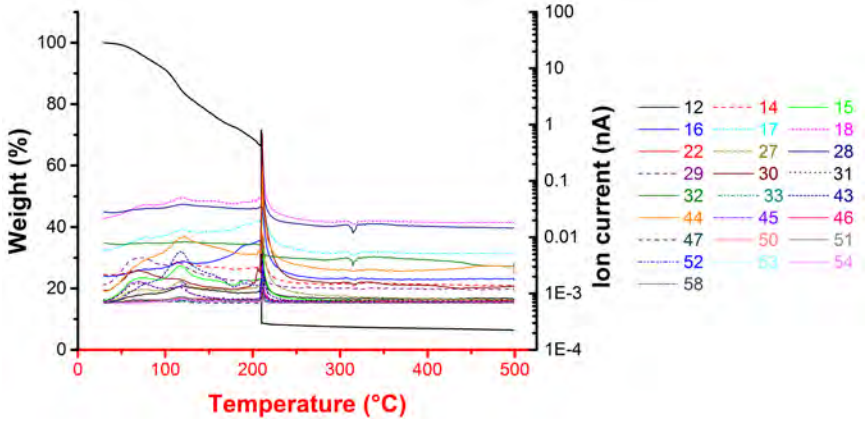

Figure 6.13: TGA (weight %) coupled with MS, ion current (nA) of 1:1 (oxidizer:fuel) 1 at% Al-doped Zn MOE precursor heated at 10 °C/ min in helium (flow 50 ml/min).

The difference in atmosphere does not change much about the thermal decomposition profile. Independent of the used atmosphere, the weight loss starts with removal of the solvent. Afterwards an one-step combustion reaction takes place. Since the same reaction occurs without the presence of oxygen, this reaction is an auto-combustion. The released gases vary according to oxidative or inert measurement. As the deposition of these precursor will take place in atmospheric conditions, the focus will be put on the thermogravimetric analysis in dry air conditions.

An additional TGA-MS analysis was done on a precursor which has been completely dried to remove the solvent. This precursor (1 at% Al-doped Zn 1:1 (oxidizer:fuel) MOE) was analyzed in dry air (flow 50 ml/ min) at 100 ℃/ min up to 500 ℃ as displayed in Figure 6.14 and Figure 6.15. This analysis was done since spin coating with precursors will be done in static air and the thermal analysis will be performed on a dried film.

If the precursor is completely dried the thermogravimetric analysis differs from the original. Figure 6.14 displays a gradual weight loss with small exothermic signals and different residual weights. This might implicate incomplete thermal burnout, although for the dried precursor less weight loss is expected. Figure 6.15 only displays the release of mass fragment m/z 17, 18, 43, 44 and 46 without thermal runaway. Up to 100 ℃ m/z 43 is released, which is assigned to CH_3CO according to Table 6.3. This ion is originative from zinc acetylacetonate (aluminum acetylacetonate) and could suggest vaporization of the metal acetylacetonates. Further on water (m/z 17 and 18), and carbon dioxide (m/z 44) are observed. The origin of these ion currents is linked to the vaporization of acetylacetonates.[282]

The thermal decomposition after 100 ℃ is not really an explosive combustion, but is more spread and differs a bit in relation to the temperature. Nevertheless, the combustion reaction in Equation 6.1 is still plausible. Mass fragments of water (m/z 17 and 18), ammonia (m/z 17), carbon dioxide (m/z 44) and nitrogen oxide (m/z 46) are observed. No nitrogen is observed, analog to previous observations and nitric oxide is converted to nitrogen dioxide according to Equation 6.2.

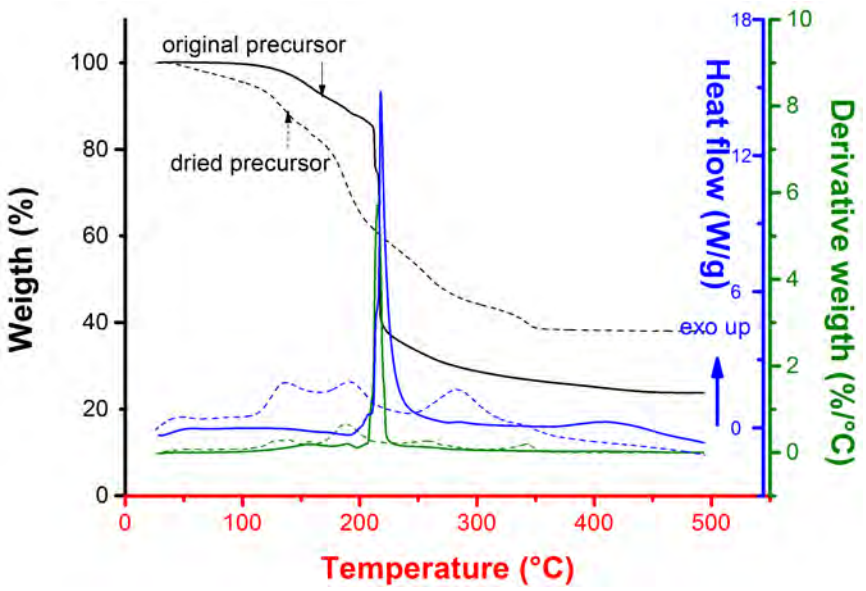

Figure 6.14: TGA (weight %), DTA (derivative weigth %/ °C) and DSC (heat flow W/ g) analysis of a completely dried 1:1 (oxidizer:fuel) 1 at% Al-doped Zn MOE precursor heated at 10 °C/ min in dry air (flow 50 ml/min).

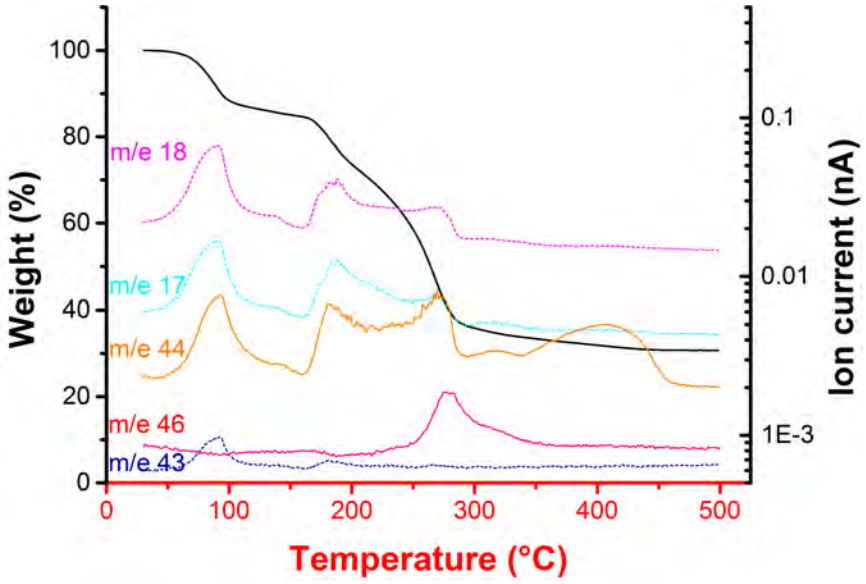

Figure 6.15: TGA (weight %) coupled with MS, ion current (nA) of a completely dried 1:1 (oxidizer:fuel) 1 at% Al-doped Zn MOE precursor heated at 10 °C/ min in dry air (flow 50 ml/min).

This thermogravimetric analysis has given us insights into the thermal decomposition of the developed (auto)combustion precursor. To mimic the behavior of a dried film after spin coating, completely dried precursor was analyzed. The dried precursor did not show the thermal runaway effect but showed similarities in thermal decomposition but at a slower pace. This tranquility could be beneficial for the synthesis of more dense n-type doped ZnO films. The exothermic signal during decomposition is reduced and the effectiveness of synthesizing crystalline n-type doped ZnO films needs to be tested. As in a next step, TCO films will be made out of n-type doped Zn MOE combustion precursors. Of course, the optimized precursor with the 1:1 oxidizer:fuel ratio is chosen as most promising one.

6.9.4 Influence of the molarity on the deposition of Al-doped ZnO films

For the 1 at% Al-doped Zn precursor different molar concentrations were independently prepared in 10 mL of MOE. A 0.1 M, 0.2 M, 0.5 M and 1 M precursor was spin coated (3000 rpm for 30 s 1000 rpm/s) onto chemically cleaned SiO_2 (200 nm)/Si substrates [277] and treated for 5 min on a hotplate at 225 °C in static air. This cycle was repeated until 10 L were deposited. The obtained films were analyzed using SEM analysis.

Recently, *Sanchez-Rodriguez et al.* indicated the difference of exothermic combustion powder synthesis and the thermal decomposition of films. They found no proof for combustion synthesis in films. [236] This makes the synthesis of crystalline n-type doped ZnO films more challenging. Although crystallization as such is an exothermic process, sufficiently high temperature are required. Except for *Hagendorfer et al.*, to my knowledge, nobody was able to deposit Al-doped ZnO at low temperatures. [111].

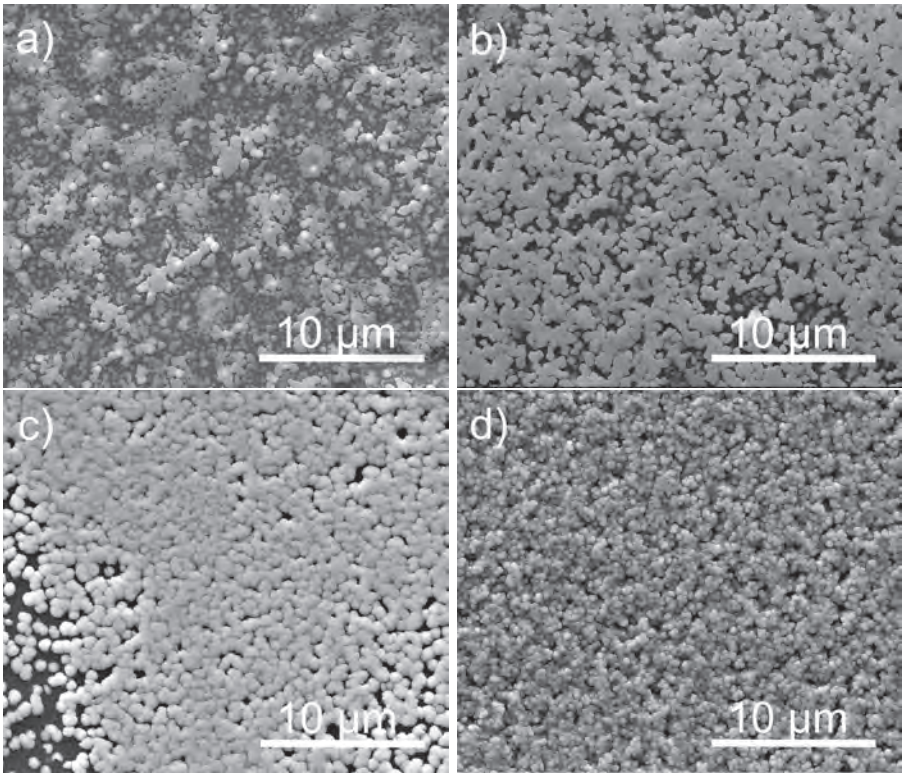

Figure 6.16: SEM images of 10 L of a) 0.1 M, b) 0.2 M, c)0.5 M, and d) 1 M 1 at% Al-doped Zn MOE precursor deposited through spin coating and treated on a hotplate at 225 °C for 5 min.

Figure 6.16 displays the top view SEM images of the 0.1, 0.2, 0.5 and 1 M precursor. The lower the concentration of the precursor, the less uniformly covered substrate. Figure 6.16d shows a completely covered substrate with a porous and rough Al-doped ZnO film if the 1 M precursor solution is used. Although the SEM images indicate a promising morphology with grains, the crystallinity of the doped ZnO films will be studied further on.

6.9.5 Influence of different dopants on the n-type doped ZnO films

In addition to the use of a 1 M 1 at% Al-doped Zn precursor, different 1 M precursors were made. A 0.5 at% Al-doped Zn, an undoped Zn precursor as well as a 0.5 at% and 1 at% In and Ga-doped Zn precursor was deposited through spin coating. The hotplate temperature was also reduced to 200 °C and each layer was treated for 5 min. In total 10 L were deposited, analog to Figure 6.16d. These films were evaluated with XRD and SEM analysis

regarding the crystallinity and the morphology.

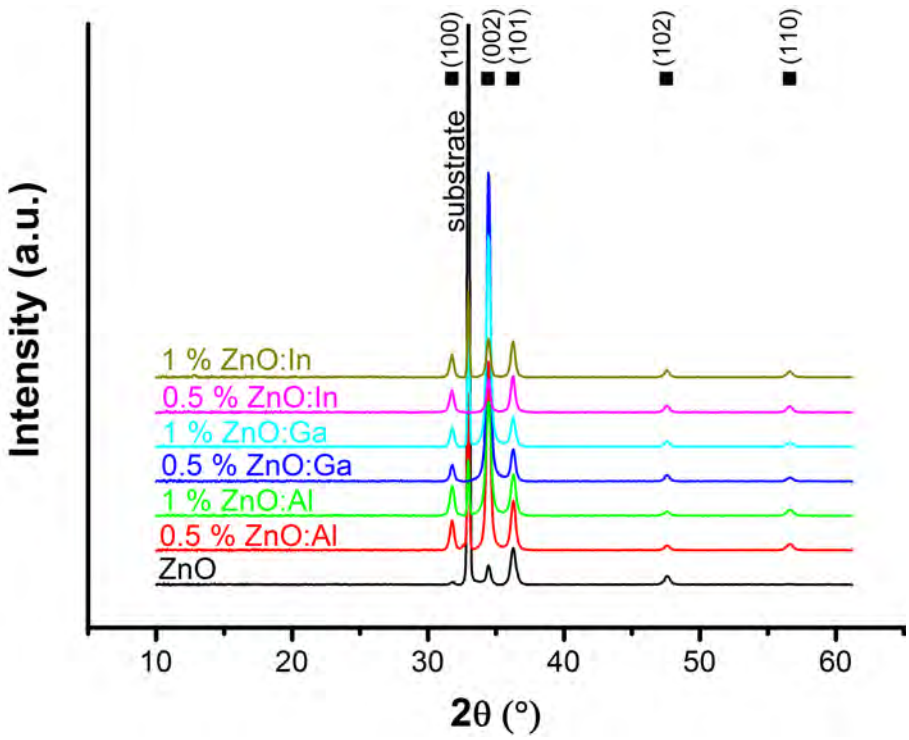

Figure 6.17: X-ray diffraction of 10 L of a 0.5 and 1 at% Al, Ga and In-doped and undoped Zn precursor deposited through spin coating and treated on a hotplate at 200 °C for 5 min. These diffractograms can be indexed with the wurtzite crystal lattice (JCPDS library file 79-0206).

The diffractograms match the wurtzite crystal lattice (JCPDS library file 79-0206) after thermal treatment of only 200 °C. The preferential orientation of the films differs. The fact that doped crystalline materials can be made is due to the high flame temperature that can be developed using acetylacetonates as a fuel. Pure ZnO films have a preferential (101) orientation, while the Al and Ga doped films have a preferential (002) orientation, which decreases with increasing the amount of dopant (0.5 at% to 1 at%). The In doped ZnO films do not have a distinct preferential orientation, since either the (101) or the (002) diffraction peak has a slightly higher intensity.

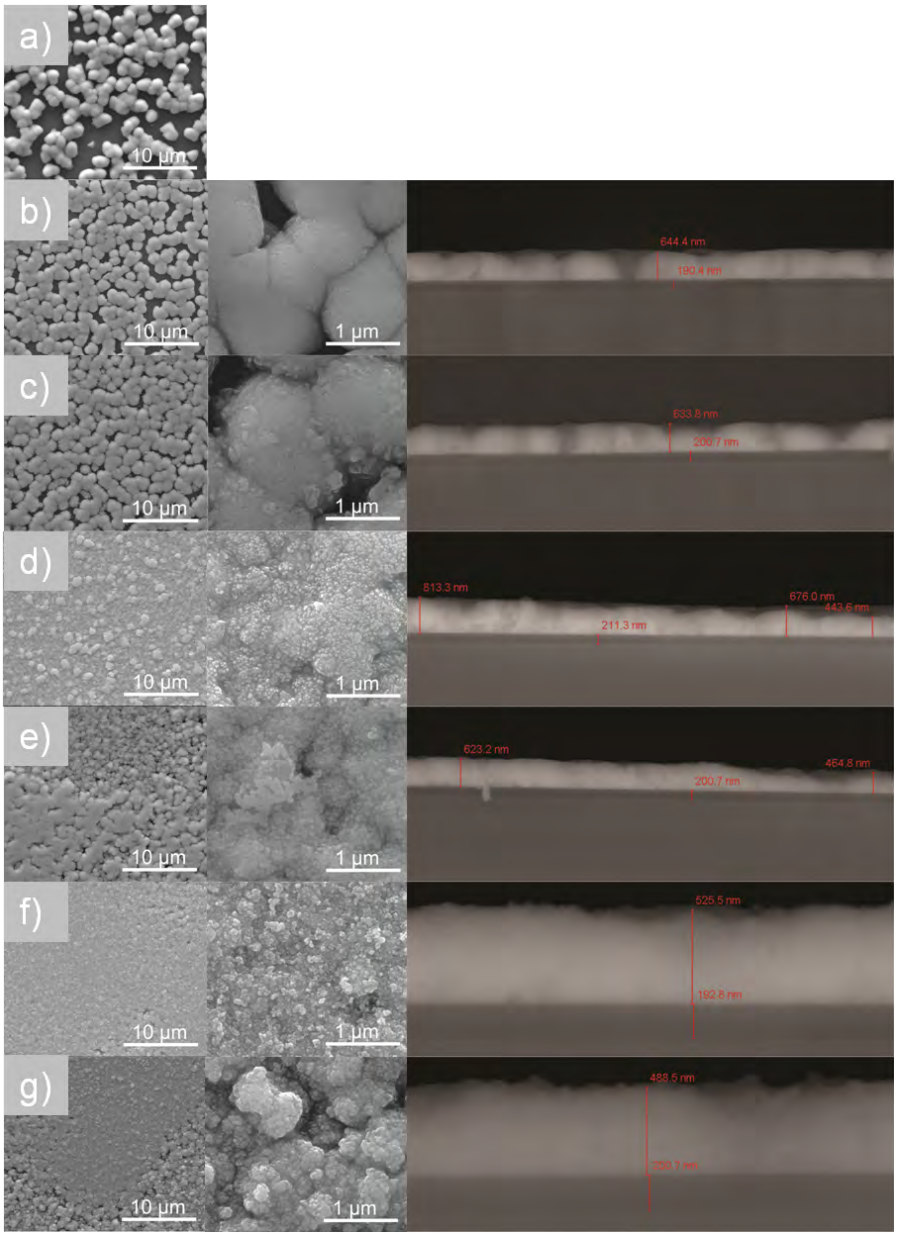

Figure 6.18: SEM of a) ZnO b) 0.5 at% ZnO:Al c)1 at% ZnO:Al d) 0.5 at% ZnO:Ga e) 1 at% ZnO:Ga f) 0.5 at% ZnO:In g)1 at% ZnO:In deposited through spin coating and treated on a hotplate at 200 °C for 5 min.

The morphology of the films varies with dopant. According to our SEM analysis in Figure 6.18 small percentages of dopants can alter the morphology completely. The pure ZnO films and these doped with Al do not completely cover

the SiO_2 (200 nm)/Si substrate (Figure 6.18a,b and c), although doping seems to improve the coverage. The cross-sectional images of the Al-doped ZnO films support this top view by the varying thickness of the layer. The average height of the film is set at approximately 600 nm. On the other hand, the Ga and In-doped ZnO films completely cover the substrate as displayed in Figure 6.18d, e, f, and g. For Ga-doping the film is really rough as seen in the top-view. The cross-sections for 0.5 at% Ga give a thickness of either $\sim$ 800 nm or $\sim$ 700 nm. For the 1 at% Ga-doping the film height is around 600 nm or at some places only $\sim$ 450 nm. For In-doping, the films are again rough but the thickness is in both cases of doping around 500 nm. Although Ga and In-doped Zn precursors are capable of completely covering the substrates, the layers are thick, rough and are not expected to be good TCOs. The difference between substrate coverage and the variation of thickness of the films for various dopants is not understood.

As all the films are rough, the transparency will be lower. Even further, the combustion synthesis creates a lot of voids by rapidly decomposing reagents and vaporizing reaction products. These empty places are barriers through which electrons have to tunnel.[118] Therefore it is not possible to measure any conductivity, since the sheet resistance probably goes out-of-range.

For all dopants crystalline n-type ZnO films are obtained with in the case of Ga and In a completely covered substrate. Small alterations of dopants have a serious impact on the morphology and the preferential orientation. Nevertheless, all films are rough and need further optimization as TCO.

6.9.6 Towards conductive layers

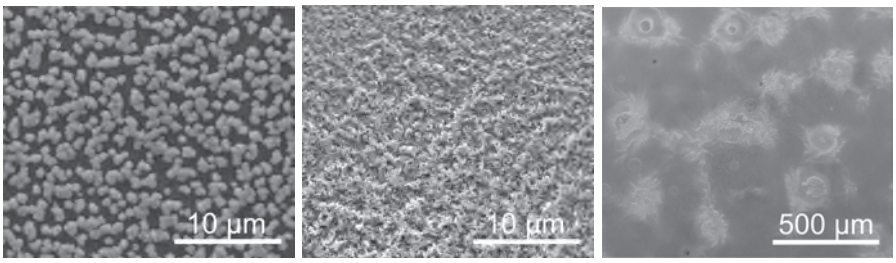

Figure 6.19: SEM images of 4 L of a 1 at% Al-doped Zn (left), In-doped Zn (middle and right) precursor deposited through spin coating (3000 rpm, 30 s and 1000 rpm/s). Each layer was treated on a hotplate at 225 °C in static air for 5 min.

Although the rough morphology has low potential of transforming to state-of-the-art transparent and conductive oxide films, the In-doped film is chosen as

the one with the most potential and compared to Al-doped film. At least this In-doped precursor results in completely covered substrates, with a thickness of approximately 500 nm for 10 spin coated layers. To evaluate the conductivity 4 L of a 1 at% In-doped and Al-doped Zn 1:1 (oxidizer:fuel) freshly prepared precursor were spin coated (3000 rpm for 30 s 1000 rpm/s) onto chemically cleaned SiO_2 (200 nm)/Si substrates and treated for 5 min on a hotplate at 225 ℃ in static air.[277]

The morphology of the obtained films is displayed in Figure 6.19. As observed in Figure 6.18b, c, f, and g (10 L), the use of the In-doped Zn precursor results in a completely covered substrate. The righter image in Figure 6.19 displays a larger area of the film, where clearly can be seen that the films are, despite the full coverage of the substrate, not homogeneous. The image on the left hand side in Figure 6.19 has a lot less material and differs a lot from the 10 L deposited at 200 ℃ (Figure 6.18) or at 225 ℃ (Figure 6.16). There is an impression that the Al-doped ZnO films the voids can be filled up if multi-step deposition are applied (difference between lefter Figure 6.19 and Figure 6.16d). In addition aging of the precursor cannot be excluded, since these precursors were prepared at different times and deposited with a varying time window. If the precursors are stored at room temperature in atmospheric conditions, precipitation occurs after a couple of months.

Further on, the 4 layered films in Figure 6.19 have been subjected to additional anneals, since, as such, no conductivity can be measured. Both the In and Al doped films were in-situ annealed, first in He, and afterwards in a 5% H_2/ 95% He atmosphere, both at 240 ℃ for 1 h with a heating rate of 10 ℃/ s. This in-situ measurement was done while monitoring the crystallinity of the films. For the reductive anneal of 1 at% In-doped ZnO film, the result is displayed in Figure 6.20. The assignment of crystalline ZnO is done based on JCPDS library file 79-0206, with a slightly preferential (101) orientation. During in-situ HT-XRD this crystallinity is consistent and no peak broadening /sharpening or reduction in intensity is observed. Furthermore, the sheet resistance is monitored during in-situ HT-XRD. Here a drop to the kOhm/□ can be observed. If the reductive anneal is terminated and the chamber is exposed to static air, a rapid increase in sheet resistance occurs, indicating an instable conductivity.

For the Al-doped ZnO films, the crystal lattice is matched with the wurtzite phase of JCPDS library file 79-0206 with a preferential (002) orientation. The same in-situ HT-XRD measurements did not change anything about the morphology nor crystallinity. Therefore no sheet resistance could be measured. Although In-doped ZnO films are able to become crystalline and conductive at <250 ℃, the sheet resistance is very instable. This is probably due to this combustion processing, generating a lot of pores and cracks inside the film. In addition, this method is so far not able to make conductive Al-doped ZnO

films. As the morphology of these films is insufficient, a further study of how to optimize film morphology is needed and elucidated in the next paragraph.

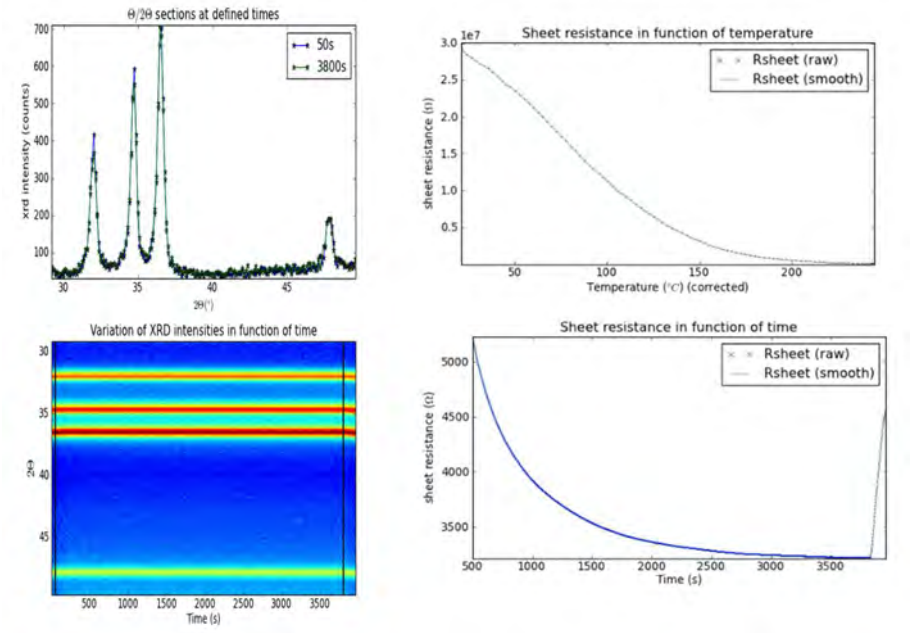

Figure 6.20: Left: In-situ HT-XRD recorded of a 4 L 1 at% In-doped Zn (1:1 oxidizer:fuel) MOE precursor. Each layer was deposited through spin coating (3000 rpm, 30 s, 1000 rpm/s) and treated at 225 °C for 5 min in static air. The in-situ HT-XRD is performed in a 5% H_2/ 95% He atmosphere at 10 °C/s up to 240 °C with an isothermal period of 1 h. Analog to Figure 6.17 this film can be indexed with the wurtzite crystal lattice.
Right: The sheet resistance of this film was monitored during the in-situ HT-XRD analysis in function of temperature and time.

6.9.7 Optimization of the morphology

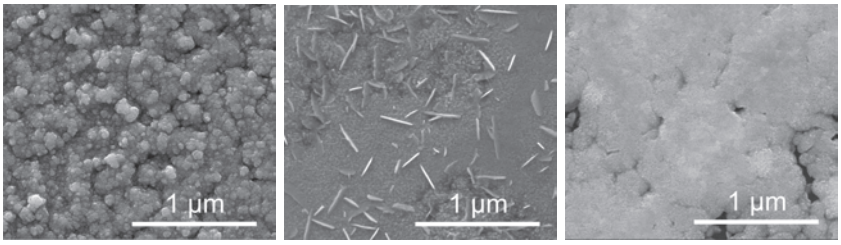

Figure 6.21: Left: SEM image of **10 L** of a **1 M** 1 at% In-doped Zn precursor deposited through spin coating (3000 rpm, 30 s and 1000 rpm/s). Each layer was treated on a hotplate at **200 °C** in static air for 5 min. Middle: SEM image of **25 L** of a **0.1 M** 1 at% In-doped Zn precursor deposited through spin coating (3000 rpm, 30 s and 1000 rpm/s). Each layer was treated on a hotplate at **200 °C** in static air for 5 min. Right: SEM image of **25 L** of a **0.1 M** 1 at% In-doped Zn precursor deposited through spin coating (3000 rpm, 30 s and 1000 rpm/s). Each layer was treated on a hotplate at **250 °C** in static air for 5 min.

As indicated in the previous paragraph, the morphology of combustion processed films is difficult to control. Nevertheless, this is necessary as the obtained conductivity will be dependent on the quality of the film. As the In-doped ZnO films already display a fully covered substrate, they are further investigated. A 1 at% In-doped Zn MOE precursor with the optimized 1:1 oxidizer:fuel ratio was prepared. The total metal concentration was either 1 M or 0.1 M. These precursors were deposited through spin coating (3000 rpm, 30 s, 1000 rpm/s) on chemically cleaned SiO_2 (200 nm)/Si substrates.[277] For the 1 M precursor 10 layers were deposited and treated on a hotplate at 200 °C for 5 minutes in static air. For the 0.1 M precursors 25 layers were deposited and thermally treated in static air at 200 or 250 °C for 5 minutes. Independently a 1 M and a 0.1 M Zn MOE precursor was deposited with the same specifications as mentioned above and treated at 200 °C for 5 minutes in static air.

The SEM images of the In-doped ZnO films, displayed in Figure 6.21, show an influence of molarity and hot plate temperature. When the left figure and middle figure are compared, the hotplate temperature stays the same, but the molarity of the deposited precursor is varied from 1 M to 0.1 M. When changing the molarity, the amount of layers is also altered, since we aim for films of at least 100 nm, which are covering the complete substrate. If the 1 M precursor is deposited, a very granular structure is obtained, as seen in the lefter Figure 6.21. For the 0.1 M precursor (middle Figure 6.21) more dense and a flake-like structure is obtained. This kind of structure is also often found in sputtered doped ZnO films and might be promising As TCO. [27] If the

temperature is increased in the thermal treatment up to 250 °C, the flake-like structure disappears again. The righter Figure 6.21 displays cracks and a lot of pores. From this comparison can be concluded that a lower molarity and a lower temperature improves the molarity of In-doped ZnO films obtained from combustion precursors.

In-doped Zn precursors are easily applicable to cover a complete substrate. For Al-doped Zn or undoped Zn precursors this is rather difficult. The difference between the ZnO films, obtained from the 1 M and 0.1 M Zn precursors is displayed in Figure 6.22. Although the coverage is still not complete for the 25 L of the Zn precursor, it is significantly improved. It looks like the grains are completely connected, but there are still a lot of pores and voids inside the films.

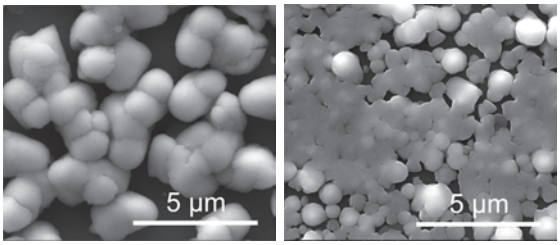

Figure 6.22: Left: SEM image of **10 L** of a **1 M** Zn precursor deposited through spin coating (3000 rpm, 30 s and 1000 rpm/s). Each layer was treated on a hotplate at 200 °C in static air for 5 min.
Right: SEM image of **25 L** of a **0.1 M** Zn precursor deposited through spin coating (3000 rpm, 30 s and 1000 rpm/s). Each layer was treated on a hotplate at 200 °C in static air for 5 min.

The 1 at% ZnO:In film received a rapid thermal processing (RTP) additional anneal in 5% H_2/ 95% He atmosphere at 10 °C/s up to 550 °C and was immediately quenched. This time a sheet resistance of 5 kOhm/□ is obtained. According to cross-sectional SEM images (Figure 6.23) the film is 190 nm thick resulting in a calculated resistivity of 95 10^{-3} Ohm cm. For the films obtained from the 1 M precursors, sheet resistance values are also within the kOhm/□. On the contrary the resistivity of the 0.1 M precursor is more stable after exposure to air. The resason why In-doping (or Ga-doping) leads to an improved morphology is more difficult to find out and, so far, no hypothesis can be made. The key of this improved morphology could improve the Al-doped ZnO films.

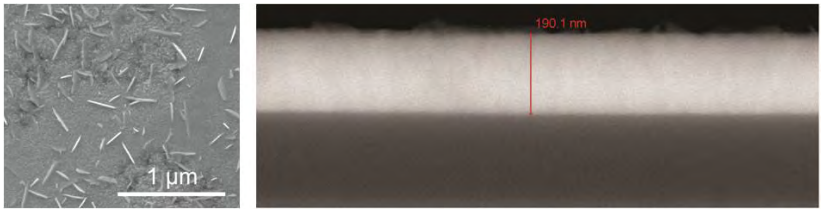

Figure 6.23: SEM and cross-sectional SEM image of **25 L** of a **0.1 M** Zn precursor deposited through spin coating (3000 rpm, 30 s and 1000 rpm/s). Each layer was treated on a hotplate at 200 ℃ in static air for 5 min.

6.9.8 Is low T processing possible for n-type doped ZnO?

A precursor has been developed which is able to deposit n-type doped crystalline ZnO through spin coating at temperature of approximately 200 ℃. These precursors have ideally an optimized oxidizer:fuel ratio of 1:1. In addition the temperature treatment of these precursors has a significant influence on the coverage of substrate by the n-type doped ZnO film. The lower the temperature, the less grains, voids and pores are formed. In addition the molarity of the precursor influences the morphology. A higher molarity will produce more gassing and thereby creating a less denser, more rougher and more porous film. These optimized ZnO:In films are conductive after RTP up to 550 ℃ in a reductive atmosphere. Independently ZnO:In films experienced a reduction in sheet resistance by exposure to UV light, although this result was only measurable for a short period of time. In future research it might be of interest to focus on the combination of RTP processing in a reductive atmosphere with UV (see Appendix 8.9), to be able to achieve conductivity at temperatures of 200 ℃ or even lower. Furthermore, these films still contain In. Although the content is reduced in comparison to ITO, the focus needs to be reoriented to ZnO:Al. First by optimizing the morphology and afterwards the additional anneals.

Some efforts have already been made to deposit fully closed and dense Al-doped ZnO films (Figure 6.24), although the parameters were not completely matched to those used for the preparation ZnO:In films. This 1 % ZnO:Al film was deposited through spin coating (3000 rpm, 30 s and 1000 rpm/s) of 25 consecutive layers of a 0.1 M precursor and treating each layer at 250 ℃ for 1 min. This resulted in a connected network of Al-doped ZnO grains with the presence of some pores. The cross-sectional SEM image shows this closed layer with a small variation of height throughout the film. Further on, investigations can be done by reducing the hot plate temperature to 200 ℃ (or even lower) for 5 min per layer. In addition, an additional in-depth (coupled) thermogravimetric analysis on films is believed to give further insights on how the precursor will be decomposed to form the film.

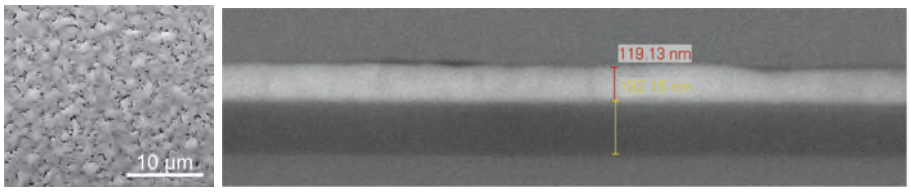

Figure 6.24: SEM and cross-sectional SEM image of **25 L** of a **0.1 M** 1 at% Al-doped Zn precursor deposited through spin coating (3000 rpm, 30 s and 1000 rpm/s). Each layer was treated on a hotplate at **250 °C** in static air for 1 min.

6.10 Conclusion

A molecular precursor in 2-butoxyethanol was able to deposit relatively thick and dense layer with a minimal sheet resistance of only 57 Ohm/ □ is obtained. From these experiments a clear difference between surface effects and the conductivity in the bulk can be distinguished. Nevertheless, this molecular precursor still needs high thermal treatments to obtain good conductive layers. As an alternative a low temperature decomposing precursor in 2-methoxyethanol has been developed with metal acetylacetonates and ammonium nitrate. Insights in the thermal decomposition of combustion precursors and the optimization of the morphology allowed to obtain conductive In-doped ZnO layers at a maximum temperature of only 240 °C. Nevertheless the conductivity decayed easily and requested further improvement in morphology. The applied temperature of the hot plate, the molarity and the use of dopants generates significantly different looking films. Although no conductive Al-doped ZnO films could be obtained, general insights with the study of In-doped ZnO films are obtained. Lower concentration of precursors, lower hot plate treatment and finding out why In-doping improves the substrate coverage, provide a very good starting point for continued research.

7 Aqueous Molecular Precursors

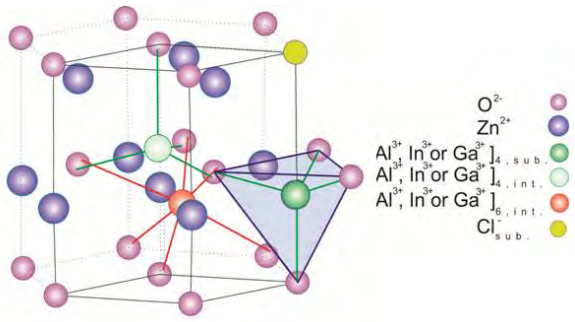

Figure 7.1: In-depth study of n-type doped ZnO conductive films

This chapter elaborates on an in-depth study of n-type doped ZnO films obtained from aqueous sol(ution)-gel precursors. Multiple dopants like Al^{3+}, Ga^{3+}, In^{3+} and Cl^{-} have been evaluated. With these, the effect of the dopant as well as it's percentage on the film's crystal structure, morphology, conductivity and transparency was studied by XRD, SEM, Van der Pauw, FTIR and UV/Vis spectroscopy. After optimization of the dopants in the optimal concentration, TCO films with at least 80 % transparency within the visible range and resistivities within the 10^{-3} Ohm cm range are obtained. Also the pure ZnO films have very good characteristics. Al, which is like Zn, abundantly available and cheap, is described to be the most elegant dopant. The transparency and conductivity of ZnO:Al films is the best performing TCO from this dopant study.

7.1 Introduction

From an ecological point of view aqueous based methods are very appealing, since they meet the current rising environmental restrictions on ecologically harmful substances and processes. The aqueous solution-gel synthesis can be considered healthier, safer and environmentally friendlier through the use of water as a solvent, instead of often teratogenic ether alcohols like 2-methoxyethanol. The high polarity (μ= 1.84 debye) and the dielectric constant (ϵ= 78.5) of water make it rather easy to dissolve ionic compounds. An additional asset is the possibility to use simple and inexpensive synthesis- and deposition equipment as well as the insensitivity to ambient moisture. This field of ACSD has evolved significantly during the last two decades, driven by the innovative research based on ferroelectric thin film materials for applications in different kinds of memory devices, piezoelectric sensors and actuators, pyroelectric detectors of infrared radiation, and integrated high-permittivity (high k) capacitors. During the last decade the interest of other applications like batteries and transparent conductive oxides has risen by the necessity of cheap, environmental friendly processed and functional devices for sustainable chemistry.

The first functional Al-doped ZnO TCO film from aqueous precursors was already made a decade ago by *Mondelaers*. [186] Even though, the framework was already set, the evaluation of the applicability has not been done. Therefore, the aqueous Zn precursor is studied from a different angle with a combination of NMR techniques, to obtain more information regarding the complexation and the ability to use aqueous Zn precursors in a multi-step deposition. The latter is rather difficult and limited by the amphoteric character of ZnO.

Further on, in addition to Al-doped ZnO other potential dopants have been implemented. Although, Al and Zn are abundantly available, non-toxic and cheap, In and Ga are studied as a dopant to verify if they can further improve the conductivity and/or transparency. In addition also Cl-doping is evaluated as n-type dopant. Due to recent publications on Cl-doped ZnO by electrodeposition [226, 227], the exploration of this dopant by aqueous sol(ution)-gel is studied in this chapter.

7.2 Synthesis

7.2.1 Aqueous Citrato Zn Precursor

An aqueous Zn^{2+} precursor was obtained based on recipes previously developed in our lab.[186] A citric acid solution is prepared by dissolving 250 mmol CA in 150 mL milli-Q water. Then, 250 mmol of solid ZnO was added stepwise

while stirring the solution (leading to a 1:1 molar ratio of CA:Zn^{2+}) and en was added drop-wise to this acidic solution (pH 3), raising the pH up to 7. The obtained solution was filtered and diluted to 250 mL with milli-Q water to obtain a clear citrato-Zn precursor. A saturated citrato-Zn precursor was obtained by stirring 50 mL of this precursor over a small amount of ZnO powder for one week: on a regular basis, additional ZnO was added, but only after the previously added portion has been dissolved completely. Once a saturated precursor was obtained, any undissolved ZnO was removed by centrifugation (5 min at 4000 rpc) and filtration.

7.2.2 Aqueous Citrato Al Precursor

For the synthesis of an aqueous Al^{3+} precursor, 20 mmol CA was dissolved in ± 15 mL milli-Q water and 20 mmol of $Al(OH)_3$ was added while stirring, leading to a 1:1 molar ratio of CA:Al^{3+}. This mixture was refluxed overnight at 80 ℃. After subsequent cooling to room temperature, the solution had a pH of 2 and en was added drop-wise to obtain an aqueous citrato-Al precursor at pH 7. Finally, the precursor was filtered and diluted to 50 mL to obtain a clear citrato-Al precursor. Citric acid can also be replaced by glycolic acid (GA) or tartaric acid (TA), in a 1:1 molar ratio of GA:Al^{3+} or TA:Al^{3+} 1:1. The reaction conditions stay the same.

7.2.3 Aqueous Citrato In Precursor

An In^{3+} precursor was obtained by dissolving 25 mmol $In(OH_3)$ in a 40 mL aqueous solution of 2.5 mol L-1 CA at ambient conditions. The solution was refluxed for 1.5 h at 120 ℃. After subsequent cooling to room temperature, the pH of the solution was raised to 8 by drop-wise addition of en. Finally, the precursor was filtered and diluted to 50 mL to obtain a clear aqueous citrato-In precursor.

7.2.4 Aqueous Citrato Ga Precursor

For the Ga^{3+} precursor, $Ga(NO_3)_3 \cdot xH_2O$ was used after determining the water of hydration by ICP-AES. There were approximately 9.13 H_2O molecules bound per $Ga(NO_3)_3$ molecule. 25 mmol was added to 25 mmol CA using 54.46 mL of a 0.459 mol L^{-1} of $Ga(NO_3)_3 \cdot xH_2O$. To obtain an end volume of 50 mL, the solution was partially vaporized on a hot plate at 85 ℃. The pH was raised to 7 with en. In the end, the precursor was filtered and diluted to 50 mL to obtain a clear aqueous citrato-Ga precursor.

7.2.5 n-type doped Zn precursor

For the dopant screening(X-doped with X= Al^{3+},Ga^{3+},In^{3+} and Cl^{-}) Zn^{2+} precursors with a total metal concentration of 0.1 M were prepared by mixing and diluting the saturated citrato-Zn precursor with the citrato-Al, Ga or In precursor or with NH_4Cl in the appropriate ratios. For the 0.1 M precursors a doping series of 0 (ZnO), 1, 2, 3, 4 and 5 (ZnO:Al, Ga, In or Cl atom% Al, Ga, In or Cl) % Al, Ga, In or Cl has been prepared.

7.2.6 Film Deposition

ZnO and X-doped ZnO films were prepared by spin coating a 0.1 M precursor solution (0.1 µm syringe filter is used) onto chemically cleaned SiO_2 (200 nm)/Si substrates or borosilicate glass substrates. After coating (30 s, 3000 rpm, 1000 rpm/s), the as deposited film was treated in succession on two hot plates in static air as follows: 45 s at 300 ℃, followed by 90 s at 450 ℃. To obtain films consisting of 25 layers, this entire cycle was repeated 24 times prior to an annealing step at 500 ℃ for 60 min (preheated tube furnace, 500 mL min-1, dry air (DA)). The films were additionally subjected to a final reductive anneal (RA). After ramping with 10 ℃ s^{-1} up to 450 ℃ the powders were subjected to a reductive anneal in 5 % H_2/95 % Ar during an isothermal period of 10 min (reductive anneal or RA) using an rapid thermal processing (RTP) setup (Annealsys).

Additionally, Zn precursors of 0.5 M and 0.8 M (0.1 µm syringe filter) were deposited by spin coating (30 s, 3000 rpm, 1000 rpm/s) onto chemically cleaned SiO_2 (200 nm)/Si substrates. The films were treated on two hot plates at 300 ℃ (2 min for the 0.5 M and 2 min 30 s for the 0.8 M) and at 450 ℃ (4 min for the 0.5 M and 5 min for the 0.8 M) in static air. For higher concentrated precursors the hot plate treatment is prolonged to make sure that all organics are removed. The obtained 5 layered (0.5 M) or 3 layered (0.8 M) films were submitted to a final annealing step at 500 ℃ for 60 min (preheated tube furnace, 500 mL min^{-1}, dry air) and compared to the 25 layered ZnO film of 0.1 M.

7.3 From Zn-precursor to dense uniform ZnO films

7.3.1 In-depth study of the aqueous citrato Zn-precursor

Through the synthesis of aqueous molecular precursors metal ions like Zn^{2+} will be submitted to different chemical processes as solvatation, hylysisdrolysis and condensation. Zn^{2+} in an aqueous solution is solvatated by 6 water molecules acting as σ -ligands in a true coordination complex as explained in section 1.5.3.

Polydentate molecules or anions and metal ions can be profoundly bound through multiple coordination bonds. The complexed cation becomes practically insensitive for pH variations in a broad range and remains soluble as the monomer, almost completely ruling out hydrolysis and condensation reactions in solution. This substitution of coordinated water molecules by ligand X^{n-} can be represented as follows:

$$[Zn(OH_2)_6]^{2+} + aX^{n-} \rightarrow [ZnX_a(OH_2)_{6-\alpha a}]^{(2-\alpha a)+} + \alpha a H_2O \tag{7.1}$$

With 6(or N) the original amount of aqua ligands, 2+ (or n) the charge of the complexing agent and α the amount of coordinating bonds is. If $\alpha = 1$, 2 or 3 a mono-, bi- or tridentate complex is formed. From equation 7.1 it is clear that the amount of water ligands is significantly reduced by complexation, which slows down the hydrolysis. Also the resulting increased steric hindrance as well as the charge transfer from complexing agent to metal ion diminishes the hydrolysis. [129] [186]

Within the literature most common complexation occurs using ethylene diamine tetraacetate (EDTA)[51] or citric acid (CA)[280]. For a lot of metal ions in addition to CA and EDTA, lactic acid[240], tartaric acid [276, 302], oxalic acid[214], glycolic acid[71], acetylacetone [254], propionic acid and others [202] can also be applied. Further on, ammonia a monodentate ligand as well as ethylene diamine, a bidentate ligand, can shield the metal ion from hydrolysis.[157]

Citric acid, a polybasic acid can occur in different forms in an aqueous solution (pka_1=3.10, pka_2=4.80, and pka_3=6.39) and is believed to create a tridentate complex with Zn^{2+}.[186] This complex ensures the formation of a condensed network in the amorphous gel during solvent evaporation by the increased viscosity. pM'-pH graphs are commonly used to determine the conditions for which no precipitation is expected.[M'] (pM'=-log [M']) has a linear relationship with the concentration of free metal ions [M^{z+}] through the Ringbom's sidereaction coefficient $\alpha_{M(X)}$:

$$[M'] = \alpha_{M(X)}[M^{z+}] \tag{7.2}$$

Whereby X is the amount of complexing ligands and $\alpha_{M(X)}$ is the ratio of the total concentration of all the species of the metal ion to the concentration of the free metal ion.

The whole proces of aqueous citrato-Zn precursor development to ZnO formation has already been studied throughout the past decade. The pH of the aqueous citrato-Zn precursor is preferably increased with either ammonia or ethylene diamine. [186] The use of ethylene diamine as a base increases the viscosity and generates more uniform ZnO films [187] but also demands the use

of a saturated precursor of Zn. [186] This necessity is enforced through the amphoteric character of ZnO [151], which makes multi-layer depostion techniques rather complicated [228].

Mondelaers et al. analyzed the citrato-Zn precursor with en through thermogravimetric analysis in combination with FTIR. [186] There is stated that the disappearance of a vibration at 2140 cm^{-1} would be the result of the formation of complexes with the $R(NH_3)^+(^-OOC)R$, groups, which are present in an unsaturated Zn precursor. [186] In order to understand the chemistry behind the Zn complexation with en an additional NMR study was done. With this study in Figure 8.14 a comparison is made of the gels from an unsaturated 0.99 M Zn precursor (dark blue), a saturated 1.77 M Zn precursor (light blue) and a blanc (black spectrum), containing only citric acid and ethylene diamine. The black spectrum indicates the expected double doublet of CA at 2.18 ppm together with a singlet of en at 2.91 ppm. At higher ppm value the signal of 1,4-dioxane can be found, which is added as an internal standard. The two CH_2 protons, present in CA are diastereotopic (symmetry axis of molecule differs from symmetry axis of two CH_2 protons) and therefore the ^1H NMR spectrum of CA displays an AB quartet. [131] For ethylene diamine, the homotopic protons of CH_2, result in a single signal. Both blue spectra display a peak broadening, an upfield chemical shift (diamagnetic) for en, and a downfield chemical shift (paramagnetic) for CA. This displacement of chemical shift is a strong indication for interaction with a hetero atom by complexation. The chemical shift of CA in the unsaturated Zn precursor (dark blue spectrum) displays in addition to the broad band, sharp signals of the double doublet. This gives an indication that not all the CA nor en is bound, but that an equilibrium is established. With increasing Zn concentration the chemical shift of en goes even further upfield and only one singlet is present, which points out a very fast exchange between the free and the bound en. This chemical shift could be calculated using the fraction of free and bound en and their chemical shift according to Equation 7.3

$$\delta_{fastexchange}(ppm) = x_{NB}\delta_{NB} + x_B\delta_B \tag{7.3}$$

with x_{NB} and x_B the fraction of free and bound en and δ the chemical shift. For CA two forms are clearly present as indicated by the broad band and the sharp signals. With increasing Zn content this signal broadens and is even further displaced. According to these results, there is CA, which is strongly bound, but also CA that rapidly exchanges between being involved in a bond or either acting free in solution.

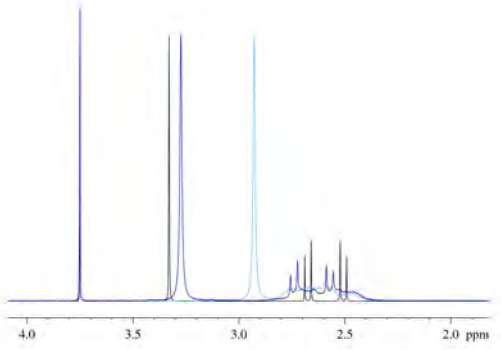

Figure 7.2: ^{1}H NMR of unsaturated 0.99 M Zn precursor (dark blue), saturated 1.77 M Zn precursor (light blue) and reference spectrum of citric acid and ethylene diamine (black) gels dissolved in D_2O.

Figure 7.3 displays the 2D NOESY spectra of both unsaturated (a) and saturated (b) Zn precursors. For both samples the presence of negative NOEs are visible for the different CA resonances, even between the sharp and broad signals, indicating an exchange between both free and bound forms. Figure 7.3a does not display negative NOEs between en and CA, while these are present in Figure 7.3b. This leads to an indication that in the saturated Zn precursor, en is for a longer time part of the complex and if en and CA are in each others neighborhood, they generate a cross peak in the 2D NOESY.

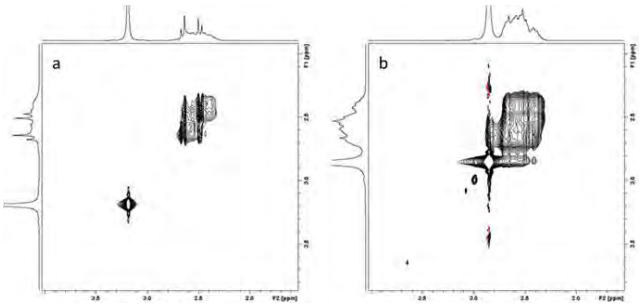

Figure 7.3: 2D NOESY of a) unsaturated 0.99 M Zn precursor (left) and b) saturated 1.77 M Zn precursor (right) gels dissolved in D_2O.

Additional, DOSY spectra were recorded to provide some information about the complexes. 1,4-dioxane was added as an internal standard to exclude effects which cannot be correlated to the complexation. Viscosity, presence of large complexes... all limit the movement and modify the diffusion coefficients. 1,4-dioxane is a rather small molecule, which is soluble in water and from which no interaction is expected with the Zn complexes. Table 7.1 and Table 7.2 gives an overview of the uncorrected and corrected values of the diffusion coefficient

in $\mu m^2/s$. For the correction values, 1,4-dioxane (an internal standard) was assigned to the diffusion coefficient in the reference solution.

Table 7.1: Uncorrected diffusion coefficients for 1,4-dioxane (DO), ethylene diamine (en) and citric acid (CA) in $\mu m^2/s$.

	Reference	Zn_{unsat}	Zn_{sat}
DO	571.51	855.93	851.11
en	355.21	389.22	295.60
CA	263.14	280.10	226.39

Table 7.2: Corrected diffusion coefficients for 1,4-dioxane (DO), ethylene diamine (en) and citric acid (CA) in $\mu m^2/s$ taking into account the diffusion coefficient of DO in the reference sample.

	Reference	Zn_{unsat}	Zn_{sat}
DO	571.51	571.51	571.51
en	355.21	259.88	198.49
CA	263.14	187.02	152.02

In Table 7.2 is observed that both the diffusion coefficient of en and CA diminish with increasing Zn concentration. This gives an indication of the fast-exchange of en and CA between acting as a complexant or being free in solution. This is an additional confirmation of the observation by the ^1H NMR in Figure 7.2. As for the chemical shift, the diffusion coefficient is an average of the bound (B) and free (NB) fraction (x), according to Equation 7.4.

$$D_{fastexchange}(\mu m^2/s) = x_{NB}D_{NB} + x_B D_B \tag{7.4}$$

According to Figure 7.2, two diffusion coefficient would be expected for CA, while only one is measured. This discrepancy might be due to either a very small difference in diffusion coefficient, which can't be measured, or by the difference in time scale. This might induce a transition from fast to slow exchange, with the broad signal in the area of the fast exchange.

From these NMR measurements, several conclusions can be made. Both CA and en form a complex with Zn. In the saturated solution negative NOEs are visible between en and CA, which both stay in each other's neighborhood for a longer period and form a complex together. The unsaturated precursor does not contain interactions between en and CA. The fraction of bound en and CA is also larger in the saturated Zn precursor as indicated by the difference in chemical shifts and diffusion coefficients. In the end, by studying the aqueous

citrato-Zn precursor with en, it seems to be possible to get around the amphoteric properties of ZnO. Saturation of the precursor is necessary to be certain that all complexing agents are bound. In that manner a multi-step deposition is possible, since the previous deposited layers will not be dissolved. In case of doping this means that either the precursors need to be prepared separately or the precursor can be saturated with a powder of the same composition as the requested film. This effect needs to be taken into consideration during the development of other aqueous precursor of Zn.

7.3.2 Morphology and Crystallinity

By the NMR study profound insights in the chemistry of the aqueous citrato-Zn precursor are gained. The next step is to make functional films based on (only) the saturated Zn precursor. To obtain the functional oxide from the amorphous gel a thermal treatment is needed to remove the organics. Once thermally treated, a crystalline wurtzite film is obtained. A comparison is made between films, spin coated in a multi-step manner using 0.1 M, 0.5 M and 0.8 M precursors, through SEM and XRD analysis (Figure 7.4). The amount of layers diminishes with increasing molarity to obtain an equally thick layer for all molarities. All X-ray diffractograms match with the hexagonal wurtzite crystal phase (JCPDS library file 36-1451) with a preferential c-axis (002) orientation. Relatively to the (100) and (101) reflections, the intensity of the (002) reflection drops significantly with increasing concentration. In addition, the SEM images show a more porous ZnO structure for higher precursor concentrations. The use of 0.1 M precursor solutions leads to dense films. Although the organic content, that needs to be thermo-oxidatively decomposed into gases, is equal, the deviating surface-to-volume ratio favors the lower molarity. Moreover, as only a thin layer is deposited, columnar growth is expected to be induced by subsequent depositions. Further on, is this multi-layer approach known to improve microstructural characteristics such as the density and an increased crystallite size of sol-gel derived thin films. [242] The resulting columnar growth (002 preferential orientation) is also described as beneficial for the conductivity properties. [193] [67] For all further deposition the preference will go to the 0.1 M (doped) Zn precursors.

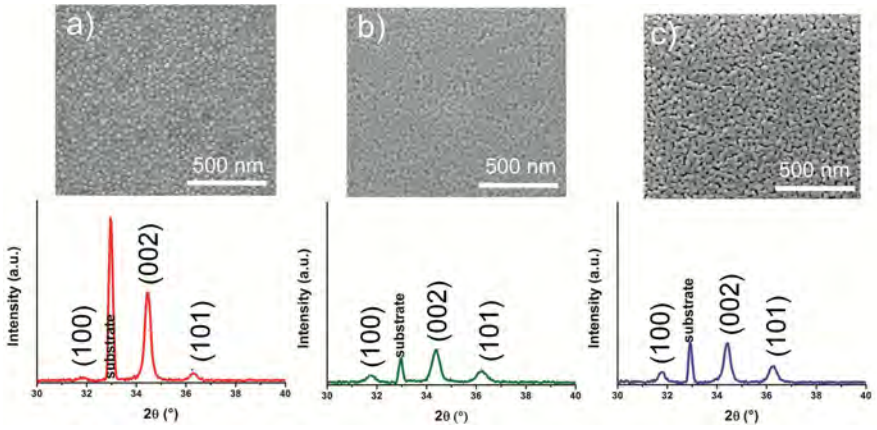

Figure 7.4: Secondary electron microscopy images and X-ray diffractiongrams of ZnO films obtained from precursors with different concentrations a) 0.1 M, b) 0.5 M and c) 0.8 M after DA anneal. All spin coated layers have a thickness of approximately 70 nm. All X-ray diffractograms can be indexed with the wurtzite crystal phase (JCPDS library file 36-1451) with a preferential (002) orientation.

7.4 Evaluation of n-type dopants in crystalline ZnO obtained from aqueous sol(ution)-gel precursors

Within the evaluation of ZnO, *Minami et al.* screened different group 13 dopings through a study of rf magnetron sputtering.[181] Here it is concluded that Al-doping generates the lowest conductivity for sputtered n-type doped ZnO films. Ideally zinc should be substituted inside the wurtzite lattice when doped with group 13 to obtain improved conductivity. Indium is in most cases doped by making binary compounds of In_2O_3-ZnO (IZO), although extrinsic doping of In in ZnO is also applied both in an amorphous or crystalline structure. To downsize the use of indium only small percentages in crystalline materials are of interest. Alternatively to the trivalent doping, group 17 elements have been incorporated, assumed to replace of oxygen inside the lattice. Cl has been incorporated inside ZnO through electro-deposition or using metal-organic chemical vapor deposition. [48, 227, 265] To our knowledge no evaluation has been done for identical solution processed n-type doped ZnO, although independently different solution processed n-type doped ZnO films have been made but more frequently in organic solvents. Here the use of water-based methods is preferred, as they are environmentally friendly. Often, this is accompanied by low cost and easy to handle starting products in combination with cheap, user-friendly equipment. This is certainly the case for the development and

evaluation of aqueous Zn^{2+}, Al^{3+}, Ga^{3+} and In^{3+} precursors. With a systematic aqueous approach towards dopant evaluation inside ZnO a well reasoned dopant can be selected.

7.4.1 Morphology and Crystallinity

The X-ray diffractograms for all (un)doped ZnO films are shown in Figure 7.5, Figure 7.6, Figure 7.7 and Figure 7.8. Although the (100) and (101) reflections are almost invisible, these peaks, together with the most prominent (002) diffraction, are ascribed to the wurtzite structure of ZnO (JCPDS library file 36-1451). Since the intensity of the peaks resulting from the (102) and (110) planes are negligible, the data shown is limited from 30 to 40° 2θ (°). As indicated, all films have a dominant (002) diffraction peak, indicating the preferred grain growth along the (002) direction. Also, the angular peak position of the (002) planes (34.46° 2θ (°)) are very close to that of the powder sample (34.43° 2θ (°)) indicating that the film is almost stress-free. [229] From time-to-time a substrate peak from Si(002) can be seen in the diffraction diffractogram at 33° 2θ. In the end, the pure ZnO, the 1 and 5 % of In-doping films before RA show additional diffraction peaks around 33° 2θ (Figure 7.7), sometimes only barely above the noise level. After RA only substrate peaks and the (002) diffraction peak of ZnO remain present (Figure 7.7).

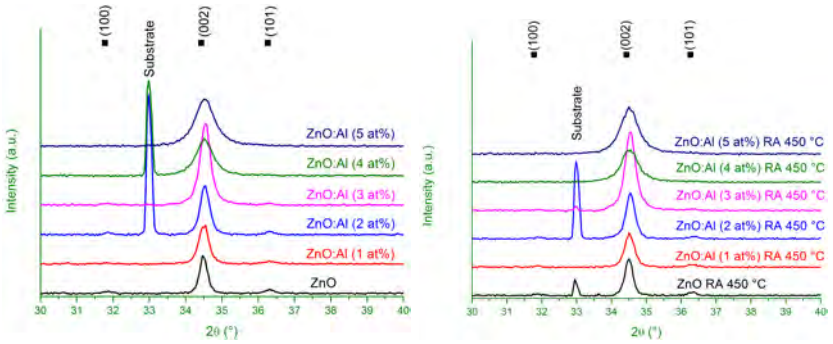

Figure 7.5: X-ray diffractograms of Al-doped ZnO films before (left) and after (right) RA which all can be indexed with the wurtzite crystal lattice (JCPDS library file 36-1451).

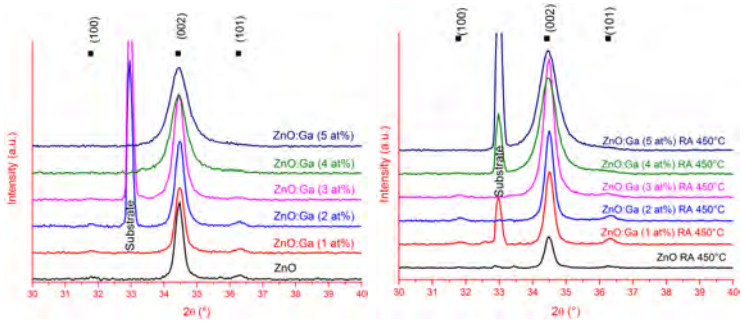

Figure 7.6: X-ray diffractograms of Ga-doped ZnO films before (left) and after (right) RA which all can be indexed with the wurtzite crystal lattice (JCPDS library file 36-1451).

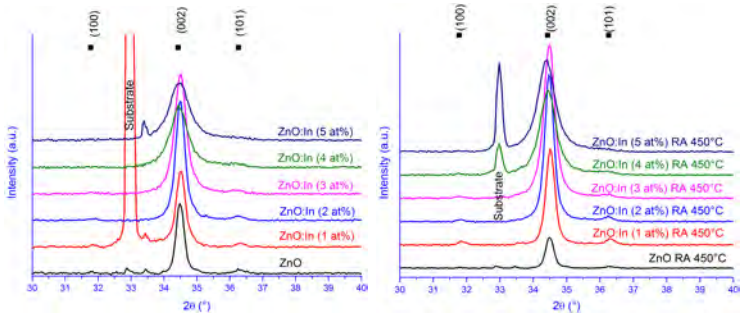

Figure 7.7: X-ray diffractograms of In-doped ZnO films before (left) and after (right) RA which can be indexed with the wurtzite crystal lattice (JCPDS library file 36-1451). For the 5 at% In-doped ZnO before RA an In rich minor phase is present.

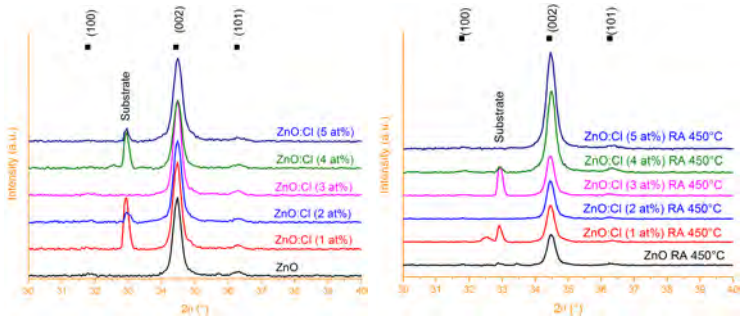

Figure 7.8: X-ray diffractograms of Cl-doped ZnO films before (left) and after (right) RA which all can be indexed with the wurtzite crystal lattice (JCPDS library file 36-1451).

The XRD results can be used to determine the grain size as displayed in Ta-

ble 7.3. This is done by inserting the Bragg angle θ and the full width at half maximum β (in rad) into the Scherrer equation:

$$D = \frac{k\lambda}{\beta \cos\theta} \tag{7.5}$$

where D is the diameter (in nm) of the crystallites forming the film. [289] Constant k is 0.9 for spherical grains and λ, the wavelength of CuK_{α} line, is 1.5406 Å. To have a valid interpretation of the calculated values, the limitations of this method have to be taken into consideration, since the effects of peak broadening due to e.g. film heterogeneities, grain boundaries and micro-stress are not taken into account. As these effects are more evident in the pre-annealed films, their calculated values are less reliable and can be smaller than the actual grain sizes. Nevertheless this is not straightforward, since the obtained grain sizes account for the cross-sectional grains and these display columnar growth for undoped ZnO and small percentages of dopants. This is a pitfall, since the applied constant is stated for spherical shapes and XRD analysis is performed perpendicular on the film surface. To determine the crystallite size, the EVA software has been applied in the full peak model (FPM) model with boundaries between 33.48 and 35.78° 2θ, including only the (002) signal. For some calculated crystallite sizes, the outcome was not reliable, as indicated by a R/R0 value strongly deviating from 1. These values are assigned with a question mark in Table 7.3.

Before and after reductive anneal, the grain sizes of Ga-, Al- and In-doped films generally decreases with increasing doping concentration. This effect is clearly visible by the peak broadening of the 002 orientation (Figure 7.5). By the introduction of dopants the number of nucleation centers increases, leading to smaller grains with increasing dopant concentration. [47, 110] Nevertheless, for Cl-doping this is not the case. This already indicates that Cl incorporation differs from the cation incorporation and questions the Cl-doping.

Introduction of extrinsic dopants is expected to have an influence on the lattice size, since the ionic radius of all dopants differs. The ionic radii of Ga (0.47 Å) or Al (0.39 Å) are smaller than the ionic radius of Zn (0.6 Å), while that of In (0.62 Å) is only slightly larger than that of Zn (0.6 Å). [246] In case the dopants solely replace Zn for Ga and Al incorporation, the crystallite lattice would shrink, while for In a lattice expansion is expected. As half of tetrahedral holes and all octahedral holes are empty, dopants could locate in these spaces, nullifying the expected lattice shrinkage. XRD results of many doped ZnO powders and films report a shift of diffraction peaks due to lattice shrinkage or enlargement. [195, 208, 298] To adequately verify this effect here an internal standard needs to be present, indicating displacement of diffraction signals. Since the signal of the substrate is sometimes perceived, other signals can be benchmarked and controlled for a shift to higher or lower 2θ value. Nevertheless no shift of

diffraction peaks can be clearly observed. For ZnO:In a sole expansion would be expected in comparison to ZnO, inducing a shift to higher 2θ values. This might be an indication that In incorporation is not that easy and possible secondary phases are formed, although they cannot be found within the detection limits of the XRD apparatus. The additional small peaks for (In-doped) ZnO in the X-ray diffractogram before reductive anneal in Figure 7.7, as discussed above, cannot be clearly assigned.

For ZnO:Cl films no distinct differences are visible in Figure 7.8. Even though oxygen (1.40 Å) and chlorine (1.81 Å) differ in ionic radii, no peak shifts can be clearly resolved and the grain sizes remains around 35 nm.

Table 7.3: Grain sizes (nm) calibrated using FPM on the 002 preferential oriented signal before (top) and after (bottom) RA.

Grain size	ZnO	1 at%	2 at%	3 at%	4 at%	5 at%
ZnO:Al	37	25	31	26	13	13
ZnO:Ga	37	?	28	24	16	13
ZnO:In	37	33	30	21	24	14
ZnO:Cl	37	34	35	37	?	?

Grain size	ZnO	1 at%	2 at%	3 at%	4 at%	5 at%
ZnO:Al	37	29	29	25	12	14
ZnO:Ga	37	32	32	18	14	12
ZnO:In	37	29	29	20	?	14
ZnO:Cl	37	35	36	42	33	29

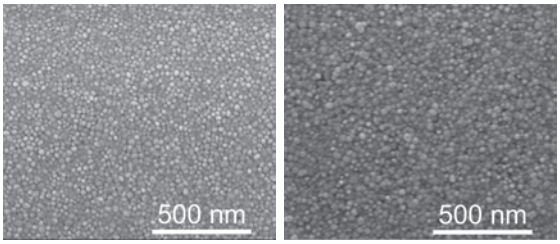

Figure 7.9: SEM images before (left) and after RA (right) of a ZnO film.

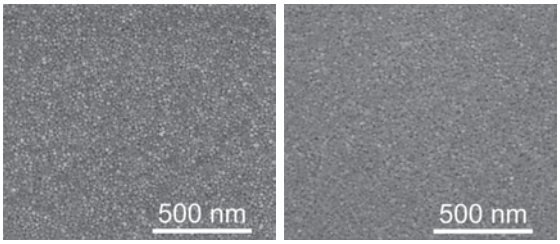

Figure 7.10: SEM images before (left) and after RA (right) of a 2 % ZnO:Al film.

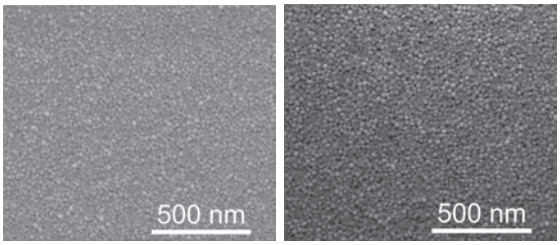

Figure 7.11: SEM images before (left) and after RA (right) of a 2 % ZnO:Ga film.

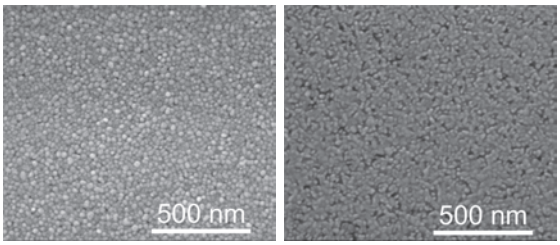

Figure 7.12: SEM images before (left) and after RA (right) of a 1 % ZnO:In film.

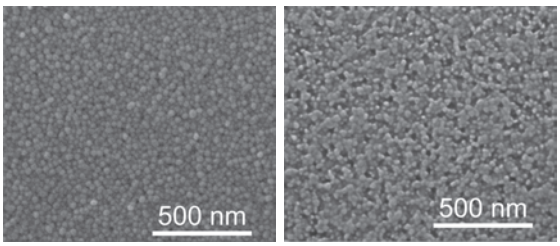

Figure 7.13: SEM images before (left) and after RA (right) of a 4 % ZnO:Cl film.

While XRD analyzes the cross-sectional crystalline areas, SEM images confirm the reduced grain size by incorporation of Al, Ga and In (Figure 7.9, Figure 7.10, Figure 7.11, Figure 7.12, and Figure 7.13) in top view. Only the best

conductive samples within their doping series are displayed as SEM images and in-depth discussed. Although the top view through SEM do not show any real conclusive morphology for the films, there is an indication that after RA more pores are displayed, certainly in case of In-doping. Also for Cl this seems to be the case. Cl could be hypothized to bond with hydrogen during the reductive anneal, leaving no Cl present in the ZnO film by the formation of HCl and resulting in a more porous film (Figure 7.13). For pure ZnO after RA the layer is still dense and the grain size stays approximately the same (Figure 7.9).

This morphology is seriously influenced by the temperature during the RA. A too high temperature or a high temperature for a too long time can lead to vaporization of the film. This effect is probably caused by the formation of water from hydrogen, coming from the reductive anneal, and oxygen present in the (doped) ZnO film. Metallic Zn will be left behind and can easily vaporize at elevated temperatures.[21] In vaporizes more easy [124], while Ga and Al seem to be able to slow down the formation of metallic zinc. The vaporization of the 1 at% Ga-doped ZnO is visualized in Figure 7.14. Here can be hypothized that for In-doped ZnO as well as Cl-doped ZnO the formation of metallic Zn occurs at lower temperature. If In and Cl-doped ZnO films had a reductive treatment at 500 °C for 10 min, the complete layer is vaporized.

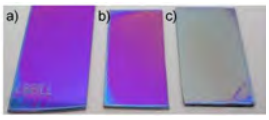

Figure 7.14: 2% Ga-doped ZnO film heated with 10 °C/s up to a) 450 °C for 10 min, b) 500 °C for 10 min and and c) 500 °C for 20 min in a 5% H_2/ 95% Ar atmosphere.

7.4.2 Conductivity

For all the (un)doped ZnO films, the sheet resistance was measured (Table 7.4) and the calculated resistivity is displayed in Figure 7.15. For pure ZnO the obtained sheet resistance is relatively low. This can be ascribed to the existence of Zn interstitials[258] and the presence of H as shallow donor[278]. Most often, there is a general agreement in literature on the ability of H as a shallow donor, although there is still a lot of controversy ongoing about Zn interstitials. [126] Oxygen vacancies are believed to be deep levels and are not expected to contribute to improved conductivity.[5] Nevertheless, as the role of oxygen is not completely resolved in literature, this will be discussed further on in Chapter 8 (8.5.2). For In and Cl doping the resistivity of ZnO cannot be improved. Within their series 1 at% In-doped ZnO results in a film with a sheet resistance of 872 Ohm/ □, and is the lowest value (excluding pure ZnO). With Cl-doping, the 4 at% ZnO:Cl results in the lowest obtained sheet resistance with Cl of 774 Ohm/

□. For Ga-doped ZnO, a lower sheet resistance of 591 Ohm/ □ is obtained, which is matched to 2 at% of Ga. For ZnO:Al 2 % the lowest sheet resistance of 263 Ohm/ □ is obtained, corresponding to a resistivity of 1.77 10^{-3} Ohm cm.

Table 7.4: Sheet resistance of X-doped ZnO films measured by VdP.

Dopant \ At% Al	ZnO	1 at%	2 at%	3 at%	4 at%	5 at%
ZnO:Al	676	278	263	404	1222	3180
ZnO:Ga	676	779	591	1700	35200	179000
ZnO:In	676	872	3060	2750	7750	11500
ZnO:Cl	676	913	933	780	774	1260

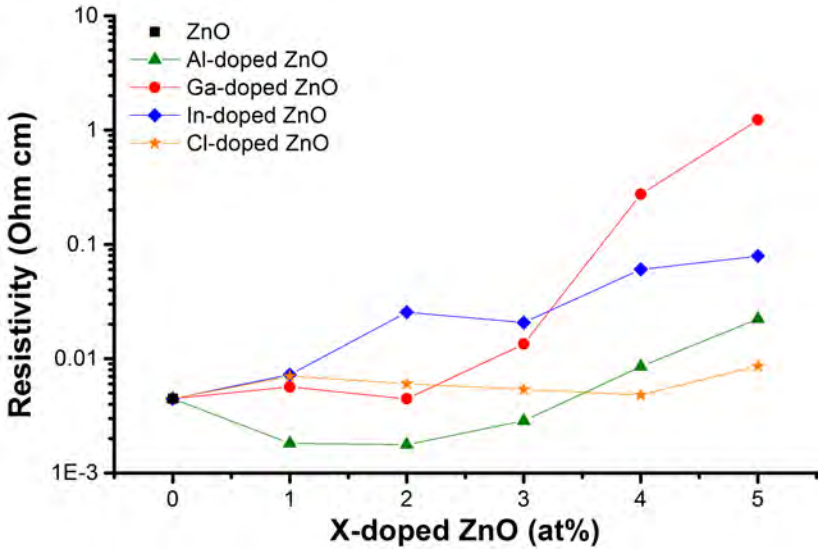

Figure 7.15: Resistivity of pure ZnO (black) and ZnO:Al (green triangle), ZnO:Ga (red circle) and ZnO:Cl (orange stars) in correlation to the doping percentages.

Interesting to note is that there is a link between the sheet resistance in Tabel 7.4 and the grain size studied with XRD in Table 7.3. For the Al, Ga and In-doped ZnO films, those films containing the largest grains, result in the lowest sheet resistance. This indicates the importance of grain boundary scattering.

For further investigations, ZnO was used as a reference and from the other samples the best conductive film of its series was further analyzed: 2 at%

ZnO:Al, 2 at% ZnO:Ga, 1 at% ZnO:In, and 4 at% ZnO:Cl films.

Indirectly Van der Pauw measurements indicate relatively low resistivity values. The inverse relationship to the conductivity, which is a product of the concentration of charge carriers, the mobility and the charge, suggests a more in-depth investigation of the best performing (doped) ZnO films. In addition to commonly applied hall bar measurements, GATR-FTIR analysis can be used to verify the presence of charge carriers.[37, 145] [112] Therefore the ZnO, 2 at% ZnO:Al, 2 at% ZnO:Ga, 1 at% ZnO:In, and 4 at% ZnO:Cl films were analyzed by GATR-FTIR in Figure 7.16. Surface plasmon absorption is observed in the IR region (4000-1500 cm^{-1}) and points out the presence of charge carriers. As the wavelength is longer than the plasma wavelength, the plasma becomes reflective. [145] [37] At plasma resonance, an absorption peak is seen in the GATR-FTIR spectrum. The place of the absorption peak/band depends on size and shape of the grains/crystallites but is situated between 4000-1500 cm^{-1}. When particles are densely packed, they couple electronically to each other. In our case grains are packed close to each other which lead to a broadening of the longitudinal plasma resonance in the optical spectrum. Figure 7.16 displays an absorption band between 3500-1500 cm^{-1} for 2 at% ZnO:Al and ZnO:Ga. Also for 1 at% ZnO:In film an absorption is visible. For Cl doping there is no indication in the GATR overview of an increased amount of charge carriers as this spectrum almost completely coincides with pure ZnO, where no absorption (due to surface plasmon absorption) is visible. The intensity of the absorption cannot be objectively interpreted as the intensity of the background varies.

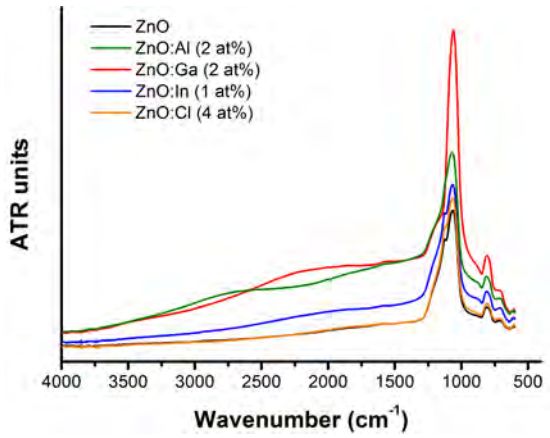

Figure 7.16: GATR-FTIR of ZnO, 2 % ZnO:Al (green), 2 % ZnO:Ga (red), 1 % ZnO:In (blue), and 4 % ZnO :Cl (orange) on top of SiO_2 (200 nm)/Si substrates.

Besides the presence of charge carriers, GATR is used to verify the absence of organics, generating n-type ZnO films. The background, as discussed above, is our substrate. Absorption peaks of the SiO_2 (200 nm)/Si substrate are visible at 1240 cm^{-1} and at 1065 cm^{-1} for the longitudinal and the transverse optic vibration, respectively.[122] In addition, there is a small absorption around 750 cm^{-1}, which cannot be assigned. Based on these GATR-FTIR results, it is hard to prove the presence of Zn-O(-M) vibrations (M= Al, Ga or In) (visible below 600 cm^{-1} and measurement range: 4000-600 cm^{-1}), but the presence of wurtzite ZnO is shown by XRD analyses in Figure 7.5, 7.6, 7.7 and 7.8.

7.4.3 Transparency

As stated before, high transmission in the visible region is desired for TCOs. Therefore the optical transmission of some (un)doped ZnO films deposited on borosilicate glass substrates is evaluated in Figure 7.17. ZnO was evaluated as a reference and in addition each best conductive doped ZnO film within their series was submitted to UV-VIS measurements. The blank borosilicate substrate was subtracted from the measurements. For all doped ZnO samples the average transmission is above 80 % within the visible region, while for ZnO the transparency is relatively lower. The Al-doped ZnO has the highest average transmission. Light with energy above the band gap is absorbed in band transitions. This band gap induces an abrupt drop in transmission and increase in absorption at shorter wavelengths (<350 nm or 3.5 eV), which shifts to shorter wavelengths with increasing carrier concentration. Al and Ga-doped ZnO films in Figure 7.17 display a blue shift or Burnstein-Moss shift, due to the filling of the states near the bottom of the conduction band.[39, 190] For the In-doped sample a minimalistic displacement to the short-wavelength spectral range can be observed. Cl-doping seems to be indifferent to a blue-shift, although the transparency increases compared to pure ZnO. Nevertheless, as the layer of ZnO:Cl 4 % (62.1 nm) is thinner than pure ZnO (73.0 nm), the improved transparency can therefore be assigned to the reduced thickness. For other dopants this is not the case, as all doped layers are approximately 70 nm thick. Although the sheet resistance of ZnO:In 1 % is not lower than pure ZnO, the transparency is significantly improved. Both sheet resistance and transparency need to be taken into consideration when applying the films as transparent conductive oxide.

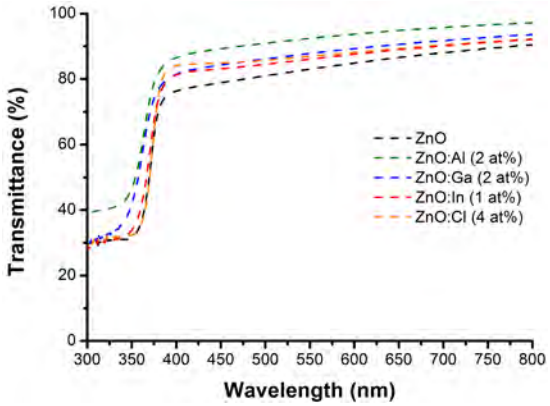

Figure 7.17: UV-Vis spectra of ZnO, 2 % ZnO:Al (green), 2 % ZnO:Ga (red), 1 % ZnO:In (blue) and 4 % ZnO:Cl (orange) films on top of borosilicate substrates after RA at 450 °C for 10 minutes in a 5 % H_2/ 95 % Ar atmosphere. The blank borosilicate substrate is used as a reference.

Influence of temperature and gases

The transparency of (Al-doped) ZnO films is evaluated before and after RA at 450 °C and 500 °C by UV-Vis spectroscopy in Figure 7.18. The transmittance of pure ZnO before and after RA at 500 °C is higher than when a reductive anneal is applied at 450 °C. The latter displays a serious transparency decrease suggesting the formation on non-vaporized metallic Zn which could also explain the low resistivity of pure ZnO annealed at 450 °C. To verify this, additional XPS measurements could resolve this, but have not been performed. For the 2 % ZnO:Al the transparency is the best for the reductive anneal at 450 °C. This is quite interesting since also the conductivity of this film (annealed at 450 °C) was the highest. As there is an inverse relationship between transparency and conductivity, the film at 500 °C is expected to have the best transmittance. Further on, a drastic decrease is observed in the ultraviolet range resulting from the band-gap absorption of ZnO (3.4 eV). This absorption displays a blue-shift (charge carriers) for ZnO:Al as compared to ZnO. This blue-shift is also present for the RA annealed samples (dotted line) when compared to the DA annealed samples (full line), suggest the presence of additional charge carriers. The origin of these charge carriers can be found in H as a shallow donor or more properly allocated Al.

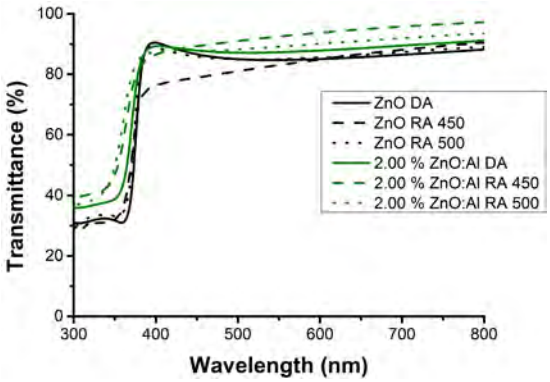

Figure 7.18: UV-Vis spectra of ZnO and 2 % ZnO:Al films on top of borosilicate substrates before (full line) and after reductive anneal at after RA at 450 ℃ for 10 minutes in a 5 % H_2/ 95 % Ar atmosphere (dashed line) or at 500 ℃ for 10 minutes in a 5 % H_2/ 95 % He atmosphere (dotted line).

7.5 Conclusion

After a comparison of different doping percentages of different group 13 and one group 17 dopants, 2% Al-doped ZnO film has the lowest obtained resistivity of 1.77 10^{-3} Ohm cm together with the highest transparency within the visible range after an anneal at 450 ℃ in a 5 % H_2/ 95 % Ar atmosphere. In addition, the synthesis of very good conductive ZnO with a sheet resistance as low as 676 Ohm/ □ and a resistivity of 4.93 10^{-3} Ohm cm is achieved. H doping is believed to be the main cause of this improved conductivity, although metallic zinc is not excluded. The serious drop in transmittance could indicate the formation of metallic species and could explain the low resistivity value of undoped ZnO. In comparison to ZnO, In and Cl-doping don't lead to an improved conductivity, although the transparency is significantly improved. Nevertheless, Cl-doping leads to a reduced thickness of the ZnO:Cl layer and the presence of Cl inside the layer can be questioned. Probably this method, due to the reductive treatment, is non-ideal to guarantee Cl-doping. In the end, also Ga-doping improves the conductivity and the transparency, but Al-doping is certainly the most elegant dopant of aqueous chemical solution deposition method. In addition to the choice of dopant, the importance of grain boundary scattering is indicated through the coherence of the largest grains of In, Ga and Al-doped ZnO films with the lowest sheet resistance.

8 The conductivity of aqueous sol(ution)-gel processed Al-doped ZnO

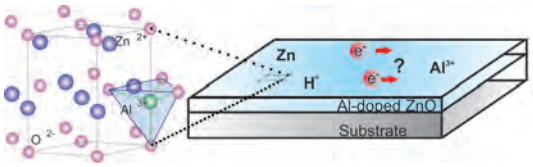

Figure 8.1: In-depth study of n-type doped ZnO conductive films

The previous chapter elaborates on different dopants in the aqueous chemical sol(ution)-gel deposition pointing out to Al to achieve the lowest resistivity. In literature most reports are made on Al-doped ZnO, as n-type doped ZnO, and although here and there insights in the conductivity mechanism might be presented, no general overview is given on how solution processed films can achieve state-of-the art characteristics. In this chapter, profound insights on the conductivity mechanism of sol(ution)-gel processed AZO with resistivities in the 10^{-3} Ohm cm range are gained through the study of the density of the film, the crystal phase, the optimum of Al doping and the relation of Al position in the ZnO lattice determined by ^{27}Al MAS NMR spectroscopy in combination with ^{1}H NMR to understand the conductivity mechanism. Since the conductivity of AZO films drops in function of time, the Al position is studied in close correlation to the observance of charge carriers with FTIR. All these influences of different factors upon the conductivity are summarized in a general overview in this chapter. In addition the exploration towards low temperature solution processing will be briefly discussed. For the first time the potential of aqueous precursors generating crystalline Al-doped ZnO at temperatures of approximately 200 °C or lower is highlighted.

8.1 Introduction

The study of the doped citrato-Zn precursor indicated that Al-doping resulted in the best performing TCO. Therefore an in-depth study of ZnO:Al is at place. In the next sections a coherence of several factors in combination with the position of Al inside the wurtzite crystal lattice is elaborated. The topography of the films, studied with SEM and AFM, is combined with HRTEM, to observe crystalline and amorphous areas. By a thorough study, the effective use and necessity of the reductive anneal is explained. The obtained conductivity after this reductive treatment, measured with Hall bar and VdP measurements, is linked to the position of Al inside ZnO through solid state nuclear magnetic resonance spectroscopy on powders, obtained from the same precursors. In addition to the Al incorporation the effect of hydrogen is discussed using NMR. This information is combined with X-ray photo-electron spectroscopy of AZO studying the metallic content of Zn and Al. By this in-depth overview, we link the properties influencing the conductivity and hopefully, in the future, will be able to manipulate Al doping in solution processing and chase resistivities in 10^{-4} Ohm cm range, as obtained by vacuum processing.

8.1.1 Al-doped Zn precursor

For the in-depth study of Al-doping (Al^{3+}-doped) Zn^{2+} precursors with a total metal concentration of 0.1 M were prepared by mixing and diluting the saturated citrato-Zn precursor with the citrato-Al precursor in the appropriate ratios. A doping series with nominal compositions of 0 (ZnO), 0.25, 0.35, 0.5, 1, 1.5, 2, 2.5, 3 or 5 (ZnO:Al at% Al) % Al were prepared.

8.1.2 Powder Synthesis

Powders were prepared from the 0.1 M (Al-doped) ZnO precursors by first drying the aqueous solutions for a couple of days in a Petri dish at 60 °C in an oven. Once dried, they were crushed into fine powders and thermally treated in alumina crucible at 300 °C (10 min) and 450 °C (30 min) on a hot plate (static air) and at 500 °C (60 min) in a tube furnace (500 mL min^{-1}, dry air (DA)). Additionally, after ramping with 10 °C s^{-1} up to 500 °C, the powders were subjected to a reductive anneal in 5% H_2/95% He during an isothermal period of 10 min (reductive anneal or RA), using the in-situ XRD setup (vide infra).

8.1.3 Film Deposition

ZnO and Al-doped ZnO films were prepared by spin coating various 0.1 M precursor solution (0.1 µm syringe filter is used) onto chemically cleaned SiO_2 (200 nm)/Si substrates or borosilicate glass substrates.[277] After coating (30

s, 3000 rpm, 1000 rpm/s), the as deposited film was treated in succession on two hot plates in static air as follows: 45 s at 300 °C, followed by 90 s at 450 °C. To obtain films consisting of 25 layers, this entire cycle was repeated 24 times prior to an annealing step at 500 °C for 60 min (preheated tube furnace, 500 mL min^{-1}, dry air). The films were additionally subjected to a final reductive anneal as described in the section of powder synthesis. Although the use of He as an inert carrier gas is not ideal from economical point of view, this choice was made to be able to monitor the XRD data during RA. As He is the smallest molecule, minimal hindrance during diffraction measurements is expected. Nevertheless equal results regarding the conductivity can be obtained by changing He with Ar (see Chapter 7) or N_2 gas, although recalibration of the equipment is needed.

8.2 Morphology and Crystallinity

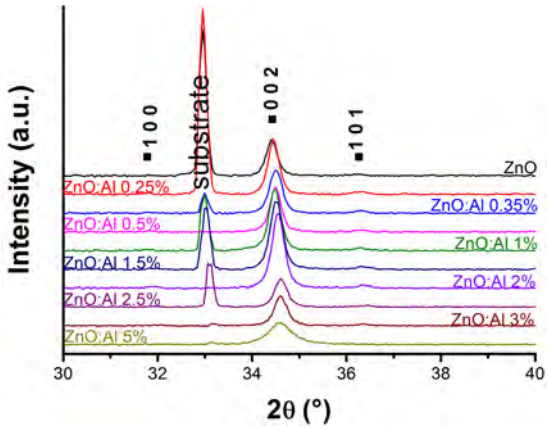

Figure 8.2: XRD analyses of (Al-doped) ZnO films after RA indicate the formation of the wurtzite crystal lattice.(JCPDS library file 36-1451)

The obtained films before reductive anneal, with doping up to 5% Al, only seem to contain the wurtzite phase (Figure 8.2). No different phases are found within the detection limits of the XRD apparatus. In addition the XRD peak broadening of the (002) orientation of the wurtzite crystal lattice with increasing Al content is ascribed to the finite size of the coherent diffracting domain (crystallite size) and defect induced strain in the crystalline network caused by extrinsic doping with Al.[46] The decreasing grain size is also visible by AFM in Figure 8.4, showing a decrease of the surface roughness for increasing Al content from ± 1.85 nm for undoped ZnO films to ± 1.4 nm for ZnO:Al 2% film. Al incorporation leads to a reduced surface roughness.[244] The decrease in surface roughness with Al doping may be caused by Al segregation at the

non-crystalline region in the boundary. [128] Also previously published articles for Al-doped ZnO powders [136] and films [46, 234] confirm this decreasing particle size upon Al-doping. Additional SEM (Figure 8.3a and c) and TEM (Figure 8.5a and c) analysis confirm the reduced grain size.

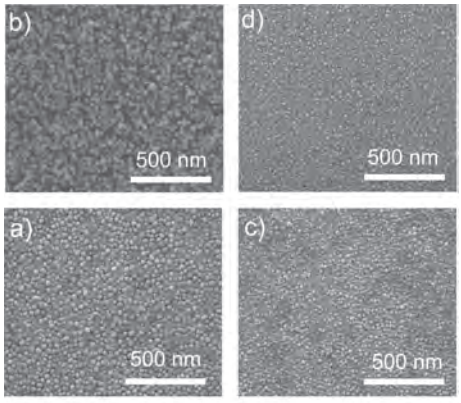

Figure 8.3: SEM micrographs of a) undoped ZnO film before RA, b) undoped ZnO film after RA, c) 2% doped ZnO:Al films before RA and d) 2% doped ZnO:Al films after RA.

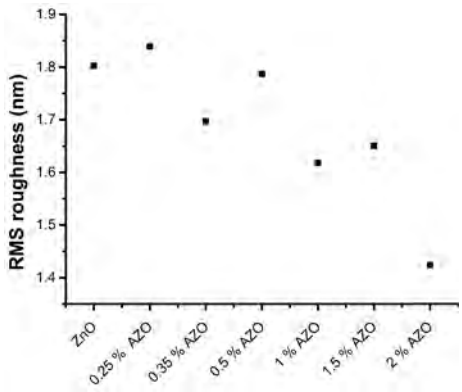

Figure 8.4: RMS roughness of undoped and Al-doped ZnO films after anneal in dry air (before reductive anneal under 5% H_2/He) as determined by atomic force microscopy.

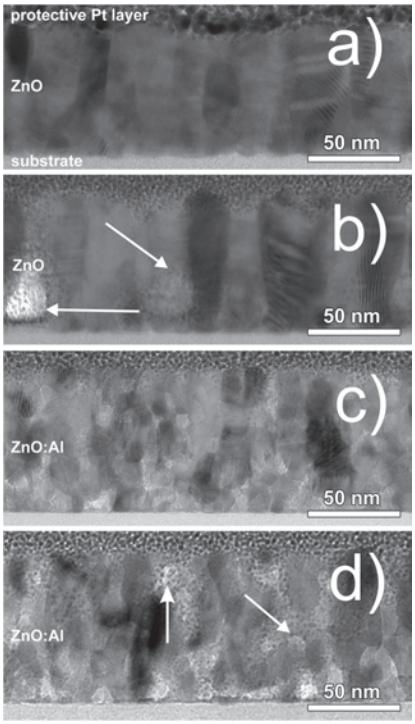

Figure 8.5: Low magnification overview images of high resolution TEM cross sections: a) ZnO before RA, b) ZnO after RA, c) ZnO:Al 2 % before RA and d) ZnO:Al 2 % after RA. All cross sections are obtained from 25 layered films. The dark dots observed in image b) and d) are Pt particles entering the respective film during the deposition of the protective Pt layer. Concentrated areas of Pt dots are indicated by a white arrow.

8.3 The reductive anneal

Most solution processed Al-doped ZnO TCO films either require a vacuum anneal or a high temperature reductive anneal.[95, 197, 301] Only recently, Al-doped ZnO and Cl-doped ZnO transparent and conductive solution processed films are obtained at low temperatures.[111, 227] As most films, including our aqueous solution based Al-doped ZnO films, require reductive anneals, an in-depth study is performed to understand its influence and functionality.

8.3.1 Crystallinity

The effect of hydrogen etching on the film properties during and after reductive anneal is discussed. Hydrogen can have different effects on the Al-doped ZnO film. During the RA the sheet resistance can be lowered (Figure 8.6a), but often this goes accompanied by a morphology change. This adaptation

can either induce desorption of oxygen or can induce grain growth. *Baik et al.* reported on the beneficial effect of grain growth through etching of small grains to larger ones by hydrogen treatment.[21] This leads to reduced grain boundary scattering for small grains and improves the conductivity, as indicated in Table 8.6. Nevertheless, for our films there is no direct proof of grain growth nor through XRD (Figure 8.6b), SEM (Figure 8.3), nor HR-TEM (Figure 8.5) analysis. The diffraction diffractogram, which is monitored in-situ during a RA, presented in Figure 8.6b, shows no peak broadening as indicated, but a small decrease in intensity of the (002) diffraction peak (red diffractogram).

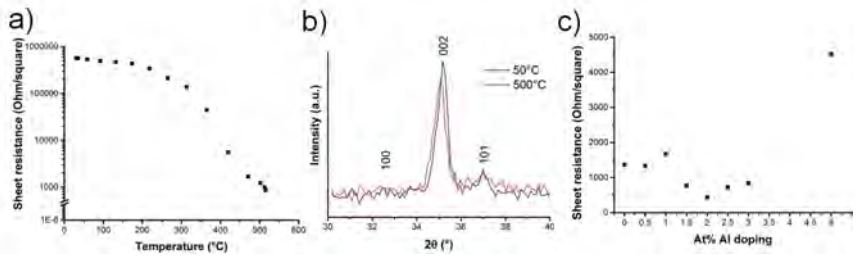

Figure 8.6: a) In-situ measurement of the sheet resistance of ZnO:Al 2% films in function of the temperature during RA. b) In-situ diffractogram of ZnO:Al 2% films at 50 °C (black) and at 500 °C (red). c) Sheet resistance i.f.o. the Al at% immediately after RA in static air and at room temperature.

The decrease in crystallinity is explained by Van de Walle [278] and Janotti [127] by the introduction of additional oxygen defects. These oxygen defects translate into an easy desorption of oxygen, leaving behind metallic Zn which can vaporize at temperatures of 500 °C. This process, finally resulting in film morphology destruction, is clearly visible for pure ZnO and to a smaller extent for ZnO:Al 2% in the TEM micrographs in Figure 8.5 by hole formation. TEM cross-section micrographs of 25 layered films coated from a 0.1 M (2% Al-doped) Zn precursor before and after reductive anneal are displayed. For the undoped ZnO film, the cross sections show a dense, columnar growth, which is less apparent for the ZnO:Al 2% film. The ZnO:Al 2% film further shows some minor penetration of Pt particles (dark dots) in regions where the material is amorphous. After the reductive anneal more Pt particles enter the ZnO(:Al) films. The enhanced penetration depth of Pt particles is due to the appearance of pores inside the films as well as to the formation of more amorphous regions. Although this reductive anneal is expected to have an effect on the grain boundaries, after RA no peak broadening is observed by XRD analysis (Figure 8.6b), which is confirmed by equal grain sizes in the TEM images (Figure 8.5). Literature reports on etching effects of hydrogen plasma leading to an increased roughness.[286] Also *Myong et al.* showed the increased roughness

in ZnO due to H incorporation. [194] Here, the main effect is the reaction of hydrogen with oxygen inside the AZO film as stated before. Al incorporation seems to prevent excessive etching and reduces the vaporization of the layer. Here, we emphasize the necessity of Al incorporation to avoid excessive oxygen removal, indirectly having an effect on the sheet resistance as stated in Table 8.6. Without Al, oxygen binds easily to the hydrogen present inside the film, creating islands of ZnO without the persistence of an interconnected network for conductivity. This leads to additional defects which significantly increase the resistivity.[118, 209] Also AFM images in Figure 8.7 displays the impact of the reductive anneal on the morphology. The undoped ZnO films show a four times increase of the surface roughness (1.8 nm - 7.5 nm) after RA, indicating void formation inside the ZnO layer. For the 2 and 5% Al-doped ZnO films, the increase in roughness is less pronounced (up to 2.3 nm for the ZnO:Al 2% film). The vaporization of the AZO layer is significantly reduced with increasing Al content as clearly observed by these SEM (Figure 8.3), by AFM (Figure 8.7), and by TEM images (Figure 8.5).

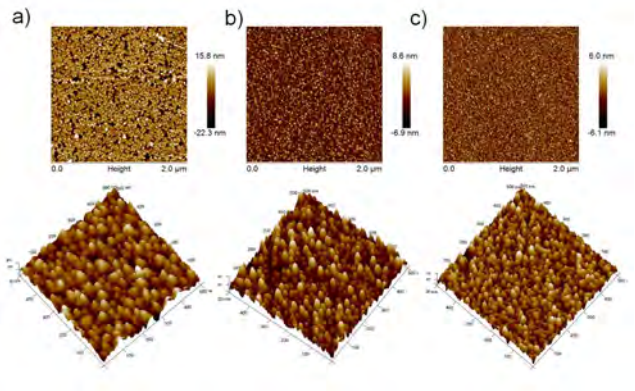

Figure 8.7: AFM images of films after reductive anneal with 5% H_2/He of a) ZnO: Rq 7.46 nm and Ra 5.36 nm, b) ZnO:Al 2%: Rq 2.30 nm and Ra 1.84 nm and c) ZnO:Al 5%: Rq 1.70 nm and Ra 1.35 nm.

8.3.2 Scattering

During the RA the sheet resistance drops drastically from the MOhm/ □ to kOhm/ □ range (Figure 8.6a) The sheet resistance of the(Al-doped) ZnO films after RA is displayed in Figure 8.6c. The lowest sheet resistance of 435 Ohm/□ is obtained for the ZnO:Al 2% film, resulting in a resistivity of 2.88 10^{-3} Ohm cm taking into account a thickness of this 64.7 nm thick film. A Hall bar measurement confirms this resistivity of 2.88 10^{-3} Ohm cm with a carrier mobility of 18.5 cm^2/V.s and a carrier concentration of 1.17 10^{20} cm^{-3}. Reproducibility was checked on an additional ZnO:Al 2% film resulting in a value of 544

Ohm/□. The sheet resistance of pure ZnO films however is not easy to determine: as the films are highly inhomogeneous, a sheet resistance of 1368 Ohm/□ could only be measured for one out of three films. The sheet resistance of the 5% Al-doped ZnO increases up to 4.5 kOhm/ □, indicating that a counteracting mechanism to the beneficial influence of n-type doping is active. This can be based on a decreasing grain size. A lower particle size as obtained with increasing Al % has a negative impact on the conductivity because of more abundant grain boundary scattering for the charge carriers. Table 8.6 indicates this effect: the smaller the grains, the higher the sheet resistance becomes.

According to Matthiesens rule not only grain boundary scattering is an important parameter in reducing the conductivity, also scattering at defects and ionized impurity scattering are of importance.[118] Defects, like porosity, have already been mentioned in Chapter 7 and in sections above. Furthermore, ionized impurity scattering can be linked to the increasing Al doping %. Ionized impurity scattering would be possible with increasing amount of charge carriers. However, according to *Minami et al.* at least 10^{21} charge carriers per cm^3 are required for this mechanism to be effective.[179] Since our carrier concentration is lower (1.17 10^{20} cm^{-3} as stated above, this is probably no explanation for the increasing resistivity with increasing content of Al. The main mechanism in contributing to an increasing resistivity with increasing Al doping is probably only grain boundary scattering. Additional Hall bar measurements are necessary for the higher % Al-doped ZnO films to exclude ionized impurity scattering completely.

8.3.3 Transparency

The transparency of (Al-doped) ZnO films is evaluated before and after RA by UV-Vis spectroscopy in Figure 8.8. The transmittance in the visible (and near-IR) range never drops below 85 % after RA, while a drastic decrease is observed in the ultraviolet range. The latter results from the band-gap absorption of ZnO (3.4 eV), displaying a blue-shift (charge carriers) for ZnO:Al as compared to ZnO, also known as the Burnstein-Moss effect.[39, 190] This blue-shift is also present for the RA annealed samples (dotted line) when compared to the DA annealed samples (full line).[112] These RA annealed samples also display an improved transmittance, which might be due to reduced thickness of the AZO film after RA (e.g. 1 at% Al: 70-57 nm, 1.5 at% Al: 71-67 nm). The formation of metallic Zn is expected to reduce the transparency. Szyszka reported a relation between the transparency and the desorption of surplus Zn. [260] Therefore the hypothesis can be made that nor metallic Zn (nor Al) has a significant influence here. This will be further discussed in Section 8.5.

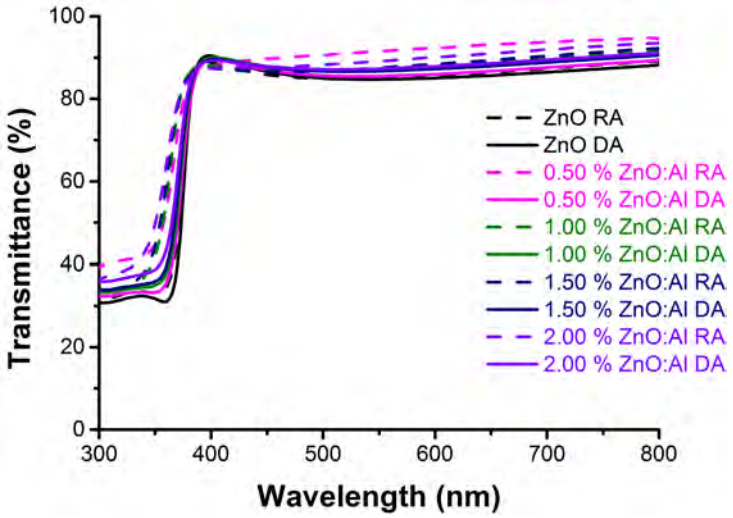

Figure 8.8: Transmittance of ZnO and Al-doped ZnO films on borosilicate glass in the 250 to 800 nm range before and after RA.

8.3.4 Temperature of reductive anneal

The beneficial influence of an increasing temperature during reductive anneal on the sheet resistance effect has been indicated above in Figure 8.6a. This figure shows that for the 2% Al-doped ZnO films, up to about 500 ℃, the sheet resistance decreases with temperature during the RA. If the temperature is further increased or time prolonged, the films are completely removed by the hydrogen etching.

Independently an experiment was setup to investigate the influence of the RA step-by-step by anneal in a 5% H_2/ 95% Ar atmosphere in a RTP setup. The used films were the 2% Al-doped ZnO as described above. 2.5 by 2.5 cm2 SiO_2 (200 nm)/Si substrates coated with 2% ZnO:Al were cut in two and one half was heated with 10 ℃/ s up to 200 ℃, 300 ℃, 400 ℃, 425 ℃, 450 ℃, 475 ℃ and 500 ℃ and kept isothermal for 10 min in this reductive atmosphere. Figure 8.9 displays the temperature influence of the RA on the macro- and microscopically morphology. From 450 ℃ the morphology starts to deteriorate and the complete layer is gradually removed.

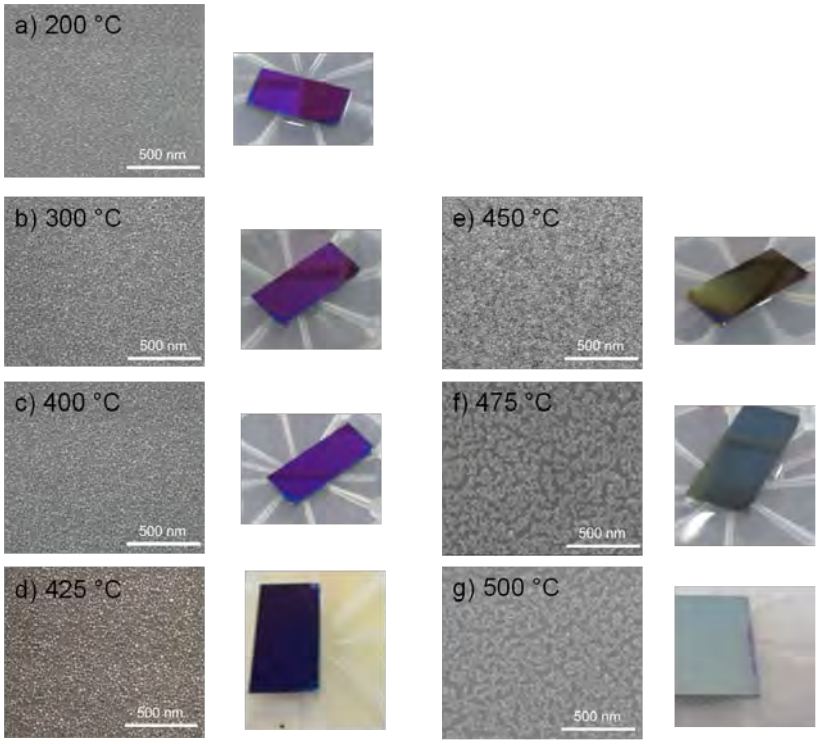

Figure 8.9: Influence of the temperature during RA on the macro- and microscopically morphology of 2% Al-doped ZnO films.

This temperature treatment also has an influence on the conductivity inside these films. GATR-FTIR analysis was done in order to monitor the charge carriers in function of the RA temperature (Figure 8.10). Also the presence or absence of organic fragments can be monitored using GATR-FTIR analysis. For all the films, indifferent of the RA temperature, the SiO_2 (200 nm)/Si substrate absorbs around 1240 cm^{-1} and at 1065 cm^{-1} for the longitudinal and the transverse optic vibration. [122] The free charge carriers can be observed by an absorption band in the IR region between 4000 and 1500 cm^{-1}.[112] As the wavelength is longer than the plasma wavelength, the plasma becomes reflective.[37, 145] At plasma resonance, an absorption peak is seen in the GATR-FTIR spectrum. For the film annealed at 200 ℃ only a small increase in absorption is present in Figure 8.10 (black). This indicates a limited amount of free charge carriers. As the temperature rises, the intensity of the absorption increases and seems to undergo a red shift up to 425 ℃. At 450 ℃ a blue shift is visible, indicating more charge carriers. For the films annealed at 475 ℃ and 500 ℃ no absorption is observed. Based on these GATR-FTIR results, it is hard to prove the presence of Zn-O(-Al) vibrations (visible below 600 cm^{-1} and measurement range: 4000-600 cm^{-1}). XRD analysis in Figure 8.11

displays the preferential (002) orientation which can be indexed as previous with the wurtzite crystal lattice (JCPDS library file 36-1451). From the point that the RA took place at temperatures of 475 ℃ or higher, no crystalline ZnO stays present, confirming the removal and morphology adaptation as seen in Figure 8.9.

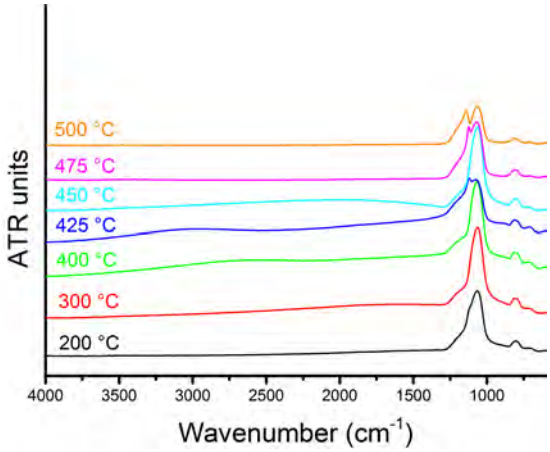

Figure 8.10: 2 % Al-doped ZnO films where the influence of the RA temperature on the charge carriers is monitored with GATR-FTIR.

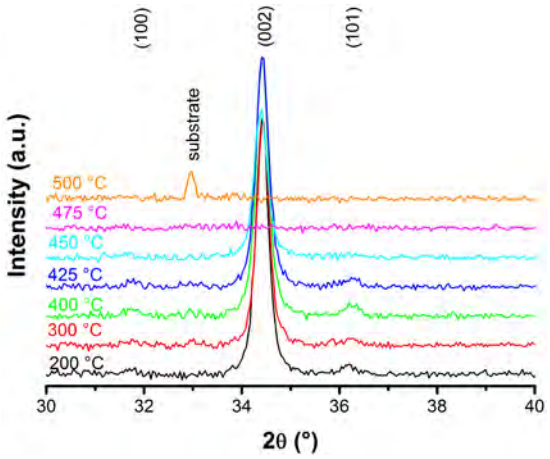

Figure 8.11: Influence of the temperature during RA on the crystallinity ex-situ monitored with XRD. All 2 % Al-doped ZnO films, except for these annealed at 475 ℃ or 500 ℃, can be indexed with the wurtzite crystal phase. (JCPDS library file 36-1451)

In addition the sheet resistance was measured with a multimeter again in func-

Table 8.1: Overview of the sheet resistance in function of the temperature during reductive anneal.

Temperature (℃)	200	300	400	425	450	475	500
Sheet resistance (kOhm/□)	330	10	1.4	0.69	0.39	/	/

tion of the applied temperature during RA. Although this method of measuring the sheet resistance is far from exact through the resistivity of the used contacts, it is a fast and high throughput method to provide a first qualitative assessment of the sheet resistance. The trend observed here is the same as in Figure 8.6.

Although the trend in sheet resistance and crystallinity is the same in this individual experiment as during in-situ measurements, some difference needs to be addressed. During the in-situ measurements an optimum of 500 °C for the RA has been established, while ex-situ experiments prefer annealing at a maximum of 450 °C. This difference might be attributed by the various setup and temperature calibration applied for both apparatus. In addition, the difference in thermal conductivity is also expected to have an influence on the heat transfer and the annealing. The thermal conductivity, correlated to the temperature and pressure, of Helium is higher than the thermal conductivity in Argon. While the in-situ measurements used 95% of the more expensive He, the ex-situ anneals were done in 95% Ar. To exclude this difference from the further experiments, the further reductive anneals were done by the same setup as the in-situ measurements at 500 °C for 10 min.

8.4 The position of Al inside the ZnO lattice

8.4.1 The comparison between powders and films

The tetrahedral substitutional Al doping is believed to contribute to an improved conductivity. Therefore, positions of Al inside the ZnO lattice were studied by ^{27}Al MAS NMR on powders obtained from the precursors. This is necessary since the sensitivity of NMR does not allow direct measuring the Al environment in the thin films. Powders were prepared by thermally treating the precursors in a crucible at the same temperatures, but with longer times as compared to the films to ensure the complete removal of the organic species. Nevertheless, some caution is necessary during interpretation of the Al/Zn ratio. Some Al contamination might be induced by the use of alumina crucibles. Nevertheless as the ratios of the powders are not completely quantitatively determined during the NMR interpretation and only a comparison is made between different powders, a negligible influence is expected. In addition we believe that the Al environment in the powders and films is similar. This

is indicated by the comparable GATR-FTIR spectra of films and the FTIR spectra of powders in Figure 8.12.

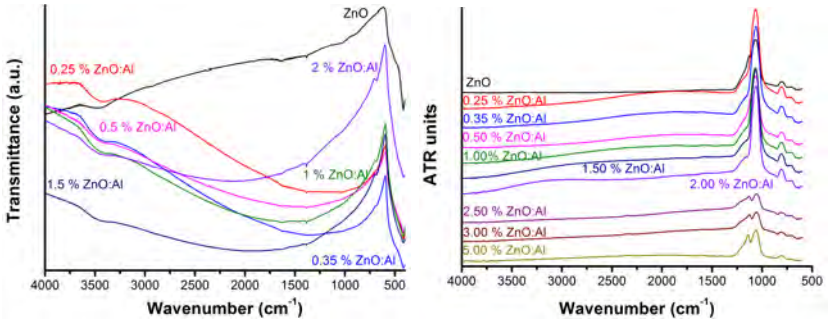

Figure 8.12: FTIR spectra of some of the reductively treated powders. (left) GATR-FTIR spectra for 25 layered 0.1 M ZnO(:Al) films after reductive anneal.(right)

8.4.2 Al allocation

MAS NMR and FTIR

To investigate what happens with the Al dopant positions during the RA, necessary to obtain relatively low sheet resistances, ^{27}Al MAS NMR measurements were performed and compared with FTIR spectra in Figure 8.13. The MAS spectrum of the dried ZnO:Al 2% precursor gel (Figure 8.13a) only shows a signal around 10 ppm (having an upfield shoulder), indicating that all Al is octahedrally (VI) coordinated by oxygen atoms.[38] Similar spectra are obtained for all other dried precursor gels with doping levels between 0.25 and 5% Al. In the corresponding FTIR spectra, the characteristic stretch vibrations of citric acid ($\nu_{C=O}$, ν_{O-H}) and bend vibrations of ethylene diamine (δ_{β}, δ_{γ}, ν_{N-H}) are clearly observed.[187] After thermal treatment of the precursor gels in an oxidative atmosphere at 500 °C to obtain the oxide phase (DA; Figure 8.13b), an additional signal appears in the MAS spectra around 86 ppm, indicative for Al with a tetrahedral (IV) oxygen coordination. This chemical shift is higher than the typical values of 56-60 ppm for 4-fold coordinated Al in alumina and aluminosilicates,[115] suggesting that no separate alumina phase is formed and Al is well dispersed within the ZnO matrix. As shown in Figure 8.13b, both signals are rather sharp, similar to the observations by *Avadhut et al.*.[17] Spinning sidebands appear at multiples of the spinning speed which reflect the chemical shift anisotropy and quadrupolar interaction of Al nuclei with local electric field gradients (EFG) typically caused by distorted coordination symmetry.[83] The FTIR spectrum becomes dominated by the vibrations of Zn-O, next to minor absorptions of some (adsorbed) water and remaining ethylene diamine. Upon reductive anneal, the FTIR spectrum changes dramatically (Figure 8.13c) due

to surface plasmon absorption. Such surface plasmon effects are also observed for the Al-doped ZnO films (righter Figure 8.12). Likewise, clear changes are also observed in the corresponding MAS spectrum (Figure 8.13c), especially around the signal representing tetrahedral Al. Also *Behrens et al.* saw an Al redistribution upon annealing in hydrogen containing atmosphere. [24] A new signal seems to appear around 46 ppm which can on the one hand be indicative for Al with a 5-fold oxygen coordination,[17, 178] but on the other hand, also for Al with distorted tetrahedral coordination. In addition to the spinning sidebands, outside the typical ^{27}Al chemical shift range for diamagnetic compounds, a Knight-shift signal appears around 220 ppm. The presence of this Knight shift, combined with the presence of the surface plasmon resonance infrared absorption, seems to be important in order to obtain an improved conductivity. Both effects are caused by the presence of free charge carriers, which are beneficial for the conductivity.[37, 294] In addition, the signal representing octahedral Al broadens. Similar features appear in all spectra up to 2% of Al-doping after the reductive anneal (Figure 8.14). For higher Al contents, the knight shift intensity decreases and disappears around 3% Al-doping.

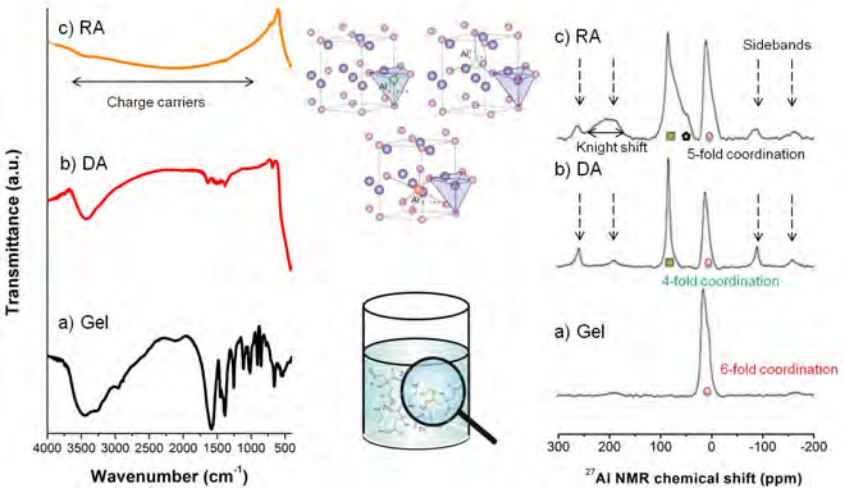

Figure 8.13: FTIR (left) and ^{27}Al NMR spectra (right) of ZnO:Al 2% powder as a gel (a), after anneal in DA (b) or after a RA (c). Before thermal treatment, at the precursor or gel stage, Al^{3+} forms a complex with citric acid (middle bottom). After thermal treatment, the Al is incorporated substitutional tetrahedral (dark green atom representation inside the ZnO lattice in the middle), interstitial tetrahedral (light green atom representation inside the ZnO lattice in the middle) and interstitial octahedral (red atom representation inside the ZnO lattice the middle).

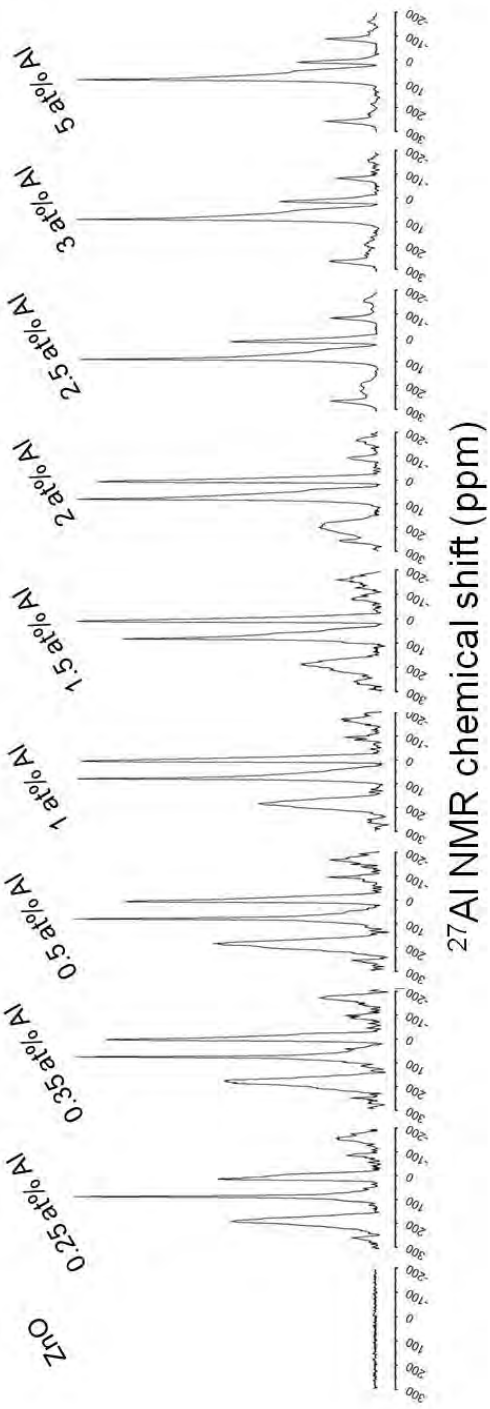

Figure 8.14: ^{27}Al NMR spectra of (Al:)ZnO powders after RA.

MQ MAS NMR

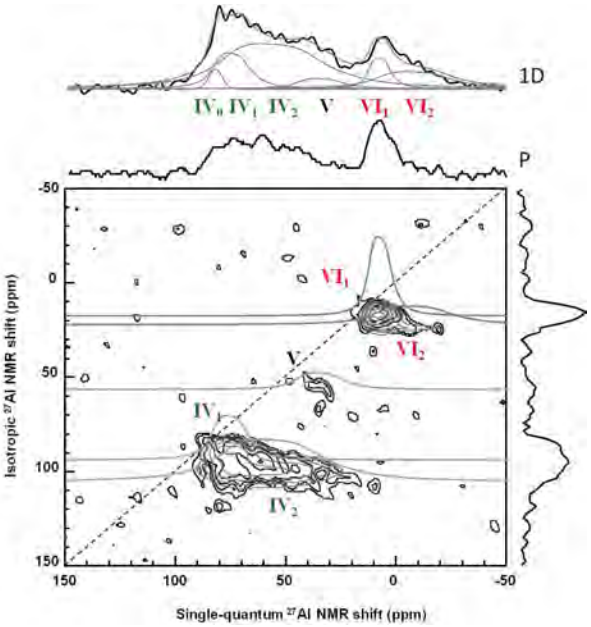

Figure 8.15: MQMAS ^{27}Al NMR spectrum of 2 % ZnO:Al powder after RA with projections P along the (horizontal) single-quantum shift axis, and the (vertical) isotropic shift axis. On top of the figure, the 1D ^{27}Al MAS NMR spectrum recorded with a short, strong 25° pulse of 0.2 μs is shown, along with a spectral fit based on the five MQMAS components supplemented with the narrow IV_0 signal. The latter is clearly observed in the 1D NMR spectra recorded with a 90° pulse of 2 mus (Figure 8.13). The line shape-simulation parameters are given in Table 8.2.

To assign the 46 ppm signal to distorted tetrahedral, penta-coordinated Al or a combination of both, a multiple-quantum (MQ) MAS NMR spectrum of the ZnO:Al 2% powder after RA has been recorded (Figure 8.15). This 2D NMR technique permits to distinguish between quadrupolar and chemical effects of the ^{27}Al NMR shift. The 2D NMR line shapes of the IV and VI signals are inhomogeneously broadened and can be roughly described by two components: one with coordination symmetry, close to the spectral diagonal (labeled IV_1 and VI_1 in Figure) and one with strongly distorted symmetry (IV_2 and VI_2). At much lower intensity level, the 2D spectrum contains indications for a minor fraction of penta-coordinated Al with a shift around 46 ppm (V in Figure 8.15). The narrow signal of substitutional Al with high tetrahedral coordination symmetry (IV_0), which is observed in the 1D ^{27}Al MAS NMR spectra recorded with a 90° pulse of 3 μs and interscan delay of 6 s (Figure 8.13c), does not

show up in the MQMAS spectrum, as a result of its weak quadrupole coupling and its slow spin-lattice relaxation.

Independent ^{27}Al spin-lattice relaxation measurements (Figure 8.17) indicate a long relaxation time in the second range for substitutional tetrahedral Al (IV_0) and a short relaxation time in the order of milliseconds for the interstitial tetrahedral Al fractions IV_1 and IV_2. The "true" shift without the quadrupolar perturbation, 85 ppm, of the IV_1 and IV_2 Al is almost the same as that of substitutional IV_0 Al. This suggests that the three tetrahedral Al species are chemically the same, but differ in their deviation from perfect coordination symmetry. The MQMAS NMR spectrum thus shows that the 46-ppm signal in the 1D NMR spectrum mainly belongs to distorted tetrahedral Al. At a much lower intensity, the 2D spectrum contains additional indications for a minor fraction of penta-coordinated Al with a true shift at 47.4 ppm (V in Figure 8.15 and Table 8.2).

Avadhut et al. have assigned the ^{27}Al NMR signal at 46 ppm to penta-coordinated Al, which is believed to have hydrogen in its coordination sphere.[17] These authors ascribed the origin of this hydrogen to reagents used during synthesis. Here, penta-coordinated Al is absent after an oxidative anneal and appears only at a minimal level after a supplemental RA (Figure 8.13). Therefore, we can conclude that hydrogen does not originate from precursor components, as it would then already be present after oxidative anneal. As an alternative, penta-coordinated Al could result from a reaction of an AlO_6 octahedron species with hydrogen gas during the RA, leading to the formation of AlO_5 and H_2O. As MQMAS indicated only a minimal amount of penta-coordinated Al, the main coordinations are tetrahedral and octahedral coordinations

MQMAS allows to separate the line shapes of the various overlapping components in the 1D ^{27}Al MAS NMR spectrum, but is not quantitative. For comparison, Figure 8.15 also contains the corresponding deconvoluted 1D ^{27}Al NMR spectrum recorded independently with a short, strong 25° excitation pulse of 0.2 μs and 6 s interscan delay. Compared to the ^{27}Al NMR spectra in Figure 8.13, the signal of the distorted tetrahedral Al is more strongly pronounced. This relative intensity difference is caused by the effect of the quadrupolar coupling of the ^{27}Al excitation by a resonant radio-frequency pulse.[170]

Although the ^{27}Al NMR spectra in Figure 8.13 and Figure 8.14 are not strictly quantitative (the distorted IV Al fraction is relatively under-emphasized), trends in the relative occupancy of Al in the tetrahedral and the octahedral positions as a function of the overall Al content can be estimated from the NMR peak areas as a function of the overall Al doping level (Figure 8.16).

By integration of the different NMR peaks (Figure 8.13, Figure 8.14 and non-displayed spectra after DA), the relative occupancy of Al in both positions is

Table 8.2: "True" chemical shift values without the effect from the quadrupolar coupling and the quadrupolar coupling constants (QCC). The T_0 fraction is actually not observed in the MQMAS spectrum. Its line shape parameters are derived from 1D ^{27}Al MAS NMR spectra (Figure 8.13 and Figure 8.15). The corresponding ^{27}Al fractions are derived from a restricted fit of the six line shape components to the 1D MAS NMR spectrum recorded with a short, strong 25° excitation pulse of 0.2 μs (Figure 8.15)

Coordination	δ_{chem} (ppm)	QCC (MHz)	fraction (%)
IV_0	82.7	0	3
IV_1	85.1	4.2	15
IV_2	84.5	7.1	53
V	47.4	4.8	6
VI_1	13.6	3.3	8
VI_2	12.3	6.0	14

derived in Figure 8.16. Before RA the relative occupancy of Al in octahedral positions is either more or less equal to the tetrahedral occupation or becomes dominating above 2 at% Al. Here no meaningful conductivity is measured for these films. The films with conductivity in the kOhm cm region are obtained after RA and have a dominating tetrahedral occupancy of Al. Above 5 % Al-doping, the octahedral content is expected to increase and eventually gahnite ($ZnAl_2O_4$) might be formed. [136] This is based on the eventual saturation of the ZnO lattice for further Al doping and secondary phases (octahedral Al coordination) of $ZnAl_2O_4$ and Al_2O_3 may be formed. These crystal phases are known to be insulators, decreasing the conductivity, as indicated in Table 8.6. [69]

Although NMR measurements of powders after RA indicate more tetrahedral occupation, inside the ZnO lattice this can either indicate substitutional or interstitial tetrahedral occupation. In an attempt to distinguish between the tetrahedral Al in substitutional (replacing Zn) and interstitial (empty tetrahedral holes in the ZnO lattice) sites, aluminum T_1 relaxation measurements have been performed for ZnO:Al 3% before and after RA.[17, 136] After RA the IV signal is broadened and also contains a minor fraction of V Al. The T_1 relaxation fits of the tetrahedral signal show a clear bi-exponential relaxation behavior (Figure 8.17) with a long ($\sim$ 2-3 s) decay time fraction, being characteristic for substitutional Al, next to a short ($\sim$ 20 ms) decay time fraction, indicative for interstitial Al (Table 8.3). For the octahedral Al signal, only two short decay time ($\sim$ 10 and 300 ms) fractions were obtained. Although, as indicated above, the tetrahedral Al fractions obtained by the T_1 relaxation measurements are not strictly quantitative, and probably even overestimate the substitutional Al, only a slight increase in this amount of tetrahedral Al

is observed upon RA. Based on the resulting Al fractions, the tetrahedral Al before RA (49 % for ZnO:Al 3 %; see Figure 8.16) can be subdivided into 37 % substitutional and 12 % interstitial Al. After RA, the tetrahedral Al (70 % for ZnO:Al 3 %; see Figure 8.16b) can be subdivided into 40 % substitutional and 30 % interstitial Al. Note that the signal of tetrahedral Al after RA also includes the minor fraction of penta-coordinated Al. This indicates that the RA only induces a minor increase of the substitutional tetrahedral Al content (3 %).

Although a high amount of Al can be found in the desired crystallographic position (tetrahedral and substitutional), no meaningful conductivity is measured (MOhm range) in films deposited from this precursor after an identical thermal treatment as was applied for these powder samples (500 °C in ambient). This indicates that the mere presence of substitutional Al, more than 1/3 of the total Al content, is not sufficient to render the layers conductive. This finding is confirmed by NMR and FTIR of 2 % Al-doped ZnO powders after DA: despite a significant amount of substitutional Al is present, no surface plasmon effect is observed by FTIR nor Knight shift in the NMR spectra. The negative acceptor behavior of Al in octahedral positions must be dominating (in correlation to the other effects as described above) over the advantageous effect of substitutional Al. The influence of the location of Al inside the ZnO lattice on the conductivity is displayed in Table 8.6 under the activation of Al.

This activation of Al is clear after RA of the ZnO:Al 3 % powders. The Al coordination shifts from octahedral to both substitutional (Sub.) and interstitial (Int.) IV Al, as observed in the NMR spectra (Figure 8.14) and the T_1 results (Table 8.3). The increase of substitutional IV coordination is however not very distinct. Alone, it cannot account for the improved conductivity. The higher substitutional content surely has a beneficial effect, but as observed in Figure 8.15, the lattice is becoming more and more irregular and different surroundings can be distinguished.

Table 8.3: Rough ^{27}Al NMR T1 relaxation times and corresponding peak-area fractions for ZnO:Al 3 % powders after DA and RA.

Anneal	4-fold (Int.)	4-fold (Sub.)	6-fold (Int.)	6-fold (Int.
DA fraction	12 %	37 %	35 %	16 %
T_1 value	20 ms	2.9 s	10 ms	0.30 s
RA fraction	30 %	40 %	20 %	10 %
T_1 value	20 ms	2.3 s	10 ms	0.30 s

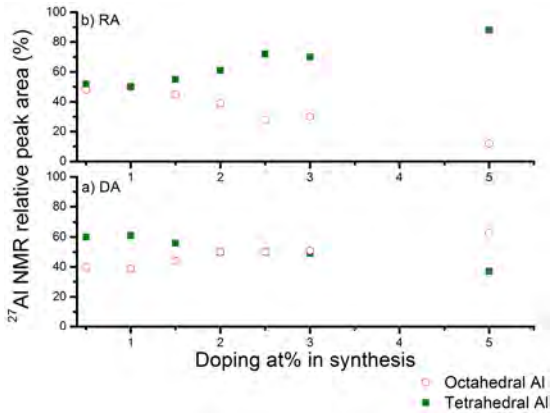

Figure 8.16: Effective Al doping and coordination inside the ZnO lattice as a function of the applied doping level a) after annealing the powders in DA and b) after the RA. The ^{27}Al NMR spectra of ZnO:Al 2 % are shown in Figure 8.13b for the anneal in DA and in Figure 8.13b for the RA. The ^{27}Al NMR spectra of all the samples after RA are displayed in Figure 8.14.

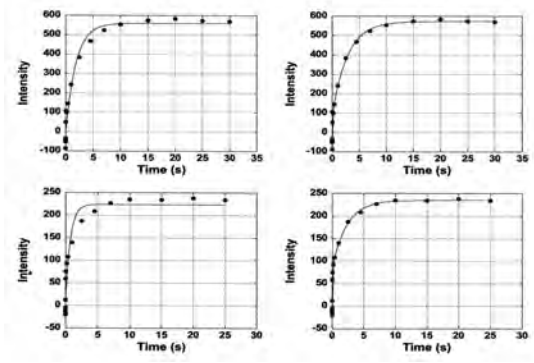

Figure 8.17: Mono- and bi-exponential ^{27}Al T_1 relaxation curve fits of the tetrahedral signal of ZnO:Al 3 % powder before (top) and after RA (bottom).

8.5 The effect of metallic Zn, H and O vacancies

8.5.1 Metallic species

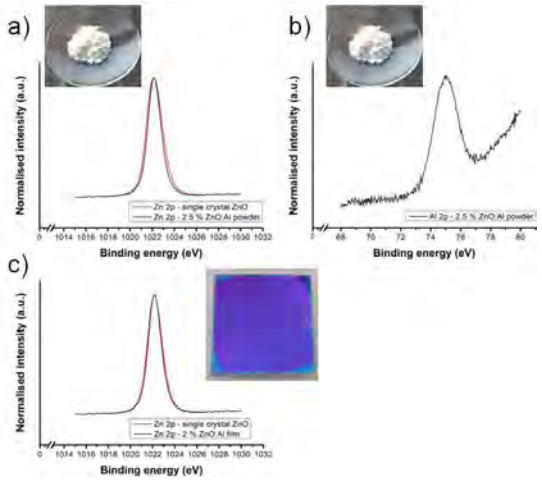

Figure 8.18: a) XPS spectra of Zn_{2p} for single crystal ZnO (reference, MTI Corporation) and ZnO:Al 2.5 % powders after RA, b) XPS spectrum of Al2p for ZnO:Al 2.5 % powders after RA and c) XPS spectra of Zn_{2p} for single crystal ZnO (reference, MTI Corporation) and ZnO:Al 2 % film after RA.

XPS analysis is performed to verify the presence of metallic Zn and Al in the 2% Al-doped ZnO film and 2.5% Al-doped ZnO powder after RA. The irregular morphology (Figure 8.3 and Figure 8.5) and rougher surface (Figure 8.7) after RA is caused by etching through hydrogen. Hydrogen enables oxygen desorption and the formation of metallic zinc (maybe even metallic aluminum). The Knight shift as observed in Figure 8.14 is indicative for this metallic behavior, although it is only present for lower amounts of doping. The contribution of metallic Zn/Al is stated to be beneficial on the conductivity of the AZO films.

To investigate the involvement of Zn^{2+} or Al^{3+} (reduced to the metallic state) in the increased conductivity,[294] XPS analysis is performed, focusing on the oxidation state of Zn and Al after reductive anneal of the ZnO:Al 2 % film and 2.5 % powder. No peaks corresponding to metallic zinc nor to metallic Al (for the powder) are recorded (e.g. 1021.5 eV and 72.6 eV, respectively) within the detection limits of the apparatus (Figure 8.18), at least providing the guarantee that the topmost nanometers of the film are free from metallic compounds.[123] A conclusive statement regarding the presence of metallic Zn in the bulk of the film cannot be easily provided. This would require a depth profiling experiment,

though the involved Ar^+ bombardment might parasitically induce metallic Zn and/or Al itself, thus rendering the outcome inconclusive again. [22] Therefore, the observed Knight shift up to 2 at% Al doping is attributed to a metallic like behavior (indicating a high electron mobility), and probably not due to metallic Zn/ Al. Here the Knight shift is assigned to other causes of generating conduction electrons in doped semiconductors (e.g. substitution of Zn^{2+} by Al^{3+} inside the ZnO lattice). The electrons in the conduction band generate an additional field, caused by their spin orientations under the influence of an external field. For metallic like behavior, a Knight shift is observed. Additional surface plasmon absorption is expected in infrared analysis. GATR and FTIR (Figure 8.12) spectra display only surface plasmon absorption of the doped ZnO films and powders. This indicates the necessity of Al inside the ZnO lattice confirming that the charge carriers inside Al-doped ZnO are established by Al incorporation inside ZnO, and not due to the formation of metallic zinc. This analysis indicates the activation of Al^{3+} inside the ZnO matrix through the RA.[17]

8.5.2 Oxygen species

The effect of oxygen needs also to be studied since the RA is able to draw oxygen from the ZnO:Al layer at elevated temperatures. Oxygen vacancies are often pointed out to contribute to an improved conductivity [11, 111, 209] although density-functional theory (FT) calculations claim that for ZnO, oxygen vacancies create too deep levels to generate charge carriers in the conduction band.[5] Nevertheless *Lany and Zunger* published a theory emphasizing the paradoxical coexistence or contribution of a metastable oxygen vacancy defect, induced by photo-excitation, to the conductivity.[155] Furthermore, grain boundary adsorption of oxygen is reported to increase the resistivity by the introduction of possible trap states for electrons inside the film.[163, 175, 284] This all makes the role of oxygen in the conductivity mechanism not very straightforward.

The oxygen content is very difficult to measure, as vacancies cannot be 'visualized' as such. The ability to control oxygen content/pressure is however one of the main differences between atmospheric solution processing and vacuum based sputtering. For vacuum deposition, this translates into Equation 8.1, whereby electrons are directly inserted into the conduction band. This technique often reports resistivities in the 10^{-4} Ohm cm range. For chemical solution deposition, the reported resistivities are usually in the 10^{-3} Ohm cm range, although sometimes solution processing is able to go even lower in the 10^{-4} Ohm cm region.[11]

Chemical solution deposition at atmospheric conditions starts from solutions where Al is octahedrally coordinated and thermal treatments take place in dry

air, resulting in ZnO:Al films with stoichiometrically coordinated oxygen. Due to incorporation of Al^{3+} more oxygen than for pure ZnO films is incorporated (Equation 8.2). The reductive anneal is subsequently needed to remove this oxygen excess, while creating electrons for the conduction band originating from Al or coming from H (Equation 8.3).

Furthermore, even adsorbed oxygen species at the surface of the film are reported to increase the resistivity. [173] As for vacuum or UV anneal, the RA is expected to remove these adsorbed oxygen species and thus has a beneficial influence on the mobility of Al-doped ZnO films.[284]

For undoped ZnO, hydrogen can be incorporated as a shallow donor (Equation 8.4) and/or Zn interstitials (Equation 8.5) can be created as discussed in-depth later on. If Al is incorporated the O/Zn ratio seems to be higher than in pure ZnO. If the film isn't doped with Al, it is less stable against a reductive treatment and gives oxygen the ability to chemically bind to hydrogen, leaving metallic zinc behind, which also easily vaporizes at a temperature of 500℃ (Figure 8.3 and Figure 8.5), as stated by our experimental results (Equation 8.5).

Tahar et al. described Al as being inactive, due to the excess of oxygen by introducing Al. They described that the donors can be activated by the removal of oxygen and/or introduction of hydrogen in the film (Equation 8.3).[261] This also seems to be the case for our sol-gel processed films, through reductive treatment.

$$\mathrm{Al_xZn_{(1-x)}O_{(1+\frac{x}{2})}} \longrightarrow \mathrm{Al_xZn_{(1-x)}O} + \frac{x}{4}\mathrm{O_2} \text{ with } xe^-_{CB} \tag{8.1}$$

$$(1-x)\mathrm{ZnO} + \frac{x}{2}\mathrm{Al_2O_3} \longrightarrow \mathrm{Al_xZn_{(1-x)}O_{(1+\frac{x}{2})}} \tag{8.2}$$

$$\mathrm{Al_xZn_{(1-x)}O_{(1+\frac{x}{2})}} + (\frac{x}{2}+\frac{y}{2})\mathrm{H_2} \longrightarrow \mathrm{H_yAl_xZn_{(1-x)}O} + \frac{x}{2}\mathrm{H_2O} \text{ with } (x+y)e^-_{CB} \tag{8.3}$$

$$\mathrm{ZnO_{(1+\frac{x}{2})}} + (x+\frac{y}{2})\mathrm{H_2} \longrightarrow \mathrm{H_yZnO} + \frac{x}{2}\mathrm{H_2O} \text{ with } ye^-_{CB} \tag{8.4}$$

$$\mathrm{ZnO} + (x)\mathrm{H_2} \longrightarrow \mathrm{ZnO_{(1-\frac{x}{2})}} + x\mathrm{H_2O} \text{ with } \frac{x}{2}e^-_{CB} \tag{8.5}$$

8.5.3 The influence of hydrogen in aqueous sol(ution)-gel processed Al-doped ZnO films

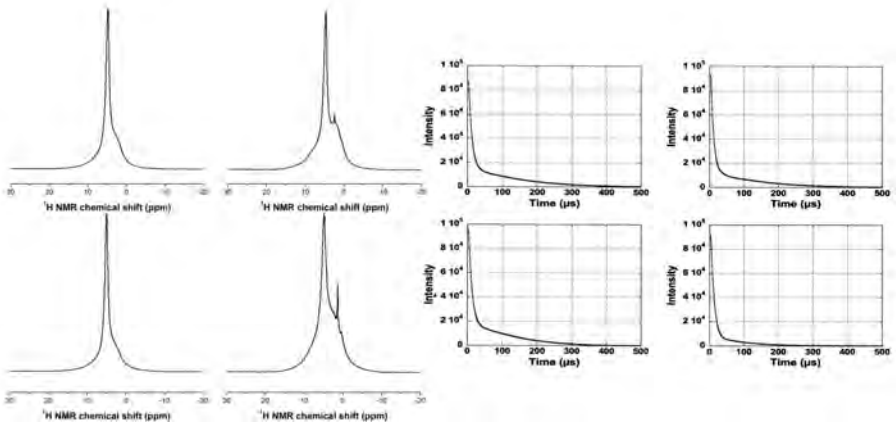

Figure 8.19: Left: ^{1}H MAS NMR spectra of ZnO and ZnO:Al 2 % powders after the DA anneal (top/bottom left) & ZnO and ZnO:Al 2 % powders after the RA (top/bottom right).
Right: ^{1}H-wideline NMR T_2 relaxation curve fits of ZnO powder and ZnO:Al 2 % after anneal in DA (top/bottom left) and ZnO powder and ZnO:Al 2 % after reductive anneal (top/bottom right).

Table 8.4: The T_{2H} decay times (μs) and their corresponding molar proton fractions (%) are presented in the following Table.

Specimen	T_{2H}^S (μs)	I_0^S (%)	T_{2H}^L (μs)	I_0^L (%)
ZnO before RA	10	86	160	14
ZnO after RA	9	90	153	10
ZnO:Al 2 % before RA	10	84.5	143	15.5
ZnO:Al 2 % after RA	10	94.5	116	5.5

As hydrogen, present in the RA gas mixture, is also reported to be a shallow donor for ZnO, ^{1}H MAS NMR is applied to check the presence of protons in the ZnO and ZnO:Al 2% samples before and after RA (Figure 8.19). In the MAS spectra before RA, a sharp signal is superimposed on a rather broad band, indicating the presence of a mobile (sharp signal) and rigid (broad signal) proton fraction. For the reductively treated powders, the relative contribution of the broad component clearly increases. In addition a very sharp signal on top of the shoulder is present around 2.5 ppm for ZnO and 1.4 ppm for ZnO:Al 2%. After RA, the 2% ZnO:Al relatively contains the lowest amount of mobile

proton species, represented by the sharp signal, while a larger amount of protons accounts for the broad signal, indicating the hydrogen reservoir. This is confirmed by ^{1}H-wideline NMR T_2 relaxation studies, showing the presence of a small mobile proton fraction (5.5%) with a decay time in the order of 100 μs, next to a large rigid proton fraction (94.5%) with a decay time in the order of 10 μs (Table 8.4). The latter is clearly stronger bound inside the ZnO lattice. For ZnO, the obtained conductivity after RA is probably due to H interstitials as a larger fraction of strongly bounded protons is found for the reservoir (90 versus 86%; see Table), but probably also by zinc interstitials. Al-doped ZnO benefits from the hydrogen reservoir, Al-doping and zinc interstitials. As already stated by *Li et al.*, intrinsic zinc interstitials and extrinsic Al dopants will generate a higher surface carrier density which also results into an increased stable conductivity inside ZnO:Al films.[161] More Al incorporation is accompanied by a larger hydrogen reservoir.

8.6 Deterioration of the conductivity in function of time

Table 8.5: Hall-bar measurements (resistivity ρ, carrier concentration n_{e-}, and mobility μ) of ZnO:Al 2 % films directly after the RA and after two months of degradation by exposure to air.

Time influence	ρ (Ohm cm)	n_{e-} (cm−3)	μ (cm^2 V^{-1} s^{-1})
No aging	2.88 10^{-3}	1.17 10^{20}	18.5
Aging (2 months)	5.96 10^{-3}	0.83 10^{20}	12.6

Finally, another important effect, which is often neglected, is the time effect after obtaining a functional transparent conductive oxide. Once the RA has been applied, the properties are sufficient to function in a device as a TCO. However, over time, the characteristics deteriorate. To assess their lifetime, we need to understand the aging effects on the ZnO:Al 2 % film/powder after the RA. It has been reported that the sheet resistance of AZO layers increases in case of storage in ambient conditions.[111, 213] Also here, an increase in resistivity is observed. This is the direct result of a decrease in carrier concentration and a drop in mobility, as displayed in Table 8.5. This decrease of charge carrier density is also confirmed by the red shift in the FTIR spectra in Figure 8.20a.[133] For the GATR spectra in Figure 8.20c, this effect can't clearly be distinguished. The link with the Al dopant position, as determined by NMR, can be found in the refill of a VI coordination and the correlation between the disappearances of the distorted IV coordination. The observed cause of the shift of Al coordination might be due to a refill of oxygen vacancies, countering the Zn

interstitials or by abolishment of the passivation of defects. To investigate the role of H, either as shallow donor or to passivate some defects ^{1}H MAS NMR spectra were recorded in function of time, but no direct conclusion could be drawn from these results since the hydrogen reservoir either increased or decreased. The exact reduction mechanism of the conductivity is not completely clear, but it is certain that FTIR, GATR and Hall-bar can verify the survival of some charge carriers with time. As the mobility drops, there is an indication that other mechanisms are also at hand which deteriorate the conductivity, like for example a surface effect. The exposure to air and its influence on the sheet resistance is ex-pressed in Table 8.6. The longer the exposure lasts, the higher the sheet resistance will become, which evidently is easier for less dense films.

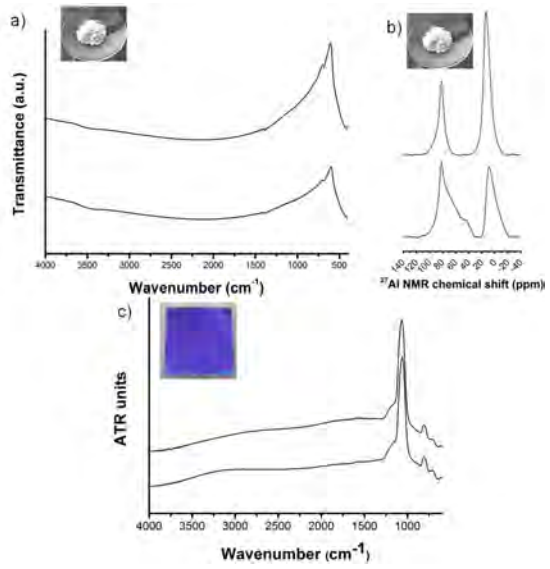

Figure 8.20: a) FTIR spectra and b) ^{27}Al MAS NMR spectra of ZnO:Al 2% powders after RA as monitored in time (top). c) GATR spectra of ZnO:Al 2% films after RA as monitored in time (below). The top spectra are obtained after approximately one year of aging in static air.

8.7 Overview of factors influencing the conductivity in Al-doped ZnO films

All the parameters summarized in Table 8.6 influence the sheet resistance (↑: increasing or ↓: decreasing), some in correlation to Al doping (indicated by X). As a general conclusion for all these experimental observations, it is clear that the film's conductivity is affected by a large number of factors. Since no etching of grains is observed after RA, nor ionized impurity scattering is confirmed, these effects are displayed and supported by literature. Also, the

influence of metallic Zn/Al on the conductivity cannot be excluded, although a Knight shift is observed up to 2 % of Al doping. Further on, no impurity phases have been found, although their influence is acknowledged. The role of oxygen and oxygen adsorbed species are covered in different effects listed in Table 8.6 as explained during this discussion. In this work, we have taken a holistic approach and studied a wide variety of factors influencing the performance of aqueous solution deposited AZO films.

8.8 Towards low temperature aqueous sol(ution)-gel processing

Although this aqueous route is very attractive from an environmental point of view, it is still a high temperature route. With the recent trend towards flexible displays and from an economical point of view, it would be of interest to synthesize of low T conductive n-type doped ZnO. Although this in-depth study, presented in the previous sections, generates profound insights in the conductivity mechanism of Al-doped ZnO, no low temperature route can be established with this precursor without adaptation. Therefore A Zn precursor needs to be adapted using combustion chemistry or can be decomposed using UV treatment.

8.8.1 UV treatment

UV treatment of sol-gel based systems dates back from the beginning of the nineties (previous century) when reports where made on the densification [199] and the crystallization of amorphous films [120]. Additionally, the use of UV is applied to reduce the crystallization temperature of the oxide, although some heating is still needed. [71] The applicable sol-gel systems are those with $\pi \longrightarrow \pi^*$ as molecular electronic transitions. These transitions are assigned to free carboxylate groups or intra ligand transitions.

An UVO_3 setup without tunable UV system is at our disposal. This apparatus is mainly used for cleaning and to ensure hydrophilic wettability of substrates.[137] Energetic photons in the UV light induce electronic excitation, rather than thermal excitation (IR), promoting chemical reactions. This results in an activation of (in)organic species through radicals and ozone. The UVO_3 equipment emits wavelengths of 185 nm and 254 nm, which are discharged by a low-pressure mercury tube. The 185 nm line produces ozone [43], while the 254 nm line excites organic molecules [154].

A preliminary experiment was done to test the applicability of the 2% Al-doped Zn aqueous citrato precursors. Instead of applying hotplate treatment at 300 °C and 450 °C, the spin coated layer on top of SiO_2 (200 nm)/ Si substrates (3000

rpm, 30 s, 1000 rpm/s) was briefly treated (1 min) at 100 °C to remove the solvent (water). Afterwards the gel was treated with UVO_3 at 150 °C for 1 hour. This resulted in a detection of the wurtzite crystal structure with XRD with a preferential (002) orientation (Figure 8.21). Nevertheless no conductivity was measured.

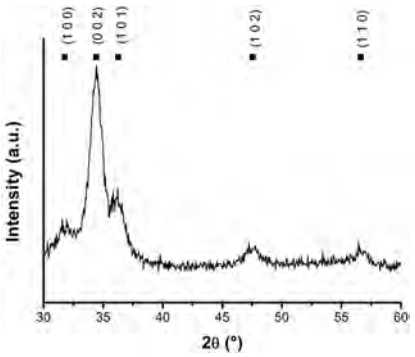

Figure 8.21: Grazing incidence diffraction of 2% ZnO:Al films

Although the use of UV radiation crystallizes ZnO at temperatures below 200 °C, the applicability of this technique is rather small. UV radiation has only a limited penetration depth ($\sim$ 100 nm). In addition no conductivity was measured, creating no direct applicability as TCO. Therefore it would be of interest to tune the existing precursors to possible high-throughput processes.

8.8.2 Combustion processing in aqueous precursors with different fuels

An aqueous sol(ution)-gel precursor with citric acid

An alternative route for aqueous sol-gel precursors can be found through combustion processing as discussed in the introduction 1.5.4 (Chapter 1). Citric acid, the used complexing agent can also act as a fuel, while an oxidizer needs to be added. [291] NH_4NO_3 is one of the smallest oxidizers and can be easily dissolved in water. As a test experiment the 0.1 M 2% Al-doped Zn precursor was used, while the amount of NH_4NO_3 was varied from 0.1 M, 0.3 M to 0.6 M. This variation was studied by thermo-gravimetric analysis. As the content of NH_4NO_3 increases, the total thermal budget is reduced to a one-step exothermic thermal decomposition at 200 °C.

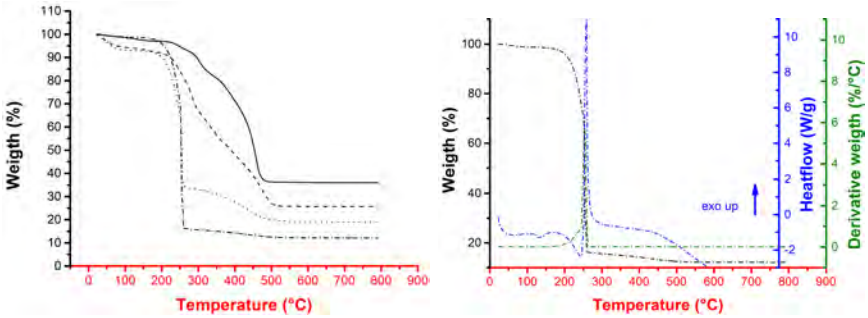

Figure 8.22: Thermogravimetric analysis of 2% Al-doped Zn precursors with different amounts of NH_4NO_3 (left): the citrato Al-doped Zn precursor without NH_4NO_3 (full line), with 0.1 M NH_4NO_3 (dashed line), with 0.3 M NH_4NO_3 (dotted line) or with 0.6 M NH_4NO_3 (dashed-dotted line). TGA (black), DTA (green) en DSC (blue) of the 0.6 M NH_4NO_3 2% Al-doped Zn precursor (right).

An aqueous sol(ution)-gel precursor with glycine

Alternatively a glycine based aqueous precursor is developed. *Exarhos et al.* reported in 1995 already the aqueous solution processing of $Zn(NO_3)_2 \cdot 6\,H_2O$ with glycine ($C_2H_5NO_2$) as a fuel, which is also believed to be a cation complexant. [85] If a comparison is made between the combustion heat of citric acid(-14 cal/ mol) and glycine, glycine generates -43 cal/ mol. This means that less glycine is needed to created the same amount of combustion heat, which can be an advantage. On the other hand, one has to take into account that a more explosive combustion reaction could generate a less adequate film morphology without uniform coating and cracks and holes.

A 50 mL precursor of 0.5 M $Zn(NO_3)_2 \cdot 6\,H_2O$ was prepared with 1 at% of Al doping through addition of $Al(NO_3)_3 \cdot 9\,H_2O$ by dissolution in a 0.5 M glycine solution. 0.5 M NH_4NO_3 was added to raise the amount of oxidizer. The thermal decomposition of this precursor was studied by thermogravimetric analysis in Figure 8.23. TGA, DTA and DSC analysis was done in function of time (directly after synthesis and after one week) on a 20 μL dried precursor. Directly after synthesis a gradual thermal decomposition is seen with weight loss up till 400 °C. The DSC analysis shows a strong exothermic signal around 200 °C, which gradually decreases and around 400 °C a smaller exothermic signal is also visible. After one week of aging, the gradual thermal decomposition is modified to one exothermic peak at 200 °C. This one-step exothermic signal generates more W/ g during combustion. Although the one-step combustion reaction seems to go to completion, a small fraction of weigth loss is still observed around 400 °C. This gradual thermal degradation transforms to a one-step combustion processing in function of 'aging' of the precursor. The ongoing combustion

reaction is given in Equation 8.6, which could be further investigated with coupled thermo-gravimetric techniques like TGA-MS and FTIR.

$$4Zn(NO_3)_2 + 4NH_4NO_3 + 4C_2H_5NO_2 \longrightarrow 4ZnO + 8CO_2 + 18H_2O + 10N_2 + 3O_2 \tag{8.6}$$

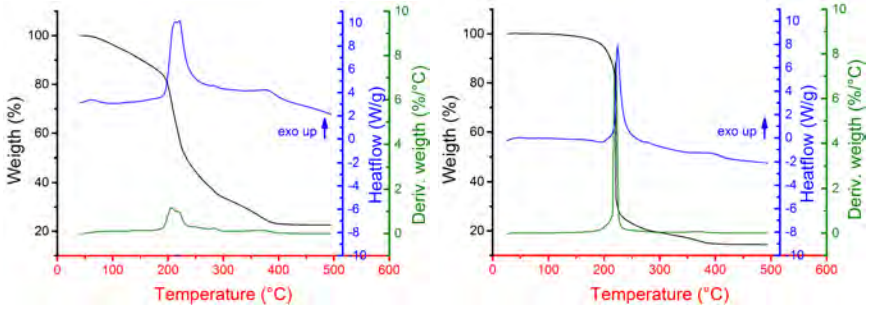

Figure 8.23: Thermogravimetric analysis: TGA (black), DTA (green), DSC (blue) of 1% Al-doped Zn precursors directly after synthesis and after one week of aging.

Even though the thermo-gravimetric analysis will generate more in-depth knowledge on the combustion reaction, the main focus is to be able to turn this precursor into a conductive Al-doped ZnO film through spin coating. Taking into account the amphoteric character of ZnO, a multi-layer spin coating deposition is limited by the pH of the precursor, which is 3. This acidic value impedes a straightforward deposition. The previous deposited layer will easily dissolve into another precursor solution. Nevertheless, it implies that the carboxylic group of glycine is deprotonated (pKa_1=2.34 and pKa_2=9.60) and makes it possible to be used as a complexing agent. Additionally there will almost be no wetting of the second layer of the precursor and the deposition will already be macroscopically impossible (Figure 8.24). (First layer deposited through spin coating (3000 rpm 30 s 1000 rpm/s) and heat treated on a hot plate at 250 ℃ for 5 min.) Therefore the pH is raised up to 7 with NH_3. While raising the pH, precipitation (from what is believed to be) Al-doped $Zn(OH)_2$, occurs.

Figure 8.24: Picture of one deposition cycle of the glycine based 1% Al-doped Zn precursor on top of a SiO_2 (200 nm)/Si SPM/APM cleaned substrate. (left) Second deposition cycle of the glycine based 1% Al-doped Zn precursor on top of a SiO_2 (200 nm)/Si SPM/APM cleaned substrate which generates macroscopically non-uniform morphologies.(right)

If NH_4NO_3 is removed from the aged precursor solution and the same ratio for glycine and the metal nitrates are retained for a 1 M precursor solution, the thermo-gravimetric analysis after aging of the precursor looks the same as in the righter figure of Figure 8.23. The TGA, DTA and DSC of the glycine based precursor without NH_4NO_3 are displayed in Figure 8.25. Again, an exothermic combustion process is visible around 200 °C. Also the wetting and coverage looks to be improved during spin coating.

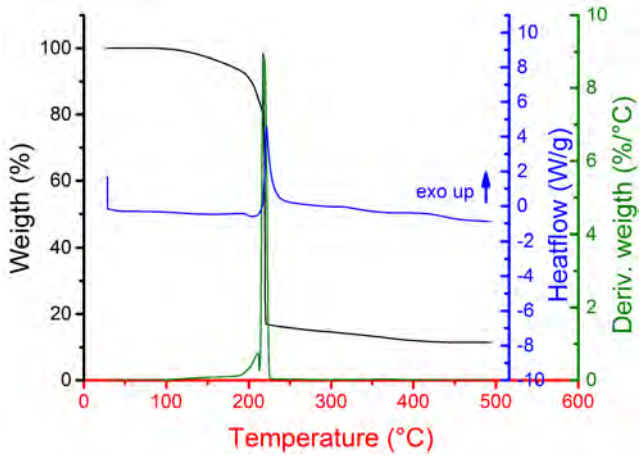

Figure 8.25: Thermogravimetric analysis: TGA (black), DTA (green), DSC (blue) of 1% Al-doped Zn precursors after aging.

Nevertheless as the pH of the precursor still is acidic, the multi-layer deposition technique is impeded. Therefore additional ZnO or Al-doped ZnO powder was added to the precursor, until it is completely saturated. Afterwards the excess of ZnO(:Al) was centrifuged into the pellet and afterwards the precursor was

filtered. The saturation of the precursors significantly improved the wetting of the NH_4NO_3 containing precursor. The saturated glycine and glycine/NH_4NO_3 1 % Al-doped Zn precursor were compared. Three layers of these precursors were deposited on chemically cleaned SiO_2 (200 nm)/Si substrates [277] and treated on a hot plate in static air for 5 min at 250 °C followed by one hour UVO_3 treatment at 150 °C. For the NH_4NO_3 containing precursor the UVO_3 treatment was also omitted. The XRD results and SEM images are presented in Figure 8.26 and Figure 8.27. The only glycine containing precursor does not induce the formation of crystalline (Al-doped) ZnO within the detection limits of the apparatus. If the precursor contains NH_4NO_3 crystalline ZnO(:Al) can be found. UVO_3 improves this crystallinity a bit. SEM images also show the presence of this material, although it is present in chunks and the layers are not completely connected. This morphology needs to be further improved to obtain TCO characteristics.

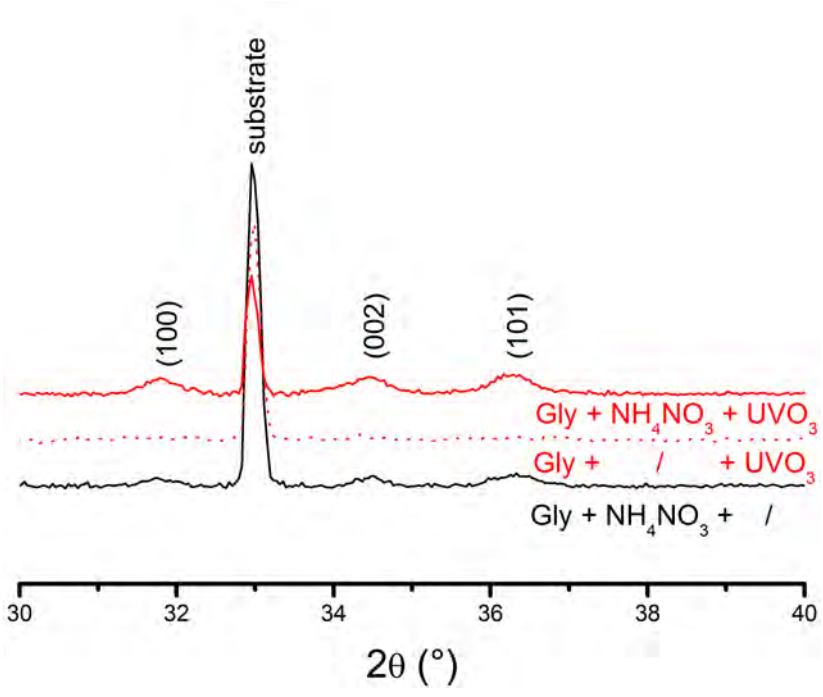

Figure 8.26: XRD analyses of (Al-doped) ZnO films from saturated glycine combustion precursor with or without NH_4NO_3 and with or without UVO_3. The films from the precursor with NH_4NO_3 indicate minor formation of the wurtzite crystal lattice.(JCPDS library file 36-1451)

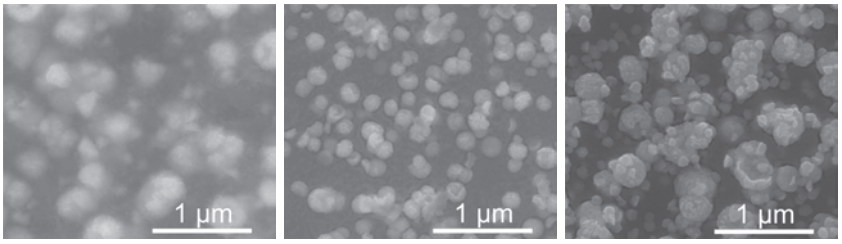

Figure 8.27: Left: SEM images of 3 L of the 1%Al-doped Zn Gly/NH_4NO_3 precursor deposited on SiO_2 (200 nm)/Si substrates treated at 250 °C for 5 min.
Middle: SEM images of 3 L of the 1%Al-doped Zn Gly precursor deposited on SiO_2 (200 nm)/Si substrates treated at 250 °C for 5 min and at 150 °C for 1 h with UVO_3.
Right: SEM images of 3 L of the 1%Al-doped Zn Gly/NH_4NO_3 precursor deposited on SiO_2 (200 nm)/Si substrates treated at 250 °C for 5 min and at 150 °C for 1 h with UVO_3

8.9 Conclusion

Many factors affect the film conductivity as summarized in Table 8.6. Key to obtaining a competitive resistivity, which is 10^{-3} Ohm cm in the order of typical sputter and solution processed films (though still higher than the best sputter deposited films), is the application of a reductive anneal at moderate temperatures in a hydrogen containing atmosphere. Therefore, the effect of the RA was investigated and the following in depth understanding was obtained.

The reductive anneal leads to the desorption of oxygen and hole formation. This adverse effect is reduced by Al incorporation and enhanced by applying high temperatures during RA. Optimal settings for this parameter are 2 % Al and annealing at 500 °C in a 5 % H_2/ 95 % He containing atmosphere. The mechanism behind the reductive anneal is more complicated than solely morphological changes. It further beneficially leads to the removal of the O excess that was induced by Al^{3+} doping, thereby activating the Al doping, and creating electrons for the conduction band, originating from aluminum or from hydrogen. Besides, adsorbed oxygen species at the surface, which increase the resistivity, are also removed in this way.

Further on, this reductive anneal is responsible for a rearrangement of the Al coordination, as indicated by a combination of NMR methods. These results allowed to estimate the amounts of octahedral and tetrahedral Al doping. The latter can through relaxation measurements be subdivided into interstitial and substitutional Al. The RA induces distortions of the increased tetrahedral Al coordination. Both interstitial and substitutional tetrahedral Al increase,

which goes hand in hand with a diminishing octahedral fraction. All these effects enhance the conductivity. Minor formation of penta-coordinated Al was evidenced as well, but is assumed not to be the major reason for the improved conductivity. Finally, the Al incorporation increases the content of a rigid H reservoir as observed by H NMR. This is assigned to interstitial H, which is beneficial to improve the conductivity.

Although the RA assists O desorption, leaving metallic zinc behind, XPS shows that no metallic Zn or Al is formed at the film surface. This cannot completely exclude the presence of metallic Zn in the bulk of the film, and the beneficial contribution to the conductivity of the AZO film cannot be overlooked completely.

In function of time it can be stated that, although charge carriers are still present after one year shelf life, the negative effects overtake the mechanism empowering the conductivity and destroying the mobility in the system. The exact origin of the reduced conductivity is also expected to be a combination of several factors. Shifts in Al coordination, refill of oxygen vacancies and the nullification of the passivation of defects are linked to this decreasing conductivity.

The thickness of the AZO films produced by the aqueous solution processing presented here is limited by its synthesis method. This system also did not reach a resistivity in the order of 10^{-4} Ohm cm, as observed in certain sputtered films. However, a detailed study as presented here, is often lacking for such films and gives new, profound insights into the mechanism behind conductive Al-doped ZnO films. Therefore, it would be of interest to extrapolate and compare these results to sputtered AZO systems or to (low temperature) chemical bath deposited films.

In addition the development of low temperature thermal decomposing precursors, either by UV or by adaptation through combustion processing, is realized. While adding ammonium nitrate to the precursor destroyed the wetting in a multi-layer deposition, this can be overcome by saturation of precursor with (Al-doped) ZnO powders. Further on, the presence of ammonium nitrate seems to be necessary to develop crystalline ZnO directly after hot plate treatment at 250 °C. This crystallinity can be a bit improved by additional UVO_3 treatment. Although the obtained insights for high temperature processed conductive AZO currently have not contributed to the understanding of the non-conductive low temperature processed AZO, a first step is set towards fundamental understanding. In the future, this study may contribute to the optimization of low temperature processed conductive AZO.

Table 8.6: General overview of different influences (left column) on the sheet resistance (middle column) of Al-doped ZnO films. If there is a correlation with the Al doping this is displayed in the right column with an X.

Effect	Influence on R	∼Al	Comments	References
Reduction	↓		overview of interactions with H	x
↗ T during RA	↓	X	Threshold too high T	x
H etch of O	↓	X	$Al_xZn_{(1-x)}O_{(1+\frac{x}{2})} + (\frac{x}{2}+\frac{y}{2})H_2 \longrightarrow H_yAl_xZn_{(1-x)}O + \frac{x}{2}H_2O$	x
Grain boundary etching	↓		small grain to large ones	[21]
H shallow donor	↓	X	$ZnO_{(1+\frac{x}{2})} + (x+\frac{y}{2})\ H_2 \longrightarrow H_yZnO + \frac{x}{2}H_2O$	x
Activation of Al	↓	X	Removal adsorbed oxygen species ↘ VI, ↗ IV, ↗ IV_{sub}	x
$Zn^{\bullet}/Al^{\bullet}$	↓		$ZnO + (x)\ H_2 \longrightarrow ZnO_{(1-\frac{x}{2})} + xH_2O$	[140]
Oxidation	↑		overview of interactions with oxygen	x
Exposure to air	↑		Aging of film after RA with $n_e \downarrow$ and $\mu \downarrow$	x
Impurity phases	↑	X	$ZnAl_2O_4$ and Al_2O_3	[69]
Porosity	↑		Low $M_{precursor}$: denser films	x
Ionized impurity scattering	↑	X	$> n_e - 10^{21}$ cm^{-3}	[179]
Grain boundary scattering	↑	X	Grains ↘ with ↗ Al %	x

Summary and outlook

After setting the framework of this manuscript by a overview of the available literature it appears that ZnO is a very attractive and cheap material as transparent conductive oxide. The conductivity can even further be improved by n-type doping. (p-type doping for ZnO is up to today not possible.) Generally trivalent elements such Al, Ga and In are used for n-type doping, although Cl-doping of ZnO is even done, but only by electro-deposition. Within this invesitgated field of solution processing, different pathways can be distinguished: a nanoparticulate route, molecular precursors or direct synthesis. Although direct synthesis through chemical bath and electro-deposition is able to obtain Al-doped ZnO and Cl-doped ZnO at low temperature ($< 100\,°C$) this method is neglected.[111, 227] From an upscaling point of view, this method is quite cumbersome due to the need of large vessels of reagents and the production of a lot of waste. Therefore the focus is put on nanoparticles and molecular precursors, which can be directly applied in more divers deposition techniques. The versatility of these routes is more widely spread. Although the deposition technique of choose here is spin coating, which is easy on a laboratory scale, the suspensions/solutions could be even applied in spray coating or ink-jet printing, provided with adaptations towards viscosity.

In the first part different synthesis routes for Al-doped ZnO nanoparticles have been explored from co-precipitation to thermal decomposition synthesis. Although each method certainly has its advantages, some shortcomings need some additional care.

Co-precipitation is able to synthesize nanoparticles with a high yield. Nevertheless the morphology obtained here is not so clear: no real spherical particles are observed, with here and there an exception. For the incorporation of Al inside the lattice, different atmospheres during calcination could steer Al allocation in a minimalistic way. The calcination in nitrogen seems to be able to push the Al more in the substitutional tetrahedral place, although no real high values have been obtained. None of this favors the use of these nanoparticles. It might be of interest to precipitate the nanoparticles under elevated temperatures, giving the dopant more energy to be substitionial tetrahedral incorporated.

Further on, the thermal decomposition of Al-doped ZnO nanoparticles is studied in-depth. Either dibenzyl ether or benzyl amine was used as a solvent for the dissolution of Zn and Al acetylacetonates. In dibenzyl ether, an in-situ stabilization method was developed where surfactants are used to tune the size and shape during synthesis. The mechanism from reagents to Al-doped ZnO nanoparticles is elaborated, showing the versatility of obtaining doped oxides through this method. After synthesis, the used ligands are chemisorbed to the nanoparticle surface to ensure steric stabilization of nanoparticles. In that manner a stable apolar suspension in hexane (or other apolar solvents) can be obtained, which can be used directly for deposition. In the end, a conductive AZO film was obtained from these building blocks. Nevertheless, still elevated temperatures are needed to remove the ligands. Further on, increased temperatures might be needed to induce grain growth and significantly reduce grain boundary scattering. Although these ligands can be exchanged to electrostatic stabilization, which can be removed at lower temperature, the questions asked are if this is sufficient to ensure conductivity throughout the films. So far every effort towards low temperature conductive AZO films has been unsuccessful.

The thermal decompostion in benzyl amine generated a high amount of rod-like nanoparticles. The obtained suspension in ethylene glycol was stable without any additives. The nanorods were intensively studied by ^{27}Al MAS NMR analysis and the largest fraction of substitutional tetrahedral Al allocation was found. This, together with the morphology, make these NRs the ideal building blocks for TCO films. Nevertheless after deposition and impregnation with a molecular precursor, that served as a glue, no improved conductivity (in correlation to pure molecular precursors) was obtained. Probably the grain boundary scattering is the dominating effect and charge carriers, which should be present in high quantities, can't be extracted from the NRs nor are mobilized through the film.

Although stable suspensions could be obtained, additional high temperature treatments are necessary each time to introduce measurable conductivity. Sintering of nanoparticles is very important and can only happen close to the melting point of the material. To reduce this temperature, very small particles are necessary. Whether these nanoparticles have a future to obtain good conductive TCOs is really the question and could be resolved by exploring further low temperature sintering methods. Laser sintering is often put forward in literature as a low temperature sintering method, although simulations show the development of local high temperatures. If low temperature sintering is really possible needs to be investigated by future work. Other sintering methods such as combustion processing might also improved the conductivity of films from NPs. A key point in figuring this out might be resolving how and why chemical bath deposition of Al-doped ZnO and electro-deposition of Cl-doped ZnO is able to obtain conductive layers.[111, 227] Nevertheless a lot of new funda-

mental insights in the chemistry behind NP synthesis have been presented and could improve the way of synthesizing building blocks for TCOs.

The second part focused on molecular or sol(ution)-gel precursors, which are obtained by the dissolution of proper metal ion containing reagents. A holistic approach has been taken to synthesis n-type doped ZnO and to understand the fundamentals behind synthesis and the functional characteristics. Hereby the focus was mainly put on Al-doped ZnO since this is to most attractive way of doping ZnO. Not only is Al abundantly available it is non-toxic and cheap. Further on the characteristics of Al-doped ZnO exceed the conductivity and transparency of In and Ga-doped ZnO in most cases.

First of all, the focus has been put on organic precursors. Butoxyethanol based precursors have been developed, which have proven to be a good alternative for teratogenic solvents such as methoxyethanol. A minimal sheet resistance of only 57 Ohm/ □ is obtained. In addition, it has been obvious that the TCO layer needs to have a minimal thickness to avoid surface effects. This thickness is strongly correlated to the molarity of the applied precursor and resulted in an improved conductivity for lower precursor concentrations.

Alternatively, aqueous citrato precursors were developed to obtain n-type doped ZnO films. Al, In, Ga and Cl have been tested. In the end a 2% ZnO:Al film results in the lowest obtained resistivity of 1.77 10^{-3} Ohm cm with the highest transparency within the visible range after an anneal at 450 ℃ in a 5 % H_2/ 95 % Ar atmosphere. The good characteristics of Al-doped ZnO (after RA), together with the abundant availability, non-toxicity and the reduced price of both Al and Zn, make AZO the ideal candidate as TCO. In addition synthesis of very good conductive ZnO with a sheet resistance as low as 676 Ohm and a resistivity of 4.93 10^{-3} Ohm cm is achieved. Nevertheless, through the reduced transparency the presence of metallic Zn can be hypothesized. Although In and Cl-doping don't lead to an improved conductivity in comparison to ZnO, the transparency is significantly better. Nevertheless, as Cl-doping leads to a reduced thickness of the ZnO:Cl layer, the presence of Cl inside the layer can be questioned. Probably this method, due to the reductive treatment, is non-ideal to guarantee Cl-doping. Also Ga-doping improves the conductivity and the transparency but Al-doping is certainly the most elegant dopant of aqueous chemical solution deposition method.

Because of the establishment of Al-doping to be the most adequate aqueous dopant, the mechanism behind the conductivity was investigated. The key to obtaining a competitive resistivity, which is 10^{-3} Ohm cm in the order of typical sputter and solution processed films (though still higher than the best sputter deposited films), is the application of a reductive anneal at moderate temperatures in a hydrogen containing atmosphere. Therefore, the effect of the

reductive anneal was investigated and the following in depth understanding was obtained.

The temperature of the reductive anneal plays a role in solution processing of ZnO and can easily remove the complete layer when it is too high or the treatment takes too long. Depending on the dopant and on the equipment/ inert gas, this temperature can vary. This is achieved through oxygen removal through reaction with hydrogen of the RA. Although there are a lot of controversial thoughts on the role of oxygen in solution processed (doped) ZnO, it is without doubt that oxygen has an influence. The reductive anneal leads to the desorption of oxygen and hole formation and activates the Al-doping by a shift of octahedral to tetrahedral coordination, also a small fraction of penta-coordinated Al is observed. Additionally the observed oxygen species at the grain boundaries and surface are removed. This surface has a big influence on the resistivity as observed before, but for denser layers a thinner layer is sufficient to counter these effects. In addition to the Al reorganization, a H reservoir was found after RA, which was larger for Al-doped films. As oxygen is being removed during RA, metallic Zn is left behind. This can easily vaporize at high temperatures, although for pure ZnO (treated at lower temperature) this is hypothesized to attribute to the improved conductivity. For doped films, it has not been found so far.

Good transparent and conductive films have been obtained through (aqueous) solution processing, from which the organic precursor seem to produce more stable films in function of time. For the aqueous deposited films this has been monitored in function of time. In function of time it can be stated that, although charge carriers are still present after one year shelf life, the negative effects overtake the mechanism empowering the conductivity and destroy the mobility in the system. The exact origin of the reduced conductivity is expected to be a coherence of several factors. Shifts in Al coordination, refill of oxygen vacancies and the lifting of the passivation of defects are linked to this decreasing conductivity.

Nevertheless, all these molecular precursors still needs high thermal treatments to obtain good conductive layers. As an alternative a low temperature decomposing precursor in 2-methoxyethanol was developed with metal acetylacetonates and ammonium nitrate. Insights in the thermal decomposition of combustion chemistry and the optimization of the morphology have rendered conductive In-doped ZnO layers at a maximum temperature of only 240 °C. Nevertheless the conductivity decayed easily and requested further improvement in morphology. The applied temperature of the hot plate, the molarity and the use of dopants generates significantly different looking films. Although no conductive Al-doped ZnO films could be obtained, general insights in the combustion chemistry are presented to improve further investigations. Further

explorations on the deposition temperature, with maybe UV treatment, could render conductive layers. Nevertheless, this should be further investigated.

In addition the development of low temperature decomposing precursors was further explored for aqueous precursors. The citrato precursors is able to decompose at low temperature, either by UV or by adaptation through combustion processing with NH_4NO_3. Alternatively a glycine based combustion precursor was developed either with or without additional NH_4NO_3. Although, this extra oxidizer is not necessary for a low temperature decomposition according to thermogravimetric analysis and it even destroys the wettability in a multi-layer deposition process like spin coating. By saturating the one with NH_4NO_3 (and the precursor with only glycine) with additional (Al-doped) ZnO powders, multiple layers can be deposited. In addition to a macroscopically better morphology, microscopically still improvements are necessary to have a fully closed layer. Nevertheless if NH_4NO_3 is present inside the saturated precursors, crystalline ZnO can be detected in the film, indicating an improved nucleation. Saturating the precursor as well as NH_4NO_3 results in improved characteristics.

Alternatively, *Weber et al.* published an aqueous based method to deposit on low temperature crystalline In and Ga-doped ZnO. [288] This method seems promising and is of interest to further explore as a facile route for low temperature deposition of Al-doped ZnO as TCO in PV devices.

The obtained insights for high temperature processed conductive AZO currently have not contributed to the understanding of the non-conductive low temperature processed AZO, but a first step is set towards fundamental investigations. In the future, this study will be able to contribute to the optimization of low temperature processed conductive AZO and can be compared to recent publications [288] [111] [227] on low temperature deposition of crystalline n-type doped ZnO, which may or may not render conductive films.

.

List of Abbreviations

$\bar{x}$	Average size
χ_i	Electronegativity of metal ion
χ_M^*	Allred-Rochow electronegativity of metal ion
χ_s	Electronegativity of solvent
ϵ_r	Dielectric constant
η	Viscosity
γ	Gyromagnetic ratio
λ	Wavelength
λ_p	Plasma wavelength
μ	Magnetic moment
μ	Mobility
μ	Polarity
ν	Frequency
ν_L	Larmor frequency
ϕ_e	Equivalence ratio in combustion processing
ψ_0	Surface potential
ψ_s	Stern potential
ρ	Resistivity
σ	Electrical conductivity
σ_i	Dimensionless shielding constant
τ	Average scattering time

θ	Bragg angle
$\tilde{\nu}$	Wavenumber
$\triangle$E	Band gap
ε	Molar absorptivity
ε	Zeta potential
k_B	Boltzmann constant
N_0	Number of protons in the lower energy state
N_j	Number of protons in higher energy state
(σ	Standard deviation
(G)ATR	(Grazing Angle) Attenuated Total Reflectance (Spectroscopy)
abs.	Absorption
ACSD	Aqueous Chemical Solution Deposition
AFM	Atomic Force Microscopy
$Al^{[4]}$	Tetrahedral coordinated Al
$Al^{[6]}$	Octahedral coordinated Al
AZO	Al-doped Zinc Oxide
B	Bound
B	Line broadening at FWHM
B	Magnetic field
b	Path length
BF	Bright Field
c	Speed of light
C_p	Heat capacity
c'	Concentration
CA	Citric acid
CB	Conduction band
CCD	Charge-Coupled Device

CIGS	Copper Indium Galium (di)Selenide
COSY	Correlation Spectroscopy
CSA	Chemical Shift Anisotropy
CVD	Chemical Vapor Deposition
CW	Continuous wave
D	Crystallite size
D	Translational diffusion coefficient
d	Thickness
DA	Dry air (anneal)
DAS	Dynamic Angle Spinning
DF	Dark Field
diffr.	Diffraction
DLS	Dynmaic Light Scattering
DOR	Double Rotation
DOSY	Diffusion Ordered Spectroscopy
E	Electric field force
E	Electric field
e	Charge carrier
E_b	Binding Energy
E_k	Kinetic Energy
EDX	Energy Dispersive X-ray
EGA	Evolved Gas Analysis
EM	Electromagnetic
em.	Emission
en	Ethylene diamine
EXSY	Exchange Spectroscopy
F	Lorentz force

FID	Free Induction Decay
fl.	Fluorescence
FPM	Full Peak Model
FTIR	Fourier Transform Infrared (Spectroscopy)
FWHM	Full width half maximum
H	Enthalpy
h	Planck constant
HAADF	High-Angle Annular Dark-Field Imaging
headspace GC-MS	Headspace Gas Chromatography Mass Spectrometry
HRTEM	High-Resolution Transmission Electron Microscopy
I	Current
I	Spin quantum number
I_{sp}	Specific Impulse
ICP-AES	Inductively Coupled Plasma Atomic Emission Spectroscopy
ITO	Indium Tin Oxide
k	Boltzmann's constant
k	Shape factor (Debye-Scherrer)
LCS	Low temperature combustion synthesis
m*	Effective mass
MAS	Magic Angle Spinning
MOCVD	Metal-Organic Chemical Vapor Deposition
MQ	Multiple-Quantum
MS	Mass Spectrometry
N	Carrier concentration
N	Coordination number
n	Carrier density
NB	Non-Bound or free

NIR	Near Infrared
NMR	Nuclear Magnetic Resonance (Spectroscopy)
NOESY	Nuclear Overhauser Effect Spectroscopy
NP	Nanoparticle
NR	Nanorod
OPV	Organic photovoltaics
P	Transmitted radiant power
p	Angular momentum
P_0	Incident radiant power
PCS	Photon Correlation Spectroscopy
PLD	Pulsed Laser Deposition
PVD	Physical Vapor Deposition
QCC	Quadrupolar coupling constant
R	Hydrodynamic diameter
r	Grain size
R_S	Sheet resistance
RA	Reductive anneal
refl.	Reflectance
RMS	Root mean square
RPC	Revolutions per cycle
RPM	Revolutions/Rotations per minute
S_N^1	Dissociative nucleophilic substitution
S_N^2	Associative nucleophilic substitution
SAED	Selected Area Electron Diffraction
sc.	Scattering
SCS	Solution Combustion Synthesis
SEM	Scanning Electron Microscopy

SHS	Self-propagating high temperature synthesis
SPM	Scanning Probe Microscope
ST	Standard synthesis (thermal decomposition in dibenzyl ether)
STEM	Scanning Transmission Electron Microscopy
STM	Scanning Tunneling Microscopy
STP	Standard temperature and pressure
T	Temperature
t	Time
T_{ad}	Adiabatic temperature
TCO	Transparent Conductive Oxide
TEM	Transmission Electron Microscopy
TGA	Thermogravimetric Analysis
trans.	Transmittance
U_E	Electrophoretic mobility
V	Voltage
v	Velocity
VB	Valence band
VdP	Van der Pauw
w	Hydrolysis ratio
wf	Work function
XPS	X-ray Photo-electron Spectroscopy
XRD	X-ray Diffraction
z	Valency cation

Appendix:UV treatment of combustion processed In-doped Zn 2-methoxyethanol precursors to films

Often high temperature treatment is needed to render conductive ZnO:In films, but in view of low temperature deposition it is of interest to investigate alternatives. *Martins et al.* introduced the use of UV the remove surface adsorbed oxygen species, which enable the conductivity inside the films.[173] In addition, *Hagendorfer et al.* were able to initiate the conductivity of chemical bath deposited Al-doped ZnO at temperatures lower than 150 °C. [111] Therefore, the hypothesis is set that UV processing might be able to remove our deteriorating species and render conductive combustion processed ZnO:In films.

An optimized 1:1 (oxidizer:fuel) MOE 0.1 M precursor was prepared with varying In content; 0, 1, 2, 3, 4 and 5 at% In. 25 L of the precursor were deposited through spin coating onto chemically cleaned quartz substrates. Each layer is thermally treated on a hotplate in static air at 200 °C for 2 min. (The previously applied temperature treatment is reduced from 5 to 2 minutes.) Afterwards the complete stack is irradiated with an UVA lamp for 1 minute and the sheet resistance was quickly measured using a multi-meter to have an idea if this treatment works.

These films were analyzed with UV-VIS (before UV treatment) to verify whether they absorb in the UV and transmit visible light. The first characteristic is important to elucidate if UV treatment can be of use to obtain conductive ZnO:In films. From Figure 28 it is clear that all films absorb up to 80 % of the UV light for the ZnO:In, while the pure ZnO film absorbs even more than 90 % of this area. The average transmission for ZnO:In is above 80 % within the visible region, with an increase between 400 and 550 nm. For undoped ZnO the transparency is only 20 %, although there is a steep increase noticeable. Nevertheless at 800 nm wavelength the transmittance is still only 60 %. This is also macroscopically visible by a foggy, white-hazed film. Light with energy above the band gap is absorbed in band transitions. This effect occurs as an abrupt drop in transmission and increase in absorption at shorter wavelengths (<350 nm or 3.5 eV). This fundamental absorption edge shifts to shorter wavelengths

with increasing carrier concentration. The In-doped films display this blue or Burnstein-Moss shift in comparison to ZnO, which is known to be caused by the filling of states near the bottom of the conduction band.[225] The 1 % ZnO:In has the lowest average transmission of the evaluated ZnO:In films. Although the transparency of these films is quite low and extremely for ZnO, the ZnO:In films processed through combustion synthesis have some potential.

After UV-treatment the sheet resistance is analyzed with the multi-meter. For the pure ZnO, the 3 and 4 at% ZnO:In, the multi-meter was incapable to quantify the sheet resistance. The 1, 2 and 5 at% ZnO:In films have sheet resistances within the MOhm/□ area which decay quickly.

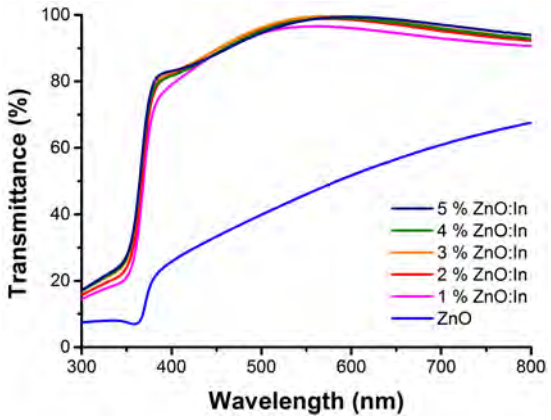

Figure 28: UV-VIS spectra of 25 L of a 0.1 M (In-doped) Zn precursor deposited through spin coating (3000 rpm, 30 s and 1000 rpm/s). Each layer was treated on a hotplate at 200 ℃ in static air for 2 min. In addition to pure ZnO films, 1, 2, 3, 4 and 5 at% ZnO:In films were evaluated.

1 Conclusion

Although no stable results are obtained with UV processing it might be a interesting route to further investigate.

Influence of temperature and gases

Different reductive annealing setups have been used as well as different inert gases, such as He, or the cheaper alternatives Ar and N_2. For the Al-doped ZnO series deposited through ACSD in Chapter 7 and Chapter 8. The sheet resistance was followed in function of doping percentages when applying either an anneal at 500℃ for 10 minutes in a 5 % H_2/ 95 % He atmosphere or at 450℃ for 10 minutes in a 5 % H_2/ 95 % Ar atmosphere (Figure 29). Although it isn't ideal to change two parameters (inert gas and temperature), some difference can be observed. Here it is clear that although the temperature in the 5 % H_2/ 95 % Ar atmosphere is lower, the lowest sheet resistance is obtained. This difference might be attributed by the various setup, heating/ cooling rate and temperature calibration applied for both apparatus. In addition, the difference in thermal conductivity is also expected to have an influence on the heat transfer and the annealing. The thermal conductivity, correlated to the temperature and pressure, of Helium is higher than the thermal conductivity in Argon. Additionally, the cooling rate is also different in various equipment. According to *Mei-zhen et al.* a faster cooling rate improves the conductivity. [176] The main message here is that although inert gases are used, it is of importance to monitor all parameters, such as heating/ cooling rate, gas and temperature, since this will influence the sheet resistance.

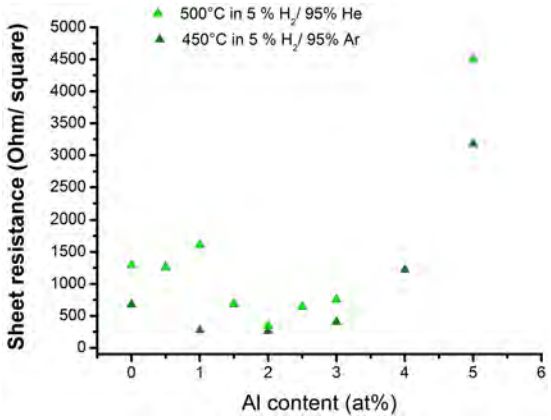

Figure 29: Sheet resistance of ZnO:Al in correlation to the doping percentages after RA at 500 °C for 10 minutes in a 5 % H_2/ 95 % He atmosphere (light green triangle)or at 450 °C for 10 minutes in a 5 % H_2/ 95 % Ar atmosphere (dark green triangle).

2 Conclusion

The use of equipment, gas, and temperature influence the obtained resistivty as well as transparency and the optimum of reductive anneal can vary. So far, the ideal set of annealing parameters here is the anneal up to 450 °C for 10 minutes in a 5 % H_2/ 95 % Ar atmosphere.

Scientific Contributions

1 Publications

H. Damm, C. De Dobbelaere, J. D'Haen, A. Hardy, M. K. Van Bael, Can solution combustion processing generate crystalline n-type doped ZnO at low temperatures? *Manuscript in preparation*

H. Damm, T. Driessen, K. Elen, C. De Dobbelaere, J. D'Haen, A. Hardy, M. K. Van Bael, Evaluation of doping agents in ZnO synthesized from aqueous molecular precursors. *Manuscript in preparation*

N. Peys, **H. Damm**, S. Gielis, K. Schellens, C. De Dobbelaere, G. Rampelberg, C. Detavernier, S. De Gendt, A. Hardy, M. K. Van Bael, Thermal decomposition study of an ammonium-oxalato/citrato-VO^{2+} solution-gel precursor for V_2O_5 formation. *Manuscript in preparation*

H. Damm, P. Adriaensens, K. Elen, C. De Dobbelaere, B. Capon, J. Drijkoningen, B. Conings, J. V. Manca, J. D'Haen, C. Detavernier, P. C. M. M. Magusin, J. Hadermann, A. Hardy, M. K. Van Bael, Factors influencing the conductivity of solution processed Al-doped ZnO. Chemistry of Materials, 2014, 26, 5839-5851
DOI: 10.1021/CM501820A

R. Dierick, B. Capon, **H. Damm**, S. Flamee, P. Arickx, E. Bruneel, D. Van Genechten, M. K. Van Bael, A. Hardy, C. Detavernier, Z. Hens, Annealing of sulfide stabilized colloidal semiconductor nanocrystals. Journal of Materials Chemistry C, 2014, 2, 178-183
DOI: 10.1039/C3TC31393J

H. Damm, A. Kelchtermans, A. Bertha, F. Van den Broeck, K. Elen, J. C. Martins, R. Carleer, J. D'Haen, C. De Dobbelaere, J. Hadermann, A. Hardy, M. K. Van Bael, Thermal decomposition synthesis of Al-doped ZnO nanoparticles: an in-depth study. RSC advances, 2013, 3, 23745-23754
DOI: 10.1039/C3RA43328E

A. Kelchtermans, K. Elen, K. Schellens, B. Conings, **H. Damm**, H. G. Boyen,

J. D'Haen, P. Adriaensens, A. Hardy, M. K. Van Bael, Relation between synthesis conditions, dopant position and charge carriers in aluminium-doped ZnO nanoparticles. RSC advances, 2013, 3, 15254-15262
DOI: 10.1039/C3RA41847B

J. Trekker, K. Jans, **H. Damm**, D. Mertens, T. Nuytten, J. Vanacken, V. Moshchalkov, J. D'Haen, T. Stakenborg, W. Van Roy, U. Himmelreich, L. Lagae, Synthesis of PEGylated Magnetic Nanoparticles With Different Core Sizes. IEEE Transactions on Magnetics, 2012, 49, 219-226
DOI: 10.1109/TMAG.2012.2221687

2 Conference Contributions

2.1 Oral Presentations

K. Elen, **H. Damm**, A. Kelchtermans, A. Riskin, A. Hardy, M. K. Van Bael, Chemical solution deposition of aluminum doped zinc oxide for transparent conducting oxides. **TCM 2014**,5^{th} International Symposium on Transparent Conductive Materials, Chania, Crete, 12th-17th October

H. Damm, C. De Dobbelaere, J. D'Haen, A. Hardy, M. K. Van Bael, Low temperature solution combustion deposition of crystalline n-type doped ZnO. **E-MRS 2014**, Lille, France, 26th-30th May

H. Damm, P. Adriaensens, K. Elen, C. De Dobbelaere, J. D'Haen, A. Hardy, M. K. Van Bael, Aluminium incorporation in doped ZnO films obtained from aqueous solution-gel precursors. **MRS spring meeting 2014**, San Francisco, USA, 21st-25th April

H. Damm, K. Elen, C. De Dobbelaere, F. Van den Broeck, J. C. Martins, J. D'Haen, P. Adriaensens, A. Hardy, M. K. Van Bael, From precursor towards incorporated Al in ZnO TCO films. **YBMRS 2013**, Blankenberge, Belgium, 2nd-3rd December

K. Elen, **H. Damm**, A. Kelchtermans, K. Schellens, A. Hardy, M. K. Van Bael, Transparent conducting films of aluminium doped zinc oxide prepared by solution based processing. **MS&T 2013**, Montreal, Canada, 28th-31st October

H. Damm, K. Elen, C. De Dobbelaere, B. Capon, F. Van den Broeck, J. C. Martins, C. Detavernier, J. D'Haen, P. Adriaensens, A. Hardy, M. K. Van Bael, Aqueous solution-gel route for processing of highly c-axis oriented dense transparent conductive Al-doped ZnO films. **Sol-Gel 2013**, Madrid, Spain, 25th-30th August

M. K. Van Bael, K. Elen, **H. Damm**, A. Kelchtermans, K. Schellens, A. Hardy, Transparent conductive oxides: from wet-chemical synthesis to photovoltaic applications. **ENFI 2013**, Hasselt, Belgium, 8th-9th July

H. Damm, K. Elen, A. Hardy, M. K. Van Bael, Solution processing of Al-doped ZnO nanoparticles and functional coatings. **BCERS 2013**, Diepenbeek, Belgium, 19th April

K. Elen, **H. Damm**, A. Kelchtermans, K. Schellens, A. Hardy, M. K. Van Bael, Solution based processing of doped zinc oxide and titanium dioxide as transparent conductive materials. **ICACC 2013**, Daytona beach, USA, 27th January-1st February

H. Damm, A. Kelchtermans, A. Bertha, H. D'Hondt, F. Van den Broeck, K. Elen, J. Hadermann, J. C. Martins, R. Carleer, J. D'Haen, C. De Dobbelaere, A. Hardy, M. K. Van Bael, In-depth mechanism study of thermal decomposition of Al-doped ZnO nanoparticles. **TCM 2012**, 4^{th} International Symposium on Transparent Conductive Materials, Crete, Greece, 21th-26th October

A. Kelchtermans, A. Bertha, K. Schellens, K. Elen, **H. Damm**, J. Hadermann, J. D'Haen, A. Hardy, M. K. Van Bael, Thermal decomposition synthesis of AZO nanocrystals for the formation of transparent conducticve oxide layers. **TCM 2012**, 4^{th} International Symposium on Transparent Conductive Materials, Crete, Greece, 21th-26th October

H. Damm, K. Elen, A. Kelchtermans, K. Schellens, A. Bertha, B. Capon, J. Hadermann, R. Carleer, C. De Tavernier, J. D'Haen A. Hardy, M. K. Van Bael, Nanoparticle synthesis and (aqueous) chemical solution deposition of Al-doped ZnO and doped TiO_2. **NanoTCM 2012**, Grenoble, France, 14th-15th June

D. Dewulf, C. De Dobbelaere, N. Peys, **H. Damm**, S. Van Elshocht, S. De Gendt, A. Hardy, M. K. Van Bael, Impact of the precursor system on Nb_2O_5 thin films: comparing citric and tartaric acid. **ChemCYS 2012**, Blankenberge, Belgium, 1st-2nd March

H. Damm, B. Capon, H. D'Hondt, A. Kelchtermans, K. Schellens, K. Elen, C. De Tavernier, J. Hadermann, A. Hardy, M. K. Van Bael, Thermal decomposition synthesis of Al-doped ZnO. **E-MRS Fall Meeting 2011**, Warshau, Poland, 19th-23th September

2.2 Poster Presentations

H. Damm, A. Hardy, M. K. Van Bael, Solution processing of n-type doped ZnO. **MS&T 2014**, Pittsburgh, USA, 12th-16th October

E. Peeters, C. De Dobbelaere, **H. Damm**, A. Hardy, M. K. Van Bael, Synthesis of epitaxial $Ca_3Mn_2O_7$ films: Study of an aqueous multi-metal ion precursor. **ChemCYS 2014**, Blankenberge, Belgium, 27th-28th February

T. Vranken, **H. Damm**, C. De Dobbelaere, J. D'Haen, M. K. Van Bael, A. Hardy, $LiMnPO_4$ Li-ion battery cathodes: Synthesis, processing and characterization of aqueous solution precursors for powders and depositions. **Sol-Gel 2013**, Madrid, Spain, 25th-30th August

E. Peeters, C. De Dobbelaere, **H. Damm**, K. Schellens, N. Pavlovic, A. Hardy, M. K. Van Bael, Exploration of Single-phase layered Perovskites as Candidate Magnetoelectrics. **Workshop of the COST MPO904 Action "Recent advances in ferro/piezoelectric and multiferroic-based composites" 2013**, Faenza, Italy, 22th-23th April

K. Elen, **H. Damm**, A. Kelchtermans, A. Hardy, M. K. Van Bael, Solution based synthesis and characterization of aluminium doped zinc oxide nanocrystals. **SIM users forum 2012**, Antwerp, Belgium, 7th December

H. Damm, A. Kelchtermans, A. Bertha, H. D'Hondt, K. Elen, J. Hadermann, R. Carleer, J. D'Haen, C. De Dobbelaere, A. Hardy, M. K. Van Bael, Mechanism insights in the thermal decomposition synthesis of Al-doped ZnO nanoparticles. **First COST MP0904 Training School "Nanostructured oxides: from laboratory research to industrial applications" 2012**, Genoa, Italy, 12th-13th March
2nd Poster Price

S. Gielis, N. Peys, D. Dewulf, C. De Dobbelaere1, N. Pavlovic, **H. Damm**, S. Van Elshocht, S. De Gendt, P. M. Vereecken, A. Hardy, M. K. Van Bael, Aqueous chemical solution deposition of $LuFeO_3$ thin films in view of energy storage applications. **E-MRS Fall Meeting 2011**, Warshau, Poland, 19th-23th September

H. Damm, A. Kelchtermans, K. Schellens, A. Hardy, M. K. Van Bael, Solution based synthesis of doped and undoped ZnO nanoparticles. **Physical Characterization Course 2011**, Vaalbeek, Belgium, 8th-13th May

Bibliography

[1] Eva software, www.bruker.com/products/x-ray-diffraction-and-elemental-analysis/x-ray-diffraction/xrd-software/overview/eva/eva-phase-analysis/phase-identification-options.html.

[2] An introduction to pulsed laser deposition, www.andor.com/learning-academy/pulsed-laser-deposition-an-introduction-to-pulsed-laser-deposition.

[3] Vacuum deposition processes, www.pfonline.com/articles/vacuum-deposition-processes.

[4] Acet, M., Mayer, C., Muth, O., Terheiden, A., and Dyker, G. Formation of extended ordered monolayers of FePt nanoparticles. *Journal of Crystal Growth 285*, 3 (Dec. 2005), 365–371.

[5] Ágoston, P., and Albe, K. Intrinsic n-Type Behavior in Transparent Conducting Oxides: A Comparative Hybrid-Functional Study of In_2O_3, SnO_2, and ZnO. *Physical Review Letters 103*, 24 (Dec. 2009), 245501.

[6] Agthe, M., Wetterskog, E., Mouzon, J., Salazar-Alvarez, G., and Bergström, L. Dynamic growth modes of ordered arrays and mesocrystals during drop-casting of iron oxide nanocubes. *CrystEngComm 16*, 8 (2014), 1443.

[7] Agura, H., Suzuki, A., Matsushita, T., Aoki, T., and Okuda, M. Low resistivity transparent conducting Al-doped ZnO films prepared by pulsed laser deposition. *Thin Solid Films 445*, 2 (Dec. 2003), 263–267.

[8] Akitt, J. W., and Mann, B. *NMR and Chemistry: An introduction to modern NMR spectroscopy, Fourth Edition.* Stanley Thornes Ltd.

[9] Aktaruzzaman, A. F., Sharma, G. L., and Malhotra, L. K. Electrical, optical and annealing characteristics of ZnO:Al films prepared by spray pyrolysis. *Thin Solid Films 198* (1991), 67–74.

[10] Alam, M., and Cameron, D. Investigation of annealing effects on sol-gel deposited indium tin oxide thin films in different atmospheres. *Thin Solid Films 420-421* (Dec. 2002), 76–82.

[11] Alam, M. J. U., and Cameron, D. C. Characterization of transparent conductive ITO thin films deposited on titanium dioxide film by a sol-gel process. *Surface and Coatings Technology 142-144* (2001), 776–780.

[12] Allen, M. L., Aronniemi, M., Mattila, T., Alastalo, A., Ojanperä, K., Suhonen, M., and Seppä, H. Electrical sintering of nanoparticle structures. *Nanotechnology 19*, 17 (Apr. 2008), 175201.

[13] Ambrozic, G., Skapin, S. D., Zigon, M., and Orel, Z. C. The synthesis of zinc oxide nanoparticles from zinc acetylacetonate hydrate and 1-butanol or isobutanol. *Journal of colloid and interface science 346*, 2 (July 2010), 317–23.

[14] Andrievski, R. A. Size-dependent effects in properties of nanostructured materials. *Rev. Adv. Mater. Sci0 21* (2009), 107–133.

[15] Armstrong, N. R., Wang, W., Alloway, D. M., Placencia, D., Ratcliff, E., and Brumbach, M. Organic/organic' heterojunctions: Organic light emitting diodes and organic photovoltaic devices. *Macromolecular Rapid Communications 30*, 9-10 (2009), 717–731.

[16] Atkinson, H. V. THEORIES OF NORMAL GRAIN GROWTH SINGLE PHASE SYSTEMS. *Acta metall. 36*, 3 (1988), 469–491.

[17] Avadhut, Y. S., Weber, J., Hammarberg, E., Feldmann, C., and Schmedt auf der Günne, J. Structural investigation of aluminium doped ZnO nanoparticles by solid-state NMR spectroscopy. *Physical chemistry chemical physics : PCCP 14*, 33 (Oct. 2012), 11610–11625.

[18] Bädeker, K. Über die elektrische leitfähigkeit und die thermoelektrische kraft einiger schwermetallverbindungen. *Annalen der Physik 327*, 4 (1907), 749–766.

[19] Baetens, R., Jelle, B. r. P., and Gustavsen, A. Properties, requirements and possibilities of smart windows for dynamic daylight and solar energy control in buildings: A state-of-the-art review. *Solar Energy Materials and Solar Cells 94*, 2 (Feb. 2010), 87–105.

[20] Bahsi, Z. B., Aslan, M. H., Ozer, M., and Oral, a. Y. Sintering behavior of ZnO:Al ceramics fabricated by sol-gel derived nanocrystalline powders. *Crystal Research and Technology 44*, 9 (Sept. 2009), 961–966.

[21] Baik, S. J., Jang, J. H., Lee, C. H., Cho, W. Y., and Lim, K. S. Highly textured and conductive undoped ZnO film using hydrogen post-treatment. *Applied Physics Letters 70*, 26 (1997), 3516.

[22] Balkanski, M. *Handbook on Semiconductors: Optical properties of solids. 2.* North-Holland, 1980.

[23] Barrett, E. P., Joyner, L. G., and Halenda, P. P. The determination of pore volume and area distributions in porous substances. i. computations from nitrogen isotherms. *Journal of the American Chemical Society 73*, 1 (1951), 373–380.

[24] Behrens, M., Lolli, G., Muratova, N., Kasatkin, I., Hävecker, M., D'Alnoncourt, R. N., Storcheva, O., Köhler, K., Muhler, M., and Schlögl, R. The effect of Al-doping on ZnO nanoparticles applied as catalyst support. *Physical chemistry chemical physics : PCCP 15*, 5 (Feb. 2013), 1374–81.

[25] Bernède, J., Cattin, L., Morsli, M., and Berredjem, Y. Ultrathin metal layer passivation of the transparent conductive anode in organic solar cells. *Solar Energy Materials and Solar Cells 92*, 11 (Nov. 2008), 1508–1515.

[26] Bieri, N. R., Chung, J., Haferl, S. E., Poulikakos, D., and Grigoropoulos, C. P. Microstructuring by printing and laser curing of nanoparticle solutions. *Applied Physics Letters 82*, 20 (2003), 3529–3531.

[27] Bingel, A., Kevin, F., Kaiser, N., and Andreas, T. Pulsed DC magnetron sputtering of transparent conductive oxide layers. *Chinese Optics Letters 11* (2013), S10201.

[28] Blandenet, G., Court, M., and Lagarde, Y. Thin layers deposited by the pyrosol process. *Thin Solid Films 77* (1981).

[29] Boal, A. K., Das, K., Gray, M., and Rotello, V. M. Monolayer Exchange Chemistry of γ -Fe2O3 Nanoparticles. *Chemistry of Materials 14*, 6 (2002), 2628–2636.

[30] Board, N. *The Complete Book on Printing Technology.* NIIR Project Consultancy Services, 2009.

[31] Boss, C. B., and Fredeen, K. J. *Concepts, Instrumentation and Techniques in Inductively Coupled Plasma Atomic Emission Spectrometry.*

[32] Böttler, W., Smirnov, V., Hüpkes, J., and Finger, F. Texture-etched ZnO as a versatile base for optical back reflectors with well-designed surface morphologies for application in thin film solar cells. *Physica Status Solidi (a) 209*, 6 (June 2012), 1144–1149.

[33] Brabec, C. J. Organic photovoltaics: technology and market. *Solar Energy Materials and Solar Cells 83*, 2-3 (June 2004), 273–292.

[34] Brenninkmeijer, C. A. M., and Röckmann, T. Mass Spectrometry of the Intramolecular Nitrogen Isotope Distribution of Environmental Nitrous Oxide Using Fragment-ion Analysis. *Rapid Communications in Mass Spectrometry 13*, 20 (1999), 2028–2033.

[35] Brunauer, S., Emmett, P. H., and Teller, E. Adsorption of gases in multimolecular layers. *Journal of the American Chemical Society 60*, 2 (1938), 309–319.

[36] Bu, W., Chen, Z., Chen, F., and Shi, J. Oleic Acid / Oleylamine Cooperative-Controlled Crystallization Mechanism for Monodisperse Tetragonal Bipyramid $NaLa(MoO_4)_2$ Nanocrystals. *Journal of Physical Chemistry C. 113* (2009), 12176–12185.

[37] Buonsanti, R., Llordes, A., Aloni, S., Helms, B. a., and Milliron, D. J. Tunable infrared absorption and visible transparency of colloidal aluminum-doped zinc oxide nanocrystals. *Nano letters 11*, 11 (Nov. 2011), 4706–10.

[38] Burdett, J. K., Price, G. D., and Pricel, S. L. Role of the Crystal-Field Theory in Determining the Structures of Spinels. *Journal of the American Chemical Society 104*, 1 (1982), 92–95.

[39] Burstein, E. Anomalous optical absorption limit in insb. *Phys. Rev. 93* (Feb 1954), 632–633.

[40] Cahn, R. W. Topology of crystal grains. *Nature 250*, 5469 (1974), 702–703.

[41] Cai, W., and Wan, J. Facile synthesis of superparamagnetic magnetite nanoparticles in liquid polyols. *Journal of colloid and interface science 305*, 2 (2007), 366–370.

[42] Calatayud, D. G., Jardiel, T., Rodríguez, M., Peiteado, M., Fernández-Hevia, D., and Caballero, A. C. Soft solution fluorine-free synthesis of anatase nanoparticles with tailored morphology. *Ceramics International 39*, 2 (Mar. 2013), 1195–1202.

[43] Calvert, J., and Pitts, J. *Photochemistry*. No. dl. 1. Wiley, 1966.

[44] Chang, H., Wang, F., Wu, J., Kung, C., and Liu, H. Enhanced conductivity of aluminum doped ZnO films by hydrogen plasma treatment. *Thin Solid Films 518*, 24 (Oct. 2010), 7445–7449.

[45] Charles, G., and Arlene, M. Comparative heat stabilities of some metal acetylacetonate chelates. *Journal of Physical Chemistry 189*, 1914 (1958), 440–444.

[46] Charpentier, C., Prod'homme, P., and Roca i Cabarrocas, P. Microstructural, optical and electrical properties of annealed ZnO:Al thin films. *Thin Solid Films 531* (Mar. 2013), 424–429.

[47] Cheong, K., Muti, N., and Ramanan, S. Electrical and optical studies of ZnO:Ga thin films fabricated via the sol-gel technique. *Thin Solid Films 410*, 1-2 (May 2002), 142–146.

[48] Chikoidze, E., Nolan, M., Modreanu, M., Sallet, V., and Galtier, P. Effect of chlorine doping on electrical and optical properties of ZnO thin films. *Thin Solid Films 516* (2008), 8146–8149.

[49] Chmelka, B. F., Mueller, K. T., Pines, A., Stebbins, J., Wu, Y., and Zwanziger, J. W. Oxygen-17 nmr in solids by dynamic-angle spinning and double rotation. *Nature 339* (1989).

[50] Cho, Y.-S., Kim, H.-M., Hong, J.-J., Yi, G.-R., Jang, S. H., and Yang, S.-M. Dispersion stabilization of conductive transparent oxide nanoparticles. *Colloids and Surfaces A: Physicochemical and Engineering Aspects 336*, 1-3 (Mar. 2009), 88–98.

[51] Choppali, U., Kougianos, E., Mohanty, S. P., and Gorman, B. P. Polymeric precursor derived nanocrystalline ZnO thin films using EDTA as chelating agent. *Solar Energy Materials and Solar Cells 94*, 12 (Dec. 2010), 2351–2357.

[52] Chopra, K. L., Major, S., and Pandya, D. K. Transparent conductors - A status review. *Thin Solid Films 102*, 1 (1983), 1–46.

[53] Choy, K. Chemical vapour deposition of coatings. *Progress in Materials Science 48*, 2 (2003), 57–170.

[54] Claridge, T. D. *[Tetrahedron Organic Chemistry Series] High-Resolution NMR Techniques in Organic Chemistry Volume 27 —— Chapter 9 Diffusion NMR spectroscopy.* 2009.

[55] Claridge, T. D. W. *High-resolution NMR techniques in organic chemistry.* Elsevier Science Ltd, 2009.

[56] Clatot, J., Campet, G., Zeinert, a., Labrugère, C., Nistor, M., and Rougier, a. Low temperature Si doped ZnO thin films for transparent conducting oxides. *Solar Energy Materials and Solar Cells 95*, 8 (Aug. 2011), 2357–2362.

[57] Connell, M. a., Bowyer, P. J., Adam Bone, P., Davis, A. L., Swanson, A. G., Nilsson, M., and Morris, G. a. Improving the accuracy of pulsed field gradient NMR diffusion experiments: Correction for gradient non-uniformity. *Journal of magnetic resonance 198*, 1 (May 2009), 121–131.

[58] Copuroğlu, M., Brien, S. O., and Crean, G. M. Sol-gel synthesis , comparative characterisation , and reliability analyses of undoped and Al-doped zinc oxide thin films. *Thin Solid Films 517*, 23 (2009), 6323–6326.

[59] Corradini, F., Marcheselli, L., Tassi, L., Tosi, G., Corradini, F., Marcheselli, L., Tassi, L., Tosi, G., Corradini, F., Marcheselli, L., Tassi, L., The, I., Hiickel, D., and Dmf, T. Static dielectric constants of the N,N-dimethylformamide/2-methoxyethanol solvent system at various temperatures. *Canadian Journal of Chemistry 70*, 12 (1992), 2895–2899.

[60] Coutts, T. J., Mason, T. O., Perkins, J. D., and Ginley, D. S. Transparent Conducting Oxides : Status and Opportunities in Basic Research. *Photovoltaics for the 21st Century: Proceedings of the International Symposium 99*, August (1999), 274–288.

[61] Craciun, V., Craciun, D., Wang, X., Anderson, T., and Singh, R. Highly conducting indium tin oxide films grown by ultraviolet-assisted pulsed laser deposition at low temperatures. *Thin Solid Films 453-454* (Apr. 2004), 256–261.

[62] Crawford, G. *Flexible Flat Panel Displays*. Wiley Series in Display Technology. Wiley, 2005.

[63] Croasmun, W., and Carlson, R. *Two-Dimensional NMR Spectroscopy: Applications for Chemists and Biochemists*. Methods in Stereochemical Analysis. Wiley, 1994.

[64] Cui, H., Feng, Y., Ren, W., Zeng, T., Lv, H., and Pan, Y. Strategies of Large Scale Synthesis of Monodisperse Nanoparticles. *Recent Patents on Nanotechnology 3*, 1 (2009), 32–41.

[65] Cui, J., Soo, Y., Chen, T., and Gibson, U. Low-Temperature Growth and Characterization of Cl-Doped ZnO Nanowire Arrays. *Journal of Physical Chemistry C 112*, 12 (Mar. 2008), 4475–4479.

[66] Czichos, H., Saito, T., and Smith, L. *Springer Handbook of Materials Measurement Methods —— Electrical Properties*, vol. 10.1007/978-3-540-30300-8. 2006.

[67] Damm, H., Adriaensens, P., De Dobbelaere, C., Capon, B., Elen, K., Drijkoningen, J., Conings, B., Manca, J. V., D'Haen, J., Detavernier, C., Magusin, P. C. M. M., Hadermann, J., Hardy, A., and Van Bael, M. K. Factors influencing the conductivity of aqueous sol(ution)-gel processed al-doped zno films. *Chemistry of Materials 26*, 20 (2014), 5839–5851.

[68] Damm, H., Kelchtermans, A., Bertha, A., Van den Broeck, F., Elen, K., Martins, J. C., Carleer, R., D'Haen, J., De Dobbelaere, C., Hadermann, J., Hardy, A., and Van Bael, M. K. Thermal decomposition synthesis of Al-doped ZnO nanoparticles: an in-depth study. *RSC Advances 3*, 45 (2013), 23745–23754.

[69] Dasgupta, N. P., Neubert, S., Lee, W., Trejo, O., Lee, J.-R., and Prinz, F. B. Atomic Layer Deposition of Al-doped ZnO Films: Effect of Grain Orientation on Conductivity. *Chemistry of Materials 22*, 16 (Aug. 2010), 4769–4775.

[70] De, S., Higgins, T. M., Lyons, P. E., Doherty, E. M., Nirmalraj, P. N., Blau, W. J., Boland, J. J., and Coleman, J. N. Silver nanowire networks as flexible, transparent, conducting films: Extremely high dc to optical conductivity ratios. *ACS Nano 3* (2009).

[71] De Dobbelaere, C., Calzada, M. L., Jiménez, R., Ricote, J., Bretos, I. n., Mullens, J., Hardy, A., and Van Bael, M. K. Aqueous solutions for low-temperature photoannealing of functional oxide films: reaching the 400 °C Si-technology integration barrier. *Journal of the American Chemical Society 133*, 33 (Aug. 2011), 12922–12925.

[72] De Roo, J., Van Den Broeck, F., De Keukeleere, K., Van Driessche, I., and Hens, Z. Unravelling the Surface Chemistry of Metal Oxide Nanocrystals, the Role of Acids and Bases. *Journal of the American Chemical Society 136*, 27 (2014), 9650–9657.

[73] Denhoff, M., and Drolet, N. The effect of the front contact sheet resistance on solar cell performance. *Solar Energy Materials and Solar Cells 93* (2009).

[74] Dong, J. J., Zhang, X. W., You, J. B., Cai, P. F., Yin, Z. G., An, Q., Ma, X. B., Jin, P., Wang, Z. G., and Chu, P. K. Effects of hydrogen plasma treatment on the electrical and optical properties of ZnO films: identification of hydrogen donors in ZnO. *ACS applied materials & interfaces 2*, 6 (July 2010), 1780–4.

[75] Downs, A. *Chemistry of Aluminium, Gallium, Indium, and Thallium.* Springer Netherlands, 1993.

[76] Duan, G.-R., Yang, X.-J., Huang, G.-H., Lu, L.-D., and Wang, X. Water/span80/Triton X-100/n-hexyl alcohol/n-octane microemulsion system and the study of its application for preparing nanosized zirconia. *Materials Letters 60*, 13-14 (June 2006), 1582–1587.

[77] Duer, M. J. *Solid State NMR spectroscopy: Principles and Applications.* Wiley-Blackwell.

[78] Earnshaw, A., and Greenwood, N. *Chemistry of the Elements 2nd edition.*

[79] Ederth, J., Heszler, P., Hultå ker, a., Niklasson, G., and Granqvist, C. Indium tin oxide films made from nanoparticles: models for the optical and electrical properties. *Thin Solid Films 445*, 2 (Dec. 2003), 199–206.

[80] Ellmer, K. Resistivity of polycrystalline zinc oxide films : current status and physical limit. *Journal of Physics D: Applied Physics 34*, 21 (2001), 3097–3108.

[81] Ellmer, K., Klein, A., and Rech, B. *Transparent Conductive Zinc Oxide: Basics and Applications in Thin Film Solar Cells.* Springer Series in Materials Science. Springer, 2007.

[82] Ellmer, K., and Mientus, R. Carrier transport in polycrystalline ITO and ZnO:Al II: The influence of grain barriers and boundaries. *Thin Solid Films 516*, 17 (July 2008), 5829–5835.

[83] Engelhardt, G., and Michel, D. *High-Resolution Solid-State Nmr of Silicates and Zeolites.* John Wiley & Sons Australia, Limited, 1987.

[84] Epifani, M., Melissano, E., Pace, G., and Schioppa, M. Precursors for the combustion synthesis of metal oxides from the sol-gel processing of metal complexes. 115–123.

[85] Exarhos, G. J., and Sharma, S. K. Influence of processing variables on the structure and properties of ZnO films. *Thin Solid Films 270*, 1-2 (Dec. 1995), 27–32.

[86] Exarhos, G. J., and Zhou, X.-D. Discovery-based design of transparent conducting oxide films. *Thin Solid Films 515*, 18 (June 2007), 7025–7052.

[87] Facchetti, A., and Marks, T. *Transparent Electronics: From Synthesis to Applications.* Wiley, 2010.

[88] Faÿ, S., Steinhauser, J., Oliveira, N., Vallat-Sauvain, E., and Ballif, C. Opto-electronic properties of rough LP-CVD ZnO:B for use as TCO in thin-film silicon solar cells. *Thin Solid Films 515*, 24 (Oct. 2007), 8558–8561.

[89] Fortunato, E., Ginley, D., Hosono, H., and Paine, D. C. Transparent Conducting Oxides for Photovoltaics. *MRS bulletin 32*, March (2007), 242–247.

[90] Fournier, J.-B., and Galatola, P. Anisotropic capillary interactions and jamming of colloidal particles trapped at a liquid-fluid interface. *Physical Review E 65*, 3 (Feb. 2002), 031601.

[91] Fritzinger, B., Moreels, I., Lommens, P., Koole, R., and Hens, Z. In Situ Observation of Rapid Ligand Exchange in Colloidal Nanocrystal Suspensions Using Transfer NOE Nuclear. *Journal of the American Chemical Society 131*, 8 (2009), 3024–3032.

[92] Frydman, Lucio; Harwood, J. S. Isotropic spectra of half-integer quadrupolar spins from bidimensional magic-angle spinning nmr. *Journal of the American Chemical Society 117* (05 1995).

[93] Füchsel, K., Bingel, A., Kaiser, N., and A., T. Transparent conductive oxides for nano-sis solar cells. 80650B.

[94] Gabbott, P. *Principles and Applications of Thermal Analysis*. Wiley, 2008.

[95] Gao, M., Wu, X., Liu, J., and Liu, W. The effect of heating rate on the structural and electrical properties of sol-gel derived Al-doped ZnO films. *Applied Surface Science 257*, 15 (May 2011), 6919–6922.

[96] García-Valenzuela, J. A., Castelo-González, O. A., Baez-Gaxiola, M. R., and Sotelo-Lerma, M. Detailed Analysis of Five Aspects Addressed to Minimize Costs and Waste in the Chemical Bath Deposition of CdS Films Using the CdB - $AC_6H_5O_7$ - AOH - $(NH_2)_2CS$ System. *Materials Sciences and Applications 2013*, June (2013), 386–405.

[97] Gardner, G. P., Go, Y. B., Robinson, D. M., Smith, P. F., Hadermann, J., Abakumov, A., Greenblatt, M., and Dismukes, G. C. Structural requirements in lithium cobalt oxides for the catalytic oxidation of water. *Angewandte Chemie International Edition 51*, 7 (Mar. 2012), 1616–1619.

[98] Gaudiana, R. Organic photovoltaics: Challenges and opportunities. *Journal of Polymer Science Part B: Polymer Physics 50*, 15 (Aug. 2012), 1014–1017.

[99] Ghosh, A., Kumari, N., Tewari, S., and Bhattacharjee, a. Structural and optical properties of pure and Al doped ZnO nanocrystals. *Indian Journal of Physics 87*, 11 (June 2013), 1099–1104.

[100] Gillaspie, D. T., Tenent, R. C., and Dillon, A. C. Metal-oxide films for electrochromic applications: present technology and future directions. *Journal of Materials Chemistry 20*, 43 (2010), 9585–9592.

[101] Ginley, D., Hosono, H., and Paine, D. *Handbook of Transparent Conductors*. Springer, 2010.

[102] Goebbert, C., Nonninger, R., Aegerter, M., and Schmidt, H. Wet chemical deposition of ATO and ITO coatings using crystalline nanoparticles redispersable in solutions. *Thin Solid Films 351*, 1-2 (Aug. 1999), 79–84.

[103] González-Cortés, S. L., and Imbert, F. E. Applied Catalysis A : General Fundamentals , properties and applications of solid catalysts prepared by solution combustion synthesis (SCS). *"Applied Catalysis A, General" 452* (2013), 117–131.

[104] Graham, R. L., Alers, G. B., Mountsier, T., Shamma, N., Dhuey, S., Cabrini, S., Geiss, R. H., Read, D. T., and Peddeti, S. Resistivity dominated by surface scattering in sub-50 nm Cu wires. *Applied Physics Letters 96*, 4 (2010), 042116.

[105] Green, M. A., Emery, K., Hishikawa, Y., Warta, W., and Dunlop, E. D. Solar cell efficiency tables (version 44). *Nuclear Fusion 22* (07 2014).

[106] Green, M. A., Ho-Baillie, A., and Snaith, H. J. The emergence of perovskite solar cells. *Nature Photonics 8* (6 2014).

[107] Gross, M., Linse, N., Maksimenko, I., and Wellmann, P. J. Conductance Enhancement Mechanisms of Printable Nanoparticulate Indium Tin Oxide (ITO) Layers for Application in Organic Electronic Devices **. *Advanced Engineering Materials 11*, 4 (2009), 295–301.

[108] Guillén, C., and Herrero, J. TCO/metal/TCO structures for energy and flexible electronics. *Thin Solid Films 520*, 1 (Oct. 2011), 1–17.

[109] Gupta, T. K. Microstructural engineering through donor and acceptor doping in the grain and grain boundary of a polycrystalline semiconducting ceramic. *Journal of Materials Research 7* (12 1992), 3280–3295.

[110] Hafdallah, A., Yanineb, F., Aida, M., and Attaf, N. In-doped ZnO thin films. *Journal of Alloys and Compounds 509*, 26 (June 2011), 7267–7270.

[111] Hagendorfer, H., Lienau, K., Nishiwaki, S., Fella, C. M., Kranz, L., Uhl, A. R., Jaeger, D., Luo, L., Gretener, C., Buecheler, S., Romanyuk, Y. E., and Tiwari, A. N. Highly Transparent and Conductive ZnO: Al Thin Films from a Low Temperature Aqueous Solution Approach. *Advanced materials 26*, 4 (Oct. 2014), 632–636.

[112] Hammarberg, E., Prodi-Schwab, A., and Feldmann, C. Microwave-assisted polyol synthesis of aluminium- and indium-doped ZnO nanocrystals. *Journal of colloid and interface science 334*, 1 (July 2009), 29–36.

[113] Hardy, An; Van Bael, M. K. Oxide electronics: Like wildfire. *Nature Materials 10* (2011).

[114] Hecht, D. S., and Kaner, R. B. Solution-processed transparent electrodes. *MRS Bulletin 36*, 10 (Oct. 2011), 749–755.

[115] Hensen, E., Poduval, D., Magusin, P., Coumans, A., and van Veen, J. Formation of acid sites in amorphous silica-alumina. *Journal of Catalysis 269* (2010).

[116] Hosono, H. Ionic amorphous oxide semiconductors : Material design , carrier transport , and device application. *Journal of Non-Crystalline Solids 352*, 9-20 (2006), 851–858.

[117] Hu, J., and Gordon, R. G. Textured aluminum-doped zinc oxide thin films from atmospheric pressure chemical-vapor deposition. *Journal of Applied Physics 71*, 2 (1992), 880.

[118] Hummel, R. *Electronic Properties of Materials*. SpringerLink : Bücher. Springer, 2011.

[119] Ianoş, R., Lazău, I., Păcurariu, C., and Sfîrloagă, P. Aqueous combustion synthesis and characterization of ZnO powders. *Materials Chemistry and Physics 129*, 3 (Oct. 2011), 881–886.

[120] Imai, H., Tominaga, A., Hirashima, H., Toki, M., and Asakuma, N. Ultraviolet-reduced reduction and crystallization of indium oxide films. *Journal of Applied Physics 85*, 1 (1999), 203.

[121] Inubushi, Y., Takami, R., Iwasaki, M., Tada, H., and Ito, S. Mechanism of Formation of Nanocrystalline ZnO Particles through the Reaction of [Zn (acac) 2] with NaOH in EtOH. *Journal of colloid and interface science 200*, 2 (1998), 220–227.

[122] Ishikawa, K., Uchiyama, Y., Ogawa, H., and Fujimura, S. Dependence of TO and LO mode frequency of thermally grown silicon dioxide films on annealing temperature. *Applied Surface 117/118* (1997), 212–215.

[123] Islam, M. N., Ghosh, T., Chopra, K., and Acharya, H. XPS and X-ray diffraction studies of aluminum-doped zinc oxide transparent conducting films. *Thin Solid Films 280*, 1-2 (July 1996), 20–25.

[124] Itoh, S., Osamura, H., and Komada, K. Thermodynamics of Indium-Tin-Oxygen Ternary System. *Materials Transactions 52*, 6 (2011), 1192–1199.

[125] Jain, S. R., Adiga, K. C., and Verneker, V. R. P. A New Approach to Thermochemical Calculations of Condensed Fuel-Oxidizer Mixtures. *Combustion and Flame 40* (1981), 71–79.

[126] Janotti, A., and de Walle, C. G. V. Fundamentals of zinc oxide as a semiconductor. *Reports on Progress in Physics 72*, 12 (2009), 126501.

[127] Janotti, A., and Van de Walle, C. G. Hydrogen multicentre bonds. *Nature materials 6*, 1 (Jan. 2007), 44–7.

[128] Jeong, S. H., Park, B. N., Yoo, D.-g., and Boo, J.-h. Al-ZnO Thin Films as Transparent Conductive Oxides : Synthesis , Characterization , and Application Tests. *Journal of the Korean Physical Society 50*, 3 (2007), 622–625.

[129] Jolivet, J., Henry, M., and Livage, J. *Metal Oxide Chemistry and Synthesis: From Solution to Solid State*. Wiley, 2000.

[130] Jun, M.-C., Park, S.-U., and Koh, J.-H. Comparative studies of Al-doped ZnO and Ga-doped ZnO transparent conducting oxide thin films. *Nanoscale research letters 7*, 1 (Jan. 2012), 639.

[131] Kalsi, P. *Spectroscopy of Organic Compounds*. New Age International (P) Limited, 2004.

[132] Kamiya, T., Nomura, K., and Hosono, H. Present status of amorphous In-Ga-Zn-O thin-film transistors. *Science and Technology of Advanced Materials 11*, 4 (Aug. 2010), 044305.

[133] Kanehara, M., Koike, H., Yoshinaga, T., and Teranishi, T. Indium tin oxide nanoparticles with compositionally tunable surface plasmon resonance frequencies in the near-IR region. *Journal of the American Chemical Society 131*, 49 (Dec. 2009), 17736–17737.

[134] Kelchtermans, A., Elen, K., Schellens, K., Conings, B., Damm, H., Boyen, H.-G., D'Haen, J., Adriaensens, P., Hardy, A., and Van Bael, M. K. Relation between synthesis conditions, dopant position and charge carriers in aluminium-doped ZnO nanoparticles. *RSC Advances 3*, 35 (2013), 15254–15262.

[135] Kemell, M., Dartigues, F., Ritala, M., and Leskelä, M. Electrochemical preparation of In and Al doped ZnO thin films for $CuInSe_2$ solar cells. *Thin Solid Films 434*, 1-2 (June 2003), 20–23.

[136] Kemmitt, T., Ingham, B., and Linklater, R. Optimization of Sol-Gel-Formed ZnO : Al Processing Parameters by Observation of Dopant Ion Location Using Solid-State 27Al NMR Spectrometry. *The Journal of Physical Chemistry 115*, 30 (2011), 15031–15039.

[137] Kern, W. *Handbook of Semiconductor Wafer Cleaning Technology.* Noyes Publications, East Windsor, New Jersey, 1993.

[138] Kikuchi, T., Kasuya, R., Endo, S., Nakamura, A., Takai, T., Metzler-Nolte, N., Tohji, K., and Balachandran, J. Preparation of magnetite aqueous dispersion for magnetic fluid hyperthermia. *Journal of Magnetism and Magnetic Materials 323*, 10 (May 2011), 1216–1222.

[139] Kim, H., Piqué, A., Horwitz, J. S., Mattoussi, H., Murata, H., Kafafi, Z. H., and Chrisey, D. B. Indium tin oxide thin films for organic light-emitting devices. *Applied Physics Letters 74* (1999).

[140] Kim, K. H., Park, K. C., and Ma, D. Y. Structural, electrical and optical properties of aluminum doped zinc oxide films prepared by radio frequency magnetron sputtering. *Journal of Applied Physics 81*, 12 (1997), 7764.

[141] Kim, M.-g., Hennek, J. W., Kim, H. S., Kanatzidis, M. G., Facchetti, A., and Marks, T. J. Delayed Ignition of Autocatalytic Combustion Precursors: Low- Temperature Nanomaterial Binder Approach to Electronically Functional Oxide Films. *Journal of the American Chemical Society 134* (2012), 11583–11593.

[142] Kim, M.-G., Kanatzidis, M. G., Facchetti, A., and Marks, T. J. Low-temperature fabrication of high-performance metal oxide thin-film electronics via combustion processing. *Nature materials 10*, 5 (May 2011), 382–8.

[143] Kingsley, J. J., and Patil, K. C. A novel combustion process for the synthesis of fine particle alpha-alumina and related oxide materials. *Materials Letters 6*, I (1988), 427–432.

[144] Klechtermans, A. Synthesis and in-depth characterization of al-doped zno nanoparticles as building blocks for tco layers.

[145] Klingshirn, C. ZnO: material, physics and applications. *Chemphyschem : a European journal of chemical physics and physical chemistry 8*, 6 (Apr. 2007), 782–803.

[146] Klinowski, J. *New Techniques in Solid-State NMR.* No. v. 246 in New techniques in solid-state NMR. Springer, 2004.

[147] Klokkenburg, M., Hilhorst, J., and Erne, B. H. Surface analysis of magnetite nanoparticles in cyclohexane solutions of oleic acid and oleylamine. *Vibrational Spectroscopy 43*, 1 (2007), 243–248.

[148] Klokkenburg, M., Vonk, C., Claesson, E. M., Meeldijk, J. D., Erné, B. H., and Philipse, A. P. Direct imaging of zero-field dipolar structures in colloidal dispersions of synthetic magnetite. *Journal of the American Chemical Society 126*, 51 (Dec. 2004), 16706–16707.

[149] Knickerbocker, S. A., and Kulkarni, A. K. Estimation and verification of the optical properties of indium tin oxide based on the energy band diagram. *Journal of Vacuum Science & Technology A 14*, 3 (1996), 757–761.

[150] Kofstad, P. Defects and transport properties of metal oxides. *Oxidation of Metals 44*, 1-2 (Aug. 1995), 3–27.

[151] Kragten, J. *Atlas of metal-ligand equilibria in aqueous solution.* Ellis Horwood series in analytical chemistry. E. Horwood, 1978.

[152] KÃ¶stlin, H., Jost, R., and Lems, W. Optical and electrical properties of doped in2o3 films. *physica status solidi (a) 29* (1975).

[153] Lackner, M. *Combustion Synthesis: Novel Routes to Novel Materials.* Bentham Science Publishers, 2010.

[154] Láng, L. *Absorption Spectra in the Ultra-violet and Visible Region.* No. v. 20 in Absorption Spectra in the Ultra-violet and Visible Region. Academic Press, 1975.

[155] Lany, S., and Zunger, A. Dopability, Intrinsic Conductivity, and Nonstoichiometry of Transparent Conducting Oxides. *Physical Review Letters 98*, 4 (Jan. 2007), 045501.

[156] Laurent, S., Forge, D., Port, M., Roch, A., Robic, C., Vander Elst, L., and Muller, R. N. Magnetic iron oxide nanoparticles: synthesis, stabilization, vectorization, physicochemical characterizations, and biological applications. *Chemical reviews 108*, 6 (June 2008), 2064–110.

[157] Lawrance, G. *Introduction to Coordination Chemistry.* Inorganic Chemistry: A Textbook Series. Wiley, 2009.

[158] Lee, J.-H., and Park, B.-O. Transparent conducting ZnO:Al, In and Sn thin films deposited by the sol-gel method. *Thin Solid Films 426*, 1-2 (Feb. 2003), 94–99.

[159] Lee, S. H., Lee, T. S., Lee, K. S., Cheong, B., Kim, Y. D., and Kim, W. M. Characteristics of hydrogen co-doped ZnO:Al thin films. *Journal of Physics D: Applied Physics 41*, 9 (May 2008), 095303.

[160] Lewis, B. G., and Paine, D. C. Applications and Processing of Transparent Conductive Oxides. *MRS bulletin 25*, 8 (2000), 22–27.

[161] Li, H., Schirra, L. K., Shim, J., Cheun, H., Kippelen, B., Monti, O. L. a., and Bredas, J.-L. Zinc Oxide as a Model Transparent Conducting Oxide: A Theoretical and Experimental Study of the Impact of Hydroxylation, Vacancies, Interstitials, and Extrinsic Doping on the Electronic Properties of the Polar ZnO (0002) Surface. *Chemistry of Materials 24*, 15 (Aug. 2012), 3044–3055.

[162] Li, Y., and Meng, J. Al-doping effects on structure and optical properties of ZnO nanostructures. *Materials Letters 117* (Feb. 2014), 260–262.

[163] Lin, J.-P., and Wu, J.-M. The effect of annealing processes on electronic properties of sol-gel derived Al-doped ZnO films. *Applied Physics Letters 92*, 13 (2008), 134103.

[164] Liu, J., RÃ¤dlein, E., and Frischat, G. H. Preparation, nanostructure and properties of indium tin oxide (ito) films on glass substrates. part 1. preparation and nanostructure. *Physics and Chemistry of Glasses 40*, 5 (1999), 277–281.

[165] Livage, J., Henry, M., and Sanchez, C. Sol-gel chemistry of transition metal oxides. *Progress in Solid State Chemistry 18* (1988).

[166] Loudet, J., Alsayed, a., Zhang, J., and Yodh, a. Capillary Interactions Between Anisotropic Colloidal Particles. *Physical Review Letters 94*, 1 (Jan. 2005), 018301.

[167] Loudet, J., Yodh, a., and Pouligny, B. Wetting and Contact Lines of Micrometer-Sized Ellipsoids. *Physical Review Letters 97*, 1 (July 2006), 018304.

[168] Ma, Q.-B., Ye, Z.-Z., He, H.-P., Hu, S.-H., Wang, J.-R., Zhu, L.-P., Zhang, Y.-Z., and Zhao, B.-H. Structural, electrical, and optical properties of transparent conductive ZnO:Ga films prepared by DC reactive magnetron sputtering. *Journal of Crystal Growth 304*, 1 (June 2007), 64–68.

[169] Madivala, B., Fransaer, J., and Vermant, J. Self-assembly and rheology of ellipsoidal particles at interfaces. *Langmuir 25*, 5 (Mar. 2009), 2718–28.

[170] Man, P. P., and Klinowski, J. Quantitative determination of aluminium in zeolites by solid-state 27al n.m.r. spectroscopy. *J. Chem. Soc., Chem. Commun.* (1988), 1291–1294.

[171] Marković, S., Mitrić, M., Starcević, G., and Uskoković, D. Ultrasonic de-agglomeration of barium titanate powder. *Ultrasonics sonochemistry 15*, 1 (Jan. 2008), 16–20.

[172] Martins, R., Fortunato, E., Barquinha, P., and Pereira, L. *Transparent Oxide Electronics: From Materials to Devices*. Wiley, 2012.

[173] Martins, R., Fortunato, E., Nunes, P., Ferreira, I., and Marques, A. Zinc oxide as an ozone sensor. *Journal of Applied Physics 96*, 3 (2004), 1398–1408.

[174] Matsubara, K., Fons, P., Iwata, K., Yamada, a., and Niki, S. Room-temperature deposition of Al-doped ZnO films by oxygen radical-assisted pulsed laser deposition. *Thin Solid Films 422*, 1-2 (Dec. 2002), 176–179.

[175] McCluskey, M. D., Jokela, S. J., Zhuravlev, K. K., Simpson, P. J., and Lynn, K. G. Infrared spectroscopy of hydrogen in ZnO. *Applied Physics Letters 81*, 20 (2002), 3807.

[176] Mei-zhen, G. A. O., Feng, Z., Jing, L. I. U., Hui-na, S. U. N., Transparent, C., Zno, A.-d., Pro, P., and S, H. Effect of Annealing Conditions on Properties of Sol-Gel Derived Al-Doped ZnO. *Chinese Physics Letters 26*, 8 (2009), 2–5.

[177] Meyer, B. K., Sann, J., Hofmann, D. M., Neumann, C., and Zeuner, A. Shallow donors and acceptors in ZnO. *Sem 20*, 4 (2005), S62–S66.

[178] Miao, S., D'Alnoncourt, R. N., Reinecke, T., Kasatkin, I., Behrens, M., Schlögl, R., and Muhler, M. A Study of the Influence of Composition on the Microstructural Properties of ZnO/Al 2 O 3 Mixed Oxides. *European Journal of Inorganic Chemistry 2009*, 7 (Mar. 2009), 910–921.

[179] Minami, T. New n -Type. *MRS bullletin 25*, 08 (2000), 38–44.

[180] Minami, T. Transparent conducting oxide semiconductors for transparent electrodes. *Semiconductor Science and Technology 20*, 4 (Apr. 2005), S35–S44.

[181] Minami, T., Sato, H., Nonto, H., and Takata, S. Group III Impurity Doped Zinc Oxide Thin Films Prepared by RF Magnetron Sputtering. *Japanese Journal of Applied Physics 25*, 10 (1985), 781–784.

[182] Minami, T., Sonohara, H., Takata, S., and Sato, H. Transparent and conductive zno thin films prepared by atmospheric-pressure chemical vapor deposition using zinc acetylacetonate. *Japanese Journal of Applied Physics 33*, 5B (1994), L743.

[183] Mitzi, D. *Solution Processing of Inorganic Materials*. Wiley, 2008.

[184] Moeck, P., and Rouvimov, S. Precession electron diffraction and its advantages for structural fingerprinting in the transmission electron microscope. *Zeitschrift für Kristallographie International journal for structural, physical, and chemical aspects of crystalline materials 225*, 2-3 (2010), 110–124.

[185] Moghri Moazzen, M. A., Borghei, S. M., and Taleshi, F. Change in the morphology of ZnO nanoparticles upon changing the reactant concentration. *Applied Nanoscience 3*, 4 (July 2012), 295–302.

[186] Mondelaers, D. De synthese en karakterisering van zno nanopoeders en dunne films bereid vanuit waterige oplossing.

[187] Mondelaers, D., Vanhoyland, G., Van den Rul, H., Van Bael, M. K., Mullens, J., and Van Poucke, L. C. Chemical Solution Deposition of ZnO Thin Films by an Aqueous Solution. *Journal of Sol-Gel Science and Technology 26*, 1-3 (2003), 523–526.

[188] Moreels, I., Fritzinger, B., Martins, J. C., and Hens, Z. Surface chemistry of colloidal PbSe nanocrystals. *Journal of the American Chemical Society 130*, 45 (Nov. 2008), 15081–15086.

[189] Moreels, I., Martins, J., and Hens, Z. Solution NMR techniques for investigating colloidal nanocrystal ligands: A case study on trioctylphosphine oxide at InP quantum dots. *Sensors and Actuators B: Chemical 126*, 1 (Sept. 2007), 283–288.

[190] Moss, T. S. The interpretation of the properties of indium antimonide. *Proceedings of the Physical Society. Section B 67*, 10 (1954), 775.

[191] Mullens, J. Chapter 12 ega - evolved gas analysis. In *Principles and Practic*, M. E. Brown, Ed., vol. 1 of *Handbook of Thermal Analysis and Calorimetry*. Elsevier Science B.V., 1998, pp. 509 – 546.

[192] Munir, Z. Field effects in self-propagating solid-state synthesis reactions. *Solid State Ionics 101-103* (Nov. 1997), 991–1001.

[193] Musat, V., Teixeira, B., Fortunato, E., Monteiro, R., and Vilarinho, P. Al-doped ZnO thin films by sol-gel method. *Surface and Coatings Technology 180-181* (Mar. 2004), 659–662.

[194] Myong, S. Y., and Lim, K. S. Highly stable and textured hydrogenated ZnO thin films. *Applied Physics Letters 82*, 18 (2003), 3026.

[195] Navale, S., Ravi, V., Mulla, I., Gosavi, S., and Kulkarni, S. Low temperature synthesis and NO_x sensing properties of nanostructured Al-doped ZnO. *Sensors and Actuators B: Chemical 126*, 2 (Oct. 2007), 382–386.

[196] Niederberger, M., and Pinna, N. *Metal Oxide Nanoparticles in Organic Solvents: Synthesis, Formation, Assembly and Application*. Engineering Materials and Processes. Springer, 2009.

[197] Nishio, K., Miyake, S., Sei, T., Watanabe, Y., and Tsuchiya, T. Preparation of highly oriented thin film exhibiting transparent conduction by the sol-gel process. *Journal of Materials Science 31*, 14 (1996), 3651–3656.

[198] Oba, F., Nishitani, S. R., Isotani, S., Adachi, H., and Tanaka, I. Energetics of native defects in ZnO. *Journal of Applied Physics 90*, 2 (2001), 824.

[199] Ohishi, T., Maekawa, S., and Katoh, A. Synthesis and properties of tantalum oxide films prepared by the sol-gel method using photoirradiation. *Journal of Non-Crystalline Solids 147-148* (1992), 493–498.

[200] Ohyama, M. Sol-Gel Preparation of Transparent and Conductive Aluminum-Doped Zinc Oxide Films with Highly Preferential Crystal Orientation. *Journal of American Ceramic Society 81*, 6 (1998), 1622–1632.

[201] Oliveira, M., Chen, K., and Ferreira, J. Influence of the deagglomeration procedure on aqueous dispersion, slip casting and sintering of si_3n_4-based ceramics. *Journal of the European Ceramic Society 22*, 9 (2002).

[202] Onsosyen, E., and Skaugrud, O. Metal recovery using chitosan. *Journal of Chemical Technology and Biotechnology (Wiley) 49* (1990).

[203] Ozin, G., Arsenault, A., Cademartiri, L., and of Chemistry (Great Britain), R. S. *Nanochemistry: A Chemical Approach to Nanomaterials*. Royal Society of Chemistry, 2009.

[204] P, P. Method of preparing lead and alkaline earth titanates and niobates and coating method using the same to form a capacitor, July 11 1967. US Patent 3,330,697.

[205] Palmer, J., and Grant, B. *The Art of Radiometry*. SPIE Press monograph. SPIE Press, 2010.

[206] Pang, Q., Shi, J., Liu, Y., Xing, D., Gong, M., and Xu, N. A novel approach for preparation of Y_2O_3:Eu^{3+} nanoparticles by microemulsion-microwave heating. *Materials Science and Engineering: B 103*, 1 (Sept. 2003), 57–61.

[207] Pang, S., Hernandez, Y., Feng, X., and MÃ¼llen, K. Graphene as transparent electrode material for organic electronics. *Advanced Materials 23* (2011).

[208] Park, K. C., Ma, D. Y., and Kim, K. H. The physical properties of al-doped zinc oxide films prepared by rf magnetron sputtering. *Thin Solid Films 305* (1997).

[209] Pasquarelli, R. M., Ginley, D. S., and O'Hayre, R. Solution processing of transparent conductors: from flask to film. *Chem. Soc. Rev. 40* (2011), 5406–5441.

[210] Patil, K. *Chemistry of Nanocrystalline Oxide Materials: Combustion Synthesis, Properties and Applications*. World Scientific, 2008.

[211] Patil, K. C., Aruna, S., and Mimani, T. Combustion synthesis: an update. *Current Opinion in Solid State and Materials Science 6*, 6 (Dec. 2002), 507–512.

[212] Perelaer, J., de Gans, B.-J., and Schubert, U. S. Ink-jet Printing and Microwave Sintering of Conductive Silver Tracks. *Advanced Materials 18*, 16 (Aug. 2006), 2101–2104.

[213] Pern, F. J., To, B., Glick, S. H., Sundaramoorthy, R., DeHart, C., Glynn, S., and Perkins, C. Variations in damp heat-induced degradation behavior of sputtered ZnO window layer for CIGS solar cells. *Proceedings of SPIE 7773* (2010), 77730R.

[214] Peys, N., Ling, Y., Dewulf, D., Gielis, S., De Dobbelaere, C., Cuypers, D., Adriaensens, P., Van Doorslaer, S., De Gendt, S., Hardy, A., and Van Bael, M. K. V_6O_{13} films by control of the oxidation state from aqueous precursor to crystalline phase. *Dalton Transactions 42* (2013).

[215] Pinna, N., Garnweiter, G., Antonietti, M., and Niederberger, M. A General Nonaqueous Route to Binary Metal Oxide Nanocrystals Involving a C-C Bond Cleavage. *Journal of the American Chemical Society 127*, 15 (2005), 5608–5612.

[216] Pretsch, E., Bühlmann, P., and Badertscher, M. *Structure Determination of Organic Compounds: Tables of Spectral Data*. SpringerLink: Springer e-Books. Springer, 2009.

[217] Puetz, J., and Aegerter, M. A. Direct gravure printing of indium tin oxide nanoparticle patterns on polymer foils. *Thin Solid Films 516* (2008), 4495–4501.

[218] Puetz, J., Al-Dahoudi, N., and Aegerter, M. Processing of Transparent Conducting Coatings Made With Redispersible Crystalline Nanoparticles. *Advanced Engineering Materials 6*, 9 (Sept. 2004), 733–737.

[219] Rahman, A., Jayaganthan, R., and Chandra, R. Study of structural and optical properties of $Zn_{1-x}Al_xO$ nanoparticles. *Materials Science in Semiconductor Processing 18* (Feb. 2014), 15–21.

[220] Ramanathan, K., Contreras, M. A., Perkins, C. L., Asher, S., Hasoon, F. S., Keane, J., Young, D., Romero, M., Metzger, W., Noufi, R., Ward, J., and Duda, A. Properties of 19.2cells. *Progress in Photovoltaics: Research and Applications 11*, 4 (2003), 225–230.

[221] Repins, I., Contreras, M. A., Egaas, B., Dehart, C., Scharf, J., and Perkins, C. L. 19,9 % - efficient ZnO / CdS / CuInGaSe Solar Cell with 81,2 % Fill Factor. *Progress in Photovoltaics: Research and Applications 16*, February (2008), 235–239.

[222] Riahi-Noori, N., Sarraf-Mamoory, R., Alizadeh, P., and Mehdikhani, A. Synthesis of ZnO nano powder by a gel combustion method. *Journal of Ceramic Processing Research 9*, 3 (2008), 246–249.

[223] Ring, T. *Fundamentals of Ceramic Powder Processing and Synthesis*. Elsevier Science, 1996.

[224] Ritter, E. J., Scott, W. J., Randall, J. L., and Ritter, J. M. Teratogenicity of Dimethoxyethyl Phthalate and Its Metabolites Methoxyethanol and Methoxyacetic Acid in the Rat. *Teratology 32*, 1 (1985), 25–31.

[225] Roth, A. P., Webb, J. B., and Williams, D. F. Absorption edge shift in zinc oxide thin films at high carrier densities. *Solid State Communications 39*, 12 (1981), 1269–1271.

[226] Rousset, J., Saucedo, E., Herz, K., and Lincot, D. High efficiency CIGS-based solar cells with electrodeposited ZnO:Cl as transparent conducting oxide front contact. *Progress in Photovoltaics: Research and Applications 19*, 5 (2011), 537–546.

[227] Rousset, J., Saucedo, E., and Lincot, D. Extrinsic Doping of Electrodeposited Zinc Oxide Films by Chlorine for Transparent Conductive Oxide Applications. *Chemistry of Materials 21*, 3 (Feb. 2009), 534–540.

[228] Rul, H., Mondelaers, D., Bael, M. K., and Mullens, J. Water-based wet chemical synthesis of (doped) ZnO nanostructures. *Journal of Sol-Gel Science and Technology 39*, 1 (Apr. 2006), 41–47.

[229] Sagar, P., Kumar, M., and Mehra, R. Influence of hydrogen incorporation in sol-gel derived aluminum doped ZnO thin films. *Thin Solid Films 489*, 1-2 (Oct. 2005), 94–98.

[230] Sahu, D., Lin, S.-Y., and Huang, J.-L. Improved properties of Al-doped ZnO film by electron beam evaporation technique. *Microelectronics Journal 38*, 2 (Feb. 2007), 245–250.

[231] Saita, S., and Maenosono, S. FePt Nanoparticles with a Narrow Composition Distribution Synthesized via Pyrolysis of Iron(III) Ethoxide and Platinum(II) Acetylacetonate. *Chemistry of Materials 17*, 14 (July 2005), 3705–3710.

[232] Saito, K., Nakamura, J., and Natori, A. Ballistic thermal conductance of a graphene sheet. *Physical Review B 76* (2007).

[233] Saito, N., and Haneda, H. Hierarchical structures of zno spherical particles synthesized solvothermally. *Science and Technology of Advanced Materials 12*, 6 (2011), 064707.

[234] Salam, S., Islam, M., and Akram, A. Sol-gel synthesis of and aluminum-doped zinc oxide thin films as transparent conducting oxides for thin film solar cells. *Thin Solid Films 529* (Feb. 2013), 242–247.

[235] Samoson, A., Lippmaa, E., and Pines, A. High resolution solid-state n.m.r. *Molecular Physics 65*, 4 (1988), 1013–1018.

[236] Sanchez-Rodriguez, D., Farjas, J., Roura, P., Ricart, S., Mestres, N., Obradors, X., and Puig, T. Thermal Analysis for Low Temperature Synthesis of Oxide Thin Films from Chemical Solutions. *The Journal of Physical Chemistry C 117*, 39 (Oct. 2013), 20133–20138.

[237] Saniz, R., Xu, Y., Matsubara, M., Amini, M., Dixit, H., Lamoen, D., and Partoens, B. A simplified approach to the band gap correction of defect formation energies: Al, Ga, and In-doped ZnO. *Journal of Physics and Chemistry of Solids 74*, 1 (Jan. 2013), 45–50.

[238] Sato, H., Minami, T., Takata, S., and Yamada, T. Transparent conducting p-type NiO thin films prepared by magnetron sputtering. *Thin Solid Films 236*, 1-2 (Dec. 1993), 27–31.

[239] Schellens, K., Capon, B., De Dobbelaere, C., Detavernier, C., Hardy, a., and Van Bael, M. Solution derived ZnO:Al films with low resistivity. *Thin Solid Films 524* (Dec. 2012), 81–85.

[240] Schleber, M., Tsach, T., Maharizi, M., Levinsky, M., Zhou, B., Golosovsky, M., and Davidov, D. Films of bscco superconductors prepared by spray pyrolysis of carboxylates. *Cryogenics 30* (1990).

[241] Schneller, T., Waser, R., Kosec, M., and Payne, D. *Chemical Solution Deposition of Functional Oxide Thin Films*. SpringerLink : Bücher. Springer Vienna, 2014.

[242] Schuler, T., and Aegerter, M. Optical, electrical and structural properties of sol gel ZnO:Al coatings. *Thin Solid Films 351*, 1-2 (Aug. 1999), 125–131.

[243] Schwartz, R. W., Schneller, T., and Waser, R. Chemical solution deposition of electronic oxide films. *Comptes Rendus Chimie 7*, 5 (2004), 433 – 461.

[244] Sengupta, J., Sahoo, R., and Mukherjee, C. Effect of annealing on the structural, topographical and optical properties of sol-gel derived ZnO and AZO thin films. *Materials Letters 83* (Sept. 2012), 84–87.

[245] Serier, H., Gaudon, M., and Ménétrier, M. Al-doped ZnO powdered materials: Al solubility limit and IR absorption properties. *Solid State Sciences 11*, 7 (July 2009), 1192–1197.

[246] Shannon, R. D. Revised Effective Ionic Radii and Systematic Studies of Interatomie Distances in Halides and Chaleogenides of Shannon & Prewitt [Acta. *Acta. Cryst. 32*, 5 (1976), 751–767.

[247] Shishiyanu, S. T., Lupan, O. I., Monaico, E. V., Ursaki, V. V., Shishiyanu, T. S., and Tiginyanu, I. M. Photoluminescence of chemical bath deposited ZnO : Al films treated by rapid thermal annealing. *Thin Solid Films 488*, 1-2 (2005), 15–19.

[248] Shukla, R. K. . A., Srivastava, A., Srivastava, A., and Dubey, K. C. Growth of transparent conducting nanocrystalline Al doped ZnO thin films by pulsed laser deposition. *Journal of Crystal Growth 294*, 2 (2006), 427–431.

[249] Si, R., Zhang, Y.-W., You, L.-P., and Yan, C.-H. Rare-earth oxide nanopolyhedra, nanoplates, and nanodisks. *Angewandte Chemie International Edition 44*, 21 (2005), 3256–3260.

[250] Simpson, J. *Organic Structure Determination Using 2-D NMR Spectroscopy: A Problem-based Approach*. Organic Structure Determination Using 2-D NMR Spectroscopy: A Problem-based Approach. Elsevier/AP, 2012.

[251] Sinnaeve, D. The Stejskal - Tanner Equation Generalized for Any Gradient Shape - An Overview of Most Pulse Sequences Measuring Free Diffusion. *Concepts Magn. Reson. Part A 40A*, 2 (2012), 39–65.

[252] Skoog, D., Holler, F., and Crouch, S. *Principles of Instrumental Analysis*. International student edition. Thomson Brooks/Cole, 2007.

[253] Sorrell, T. *Interpreting spectra of organic molecules*. Series of books in organic chemistry. University Science Books, 1988.

[254] Stary, J., and Liljenzin, J. O. Critical evaluation of equilibrium constants involving acetylacetone and its metal chelates. *Pure and Applied Chemistry 54*, 12 (1982), 2557–2592.

[255] Sun, B., Baltisberger, J., Wu, Y., Samoson, A., and Pines, A. Sidebands in dynamic angle spinning (das) and double rotation (dor) nmr. *Solid State Nuclear Magnetic Resonance 1*, 5 (1992), 267 – 295.

[256] Sun, S., Murray, C. B., Weller, D., Folks, L., and Moser, A. Monodisperse FePt Nanoparticles and Ferromagnetic FePt Nanocrystal Superlattices. *Science 287*, 5460 (2000), 1989–1992.

[257] Sun, S., Zeng, H., Robinson, D. B., Raoux, S., Rice, P. M., Wang, S. X., and Li, G. Monodisperse MFe2O4 (M = Fe, Co, Mn) nanoparticles. *Journal of the American Chemical Society 126*, 1 (Jan. 2004), 273–9.

[258] Sun, Y., and Wang, H. The electronic properties of native interstitials in ZnO. *Physica B: Condensed Matter 325* (Jan. 2003), 157–163.

[259] Suzuki, A., Matsushita, T., Wada, N., Sakamoto, Y., and Okuda, M. Transparent Conducting Al-Doped ZnO Thin Films Prepared by Pulsed Laser Deposition. *Japanese Journal of Applied Physics 35*, 1A (1996), L56–L59.

[260] Szyszka, B. Transparent and conductive aluminum doped zinc oxide prepared by mid-frequency reactive magnetron sputtering. *Thin Solid Films 351* (1999), 164–169.

[261] Tahar, R. B. H., and Tahar, N. B. H. Mechanism of carrier transport in aluminum-doped zinc oxide. *Journal of Applied Physics 92*, 8 (2002), 4498.

[262] Tang, W., and Cameron, D. C. Aluminum-doped zinc oxide transparent conductors deposited by the sol-gel process. *Thin Solid Films 238* (1994), 83–87.

[263] Tarasov, K., and Raccurt, O. A wet chemical preparation of transparent conducting thin films of Al-doped ZnO nanoparticles. *Journal of Nanoparticle Research 13*, 12 (Sept. 2011), 6717–6724.

[264] Tchelidze, T., Chikoidze, E., Gorochov, O., and Galtier, P. Perspectives of chlorine doping of ZnO. *Thin Solid Films 515*, 24 (Oct. 2007), 8744–8747.

[265] Tchelidze, T., Chikoidze, E., Gorochov, O., and Galtier, P. Perspectives of chlorine doping of ZnO. *Thin Solid Films 515*, 24 (Oct. 2007), 8744–8747.

[266] Tellier, C. R., and Tosser, A. J. The Mayadas-Shatzkes conduction model treated as a Fuchs-Sondheimer model. *Thin Solid Films 44* (1977), 201–208.

[267] Thu, T. V., and Maenosono, S. Synthesis of high-quality Al-doped ZnO nanoink. *Journal of Applied Physics 107*, 1 (2010), 014308.

[268] Tokumoto, M., Smith, a., Santilli, C., Pulcinelli, S., a.F Craievich, Elkaim, E., Traverse, a., and Briois, V. Structural electrical and optical properties of undoped and indium doped ZnO thin films prepared by the pyrosol process at different temperatures. *Thin Solid Films 416*, 1-2 (Sept. 2002), 284–293.

[269] Tokumoto, M. S., Smith, A., Santilli, C. V., Pulcinelli, S. H., Elkaim, E., and Briois, V. Effect of In concentration in starting solution on the structural and electrical properties of ZnO films prepared by the pyrosol process at 450 °C. *Journal of Non-Crystalline Solids 273*, 1-3 (2000), 302–306.

[270] Trekker, J., Jans, K., Damm, H., Mertens, D., Nuytten, T., Vanacken, J., Moshchalkov, V., D'Haen, J., Stakenborg, T., Van Roy, W., Himmelreich, U., and Lagae, L. Synthesis of PEGylated Magnetic Nanoparticles With Different Core Sizes. *IEEE Transactions on Magnetics 49*, 1 (Jan. 2013), 219–226.

[271] Trottier, C. M., Glatkowski, P., Wallis, P., and Luo, J. Properties and characterization of carbon-nanotube-based transparent conductive coating. *Journal of the Society for Information Display 13*, 9 (2005), 759–763.

[272] Tsang, W., Wong, F., Fung, M., Chang, J., Lee, C., and Lee, S. Transparent conducting aluminum-doped zinc oxide thin film prepared by sol-gel process followed by laser irradiation treatment. *Thin Solid Films 517*, 2 (Nov. 2008), 891–895.

[273] Tsuchiya, T., Emoto, T., and Sei, T. Preparation and properties of transparent conductive thin films by the sol-gel process. *Journal of Non-Crystalline Solids 178* (1994), 327–332.

[274] Tsunashima, A., Asai, T., Kodaira, K., and Matsushita, T. Preparation of tin-doped indium oxide thin films by thermal decomposition of metal octanoates. *Chemistry Letters 7*, 8 (1978), 855–856.

[275] Tsunekawa, S., Ishikawa, K., Li, Z., Kawazoe, Y., and Kasuya, A. Origin of Anomalous Lattice Expansion in Oxide Nanoparticles. *Physical Review Letters 85*, 16 (2000), 3440–3443.

[276] Van Bael, M. K., Kareiva, A., Nouwen, R., Schildermans, I., Vanhoyland, G., D'Haen, J., Olieslaeger, M. D., Franco, D., Mullens, J., Yperman, J., and Poucke, L. C. V. Sol-gel synthesis and properties of $YBa_2(Cu_{1-x}M_x)_4O_y$ ($M = Co, Ni$) and effects of additional replacement of yttrium by calcium. *International Journal of Inorganic Materials 1*, 1999 (2006), 259–268.

[277] Van Bael, M. K., Nelis, D., Hardy, A., Mondelaers, D., Van Werde, K., D'Haen, J., Vanhoyland, G., Van Den Rul, H., Mullens, J., Van Poucke, L. C., Frederix, F., and Wouters, D. J. Aqueous chemical solution deposition of ferroelectric thin films. *Integrated Ferroelectrics 45* (01 2002).

[278] Van De Walle CG. Hydrogen as a cause of doping in zinc oxide. *Physical review letters 85*, 5 (July 2000), 1012–1015.

[279] Van Den Rul, H., Van Bael, M. K. V., Hardy, A., Van Werde, K., and Mullens, J. Aqueous Solution-Based Synthesis of Nanostructured Metal Oxides. In *Handbook of Nanoceramics and Their Based Nanodevices*, vol. XX. 2008, pp. 1–34.

[280] Van Werde, K., Mondelaers, D., Vanhoyland, G., Nelis, D., Van Bael, M. K., Mullens, J., Van Poucke, L. C., Van Der Veken, B., and Desseyn, H. O. Thermal decomposition of the ammonium zinc acetate citrate precursor for aqueous chemical solution deposition of zno. *Journal of Materials Science 37* (2002).

[281] Virlet, A. L. J. Towards high-resolution nmr of more nuclei in solids: Sample spinning with time-dependent spinner axis angle. *Chemical Physics Letters 152* (1988).

[282] Von Hoene, J., Charles, R. G., and Hickam, W. M. Thermal decomposition of metal acetylacetonates: Mass spectrometer studies. *The Journal of Physical Chemistry 62*, 9 (1958), 1098–1101.

[283] Vosgueritchian, M., Lipomi, D. J., and Bao, Z. Highly conductive and transparent pedot:pss films with a fluorosurfactant for stretchable and flexible transparent electrodes. *Advanced Functional Materials 22*, 2 (2012), 421–428.

[284] Vunnam, S., Ankireddy, K., Kellar, J., and Cross, W. Highly transparent and conductive Al-doped ZnO nanoparticulate thin films using direct write processing. *Nanotechnology 25*, 19 (May 2014), 195301.

[285] Wang, A., Dai, J., Cheng, J., Chudzik, M. P., Marks, T. J., Chang, R. P. H., and Kannewurf, C. R. Charge transport, optical transparency, microstructure, and processing relationships in transparent conductive indium-zinc oxide films grown by low-pressure metal-organic chemical vapor deposition. *Applied Physics Letters 73*, 3 (1998), 327–329.

[286] Wang, F.-H., Chang, H.-P., Tseng, C.-C., and Huang, C.-C. Effects of H2 plasma treatment on properties of ZnO:Al thin films prepared by RF magnetron sputtering. *Surface and Coatings Technology 205*, 23-24 (Sept. 2011), 5269–5277.

[287] Wang, X., Zhi, L., and Müllen, K. Transparent, conductive graphene electrodes for dye-sensitized solar cells. *Nano Letters 8*, 1 (2008), 323–327.

[288] Weber, D., Botnaras, S., Pham, D. V., Merkulov, A., Steiger, J., Schmechel, R., and De Cola, L. A Facile Solution-Doping Method to Improve a Low-Temperature Zinc Oxide Precursor: Towards Low-Cost Electronics on Plastic Foil. *Advanced Functional Materials 24*, 17 (May 2014), 2537–2543.

[289] Weller, M. *Inorganic Materials Chemistry*. Ocp Series. Oxford University Press, 1994.

[290] Wu, H., Yang, Y., and Cao, Y. C. Synthesis of colloidal uranium-dioxide nanocrystals. *Journal of the American Chemical Society 128*, 51 (Dec. 2006), 16522–16523.

[291] Wu, K., Yu, C., Chang, Y., and Horng, D. Effect of pH on the formation and combustion process of sol-gel auto-combustion derived NiZn ferrite/SiO_2 composites. *Journal of Solid State Chemistry 177*, 11 (Nov. 2004), 4119–4125.

[292] Wu, Z., Chen, Z., Du, X., Logan, J. M., Sippel, J., Nikolou, M., Kamaras, K., Reynolds, J. R., Tanner, D. B., Hebard, A. F., and Rinzler, A. G. Transparent, conductive carbon nanotube films. *Science (New York, N.Y.) 305*, 5688 (Aug. 2004), 1273–6.

[293] Xu, X., Zhuang, J., and Wang, X. Sno2 quantum dots and quantum wires: Controllable synthesis, self-assembled 2d architectures, and gas-sensing properties. *Journal of the American Chemical Society 130*, 37 (2008), 12527–12535.

[294] Yuan, C. C., Yang, Y.-F., Xi, X. K., Cui, J., and Xiang, J. F. Solid state 27Al NMR investigation of Knight shift tensors of LnAl2 (Ln = Y, La and Lu) and correlation with DFT calculations. *Solid state nuclear magnetic resonance 41* (Feb. 2012), 28–31.

[295] Yunker, P. J., Still, T., Lohr, M. a., and Yodh, a. G. Suppression of the coffee-ring effect by shape-dependent capillary interactions. *Nature 476*, 7360 (Aug. 2011), 308–11.

[296] Zamiri, R., Singh, B., Scott Belsley, M., and Ferreira, J. Structural and dielectric properties of Al-doped ZnO nanostructures. *Ceramics International 40*, 4 (May 2014), 6031–6036.

[297] Zhan, Z., Zhang, J., Zheng, Q., Pan, D., Huang, J., Huang, F., and Lin, Z. Strategy for preparing al-doped zno thin film with high mobility and high stability. *Crystal Growth & Design 11*, 1 (2011), 21–25.

[298] Zhang, Y., Yang, Y., and Zhao, J. Optical and electrical properties of aluminum-doped zinc oxide nanoparticles. *Journal of Materials Science 46*, 3 (2010), 774–780.

[299] Zhang, Z., Zhong, X., Liu, S., Li, D., and Han, M. Aminolysis route to monodisperse titania nanorods with tunable aspect ratio. *Angewandte Chemie International Edition 44*, 22 (2005), 3466–3470.

[300] Zhao, J., Tan, R., Zhang, Y., Yang, Y., Guo, Y., and Zhang, X. Characterization of Aluminum-Doped Zinc Oxide Nanoparticle. *Journal of American Ceramic Society 94*, 3 (2011), 725–728.

[301] Zhu, M., Huang, H., Gong, J., Sun, C., and Jiang, X. Role of oxygen desorption during vacuum annealing in the improvement of electrical properties of aluminum doped zinc oxide films synthesized by sol gel method. *Journal of Applied Physics 102*, 4 (2007), 043106.

[302] Zhuang, H. R., Kozuka, H., and Sakka, S. Preparation of superconducting Bi-Sr-Ca-Cu-O ceramics by the sol-gel method. *Journal of Materials Science 25*, 11 (Nov. 1990), 4762–4766.

[303] Zürcher, S., and Graule, T. Influence of dispersant structure on the rheological properties of highly-concentrated zirconia dispersions. *Journal of the European Ceramic Society 25*, 6 (Mar. 2005), 863–873.